

Doctoral Programme in Mechanical, Fluids and Aerospace Engineering

Universitat Politècnica de Catalunya (UPC)

Departament de Ciència dels Materials i Enginyeria Metal·lúrgica (CMEM)

Escola Superior d'Enginyeries Industrial, Aeroespacial i
Audiovisual de Terrassa (ESEIAAT)

Development of the *In Situ* Forming of a Liquid Infused Preform (ISFLIP) process

**A new manufacturing technique for high performance
Fibre Reinforced Polymer (FRP) components**

(Vol. 1 of 2 Vol.)

by

Jaime Juan Muñoz

Supervisor: Dr. Núria Salán Ballesteros

Thesis submitted to the Universitat Politècnica de Catalunya (UPC)

for the degree of Doctor of Philosophy, May 2017

This page intentionally left blank

Abstract

A problem is not a problem anymore if no solution exists; therefore, in the present dissertation, a novel manufacturing technique, the *In Situ* Forming of a Liquid Infused Preform (ISFLIP), is proposed as a solution to some typical problems that manufacturing of Fibre Reinforced Polymer (FRP) parts through Vacuum Infusion (VI) involves, such as not taking advantage of the full potential of FRPs, long processing times and lack of reproducibility.

ISFLIP is a hybrid process between VI and diaphragm forming in which a flat preform of a stack of reinforcement fabrics is firstly impregnated with a low viscosity matrix and, then, formed over a mould while the matrix is still in the low viscosity state. Being focused on high performance FRPs and shell components, from simple to complex double curvature shapes, a number of trade-offs between VI and diaphragm forming were overcome to lay the foundations from which ISFLIP ability to manufacture FRP components has been proven.

In order to adopt a VI manufacturing methodology that fitted ISFLIP targets, important contributions to more general VI have also been made in terms of part quality optimization, addressing the major concern that void content is in VI, with competitive manufacturing times. An effective vacuum degassing process in which bubble formation is enhanced through high speed stirring, and a non-conventional filling and post-filling strategy are proposed for this purpose. Eventually, void content was virtually eliminated and post-filling time minimized without affecting fibre content.

In ISFLIP, textile preforms are formed together with a series of auxiliary materials (plastic films and sheets, textile fabrics and knitted meshes), most of them showing different in-plane deformation mechanisms. Forming performance of preforms, as well as final part quality, are severely affected by interactions between all these materials different in nature. Uncertainties on this respect and an initial evaluation of attainable shapes were also addressed to define a more focused research plan to the final goal, still distant, of implementing ISFLIP in a real production environment.

Results obtained throughout the research project give cause for reasonable optimism in ISFLIP potential and future prospects.

Resumen

Un problema deja de ser un problema si no existe solución; por lo tanto, en esta disertación, una novedosa técnica de fabricación, el Conformado In Situ de una Preforma Infusionada con resina Líquida (ISFLIP, por sus siglas en inglés), se propone como solución a algunos problemas típicos relacionados con la fabricación de piezas de Polímero Reforzado con Fibra (FRP) a través de la Infusión por Vacío (VI), problemas tales como el desaprovechamiento de todo el potencial de los FRPs, largos tiempos de procesado y falta de reproducibilidad.

ISFLIP es un proceso híbrido entre la VI y el conformado por membrana elástica en el que una preforma plana formada a partir de un apilado de tejidos de refuerzo es en primera instancia impregnada con una resina de baja viscosidad y, entonces, conformada sobre un molde mientras que la matriz permanece todavía en el estado de baja viscosidad. Estando centrado en los FRPs de altas prestaciones y en componentes con formas tipo concha, desde curvaturas simples hasta formas con doble curvatura complejas, un número importante de compensaciones entre la VI y el conformado por membrana se han ido superado para asentar las bases a partir de las cuales se ha probado la capacidad de ISFLIP para fabricar componentes de FRP.

Con la vista puesta en implementar una metodología de fabricación por VI que cumpliera los objetivos definidos para ISFLIP, también se han realizado importantes contribuciones de carácter más general relacionadas con la VI en términos de optimización de parámetros de calidad de las piezas, abordando la gran preocupación que la porosidad final supone en la VI, y consiguiendo unos tiempos de fabricación competitivos. Con este propósito se han propuesto un proceso de desgasificación por vacío muy efectivo en el que se favorece la nucleación de burbujas mediante la agitación a alta velocidad, y una prometedora y no convencional estrategia de llenado y post-llenado de la preforma. Finalmente, se consiguió virtualmente eliminar la porosidad atrapada en las piezas, minimizando el tiempo de post-llenado sin afectar la fracción de fibra contenida.

En ISFLIP las preformas textiles se conforman junto con una serie de materiales auxiliares (films y hojas plásticas, mallas y tejidos textiles), que muestran diferentes mecanismos de deformación en plano. El conformado de las preformas y el acabado final de las piezas se ve severamente afectado por todas las interacciones entre todos estos materiales diferentes en naturaleza. También se han abordado las incertidumbres que surgen al respecto y una evaluación inicial de las geometrías abarcables para definir un plan de investigación más concreto con el que poder afrontar la meta final, todavía distante, de implementar ISFLIP en un entorno productivo real.

Los resultados obtenidos a lo largo de este proyecto de investigación permiten ser razonablemente optimistas en cuanto al potencial de ISFLIP y sus expectativas.

Keywords

Composite material, Degassing, Design of Experiments (DOE), Dry Fibre technology, Fibre Reinforced Polymer (FRP), Fibre volume fraction, Forming, Manufacturing, Porosity, Vacuum Infusion (VI).

Preface

The initial motivation and origin of this project was to solve the recurring problem of dry fibre textiles manipulation. The inevitable fabric distortions during handling and the intricate manual forming over complex shape moulds compromise reproducibility of parts manufactured through Liquid Composite Moulding (LCM) techniques, such as Vacuum Infusion (VI).

In response to this issue, and taking advantage of the experience of the Institut d'Investigació Tèxtil i Cooperació Industrial de Terrassa. (INTEXTER) in textiles and SENER Ingeniería y Sistemas interest in composite manufacturing, a novel manufacturing technique combining VI and forming was proposed to mitigate the detrimental effects of dry fabrics manipulation. The development of this new process, the *In Situ* Forming of a Liquid Infused Preform (ISFLIP), was the main core of the research project presented in this dissertation, reaching also noteworthy conclusions concerning VI manufacturing.

After starting working with composite materials during my final degree project, I was suggested by SENER to conduct a doctorate on the field of Fibre Reinforced Polymer (FRP) manufacturing in collaboration with the Departament de Ciència dels Materials i Enginyeria Metal·lúrgica (CMEM) of the Universitat Politècnica de Catalunya (UPC). Then, INTEXTER arose as an ideal partner to achieve this milestone, which supposed a new research line for all the participants.

I am proud of having overcome the challenge of playing a lead role in an investigation project, in a topic about which I am passionate, being responsible for all major areas of concept formation, data collection and analysis. The very first result obtained from this thesis was a Spanish patent containing ISFLIP processing sequence and the main tooling systems [1]. Besides, a version of Chapter 4 has been submitted for publication in the Journal of Composite Materials [2], and a version of Chapter 5 has been also submitted for publication in the Journal of Composite Materials [3].

All of the work presented henceafter was conducted in the research facilities of the Laboratori de Material Compòsits Avançats (COMPOLAB) at INTEXTER and in the laboratories of CMEM; as well as in the premises of the Division of Mechanics, Materials and Design of the Department of Engineering of the University of Cambridge as a student visitor during a three months period.

Acknowledgments

I do not have enough words to express my gratitude to my supervisor, Dr. Núria Salán, for the way she has guided me on the path to complete this academic pursuit, being the best mentor I could have ever wished for.

I would like to thank the support of all those whom I was privileged to work with: Víctor Morell of SENER Ingeniería y Sistemas for his guidance and continuous support; Dr. Pere Pagès, my first supervisor, his experience and direction have been priceless; Dr. Jose Antonio Tornero and the whole technical staff of the Institut d'Investigació Tèxtil i Cooperació Industrial de Terrassa. (INTEXTER) for their invaluable help; and the technical staff of the Departament de Ciència dels Materials i Enginyeria Metal·lúrgica (CMEM) at Barcelona and Terrassa for their assistance in the technical work.

I must also express my gratitude to Dr. Hugh Shercliff for his inspiration and kindly embracing me at the Department of Engineering of the University of Cambridge.

This work would not have been possible without the financial support received from SENER Ingeniería y Sistemas and the Escola Superior d'Enginyeries Industrial, Aeroespacial i Audiovisual de Terrassa (ESEIAAT).

Agradecimientos

El desarrollo de esta tesis doctoral ha sido un proceso lento y largo, y lleno de esfuerzo por mi parte. Esfuerzo que no hubiese conducido a ninguna parte sin la ayuda de un sinfín de personas a las cuales intentaré expresar mi agradecimiento, siendo plenamente consciente que unas simples líneas no serán suficientes en ningún caso.

He tenido siempre la suerte de contar con “jefes” que se han preocupado por mí de forma desinteresada, tanto mi directora de tesis, la célebre Dra. M. Núria Salán, como Víctor Morell durante mi etapa en SENER.

Núria ha sido mi hombre, como me dijo el primer día que nos conocimos. No solo me ha ayudado en cualquier aspecto relacionado con la tesis; sino que prácticamente me ha adoptado, y alimentado muchos días. La tesis me ha hecho mejor investigador; pero también ha forjado una mejor persona, y en eso Núria ha sido fundamental. Una mujer inteligente, fuerte y decidida.

Víctor fue la persona que me introdujo en los materiales compuestos paso a paso. Me ayudó a arrancar la tesis y obviamente sin ese apoyo no hubiese llegado al final. Aunque en los últimos tiempos hayamos desconectado un poco, siempre le estaré agradecido por la ayuda y el cariño que me brindó en su día.

Quiero agradecer a mi familia (mis padres, Jaime y Dolores, y mi hermana, Antonia) haberme sostenido financiera y emocionalmente, la investigación en España no está viviendo su mejor época y el dinero no emana de las fuentes; pero ha sido sobre todo en la parte emocional, que no es uno de mis puntos fuertes, donde he necesitado más ayuda. Ha habido más de un punto de inflexión a lo largo de la tesis que sin su apoyo no hubiese superado.

Gracias a mis amigos (mallorquines y catalanes) por aguantar mi humor negro (por llamarlo de alguna forma), mis rarezas, mis conexiones y desconexiones, que siempre les diga que tengo que escribir, por ayudarme a desconectar cuando era necesario, y por no preguntarme cuando voy a entregar la tesis por fin. A todos ellos (Javi, Kike, Pep, Alfonso, Arty y Jaume; Jordi, Xavi, Georgina, Fraga y Pepe; Alejandro, Luis y Jordi; y que me perdonen los que no cito porque no terminaría nunca...ánimo Javierata) mil gracias.

Finalmente, quiero también dedicarles un agradecimiento especial a los compañeros que me han ayudado a andar este camino del departamento de materiales, tanto en Barcelona (Francesc, Álvaro y Fernando) como en Terrassa (Fran, Josep y Elisa), y de INTEXTER (José Antonio, José, Kiku, Mari Carmen y Víctor), que siempre me han tratado con la mayor de las amabilidades y me han ayudado en todo lo posible sin un solo reproche.

Gracias a todos, de corazón.

Summary

List of figures	xi
List of tables	xv
List of abbreviations	xvi
List of symbols	xviii
Chapter 1 Introduction	1
1.1. The challenge of LCM processes	1
1.2. Research objectives	3
1.3. Scope and outline of the thesis	4
Chapter 2 Literature review	7
2.1. Textile composites	7
2.1.1. <i>Fibres</i>	7
2.1.2. <i>Textile architectures</i>	9
2.1.3. <i>Resins</i>	11
2.1.4. <i>Prepreg vs. dry fibre</i>	12
2.1.5. <i>Manufacturing properties</i>	15
2.2. Preforming	24
2.2.1. <i>Stamping</i>	26
2.2.2. <i>Diaphragm forming</i>	26
2.3. Liquid Composite Moulding (LCM)	28
2.3.1. <i>Part quality</i>	29
2.3.2. <i>Vacuum Infusion (VI)</i>	33
2.3.3. <i>Hybrid VI-forming</i>	42
Chapter 3 In Situ Forming of a Liquid Infused Preform (ISFLIP)	45
3.1. Manufacturing method	46
3.1.1. <i>Set-up</i>	48
3.1.2. <i>Infusion</i>	48
3.1.3. <i>Forming</i>	49

3.1.4. Curing.....	50
3.2. Manufacturing Triangle (MT)	51
3.2.1. Materials and properties	52
3.2.2. Part shape.....	54
3.2.3. Part size.....	56
3.2.4. Tolerances	58
3.2.5. Look & feel and roughness.....	59
3.2.6. Defects and reproducibility	60
3.2.7. Production volume, part price and investment.....	62
3.3. SWOT analysis	68
3.4. Prototype.....	70
3.4.1. Requirements	70
3.4.2. Design.....	71
3.4.3. Built	76
3.5. Research strategy	76
3.6. Conclusions	78
Chapter 4 Void content minimization via effective degassing.....	81
4.1. VI manufacturing: decision-making.....	82
4.2. Materials and methods.....	87
4.2.1. Specimens	87
4.2.2. Test procedures	87
4.2.3. Fractional factorial design.....	91
4.3. Results	93
4.3.1. Porous area fraction.....	93
4.3.2. Fibre and void volume fractions.....	93
4.3.3. Void size, shape and spatial distribution.....	96
4.3.4. Flexure response	98
4.3.5. Screening of degassing procedures	99
4.4. Discussion.....	104

4.5. Conclusions	106
Chapter 5 High performance FRPs being competitive in time via control of filling and post-filling conditions	109
5.1. VI manufacturing: decision-making.....	110
5.2. Materials and methods.....	114
5.2.1. <i>Specimens</i>	114
5.2.2. <i>Test procedures</i>	114
5.2.3. <i>Factorial designs</i>	118
5.3. Results	121
5.3.1. <i>Porous area fraction</i>	121
5.3.2. <i>Fibre volume fraction</i>	122
5.3.3. <i>Void size, shape and spatial distribution</i>	124
5.3.4. <i>Flexure response</i>	126
5.3.5. <i>Screening of filling and post-filling conditions</i>	129
5.4. Discussion.....	132
5.5. Conclusions	136
Chapter 6 Evaluation of uncertainties of the forming stage of ISFLIP	137
6.1. Materials and methods.....	138
6.1.1. <i>Specimens</i>	138
6.1.2. <i>Manufacturing</i>	140
6.1.3. <i>Materials characterization</i>	144
6.1.4. <i>Specimens characterization</i>	148
6.2. Results	152
6.2.1. <i>Reinforcements and auxiliary materials</i>	152
6.2.2. <i>Formability of hemisphere shape specimens</i>	158
6.2.3. <i>'C' cross-section profiles</i>	162
6.3. Discussion.....	169
6.4. Conclusions	174
Chapter 7 Discussion and conclusions.....	177

7.1. Discussion.....	177
7.2. Recommendations for future research.....	183
7.3. Conclusions	185
Bibliography	187
Appendices	205

List of figures

Figure 1.1. Classification of LCM variants according to the innovation focus.	3
Figure 1.2. Thesis outline.	5
Figure 2.1. Properties of fibrous materials often used in high performance composites (Kevlar is a registered trademark of Dupont Corporation for aramid fibres, and Spectra is a registered trademark of Honeywell International Inc for PE fibres): (a) tensile properties and (b) cost (data extracted from [49]).	8
Figure 2.2. Main textile architectures used in FRPs: (a) 2D weave, (b) 3D weave, (c) triaxial braid, (d) weft-knit and (e) non-crimp (adapted from [63]).	9
Figure 2.3. Properties of some typical epoxy FRP laminates: (a) tensile properties, (b) specific tensile properties and (c) cost (data extracted from [49]).	14
Figure 2.4. Typical woven fabric shear behaviour curve (adapted from [99]).	16
Figure 2.5. Experimental set-ups used to evaluate intra-ply shear properties: (a) picture frame and (b) bias extension (adapted from [100]).	16
Figure 2.6. Experimental set-up for a pull-through test used to evaluate tool- and ply-ply shear properties: (a) start of test, (b) end of test and (c) side view of the set-up at the end of test (adapted from [54]).	18
Figure 2.7. Exaggerated representation of dual-scale flow: (a) capillary forces dominate and (b) viscous forces dominate.	21
Figure 2.8. Characterization methods of unsaturated in-plane permeability: (a) rectilinear low and (b) radial flow (adapted from [61]).	23
Figure 2.9. Composite forming techniques: (a) stamping, (b) single diaphragm forming (only vacuum assisted) and (c) double diaphragm forming (only vacuum assisted).	25
Figure 2.10. LCM techniques: (a) RTM, (b) VI, (c) CRTM and (d) SCRIMP.	28
Figure 2.11. Void formation due to resin flow through heterogeneous dual-scale porous media.	31
Figure 2.12. Typical flow chart of VI process.	34
Figure 2.13. Characteristic gradient of pressure during preform filling.	36
Figure 2.14. Filling patterns: (a) simple and (b) advanced.	37
Figure 2.15. Hybrid VI-forming techniques: (a) FRTM and (b) RIDFT.	42
Figure 3.1. Flow chart of ISFLIP process (only curing step carried out at higher than ambient temperature).	46
Figure 3.2. Representative ISFLIP preform assembly.	47

Figure 3.3. Pressure diagrams for preform clamping during the infusion stage: (a) pressure levels and (b) bagging film collapse on HPDM according to pressure levels.	49
Figure 3.4. Pressure diagrams of semi-infinite membranes: (a) equilibrium of stresses in an infinitesimal portion of a curved diaphragm and (b) limit conditions for separation of diaphragms (assuming the worst case with equal stretching of both diaphragms).....	50
Figure 3.5. Hierarchical structure of the Manufacturing Triangle (extracted from [253]).	51
Figure 3.6. Taxonomy of shapes for shaping processes: appropriate shapes for ISFLIP (adapted from [255]).....	54
Figure 3.7. Potential applications of ISFLIP: (a) leaf spring [257], (b) double-curved “C” spar [258], (c) single beam composite beam [259], (d) leading edge spar [260], (e) car “B” pillar structure [261], (f) Gaudi chair [262], (g) simple car floor pan , (h) bottom a bicycle trailer [263], (i) shells of wind turbine blades [264], (j) radiotherapy boards [265], and (k) kayak deck and hull [266].	56
Figure 3.8. Inappropriate applications for ISFLIP: (a) elongated helicopter canopy [186], (b) complex auto floor pan [7], (c) complex auto part [267], and (d) reentrant washing machine tube [267].....	57
Figure 3.9. Flow charts of VI, ISFLIP and RTM (only steps which can significantly affect cycle time are shown).....	66
Figure 3.10. Representative part size and economic production volume for VI, ISFLIP and RTM.....	67
Figure 3.11. Design of ISFLIP prototype.....	71
Figure 3.12. Vacuum table design: (a) vacuum table and supporting structure ,(b) exploded view of vacuum table.	72
Figure 3.13. Double diaphragm tooling design: (a) expanded view of the three frames (without silicone diaphragms), (b) cross-section of a single diaphragm frame, (c) cross-section of the uncoupled double diaphragm tooling, and (d) cross-section of the coupled double diaphragm tooling and the vacuum table.	74
Figure 3.14. Heating chamber: (a) supporting structure of IR panels and (b) enclosure details.....	75
Figure 3.15. Built prototype.	77
Figure 4.1 Flow chart and governing parameters of VI process.....	83
Figure 4.2. Vacuum degassing configurations.	83
Figure 4.3. VI preform assembly (schematic dimensions are only representative).	84
Figure 4.4. Generic pattern of samples: size, distribution and codification rules.....	88
Figure 4.5. Manufactured specimens: porous area fraction, s_0 , and thickness measured at samples MYZ.....	94

Figure 4.6. Results of the loss on ignition method: (a) Fibre volume fraction, v_f' , and (b) void volume fraction, v_0'	95
Figure 4.7. Size, occurrence and total content (void area fraction, a_0) of inter-tow and intra-tow voids.....	96
Figure 4.8. Detail views of micrographic samples belonging to specimen 4 and void area fraction, a_0 , of the corresponding whole sample (not only the partial cross-section depicted).....	97
Figure 4.9. Shape descriptors of inter-tow voids: inter-tow void area, A_0^{inter} ; Feret's diameter, ϕ_{Feret} ; Feret's angle, φ_{Feret} ; and aspect ratio, AR	97
Figure 4.10. Flexural properties vs. estimated fibre volume fraction, \hat{v}_f' , and void volume fraction, v_0' : (a-b) flexural strength, σ_{fM} , and (c-d) flexural modulus, E_f	98
Figure 4.11. Coefficients of variation of measured quality attributes, and monitored nuisance and allow-to-vary factors.....	100
Figure 4.12. Noteworthy dependencies between response variables (porous area fraction, s_0 , and void volume fraction, v_0') and covariates (time until filling, $t_{0 \rightarrow fill_0}$; time until filling end, $t_{0 \rightarrow fill_{end}}$; and filling time, t_{fill}).....	100
Figure 4.13. Cube plots of the input data of the screening experiment.....	101
Figure 4.14. Effects of main factors and two-factor interactions (interaction effects are aliased according to $l_{NS} = l_{PT}$, $l_{NP} = l_{ST}$, $l_{NT} = l_{SP}$).....	102
Figure 4.15. Initial qualitative evaluation of effect significance before conducting the ANOVA and resultant models from the ANOVA.....	103
Figure 5.1. Flow chart and governing parameters of VI process.....	111
Figure 5.2. Vacuum degassing equipment.....	112
Figure 5.3. Preform assemblies (schematic dimensions are only representative).....	113
Figure 5.4. Generic pattern of samples: size, distribution and codification rules.....	115
Figure 5.5. Detail views of each Porous Area Type (PAT).....	121
Figure 5.6. Manufactured specimens: porous area fraction, s_0 , according to each Porous Area Type (PAT), and thickness measured at samples MYZ.....	122
Figure 5.7. Fibre volume fraction, v_f' , obtained through the loss on ignition method (bars), and estimated fibre volume fraction from thickness measures, v_f^h (dots).....	123
Figure 5.8. Detail views of micrographic samples for each Porous Area Type (PAT), and void area fraction, a_0 , of the corresponding whole sample (not only the partial cross-section depicted).....	124

Figure 5.9. (a) Total content (void area fraction, a_0) of inter-tow and intra-tow voids, and (b-d) shape descriptors of inter-tow voids (inter-tow void area, A_0^{inter} ; Feret's diameter, ϕ_{Feret} ; Feret's angle, φ_{Feret} ; and aspect ratio, AR).	125
Figure 5.10. Flexural properties vs. estimated fibre volume fraction, \hat{v}_f' , Porous Area Type (PAT) and testing orientation: (a-b) flexural strength, σ_{fM} , and (c-d) flexural modulus, E_f	127
Figure 5.11. Interval plots of Tukey's test (overall confidence level 95% and individual confidence level 99,7%): (a) flexural strength, σ_{fM} , and (b) flexural modulus, E_f	128
Figure 5.12. Coefficients of variation of measured quality attributes, and monitored nuisance and allow-to-vary factors.	129
Figure 5.13. Plots of the statistical analysis of the first stage of the screening experiment of filling and post-filling conditions.	130
Figure 5.14. Plots of the statistical analysis of the second stage of the screening experiment of filling and post-filling conditions.	132
Figure 6.1. Hemisphere mould (dimensions in mm).....	140
Figure 6.2. Modular 'C' variable cross-section profiles: (a) single joggle and (b) double joggle (dimensions in mm).	141
Figure 6.3. Flowchart and governing parameters of ISFLIP process.	142
Figure 6.4. ISFLIP preform assemblies for hemisphere shape specimens (schematic dimensions are representative): (a) upper demoulding by peel-ply and (b) upper demoulding by perforated release film.....	143
Figure 6.5. Geometric analysis of bias extension test samples for trellis shear characterization: (a) initial state and (b) deformed state (adapted from [100]).	145
Figure 6.6. Real picture of a deformed sample depicting the two angles experimentally measured.....	146
Figure 6.7. Experimental set-up of the friction test: (a) schematic drawing and (b) test execution.	147
Figure 6.8. Experimental set-up of the compression test of 'L' shape samples: (a) schematic drawing and (b) test execution (deformed sample at failure).....	149
Figure 6.9. Free-body diagram of a compressed 'L' shape sample.	150
Figure 6.10. Ideal unloading-loading hysteresis loop during compression tests of 'L' shape samples.....	151
Figure 6.11. Results of the bias-extension tests: (a) normalized to the width tensile load, F/w , vs. crosshead displacement, δ , curve and (b) normalized shear force, F_{sh} , vs. shear angle, γ , curve.....	153
Figure 6.12. Results of the tensile tests of elastic diaphragms, and films and High Permeability Distribution Media (HPDM) listed in Table 6.2 (0° and 90° referring to longitudinal and transversal directions, respectively)	155

Figure 6.13. Static coefficients of friction of reinforcement and auxiliary materials of the preform assembly. Base materials are (a) GTWF, (b) CTWF, (c) HE bagging film and (d) conventional peel-ply fabric (error bars showing min. and max. values).....	157
Figure 6.14. Hemisphere shape specimens: preform assembly and orientation details, and isometric views (flow direction through HPDM in direction x).....	159
Figure 6.15. Hemisphere shape specimens: top views.	160
Figure 6.16. (a) Shear angles resulting from kinematic draping over the hemisphere geometry (including diaphragm thickness) with LMAT Interactive Drape software, and (b) measured location (distance from origin) and shear angle at the initial point of wrinkles (error bars showing min. and max. values).....	162
Figure 6.17. ‘C’ cross-section profile specimens: preform assembly and orientation details, and perspective views (flow direction through HPDM in direction x).....	164
Figure 6.18. Shear angles resulting from kinematic draping over the joggle geometries of the moulds (including diaphragm thickness) of the ‘C’ cross-section profiles with LMAT Interactive Drape software: (a) simple joggle and (b) double joggle.....	165
Figure 6.19. Schematic drawing of ‘L’ shape samples location into each specimen and nominal dimensions (dimensions in mm).....	166
Figure 6.20. Load, F , vs. crosshead displacement, δ , curve of sample B22’: (a) complete curve and (b) detail of loading-unloading hysteresis loop for computing the kinematic coefficient of friction.....	166
Figure 6.21. Results of the compression tests of ‘L’ shape samples: (a) crosshead load at failure and Curved Beam Strength (CBS), and (b) resultant stresses at failure.....	167
Figure 6.22. Micrographs of ‘L’ shape samples, highlighting inter-laminar cracks (red).....	169

List of tables

Table 1.1. List of recently appeared LCM variants.....	2
Table 3.1. Equipment costs for VI, ISFLIP and RTM.....	65
Table 3.2. Strengths and weaknesses of the SWOT analysis of ISFLIP.	68
Table 3.3. Opportunities and threats of the SWOT analysis of ISFLIP.....	69
Table 3.4. Design requirements for ISFLIP prototype.	70
Table 4.1. Textile properties of E-Glass 2/2 Twill-Weave Fabric (GTWF).....	87
Table 4.2. Design factors of the screening experiment of degassing procedures.	91

Table 4.3. The 2_{IV}^{4+1} fractional factorial design, principal one-half fraction, applied to the screening experiment of degassing procedures.	92
Table 4.4. ANOVA tables including Sum of Squares (SS); Degrees of Freedom (DF); Mean Squares (MS); F-statistic, F_0 , associated to each term; and level of significance, p , associated to each F-statistic.	103
Table 5.1. Design factors of the screening experiment of filling and post-filling conditions.	119
Table 5.2. The 2^2 factorial design applied to the first stage of the screening experiment of filling and post-filling conditions.	119
Table 5.3. The 2^2 factorial design applied to the second stage of the screening experiment of filling and post-filling conditions.	119
Table 5.4. ANOVA tables for analysis of porous area fraction, s_0^{II+III} [%], including Sum of Squares (SS); Degrees of Freedom (DF); Mean Squares (MS); F-statistic, F_0 , associated to each term; and level of significance, p , associated to each F-statistic.	131
Table 6.1. Textile properties of reinforcements.	138
Table 6.2. Consumable materials (all materials belong to the catalogue of Airtech Advanced Materials Group).	139
Table 6.3. Qualitative impact on formability and specimen quality, and future prospects of auxiliary materials.	174

List of abbreviations

1D	One-dimensional	CRTM	Compression RTM
2D	Two-dimensional	CTE	Coefficients of Thermal Expansion
3D	Three-dimensional	CTWF	Carbon Twill Weave Fabric
ANCOVA	Analysis of Covariance	CBS	Curved Beam Strength
ANOVA	Analysis of Variance	DGEBA	Diglycidyl Ether of Bisphenol A
AFP	Automated Fibre Placement	DF	Degrees of Freedom
ATL	Automated Tape Laying	ETFE	Ethylene Tetrafluoroethylene
CAPRI	Control Atmospheric Pressure Resin Infusion	FASTRAC	Fast Remotely Actuated Channelling
CIRTM	Co-Injection RTM	FRP	Fibre Reinforced Polymer
CHPDM	Conventional HPDM	FFC	Flow Flooding Chamber
CPWF	Carbon Plain Weave Fabric	FRTM	Flexible RTM
		GTWF	Glass Twill Weave Fabric

HE	High Modulus	QI	Quasi-Isotropic
HM	High Modulus	RARTM	Rubber Assisted RTM
HPDM	High Permeability Distribution Medium	RFI	Resin Film Infusion
HP-RTM	High Pressure RTM	RIDFT	Resin Infusion between
HS	High Speed		Double Flexible Tooling
HT-VARTM	High Temperature VARTM	RTM	Resin Transfer Moulding
ILNS	Inter-Laminar Normal Strength	SS	Sum of Squares
IM	Intermediate Modulus	SWOT	Strengths, Weakness,
IR	Infrared radiation		Opportunities and Threats
ISFLIP	<i>In Situ</i> forming of a Liquid Infused Preform	TERTM	Thermal Expansion RTM
		TP	Thermoplastic
KHPDM	Knitted HPDM	T-RTM	Thermoplastic RTM
LCM	Liquid Composite Moulding	TS	Thermoset
LRTM	Light RTM	UD	Unidirectional
MD	Medium Density	UHM	Ultra High Modulus
MS	Mean Squares	VACRTM	Vacuum Assisted Compression RTM
MT	Manufacturing Triangle	VAP	Vacuum Assisted Process
NP	Non-Perforated	VARTM	Vacuum Assisted RTM
OOA	Out-Of-Autoclave	VI	Vacuum Infusion Process
OT	Orthotropic	VIPR	Vacuum Induced Preform Relaxation
PA	Polyamide	WF	Woven fabric
PAT	Porous Area Type	SCRIMP	Seeman's Composite Resin
PBT	Polybutylene Terephthalate		Infusion Moulding Process
PE	Polyethylene	SM	Standard Modulus
PP	Polypropylene	SRIM	Structural Reaction Injection Moulding

List of symbols

v	Volume fraction	θ	Contact angle between solid and fluid*
m	Mass fraction	Φ_f	Fibre diameter
ρ	Density	Ca^*	Modified capillary number
n	Number of units of a set of elements*	C_{air}	Air solubility at a fixed temperature
h	Thickness	H	Henry's law solubility constant
l	Length*	P_{air}	Partial pressure of air
w	Width	ϕ	Preform porosity
P	Pressure	α	Relative position
P_{diaph}	Pressure between diaphragms	x	Absolute position
P_{mould}	Pressure into the mould cavity	x_f	Flow front position
T	Temperature	u_f	Macroscopic resin velocity at the flow front
t	Time	L	Filling length*
$t_{0 \rightarrow fill_0}$	Time until filling from resin mixing	n	Production volume*
$t_{0 \rightarrow fill_{end}}$	Time until filling end from resin mixing	\dot{n}	Production rate
RH	Relative humidity	C	Part price
k, K	Permeability	M	Component mass*
k_{unsat}	Unsaturated permeability	C_m	Material cost
k_{sat}	Saturated permeability	f	Scrap fraction
\mathbf{K}	Second order tensor of permeability	C_t	Tooling cost
u	Volume-averaged velocity	n_t	Tool life
μ	Dynamic viscosity	C_c	Capital cost of equipment
Q	Flow	L	Time fraction for which equipment is productive*
R_{inj}	Injection radius	t_{wo}	Capital write-off time
R_{mould}	Preform radius	\dot{C}_{oh}	Overhead rate
σ_f	Compaction pressure on preform*	S_0	Porous area fraction
P_c	Capillary pressure	S_0	Porous area
γ	Surface tension*		

* Symbol repeated to refer to more than one concept in different contexts throughout the dissertation.

\bar{V}_0^{surf}	Average surface void volume	τ	Shear stress
a_0	Void area fraction	ε	Strain
A_0	Void area	E	Modulus of elasticity
\emptyset_{Ferret}	Feret's diameter	F	Load
φ_{Ferret}	Feret's angle	s	Deflection at the mid-point
AR	Aspect ratio	l'	Span between supports
l	Effect of a factor or interaction*	δ	Crosshead displacement
y	Response variable	F_{sh}	Normalized shear force
p	Statistic used in hypothesis testing	γ	Shear angle*
F_0	F -statistic of the null hypothesis	θ	Half of angle formed by warp and weft yarns*
R^2	Coefficient of determination	F_n	Normal force
R_{adj}^2	Adjusted coefficient of determination	μ_{st}	Static coefficient of friction
v_f^h	Thickness-based fibre volume fraction	μ_{kn}	Kinematic coefficient of friction
n_l	Number of layers	M	Bending moment*
ρ_A	Area density	r	Coordinate in the radial direction
σ	Stress	θ	Coordinate in the circumferential direction*

Superscripts

<i>intra</i>	Intra-tow	<i>wet</i>	Saturated
<i>inter</i>	Inter-tow	—	Average
<i>inlet</i>	Inlet	^	Estimated
<i>vent</i>	Vent	'	Adjusted
<i>dry</i>	Non-saturated		

Subscripts

f	Fibre*	0	Initial*
r	Resin*	i	Inner
0	Void*	o	Outer

* Symbol or subscript repeated to refer to more than one concept in different contexts throughout the dissertation.

<i>m</i>	Mean	<i>amb</i>	Ambient
<i>lock</i>	Locking	<i>atm</i>	Atmospheric
<i>deg</i>	Degassing	<i>vac</i>	Vacuum
<i>deb</i>	Debulking	<i>f</i>	Flexural*
<i>fill</i>	Filling	<i>r</i>	Radial direction*
<i>pfill</i>	Post-filling	<i>θ</i>	Circumferential direction
<i>cure</i>	Curing	<i>M</i>	Maximum stress (strength)
<i>inj</i>	Injection		

* Subscript repeated to refer to more than one concept in different contexts throughout the dissertation.

Chapter 1

Introduction

1.1. The challenge of LCM processes

In advance composite manufacturing, Liquid Composite Moulding (LCM) is becoming a promising alternative to autoclave manufacturing of prepreg-based Fibre Reinforced Polymer (FRP) parts; although LCM is still lagging behind in terms of product quality. Differences between LCM and prepreg-based autoclave manufacturing do not arise only from the fabrication process, but also from their compatible materials. However, LCM processes, which mostly belong to the category of Out-Of-Autoclave (OOA) manufacturing, are gaining importance due to their potential to significantly reduce capital costs and environmental impact of autoclave fabrication [4–6].

Moreover, long processing times are usually associated with FRP manufacturing. In the field of LCM, new developments in new resin systems [7–9] and more efficient dry preform technologies [10,11] are emerging to reach production volumes and part prizes achievable in metal and polymer manufacturing. Unfortunately, in LCM, processing time and part quality are often at odds with each other.

LCM encompasses FRP manufacturing techniques in which a preform of dry fibre reinforcements is impregnated with a liquid resin by the action of a gradient of pressure between the preform and a container with the resin. LCM processes may be split in two categories according to the driven pressure nature [12]: Resin Transfer Moulding (RTM), in which resin is pushed to the preform by a higher than the atmospheric pressure, or Vacuum Infusion (VI), in which resin is drawn out by a close to the vacuum pressure.

RTM is widely accepted in the fabrication of high performance FRP parts. Several successful studies of RTM applications in the automotive and aeronautic industries in terms of cost competitiveness, quality and performance of the final part are available [13–15]. Nevertheless, VI capability of manufacturing high performance composites still raises concerns in terms of reproducibility, part performance (fibre and void volume contents) and shape tolerance (thickness variability); although, flexibility and scalability of VI, from small to large and highly integrated structures, and its cost-effectiveness have drawn the attention of the manufacturing industry.

VI has been used in the past for manufacturing parts in which the potential advantages of FRP were not fully realized due to uncertainty over performance [12,16]. Further investigation is needed for a better understanding of VI to achieve similar levels of quality and reliability of both prepreg-based parts (autoclave) and even RTM.

Freedom of tailoring material properties to meet performance requirements is one of the most important features possessed by FRP composites; however, high flexibility is needed from the manufacturing point of view to get profit of this feature within a real cost-effective scenario. Consequently, a broad range of LCM techniques have emerged in the last year trying to overcome the stated challenge and getting LCM technologies closer to high performance composites. In Table 1.1, it is listed some of the most outstanding techniques appeared during the last years.

Table 1.1. List of recently appeared LCM variants.

Acronym	Name	Acronym	Name
CAPRI	Control Atmospheric Pressure Resin Infusion [17,18]	CIRTM	Co-Injection RTM [19,20]
CRTM	Compression RTM [21–23]	FASTRAC	Fast Remotely Actuated Channelling [24]
FFC	Flow Flooding Chamber [25,26]	FRTM	Flexible RTM [27]
HP-RTM	High pressure RTM [28]	HT-VARTM	High Temperature VARTM [29]
LRTM	Light RTM [30]	RARTM	Rubber Assisted RTM [31]
RFI	Resin Film Infusion [32]	RIDFT	Resin Infusion between Double Flexible Tooling [33–37]
SCRIMP	Seeman's Composite Resin Infusion Moulding Process [38]	SRIM	Structural Reaction Injection Moulding [39]
TERTM	Thermal Expansion RTM [40]	T-RTM	Thermoplastic RTM [7,41]
VACRTM	Vacuum Assisted Compression RTM [42]	VAP	Vacuum Assisted Process [43–46]
VARTM	Vacuum Assisted RTM	VIPR	Vacuum Induced Preform Relaxation [47,48]

A classification of the variants listed in Table 1.1, according to the LCM category to which they belong (RTM or VI) and their motivation, is shown in Figure 1.1. Innovations are mainly focused on reducing processing time by adding faster resin delivery systems (CRTM, FASTRAC, FFC,

HP-RTM, SCRIMP, VACRTM and VIPR), or by making easier fabric stacking (RIDFT and FRTM) or assembly preparation (LRTM); on improving flow control and the final properties of the part (CAPRI, VAP and VARTM); on providing additional compaction to preforms (RARTM and TERTM); or on special resin delivery states (CIRTM, HT-VARTM, RFI, SRIM and T-RTM).

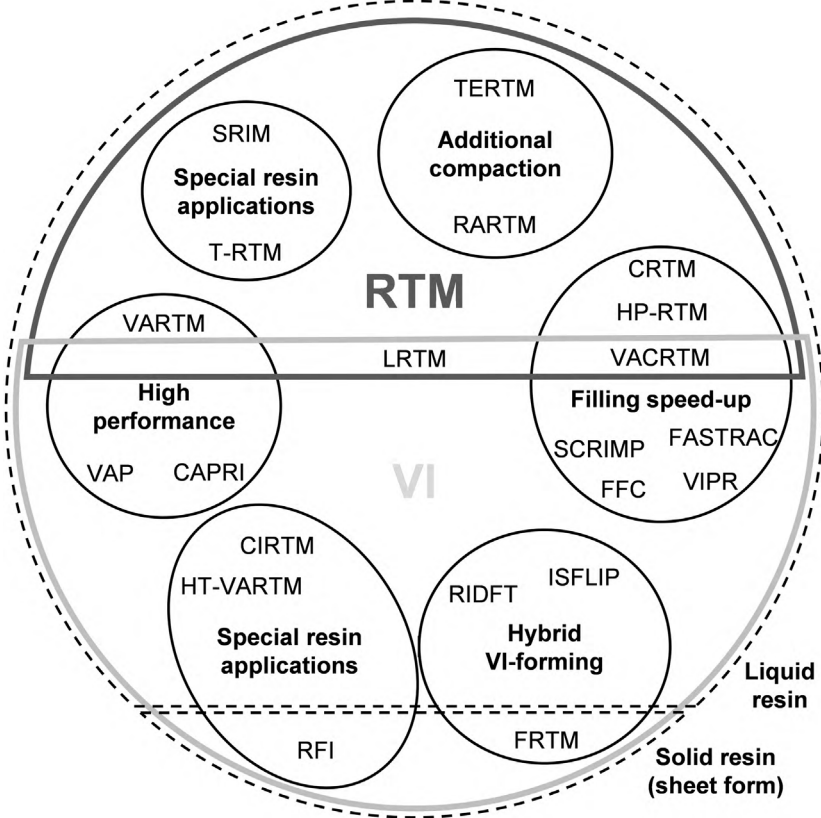


Figure 1.1. Classification of LCM variants according to the innovation focus.

In general, LCM and, specifically, VI techniques are in a turning point that will make the difference in their future prospects. They are beginning to be used in applications which require high quality and reliability levels, such as automotive and aerospace primary structural components, wind turbine blades, railroad bridge girders, and high-speed vessels. These emerging challenges must be faced while competing with alternatives that are already present in the industry.

1.2. Research objectives

This research project was focused on the development and assessment of the *In Situ* Forming of a Liquid Infused Preform (ISFLIP) process, as a real alternative to manufacture high performance FRP parts with shorter processing times and higher reproducibility than other conventional VI variants.

ISFLIP is a hybrid process between VI and diaphragm forming, also included in Figure 1.1, in which a flat preform of a stack of reinforcement fabrics is firstly impregnated with a low viscosity resin and, then, formed over a mould while the resin is still in the low viscosity state. This process sequence is possible because the preform assembly (preform and auxiliary materials which are air-tightly sealed by bagging films) is clamped between a couple of elastic diaphragms, which keep the preform flat during the infusion stage and allow its subsequent vacuum forming. Shell components, from simple to complex double curvature shapes, can be achieved.

After ISFLIP ideation, the very first objective addressed was *establishing the basis for ISFLIP*. A rigorous analysis of the internal and external factors of the process was performed in order to determine its key aspects and prospects, from which a research strategy was outlined. Considering the early stage of development of ISFLIP, a series of goals were stated as a starting point for a longer development. These goals are detailed in the following paragraphs:

Making ISFLIP a reality in order to proof ISFLIP concept and make possible the later technological development. Achieving this objective involved the definition of an effective and implementable processing sequence, and the construction of a functional prototype that could hold ISFLIP test campaigns.

Identifying a VI manufacturing methodology which fitted the targets of high performance FRP and short processing times. High performance composites are usually associated with the optimization of two quality attributes: maximizing fibre content and minimizing void content. Porosity is a major concern in VI manufacturing due to resin gelation at pressures close to absolute vacuum. Besides, trade-offs between component quality attributes and processing times are typical in VI due to the operational limitations of the manufacturing process.

Assessing uncertainties associated to the forming stage of ISFLIP to determine later, more focused development routes. Although diaphragm forming is a well-known and widespread manufacturing process, in ISFLIP, a series of auxiliary materials are being formed together with the stacked preform, which is embedded in a low viscosity matrix, giving rise to material interactions that might affect the overall forming performance and final part quality.

1.3. Scope and outline of the thesis

This dissertation covers the research activities carried out to achieve the objectives defined in the previous section, which are framed into the early stage of development of ISFLIP. Consequently, this dissertation does not pretend to present a complete development of a manufacturing process

until its industrialization, but an initial effort that should set the path of future investigation. As a hybrid VI-forming process, noteworthy conclusions on general VI manufacturing of great interest to the research community were also drawn.

A diagram interconnecting the major research objectives with each main chapter heading of the thesis is shown in Figure 1.2.

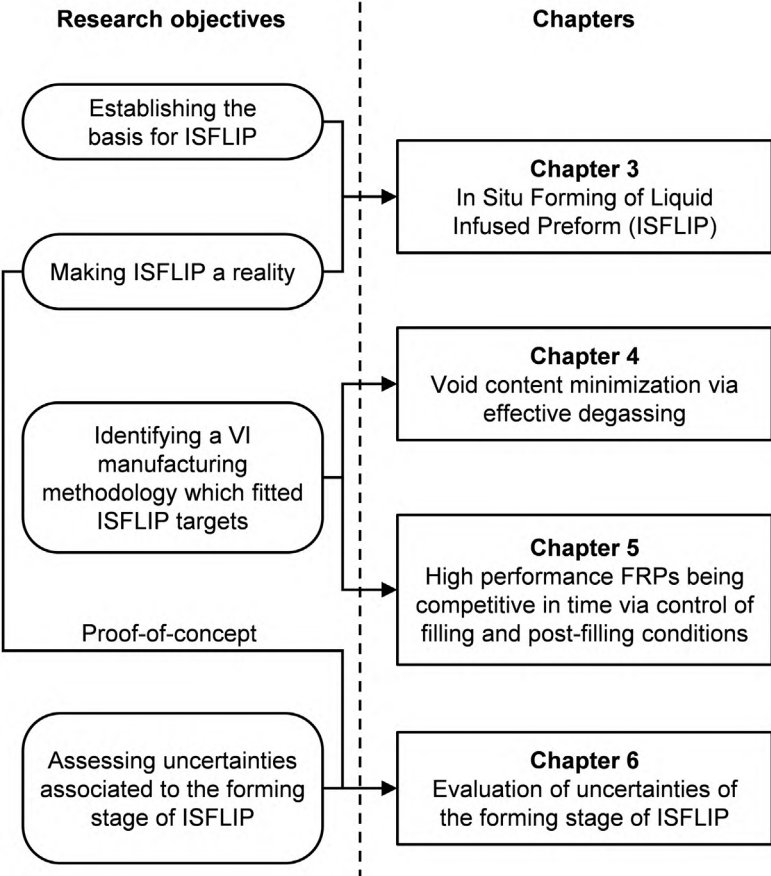


Figure 1.2. Thesis outline.

Each main chapter cited in Figure 1.2 has been outlined as an independent unit of work that, from the literature review presented in Chapter 2, states a specific problem, defines a working methodology, presents the obtained results, discuss the main implications and sets out the main conclusions reached.

A general background of LCM processing and the problems to which ISFLIP would serve as a response is presented in Chapter 1. The major research objectives and the organization of the dissertation is also given in this first chapter.

Chapter 2 is mainly focused on the state-of-the-art of VI manufacturing. After a brief presentation of materials often involved in VI and the most relevant manufacturing properties, an insight into different preforming and forming techniques of FRP is given. Afterwards, implications

of the main manufacturing steps of VI and quality limitations usually associated to the process are presented. Finally, hybrid VI-forming techniques are introduced.

Chapter 3 introduces ISFLIP through a rigorous exploration of function, quality and cost of potential parts to be manufactured, leading to a SWOT analysis from which the research strategy of ISFLIP was outlined. A detailed manufacturing procedure, and the key points of the design and implementation of a functional prototype are also provided.

In Chapter 4, efficacy of different degassing procedures based on vacuum degassing assisted by adding nucleation medium, High Speed (HS) resin stirring and/or later pressurization during different time intervals is analysed in terms of final void content. Degassing is a fundamental step to minimize or even avoid resin outgassing and enhance dissolution of voids created during preform impregnation. The importance of enhancing bubble formation during degassing is highlighted.

In Chapter 5, it is addressed the possibility of manufacturing VI specimens with short processing time without any detrimental effect on fibre and void contents. A series of specimens were manufactured to analyse the effects of a variation in typical through-thickness resin flow in preforms, different filling gradients of pressure, incrementing vent pressure between filling and post-filling, and turning inlet into vent at the onset of the post-filling step. The results led to a promising VI procedure, obtaining specimens with high fibre content and virtually no porosity even at turning inlet into vent, thanks to increasing vent pressure after preform filling.

Although Chapters 4 and 5 were outlined to find a VI manufacturing methodology which fitted ISFLIP targets, both chapters are completely focused on conventional VI. However, drawn conclusions served to implement an effective manufacturing procedure in ISFLIP as shown in Chapter 6.

Chapter 6 presents the proof-of-concept of ISFLIP while addressing formability of ISFLIP specimens according to different geometries: hemisphere shape (uniform double curvature), and 'C' variable cross-section profile (single curvature shape with intermediate joggles). Auxiliary materials included into the preform assembly have an essential role in attainable shapes, since the whole preform assembly is formed at one, adding complexity to the overall formability performance. Besides, a major inconvenient of combining plastic films with textile fabrics and knitted meshes is that dominant in-plane deformation mechanisms are different.

Finally, the findings and conclusions of this study, and suggestions for future research are discussed in Chapter 7.

Chapter 2

Literature review

2.1. Textile composites

A “composite material” is defined as the combination of two or more constituent materials which presents characteristics different from the individual components. Unlike metal alloys, each constituent material preserves its chemical, physical and mechanical properties.

FRPs are a class of composite material formed by a thermoset (TS) or thermoplastic (TP) polymeric matrix which is reinforced by fibrous materials. Fibres can be spread into the matrix in continuous (long fibres) or discontinuous (short fibres) forms. Continuous reinforcements offer better mechanical properties than discontinuous reinforcements. Furthermore, arrangements of aligned fibres enhance fibre packing, achieving higher fibre volume fractions than in case of random distributions of fibres and, thus, resulting also in better mechanical properties.

This thesis deals with continuous, aligned fibre-based reinforcements, since it is focused on high performance composites. Nowadays, textiles are the most common form of continuous and orientated fibre reinforcements. In this section, it is given a brief introduction to constituent materials of FRPs associated to LCM.

2.1.1. Fibres

The most common fibres used as reinforcements in high performance FRPs are glass, carbon, aramid and polyethylene (PE). Fibrous materials offer extraordinary mechanical properties due to the presence of far fewer defects than does the bulk materials (Figure 2.1.a). However, their

producing costs are higher than equivalent bulk materials and more typical metal alloys, constituting a hurdle really difficult to overcome in most markets and applications (Figure 2.1.b).

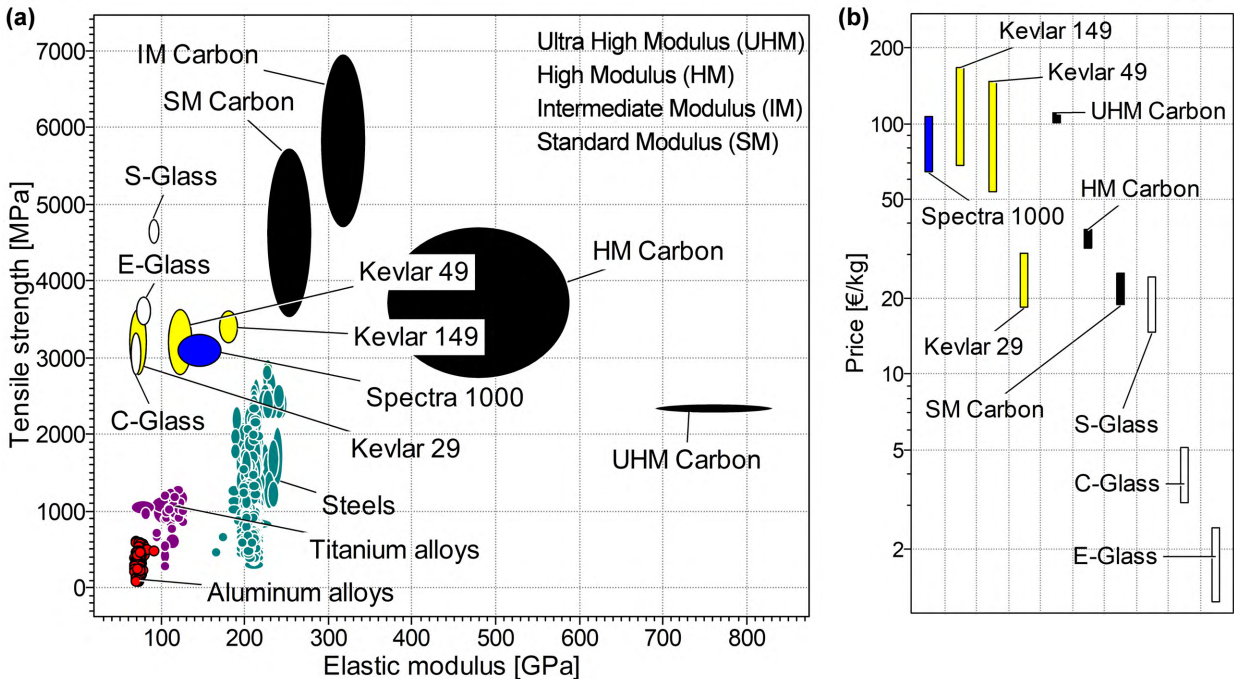


Figure 2.1. Properties of fibrous materials often used in high performance composites (Kevlar is a registered trademark of Dupont Corporation for aramid fibres, and Spectra is a registered trademark of Honeywell International Inc for PE fibres): (a) tensile properties and (b) cost (data extracted from [49]).

Glass fibres offer the best ratio cost/properties; although their use in high performance structural applications is limited due to their low stiffness. Aramid fibres present high specific tensile properties; but they show poor compression response, and are difficult to cut and machine. Aramid fibres are mostly used in applications which require high impact resistance due to their superior toughness. Finally, carbon fibres stand out in stiffness, showing the highest elastic modulus among presented fibrous materials. They are usually classified according to their elastic modulus to covered the wide range of offered mechanical properties. Carbon fibres are mainly used in high performance structural applications in which benefits of their superior performance outweigh their high cost.

In general, FRP manufacturing is not affected by the material of the involved reinforcements, apart from the manufacturing temperature which is obviously limited by the service temperature of the polymeric fibres. Nevertheless, textiles in which fibres are arranged depend on fibre material. Mechanical properties of some fibres facilitate the adoption of certain textile architectures. Additionally, supplying some fibre materials in particular arrangements may not result cost-effective, although being physically feasible. Different textile architectures can affect manufacturability. Permeability in textile reinforcements differs among different architectures,

affecting preform filling in LCM [50–53]. Likewise, drapeability also varies among textile architectures [54,55].

Although different fibrous materials do not affect the overall performance of LCM, some slight variations may certainly appear between them. Preform compaction should be affected by fibre diameter and different friction coefficients [56,57]. Besides, in case of flow through dual scale porous media, flow through tows is governed by capillarity forces which depends on fibre diameter and the contact angle between the fibre and the matrix [58–60]. Contact angle between fibre and matrix and, thus, fibre wettability depends on surface energy of involved materials. Fibre free surface energy must be higher than matrix surface energy in liquid state to guarantee fully wet out. The surface energies for glass and TS polymers are 500 dynes/cm^2 and $30 - 40 \text{ dynes/cm}^2$, respectively. However, carbon has a surface energy of around 50 dynes/cm^2 ; hence, special care must be taken while selecting the polymeric matrix to ensure that it can wet the fibre [61].

2.1.2. Textile architectures

As previously mentioned, textiles are the most common form of fibre arrangement into FRPs, and specifically in LCM manufacturing. The term “textile” refers to an interlaced structure consisting of yarns. Textile-based materials offer a good balance in terms of cost of raw materials and manufacture. While direct use of fibres or yarns might be cheaper in terms of material costs, they are difficult to handle and to form into complex component shapes. Textile reinforcements make easy preforming and can be produced in large quantities at reasonable cost using automated manufacturing techniques [62]. Some textile architectures often used in FRP are shown in Figure 2.2.

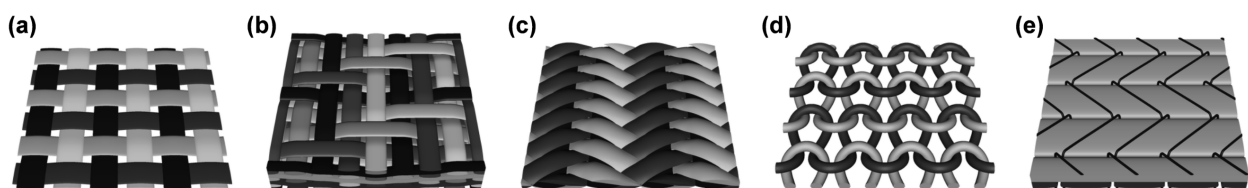


Figure 2.2. Main textile architectures used in FRPs: (a) 2D weave, (b) 3D weave, (c) triaxial braid, (d) weft-knit and (e) non-crimp (adapted from [63]).

At this point, it is worthwhile introducing some textile-related concepts. The term “yarn” embraces a wide range of 1D fibrous objects. A yarn has substantial length and relatively small cross-section and is made of fibres and/or filaments, with or without twist. Untwisted, thick yarns are termed “tows”. Flat tows are called “rovings” in composite terminology. In high performance FRP, fibre

yarns are normally untwisted, thus the term “tow” is quite common. Besides, the term “roving” is usually used to refer to untwisted glass fibre tows, in contrast to glass fibre twisted yarns.

Textiles are hierarchically structured fibrous materials. Three hierarchical levels and associated scales can be distinguished [64]: fibres at the microscopic scale (10^{-3} m), yarns at the mesoscopic scale (10^{-1} m) and fabrics at the macroscopic scale (10^0 m). This intricate structure leads to high complexity at addressing not only final properties of textile composites, but also properties associated to part manufacture [56,65–69].

Textile definition starts from the microscopic level with the “fibre material and diameter”. It continues at yarn scale with “linear density”, which is the mass of a yarn per unit of length (inverse to “yarn count”, which is the number of fibres into the yarn); “yarn dimensions”, width and height; and “twist”, which is the number of turns per units of length. Finally, at the fabric level, textiles are characterized by “warp ends count” (inverse to “warp spacing”) and “weft picks count” (inverse to “weft spacing”), and “weave pattern”, from which yarn crimp and surface density result. In woven textiles, warp yarns are those yarns aligned with the direction of the weaving machine, while weft yarns are those yarns across the width of the weaving machine. Depending on the ratio of yarn width to yarn space (warp and weft yarns), dense fabrics are considered those that show a ratio close to the unity, while open fabrics show a yarn space considerably larger than yarn width.

Textile preforms, arrangement of fibrous reinforcements that has been formed into a shape which closely resembles the final part, can be created through directly weaving or braiding 3D fabrics, or through stacking 2D fabrics. Preforms must be designed by selecting adequate fibre and fabric types, and the total fibre volume considering the required mechanical performance, permeability to resin flow, fibre wet out, formability, surface finish and cost. Since ISFLIP involves a forming stage which requires sliding between adjacent layers, only 2D fabric stack preforms are suitable: woven and non-crimped fabrics.

Woven fabrics provide strength and stiffness in two directions, resulting in excellent handling characteristics and good drape. There are three main weave styles: plain weave, twill weave and satin weave. Low crimp gives better mechanical performance, because straighter fibres carry greater loads, and provides a smoother finish in FRP parts. A drapeable fabric is easier to lay up over complex forms. Reducing yarn interlacing improves drapeability [70]; but, more often than not, worsen handling and cutting. Satin weaves offer higher drapeability than twill weaves, which in turn present higher drapeability than plain weaves.

Woven fabrics compromise mechanical performance of FRP because of the crimp that causes fibre misalignments. Non-crimped fabrics combine unidirectional crimp-free fibre layers by assembling them together by stitching (sewing or knitting) and/or bonding by chemical agents; although stitching also causes local deviations to fibre orientations that may impact mechanical performance [71,72]. Considering rolling direction is 0° , layers with fibre orientated at 0° , 90° , $+45^\circ$ and -45° are usually combined.

Fibre, tow or fabric stabilization though TS or TP binders is not exclusive of non-crimped fabrics; actually, fabric stabilization is being extended in the recent years in order to facilitate fabric handling and preforming, and avoid undesired fabric distortions or fraying [10,73]. Binders must be compatible with the matrix system in order not to adversely affect matrix polymerization.

2.1.3. Resins

While the broad range of reinforcement possibilities in FRPs comes from the vast variety of textile architectures available, rather than from the number of fibrous materials; matrix variety comes from the huge spectrum of polymer formulations. In LCM, TS resins are usually used because of their low viscosity (0,1-0,5 Pa·s). Use of TP resins is not practical due to their high melt viscosity (typically $10^2 - 10^6$ Pa·s), although this problem can be solved by using low viscous polymeric precursors that later polymerize to the TP matrices.

TS resins account for most of the FRP market due to the wide range of formulations which can be tailored to specific needs, low temperature processability and excellent fibre wet-out. The most widely used TS resins in commercial applications are unsaturated polyesters and epoxies. Unsaturated polyester resins are mainly found in low performance applications, they are usually coupled with glass reinforcements, whereas epoxy resins are used in high performance composites. Epoxies are more expensive than unsaturated polyester resins, but they produce stronger and more temperature-resistant FRP parts, as well as showing lower contraction at curing. An important drawback of polyesters resins is the controversial emission of styrene as a by-product of the cure reaction [74–76].

Other TS matrices that can be found in FRP components manufactured by LCM are vinyl-ester, phenolic and bismaleimide resins. Vinyl-ester resins are placed between unsaturated polyester and epoxies in mechanical performance, cure contraction and cost; phenolic resins are mainly used in applications which require flame-resistant and low smoke products; and bismaleimide are applied to high performance structural components requiring high toughness and high temperature resistance.

On the other hand, although interest in TP have existed for a long time, the focus on reactive processing of TP composites which can be obtain through LCM is relatively recent [8]. TP matrices are recyclable by nature, allows short processing times and offer higher toughness; but, in most cases, they also must be processed at higher temperatures ($> 140^{\circ}\text{C}$) than TS resins, which can be normally processed at ambient temperature. Proposed approaches to manufacture TP-FRP via LCM involve filling a preform with a low viscosity mono- or oligomeric precursor, which polymerises *in situ* after initiating the polymerization reaction by heating or adding a catalyst system to the precursor prior to impregnation. Due to their low molecular weight, precursors have extremely low melt viscosities. Research efforts have mainly concentrated on reactive polymerization of polyamide-6 (PA-6) [77–79], polyamide-12 (PA-12) [7] and polybutylene terephthalate (PBT) [80–82]. All three reactive PA-6, PA-12 and PBT polymers must be processed (perform filling) at temperatures above 140°C . Additionally, reactive acrylic TP matrices can also be obtained at ambient temperature [83].

In response to short processing times offered by new reactive TP matrices, new developments in epoxy resin formulations now allow to fully cure resins in short cycle times (< 15 min) at high temperature ($> 100^{\circ}\text{C}$) [7,9,84].

2.1.4. Prepreg vs. dry fibre

Manufacturing technologies associated to FRP parts can be split into two categories according to the initial state of the raw materials: pre-impregnated reinforcements (prepregs) and dry fibre.

On the one hand, “*prepregs*” refer to reinforcements that are already impregnated with the polymeric matrix before being shaped to the final part geometry. In case of TS matrices, resin stays partially cured (B-stage) before carrying out the complete polymerization once all pre-impregnated reinforcements are placed on the mould. In order to guarantee that resins remain only partially cured, prepreg materials must be stored at temperatures under the freezing point, having a shelf life around twelve months. Out life, maximum accumulated time allowed at room temperature before proceeding with the complete cure, is usually under one month.

On the other hand, in *dry fibre technologies*, preforms are created from a set of textile fabrics in which the polymeric matrix is not present yet, since they are later impregnated by hand or through any LCM variant. It is worthwhile stressing the difference between prepregs, in which the matrix is already present, and bindered fabrics, in which the matrix is not present although there is some kind of chemical agent that stabilizes the fabric. Therefore, bindered fabrics belong to the category of dry fibre reinforcements.

Prepregs-based FRP parts show higher reproducibility than dry fibre-based FRPs due to the closer control of fibre and resin contents into the final part. In aerospace applications, autoclave manufacturing of unidirectional (UD) fibre reinforced prepregs with toughened epoxy resins is the state-of-the-art in high performance applications. Fibre volume fractions of 60-70% are usual in prepreg-autoclave manufacturing. However, numerous disadvantages are involved: high material cost, massive investment, costly tooling, long cycle time, excessive energy consumption and huge footprint [4–6]. Dry fibre processing is a promising OOA alternative to prepreg-autoclave manufacturing, although parity in part quality has not been achieved yet (another alternative is OOA prepregs, but these materials and involved technologies are out of the scope of this work).

The most common strategy of toughening epoxy resins is through TP tougheners; however, resulting viscosities are too high to flow through the low permeability textile preforms usually used in LCM manufacturing. Epoxies derive mechanical performance, and chemical and thermal resistance from cross-link density and chain rigidity, opposing the requirement of low viscosity. Even certified epoxy resins to be used in aeronautic primary structures which can be infused at high temperature, such as Hexflow RTM6 (Hexcel) and Cycom PR 520 RTM (Cytec), show fracture toughness significantly lower than their toughened counterparts. There are two basic methods for counteracting epoxy brittleness which are compatible with infusion: adding nano-fillers to the epoxy which do not significantly affect its rheological behaviour [85–88], and adding tougheners to the preform to be dissolved or dispersed into the epoxy before its full cure [89–93]. The second approach, mainly based on TP tougheners in form of scrims [89,90], powders [89,91] or soluble stitches [92], can also be helpful at facilitating preforming through fabric or even preform stabilization, which actually is crucial to achieve high reliability levels.

Another interesting attempt to bridge the gap between UD prepregs and dry fibre technologies is spread tow fabrics [94,95]. Carbon fibre tows are spread into wider tapes, tightly aligning individual filaments. Tapes are preferably stabilized with any kind of binder material, typically TP, to prevent spread tows to recover their previous narrow yarn shape during handling. Then, spread tows are interlaced in a woven structure. Spread tow fabrics allow to reduce layer thickness and diminish fibre crimp (straighter fibres), which increases mechanical performance. Besides, size of resin rich areas formed due to yarn interlacing between layers is also reduced, since available space is minimized. Additionally, stabilized textiles improve cutting and handling as previously mentioned.

Figure 2.3 shows tensile properties and cost for some typical epoxy FRP parts. While mechanical performance is considerably reduced from the extraordinary mechanical properties

offered by the fibrous materials, additional processing costs cause an increment on part price. It is worth noting the huge difference between tensile properties according to fibre direction into the laminates (logarithmic scales are used in both axis of Figure 2.3.a), which is caused by the high anisotropy of continuous, aligned fibre reinforcements. In practice, all fibre reinforcements cannot be orientated along the loading direction, since some fibre fraction must provide structural integrity to the component in the transversal direction.

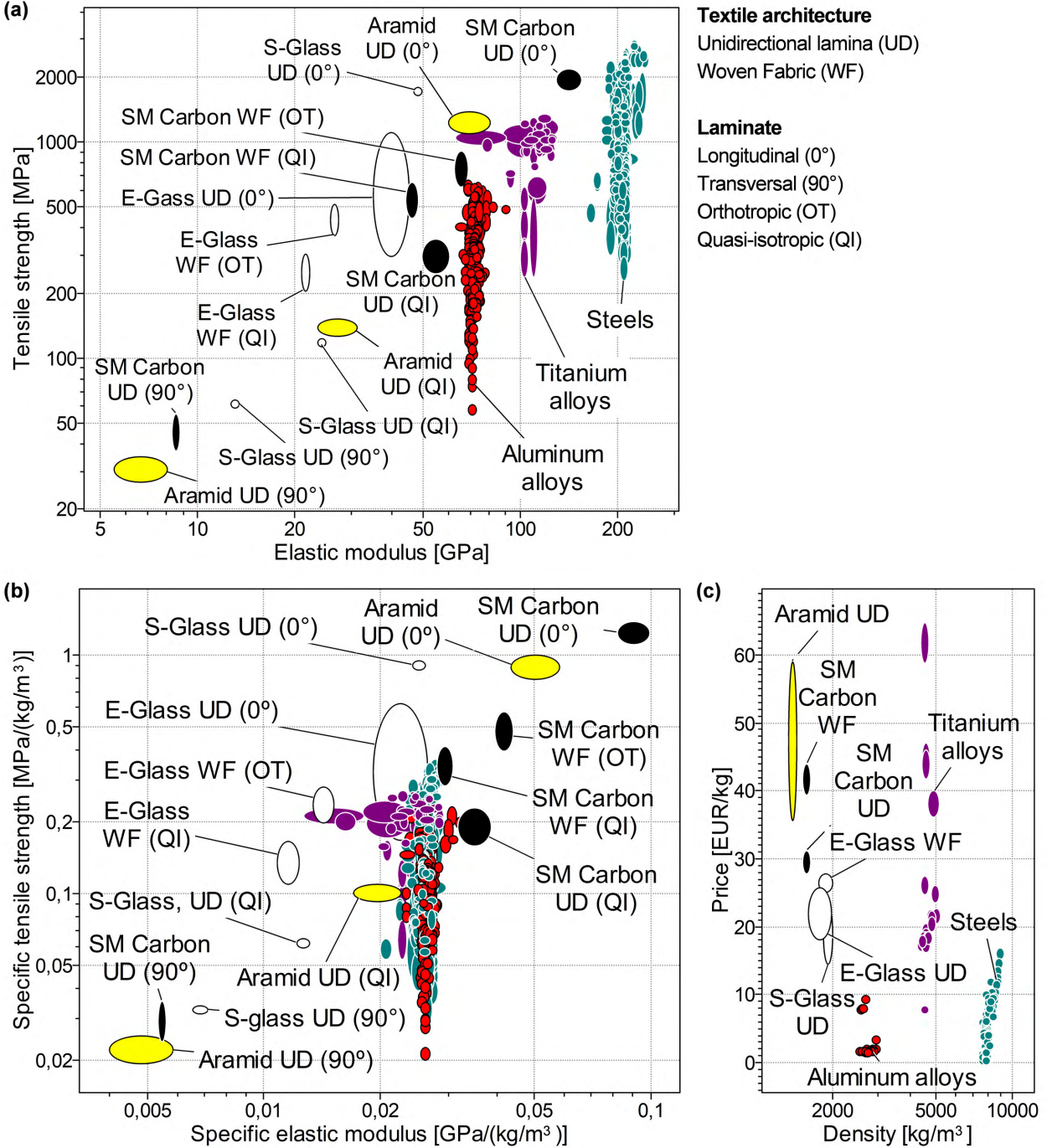


Figure 2.3. Properties of some typical epoxy FRP laminates: (a) tensile properties, (b) specific tensile properties and (c) cost (data extracted from [49]).

2.1.5. Manufacturing properties

A general trend in FRP manufacturing is the lack of standardization in the characterization of textile reinforcements. A number of deformation mechanisms can be identified when textiles, initially flat, accommodate to non-flat shapes: intra-ply shear, intra-ply tensile loading, ply-tool or ply-ply shear, ply bending and compaction. The two primary deformation modes in forming of multi-layer composites are intra-ply shear and ply-ply shear, although dependences on other deformation mechanisms may occur and also be significant. Preform compaction is crucial in another important preform property such as permeability, which is fundamental to explain preform filling and post-filling in LCM.

2.1.5.1. Intra-ply shear

Intra-ply shear happens when textiles are subjected to in-plane shear. It is considered the primary deformation mechanism for aligned-based reinforcements. In combination with low bending resistance, textiles can adapt to 3D shapes with double curvature due to intra-ply shear.

Depending on the textile architecture, intra-ply shear happens in one way or another [96]. UD non-crimped fabrics chemically assembled (bindered or prepregs) deform by shearing along the fibre direction. Woven, braided and non-crimped fabrics (assembled by stitching) deforms by trellis shear such that yarns rotate at cross-overs. Knitted fabrics may deform in three ways: yarn straightening, trellis shearing and yarn slippage. Therefore, trellis shear is the dominant deformation mechanism of the reinforcements on which ISFLIP is focused.

During trellis shearing, yarns are compacted while rotating. Once adjacent yarns come into contact, shear resistance increases significantly, since yarns are no longer able to freely rotate and they begin to exert a compressive force on each other as the fabric is further deformed. The angle at which free rotation stops is called “locking angle”. Deformation beyond the locking angle is one of the main sources of wrinkle formation on fabrics. All these deformation stages are shown in Figure 2.4.

The two most widely used test methods to characterize trellis shear are the picture frame test (Figure 2.5.a) and the bias extension test (Figure 2.5.b). In the picture frame test, a loading frame is used, imposing a simple pint-jointed net deformation on a square fabric sample. In the bias extension test, a rectangular fabric sample is tested in tension at $\pm 45^\circ$ to the principal fibre directions. In spite of not being standardized, a group of researchers have made a collaborative effort to benchmark both characterization tests [97]. Deformation mechanisms involved in picture

frame are closer to those that occur during textile forming; however, bias extension offers a quick and reliable way of determining the locking angle with no special jigs [98].

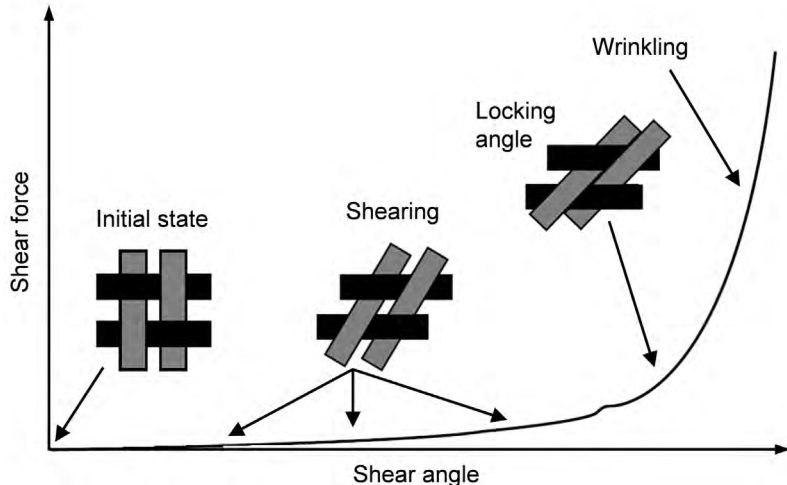


Figure 2.4. Typical woven fabric shear behaviour curve (adapted from [99]).

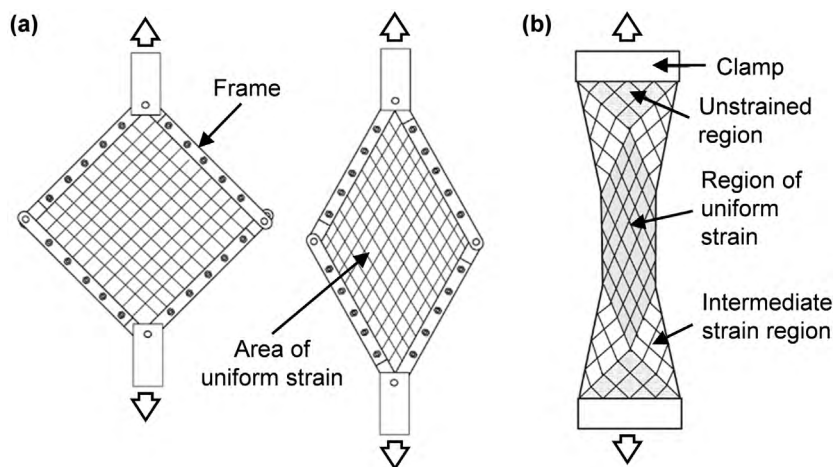


Figure 2.5. Experimental set-ups used to evaluate intra-ply shear properties: (a) picture frame and (b) bias extension (adapted from [100]).

Trellis shear behaviour depends on the textile architecture and, in case of including any TP or TS matrix or binder, or being a commingled fabric (ceramic and polymeric fabrics are combined into the yarns), on temperature and shear rate [54,97,98]. It must be noted that forming processes start from a stack of textile reinforcements which must be previously stabilized to allow its transfer to the forming station, and the chemical stabilization in form of prepreg, or commingled or bindered fabrics is pretty common. Therefore, higher than ambient temperature characterization is usually necessary. Viscous matrices or binders affects yarn rotation and rearrangement of fibres into the yarns which happen during intra-ply shear. Low viscosity and velocity facilitate involved fibre movements. In case of TP polymers being present, characterization above the melting point is needed.

Woven and braided fabrics show a symmetrical shear behaviour; however, non-crimped fabrics often present an unsymmetrical shear response. In one shear direction, behaviour is comparable to woven fabrics, while in the perpendicular direction, shear resistance is considerably larger and the locking angle smaller [54]. Satin weaves offer higher drapeability than twill weaves, which in turn present higher drapeability than plain weaves [54,55].

In hand lay-up, intra-ply shear is the only deformation mechanism involved in the preforming stage; however, in more sophisticated forming processes, such as stamping and diaphragm forming, several deformation mechanisms are involved and, although the main deformation mode is intra-ply shear, shear behaviour is severely affected by other deformation mechanisms such as intra-ply tension [101–103] and compaction [104,105].

When fabric yarns are loaded in tension, intra-ply shear rigidity increases. Required load to reach a specific shear angle is bigger. This can be intuitively understood due to the increased normal forces acting in weave cross-overs, which increases internal sliding friction during deformation of the fabric. Nevertheless, larger shear angles without wrinkle formation can be reached when fabrics are also loaded in tension [106–108], that is especially interesting in stamping processes in which intra-ply tension in fabrics being formed can be controlled through the clamping force exerted by blank-holders. Tension and the out-of-plane bending behavior also play an important role in wrinkling, not only the shear behaviour.

The effect of compaction pressure on trellis shear is similar to that of in-plane tension; since normal forces acting in weave cross-overs also increase, resulting in higher shearing resistance. Unlike combined tension-shear loading, which resulted in larger locking angles, combined compaction-shear loading results in smaller locking angles at which wrinkling occurs [104,105].

2.1.5.2. Tool- and ply-ply shear

In multi-layer forming, ply-ply shear is fundamental. In case of double curvature shapes, in which successive layers containing fibre tows in different directions are present, intra-ply shear deformation considerably differs between successive layers; therefore, some slippage between plies must exist to each ply accommodate to the 3D shape. Interactions between successive plies can lead to transferring compression loads which can cause tow buckling and, thus, wrinkling [109,110]. Formability of quasi-isotropic laminates is severely limited with respect to orthotropic counterparts [111,112]. On the other hand, ply-tool friction is one of the mechanism through which forming loads are transferred to the fabrics (e.g. blank-holders in stamping).

As in case of intra-ply shear, there is not any standard method to characterize friction behaviour of textile reinforcements. Most of characterization attempts are based on pull-out (or pull-through) tests [113–115], capstan set-ups [116] and variations of the standard method UNE-EN ISO 8295-2005 to characterize coefficients of friction for plastic films and thin sheets [117]. Although, more accurate devices able to measure even yarn interaction between different fabrics have been developed [118].

Pull-out and pull-through tests present the advantage of allowing to easily keep a constant temperature during the test. The fabric sample is clamped with a constant force between two heated plates whose surface is covered with the other material (tool or fabric) under study. The friction area reduces during pull-out tests; while, it remains unchanged during the pull-through test, since the fabric sample is pulled between the two blocks during testing (Figure 2.6).

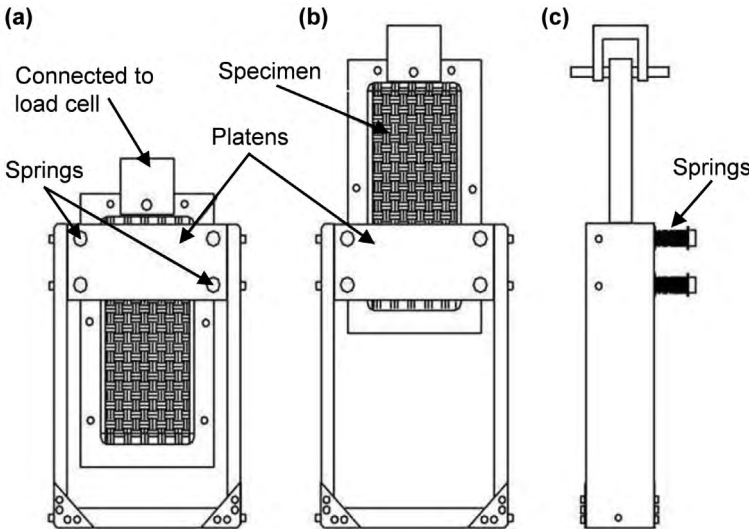


Figure 2.6. Experimental set-up for a pull-through test used to evaluate tool- and ply-ply shear properties: (a) start of test, (b) end of test and (c) side view of the set-up at the end of test (adapted from [54]).

As in case of intra-ply shear, both static and dynamic friction coefficients depend on temperature and, the later, on sliding velocity [114,115]. Besides, friction coefficients also depend on the compaction pressure. Contrary to expectations, friction coefficients decrease as compaction pressure increases; but, obviously, higher normal loads imply higher absolute friction resistance [114,115]. Combined effects of temperature, sliding velocity and pressure on dynamic friction coefficients can be addressed through the Stribeck curve. If present matrices are in a low viscosity state (over the melting point in case of TP), hydrodynamic lubrication occurs between fabrics or between fabric and tool [114].

Fabric orientation and shearing also affects friction coefficients due to the wavy surface of textile reinforcements and the orientated arrangement of fibres [116–118].

2.1.5.3. Compaction

Final part properties associated to fibre volume fraction, v_f , and manufacturing features such as permeability in LCM are affected by reinforcement compaction during preforming. Actually, preform permeability depends on v_f , which, in turn, depends on the compaction pressure exerted on the preform.

Multi-layer textile preforms show a complex inelastic compressive behaviour, exhibiting phenomena such as dependence on compaction velocity, stress relaxation and stress-strain hysteresis [119,120]. The inelastic behaviour of fibre reinforcements is caused by fibre-fibre frictional sliding into yarns, and between yarns of the same fabric and of different fabrics, which shows rate-dependent and rate-independent components, and permanent deformation. On complete unloading, some strain energy remains locked in the fibres as a consequence of fibre rearrangement, leading to the above-mentioned stress-strain hysteresis [57,121–123]. Compaction pressure to achieve a target deformation decreases in successive compaction cycles [122]. Conversely, deformation achieved for a constant compaction pressure increases in successive compaction cycles [121]. Besides, most of deformation energy is lost in the first compaction cycles.

A single test method to characterize compressive behaviour of stacked preform does not exist since it is difficult to capture all involved phenomena. Tests are based on exerting a compaction pressure over a flat preform, but, through different testing conditions, specific preform responses can be obtained.

In RTM-like processes, v_f and, thus, thickness are determined by the complete rigid mould cavity; hence, importance of preform compressive behaviour resides in predicting overall loads and stresses exerted on moulds to achieve expected v_f and minimize mould deflections [124,125]. Characterization attempts are usually based on measuring the compaction pressure required to keeping a constant deformation rate until reaching a target deformation, and then holding that deformation over time. A peak of pressure, whose magnitude depends on compaction speed, is found as the target deformation is reached, from which stress relaxation occurs [124–127].

Conversely, in VI techniques, predicting v_f along the process is a massive task because of the flexible one mould half and the successive loading-unloading cycles carried out. Preforms are compacted in the debulking step, unloading due to resin flow during preform filling and re-loaded again at the post-filling step. Even, if fabrics are cut under vacuum compaction, an additional loading-unloading cycle has to be considered. Furthermore, preform wetting during filling changes

the compaction response of the preform [57,126,128]. Some attempts to characterize the complete processing cycle are available in the literature, emphasizing the importance of fibre settling and relaxation at different steady compaction pressures [123,129,130].

Achieving narrow v_f and, thus, thickness tolerances is challenging in VI-like processes because of the dependence on the compressive pressure history exerted on the preform during the whole manufacturing process [129–131], and the long time needed to equilibrate the gradients of pressure and thickness trapped into the preform during filling [132–134]. In addition, the problem of achieving tight tolerances in combination with the inevitable variability of common preforms [135–137] may result in an important lack of reproducibility between parts, or even into the same part.

Apart from the general trends described above and expected dependence on fabric characteristics [56,57], in thin preforms, resultant thickness per layer for different compaction pressures depends on the number of layers of the stack. Yarns in adjacent layers are likely to embed or nest in one another [65,138,139]. Nesting is also greatly affected by relative fibre orientation between layers and even by the presence of binders [57,125,129]. Nesting in multi-layer orthotropic laminates is more severe than in quasi-isotropic laminates in which fibre between layers is rotated $\pm 45^\circ$.

2.1.5.4. Permeability

Permeability of fibrous textiles, k , is one of the key parameters governing preform filling. It corresponds to the ease of a fluid to flow through a porous medium. In porous media such as textile reinforcements, permeability is anisotropic, thus it is described through a second order tensor, \mathbf{K} , which is symmetric. Matrix flow through textile preforms during impregnation is normally addressed by Darcy's law:

$$\mathbf{u} = -\frac{\mathbf{K}}{\mu} \nabla P \quad (1)$$

where \mathbf{u} is the volume-averaged velocity into the porous medium, μ is the dynamic viscosity and ∇P is the gradient of pressure.

Darcy's law assumes single-phase flow of a viscous fluid behind a progressing flow front and that the porous medium behind the flow front is fully saturated. Nevertheless, aligned fibre-based textile reinforcements present two clearly different porosity scales, microscopic (intra-tow) and mesoscopic (inter-tow), that induce a dual-scale flow.

Darcy's law can still be applied to both scales, which are connected through a sink term in the continuity equation [58,140,141]; however, while inter-tow flow is governed by inlet and vent pressures, intra-tow flow is governed by capillary suction. From a thermodynamic approach, it can be concluded that capillary pressure, P_c , governing intra-tow flow is proportional to the resin surface tension, γ , and the cosine of the contact angle between resin and fibre, θ , and inversely proportional to the fibre diameter ϕ_f [58–60]:

$$P_c \propto \frac{\gamma}{\phi_f} \cos \theta \quad (2)$$

A partially saturated region is created due to this dual scale nature, being the region where the macroscopic front has reached and occupied the spaces between the yarns, but the pores into the yarns are not yet completely filled, or vice versa (Figure 2.7). The former situation happens when viscous forces dominate resin flow and the later, when capillary forces dominate.

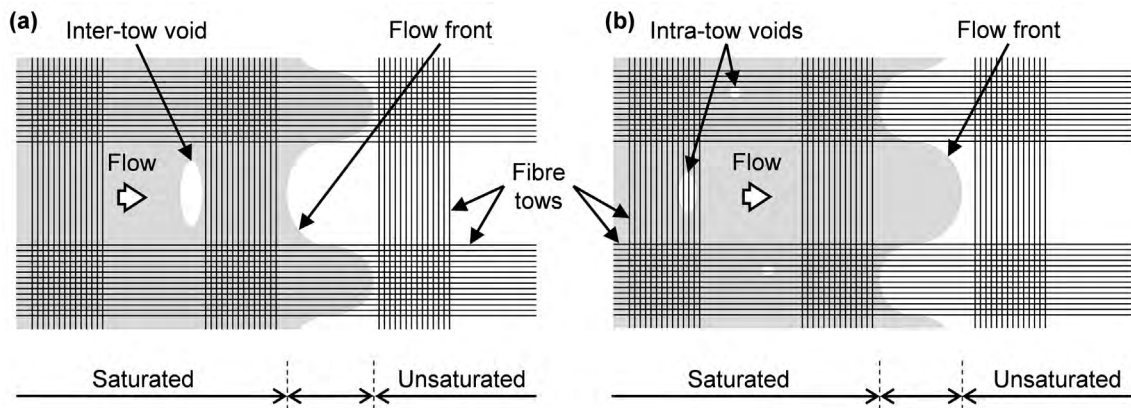


Figure 2.7. Exaggerated representation of dual-scale flow: (a) capillary forces dominate and (b) viscous forces dominate.

Another approach to address the unsaturated flow in dual-scale preforms is to assign a permeability term called “unsaturated permeability”, k_{unsat} , to fibre textiles that is different from its “saturated permeability”, k_{sat} , which is measured after fully filling the preform and steady-state conditions have been established [142–144]. k_{sat} refers to the intrinsic material feature introduced by Darcy's law in Equation (1); while k_{unsat} accounts for not only preform features; but it is also a function of pressure and the nature of the fluid, both affecting capillary suction [53,145,146]. Transient k_{unsat} is a consequence of the viscous versus capillary flow ratio and can be determined by tracking the flow front velocity; while steady-state k_{sat} measures the resin flow and pressure drop once the preform is already fully impregnated. Experimental results show that k_{sat} and is

systematically higher than k_{unsat} [142,147,148]. When fully saturated, the flow is predominantly between the fibre tows and not through them [148,149].

The use of k_{unsat} to capture the effects of unsaturated flow near the resin front is more of an ad hoc approach rather than an exhaustive scientific one; nevertheless, the sink term-based approach requires not only the bulk permeability of the material, k_{sat} , but also the microscale permeability of the fibre yarns [150–152]. Therefore, experimental characterization of preform permeability is more manageable from the point of view of the second approach; although, k_{unsat} will depend on experimental conditions [53,145,146].

Three principal permeability directions can be obtained through diagonalizing the second order tensor, \mathbf{K} . It is normally assumed that two of them, K_1 and K_2 , are contained in the plane of the fibre bed, and the third one, K_3 , is orientated through the thickness. Interest in principal directions lies in directional injection of fibrous preforms. Preforms are often injected in the plane of the fibre bed, or through the thickness of the preform; since, due to the typical slimness of textile preforms, real 3D flows do not often happen.

Permeability characterization attempts are usually focused on in-plane permeabilities. In rectilinear flow methods, k_{sat} and k_{unsat} permeabilities are measured in three directions: K_{0° (warp), K_{45° and K_{90° (weft). From the measured values, K_1 and K_2 (saturated and unsaturated) are computed and their relative orientation with respect to warp and weft directions (Figure 2.8.a). The in-plane flowing pattern is usually an ellipsoid, which can be alternatively tracked through radial flow methods (Figure 2.8.b). Tracking radial flow, unsaturated values of K_1 and K_2 , and their relative orientation can be measured in a single experiment, instead of the three experiments required in case of using the rectilinear flow approach.

Permeability must be computed in the range of fibre volume fraction, v_f , levels occurring during processing. Obviously, higher v_f involves lower preform permeability, since the available space to resin flow decreases.

In the absence of standards, a series of benchmark exercises were carried out by different researchers in a route to find a standard in-plane permeability characterization procedure [147,153]. Large variability is often obtained in permeability measurement experiments, not only due to scatter in preforms [154], but due to lack of calibration between set-ups and experimental procedures. This conclusion was drawn from the first benchmark attempt [147]; however, in the second benchmark exercise, variability of the results was considerably reduced thanks to a more rigorous definition of the testing conditions [153].

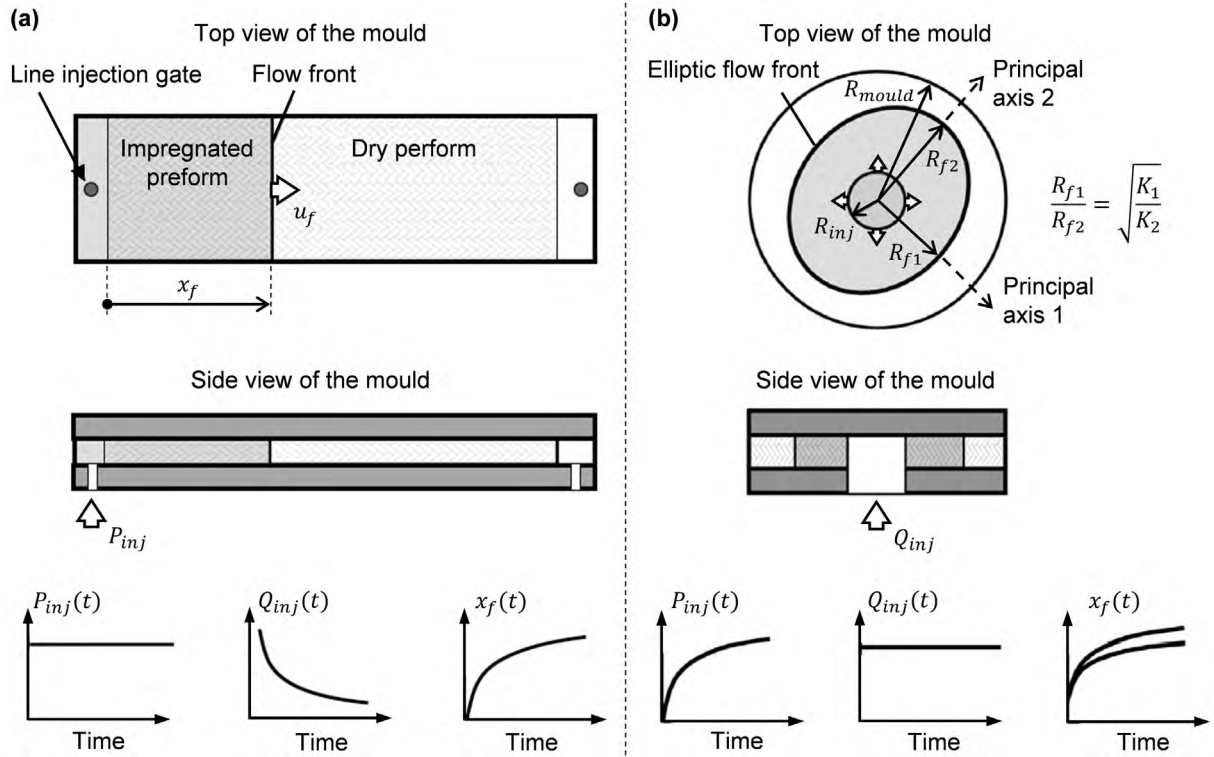


Figure 2.8. Characterization methods of unsaturated in-plane permeability: (a) rectilinear flow and (b) radial flow (adapted from [61]).

In conventional woven fabrics, K_1 and K_2 tend to match the fibre directions into the fabric [50,147,153]. Although in dense textiles, in which yarn width occupies most of yarn space, difference between warp and weft crimps can cause deviations of K_1 and K_2 with respect to the fibre directions [50]. In case of equal yarn-related parameters, plain weave fabrics show higher permeability than twill weave counterparts, that in turn show higher permeability than satin weave fabrics [50–53]. Sensitivity of permeability to v_f is larger for dense textiles than for open textiles [50], which show higher permeability since absolute v_f is lower.

Intra-ply shear also affects v_f since yarns are compacted against each other while rotating, hence permeability of sheared fabrics is lower than in their undeformed state [155–157]. Furthermore, directions of K_1 and K_2 , and anisotropy (K_2/K_1) also vary.

Through-thickness permeability, K_3 , measurements are not as common and only saturated K_3 can be measured [148,158]; although in LCM variants such as SCRIMP or CRTM, in which through-thickness predominates, K_3 is crucial in preform filling. K_3 is often an order of magnitude smaller than in-plane permeability and shows specially high sensitivity to nesting between layers [148,158]; however, since through-thickness filling length is several orders of magnitude smaller than in-plane filling lengths, preform filling is speeded up when through-thickness flow is forced.

Other non-conventional characterization methods are focused on simultaneously computing in-plane and through-thickness permeabilities [159], or computing in-plane permeability of high permeability distribution media and through-thickness preform permeability in a single experiment [160,161].

In FRP, higher v_f generally involves better mechanical performance; however, it also involves lower preform permeability as previously mentioned. Typical low permeability values associated to textile preforms are the reason for which low viscosity matrices are needed in LCM.

2.2. Preforming

When analysing the manufacturing cost breakdown of a FRP part, labour cost often stands out as a main contributor due to highly manual participation of human operators, mainly in the preforming stage [10,11,162,163]. Short cycle times requires establishing a fully automated production chain [7,10]. Beyond 3D preforms created through weaving or braiding, which do not fall within the scope of this thesis, automating the preforming stage is challenging because of the complex manipulation of textile reinforcements and the huge investment usually involved; nevertheless, automation benefits, apart from reducing labour costs, are undeniable: achieving shorter processing time and gaining reproducibility due to the tighter control of the manufacturing process [164].

Manual handling and layup involves a critical dependence of part success on labour skills, since accuracy and repeatability in preform manufacturing are crucial. However, handling and layup automation has proved to be a very complex task due to the easy architecture distortion and low bending stiffness of textile reinforcements [165–167]. Furthermore, non-stabilized fabrics are prone to fray when are manipulated. Lay-up errors can cause wrinkles, dry spots and fibre misalignments, resulting in fatal component failures.

In advance prepreg-based FRP manufacturing, the two main technologies for layup automation are Automated Tape Laying (ATL) and Automated Fibre Placement (AFP) [168]. Both technologies are based on continuous feeding systems of UD prepreg tapes or tows, and are mainly applied to smooth and large part geometries such as aircraft wings. Productivity of ATL and AFP systems can exceed 50 kg/h over flat tools, but they can be prohibitively expensive. Specially adapted AFP systems can also be applied to bindered dry fibre tows [11,169].

Another approach to automate layup focuses on pick and place systems, in which textiles are previously trimmed in a cutting table and then stacked by a pickup robot. Achievable geometries

are also limited to simple part shapes [166,167]. These systems can be applied to both prepreg and dry fibre technologies. Stabilization of fabrics and preforms (in form of prepreg, commingled fabrics, or sewed or bindered dry textiles) is necessary to avoid fabric distortion during textile manipulation. A novel layup system, also appropriate for dry fibre reinforcements, allows the continuous spreading of non-crimped fabrics with curved trajectories by fabric shifting [170–172]; although it cannot deal with highly double-curved shapes.

More complex geometries require a later forming stage, being stamping and diaphragm forming the two most common forming techniques at industrial and lab scales (Figure 2.9). Forming of TS or TP prepreg stacks or bindered preforms is carried out at high temperature to guarantee that the TS or TP chemical agent is in a low viscosity state, facilitating deformation of textile reinforcements. In case of a TS polymer being present, resins must stay partially cured, in a B-stage state.

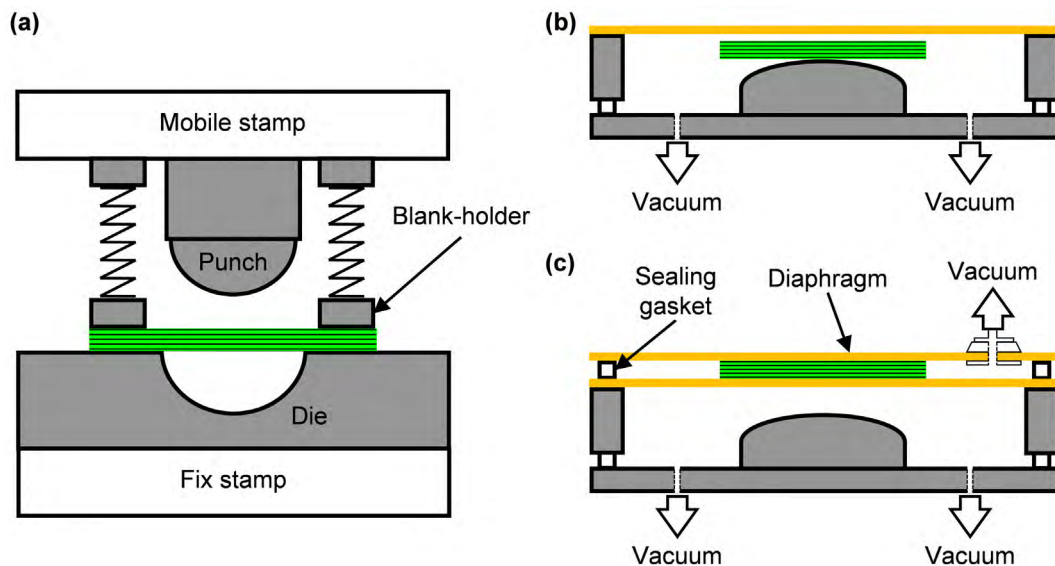


Figure 2.9. Composite forming techniques: (a) stamping, (b) single diaphragm forming (only vacuum assisted) and (c) double diaphragm forming (only vacuum assisted).

According to the heating procedure followed, forming attempts can also be split in isothermal and non-isothermal. Isothermal heating involves conducting the heating and forming stages in the same working station; while, non-isothermal heating involves a rapid transfer of the stack of reinforcements between the heating and forming stations. Due to the possibility of parallelizing heating, and forming and cooling, shorter cycle times can be reached in non-isothermal attempts.

2.2.1. Stamping

In stamping, a stack of stabilized textile reinforcements is formed between two rigid mould halves. One mould half (punch) moves vertically with respect to the other (die) to force the stack of textiles to adapt to the mould geometry. Following an isothermal or non-isothermal procedure, stabilized textiles are formed at higher than ambient temperature.

Rigid mould stamping is usually applied to TP prepregs and combined with non-isothermal heating to achieve short cycle times [110,112,173–175]; although in the literature it can be also found applications to TS prepregs [106,109] and dry textiles [107,108]. In stamping of stacks of TP prepregs, from which final components are already produced, the reconsolidation stage after forming is crucial to obtain high quality parts and minimize void content [174,175].

Stamping of bindered preforms in combination with RTM-like processes, such as CRTM, HP-RTM or T-RTM, is being adopted as the state-of-the-art manufacturing routing in the automotive sector to achieve short cycle times and large production volumes [7,10].

A common feature of stamping processes is the blank-holder, which maintains reinforcements in the right place to guarantee final fibre orientations and transmits membrane tensile loads to the textiles. These membranes stresses permit obtaining higher shearing angles without visible wrinkling, thus maximising fabrics drapability and reducing forming defects [106–108]. Besides, blank-holders allow to control the deformation sequence by applying selective resistance to different fabric zones [176].

Nevertheless, it is worth mentioning that more complex part shapes can be manually formed [177]. In automated forming attempts, textiles with different fibre orientations are formed together, limiting the drapability of the whole stack with respect to the drapability of each individual ply [110–112,173].

2.2.2. Diaphragm forming

Although apparently similar, substantial differences exist between single and double diaphragm forming processes:

In *single diaphragm forming*, the stack of reinforcements is placed over a formed tool and an air-tight cavity is created between the tool support and the diaphragm. Then, air is evacuated from the sealed cavity and/or pressure is increased out of the cavity to force the diaphragm and, consequently, the laminate conforming to the rigid mould. Only loads normal to the diaphragm

surface can be transferred to the stack, hence it is not appropriate to double curvature shapes since the risk of wrinkle formation is great [164].

In *double diaphragm forming*, reinforcements are clamped between two diaphragms due to air evacuation, vacuum is generated into the air-tight cavity formed by the two diaphragms. Then, as in case of single diaphragm forming, the set of diaphragms and the stack is forced to adapt to a rigid mould. As the diaphragms are stretched, surface friction between the laminate and the diaphragms transmits tensile forces to the laminate, creating out-of-plane support and suppressing wrinkling. However, although double diaphragm configurations reduce the risk of wrinkle formation, it is proven that intra-ply shear behaviour is altered due to the compaction pressure exerted on the preform [105].

Diaphragm materials are chosen in function of the processing temperature. Latex is usual at low forming temperatures ($< 80^{\circ}\text{C}$), silicone diaphragms in case mid-range temperatures (80°C - 200°C), and superplastic aluminium or polyimide films such as Upilex-R at high temperatures ($> 200^{\circ}\text{C}$) [178]. Both latex and silicone are hyperelastic materials, so they can be re-used many times. Material cost also increases as temperature resistance increases. Silicone rubber is the most used material in FRP forming, since it covers the typical range of processing temperatures of TS and TP matrices. More than 500 forming cycles can often be carried out with the same silicone sheet before failure; although permanent deformation due to Mullins effect must be accounted for [179].

Isothermal heating combined with diaphragm forming is often applied to TS prepreg stacks which, after being formed, are subjected to long cure cycles [180–182]. Forming of sub-components which are then assembled in larger components that are cured in autoclaves is typical in aeronautics. On the other hand, non-isothermal heating is normally applied to diaphragm forming of TP prepregs to reduce processing time and cost [183–186].

Apart from wrinkling caused by excessive shear, wrinkle formation due to a geometry recess is common in diaphragm forming [180,181]. Membrane compression loads arise forcing the stack to form wrinkles to conform to the forming geometry. Geometry recess depends on the forming shape and the forming sequence, hence corrective measures in diaphragm forming are difficult to be implemented. Conversely, in stamping, blank-holders can be designed to avoid a geometry recess and, thus, wrinkling.

Diaphragm forming offers higher flexibility and lower capital investment than stamping processes; however, attainable shapes do not allow as large shear angles as those usually achieved in stamping.

2.3. Liquid Composite Moulding (LCM)

LCM encompasses FRP manufacturing techniques in which a preform of dry fibre reinforcements is impregnated with a liquid resin by the action of a gradient of pressure between the preform and a container with the resin. LCM processes may be split in two categories according to the driven pressure nature [12]: Resin Transfer Moulding (RTM), in which resin is pushed to the preform by a higher than the atmospheric pressure, or Vacuum Infusion (VI), in which resin is drawn out by a close to the vacuum pressure.

In RTM, preforms are placed into a completely rigid mould cavity and the resin is introduced into the mould to impregnate the preform at a higher than atmospheric pressure (Figure 2.10.a). Besides, compaction pressure, σ_f , exerted on the preform is independent from the pressure, P , which governs resin flow through preforms, which is described by Darcy's law (Equation (1)).

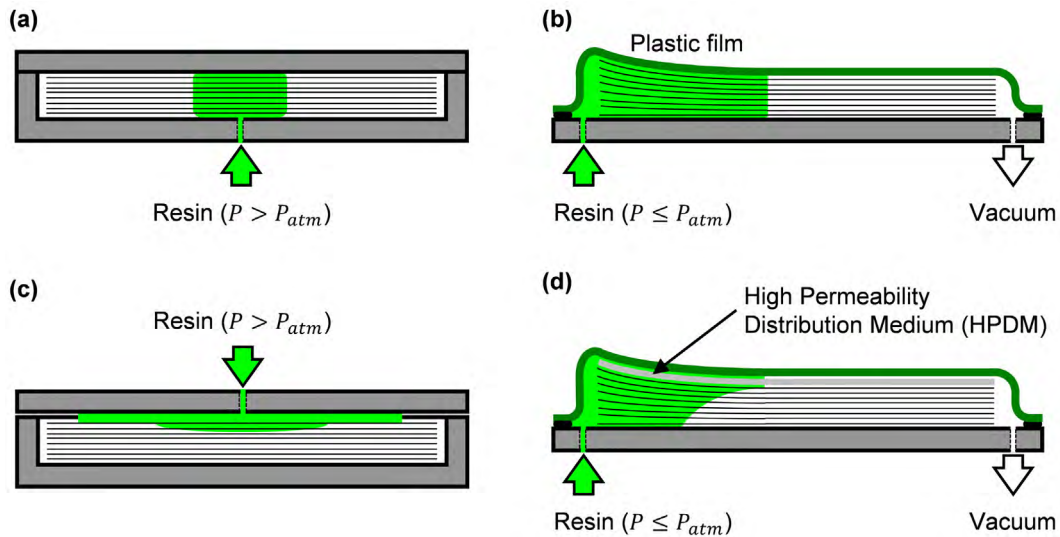


Figure 2.10. LCM techniques: (a) RTM, (b) VI, (c) CRTM and (d) SCRIMP.

Conversely in VI, one mould half is flexible and the resin impregnates the preform at a lower than atmospheric pressure due to vacuum suction (Figure 2.10.b). Consequently, preform compaction pressure, σ_f , and governing pressures, P , are coupled in VI through Terzaghi's relation [187],

$$P_{atm} = P + \sigma_f \quad (3)$$

where P_{atm} is the atmospheric pressure.

Both initial conceptions of RTM and VI assumed in-plane flow through textile preforms; however, due to the long filling times caused by typical low preform permeabilities, a series of variants appeared to speed-up the filling stage by forcing through-thickness flow:

- The Compression Resin Transfer Moulding (CRTM) [21–23], depicted in Figure 2.10.c, is a variant of RTM in which resin is injected into a gap created between the preform and the upper half mould since the mould is not completely closed. Once the required amount of resin is introduced into the gap, the mould is closed while squeezing the resin into the preform.
- In the Seeman’s Composite Resin Infusion Moulding Process (SCRIMP) [38], shown in Figure 2.10.d, a High Permeability Distribution Medium (HPDM) is placed over the preform, enhancing in-plane flow through the HPDM and the subsequent through-thickness preform impregnation.

Schematics shown in Figure 2.10 do not include auxiliary materials (disposable materials), other than bagging film and HPDM, typically used in VI and SCRIMP: peel-ply, release film, resin distribution and connecting channels, or tacky tape.

2.3.1. Part quality

Product quality differences between RTM and VI arise from the different operational principles described above. VI is still lagging behind RTM in terms of product quality; although, VI also offers some advantages such as flexibility, scalability and cost-effectiveness [188–190].

In manufacture of FRP parts, material is frequently created not before, but during the manufacture of the component. The quality of the manufactured material is often assessed through the fibre volume fraction, v_f , and void volume fraction, v_0 . The former quality attribute directly points out to the material properties, since it refers to the fractions of the constituents; while the later refers to the quantity of defects contained in the composite material. Cause and effect diagrams of v_f and v_0 are provided in Appendix A.

2.3.1.1. Fibre volume fraction, v_f

Properties of FRP parts depend on the combination of their main constituents. Both fraction contents of each constituent and their distribution into the part affect final properties: mechanical, electrical, thermal... Nevertheless, properties are usually referred through v_f to keep easier comparisons between different applications.

In multi-layer textile preforms, v_f is a function of the compaction pressure exerted on the preform, σ_f . In RTM, achievable v_f is in general higher than in VI due to the higher pressures

usually involved. In VI, σ_f cannot exceed the atmospheric pressure, P_{atm} ; since, due to the one mold half which is flexible, σ_f is coupled with the pressure which governs resin flow through preforms through Terzaghi's relation [187].

In RTM, final part v_f and, thus, thickness are determined by the complete rigid mould cavity; hence, importance of preform compressive behaviour resides in predicting overall loads and stresses exerted on moulds to achieve required v_f and minimize mould deformation [124,125].

Achieving tight v_f and, thus, thickness tolerances in VI is challenging because of the dependence on the compressive pressure history exerted on the preform during the whole manufacturing process [129–131], and the long time needed to equilibrate the gradients of pressure and thickness trapped into the preform during filling [132–134]. This situation becomes even more complicated at considering the highly complex inelastic compressive behaviour of multi-layer textile preforms exhibiting phenomena, such as dependence on compaction velocity, stress relaxation and stress-strain hysteresis [119,120].

The Controlled Atmospheric Pressure Resin Infusion (CAPRI) [17], patented by Boeing, takes advantage of the compressive stress-strain hysteresis shown by textile preforms to increase v_f through a multiple-cycle debulking, and of low preform relaxation at pressures far from P_{atm} to reduce into-part thickness variability by holding a reduced gradient of pressure during filling (resin container is kept at partial vacuum) [18].

2.3.1.2. Void volume fraction, v_0 (porosity)

Void content is crucial in matrix performance. Mechanical properties of FRP laminates such as compression, inter-laminar shear and flexural strengths, and fatigue behaviour are seriously affected by void content [191–194]. If porosity is extended to the surface, even surface finish of FRP components may be altered, deteriorating components aesthetics [195] and later bonding [196].

The main causes of void formation in VI and RTM manufacturing are resin flow through heterogeneous dual-scale porous media, outgassing of air dissolved into the resin, evaporation of volatile components of the resin, resin shrinkage at gelation and leakage in connections and moulds. The two former causes stand out as the most influential in final porosity and are usually addressed by controlling processing conditions.

Several studies are focused on predicting void formation due to resin flow through dual-scale porous media [197–199], often addressed in the literature through the modified capillary number, Ca^* [200,201]:

$$Ca^* = \frac{\mu \cdot u_f}{\gamma \cdot \cos \theta} \quad (4)$$

where μ is the dynamic viscosity, u_f is the macroscopic resin velocity at the flow front, γ is the resin surface tension and θ is the contact angle between the fibre and the resin. Ca^* is closely connected to the capillary pressure, P_c , introduced in Equation (2). Besides, it is worth recalling that u_f is given by Darcy's law (Equation (1)). Void formation is negligible in a specific range of Ca^* ; while intra-tow and inter-tow voids are formed at higher and lower values of Ca^* respectively (Figure 2.11).

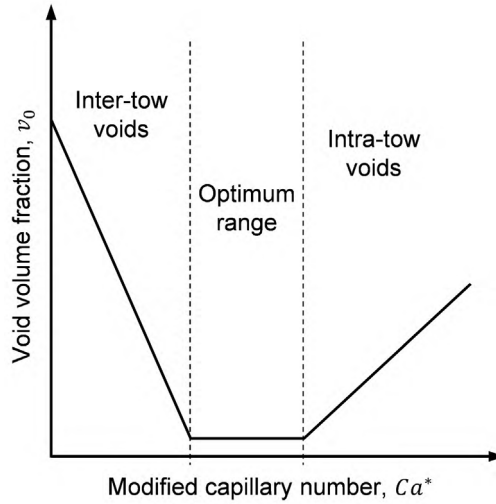


Figure 2.11. Void formation due to resin flow through heterogeneous dual-scale porous media.

On the other hand, resin outgassing is not a common subject in FRP manufacturing research, even though it is a major concern in VI manufacturing since resin is prone to outgas at vacuum pressures due to its minimum air solubility as stated by Henry's law: *the amount of a given gas that dissolves in a volume of liquid is directly proportional to the partial pressure of the gas in equilibrium with the liquid*. Therefore, air solubility in equilibrium is given by Henry's law as

$$C_{air} = H \cdot P_{air} \quad (5)$$

where C_{air} is the solubility of air at a fixed temperature, P_{air} is the partial pressure of air and H is the Henry's law solubility constant, which depends on temperature (decreasing with rising

temperatures) and the liquid nature. Consequently, outgassing behaviour of resins is a function of the outgassing conditions, pressure and temperature [202–204].

Air solubilities by volume in epoxy and polyester resins at ambient conditions are 2,2% [203] and 2,6-3,4% [205], respectively. If outgassing occurs at a pressure near full-vacuum, for example 5 kPa absolute pressure, gas volumes are multiplied by 20 since the product of pressure and volume remains constant at constant temperature as given by the ideal gas law ($P_{air} \cdot V_{air} = const.$).

Evaporation of volatile components may become a real problem in VI when using styrene based resins such as unsaturated polyester and vinyl-ester [188,206]. Unsaturated polyester and vinyl-ester resins are formulated with high styrene contents to achieve a viscosity level appropriate to VI. Although boiling temperature of styrene at atmospheric pressure is over 140°C, and its boiling pressure at ambient temperature is under 1 kPa; if curing was carried out at high temperature while holding a high level of vacuum, styrene evaporation should occur [207].

Matrix shrinkage during polymerization and different Coefficients of Thermal Expansion (CTE) of fibres and matrix may cause fibre readout, which looks like a wavy surface that might be interpreted as a kind of surface porosity [195,208,209]. Large yarns favoured the formation of big resin reach areas trapped between fabrics and moulds that lead to the mentioned fibre readout, which is magnified at higher polymerization temperatures. Resin shrinkage of epoxy resins at cure is negligible in comparison to other resin systems such as unsaturated polyester and vinyl-ester [210–213].

Finally, another cause of massive void formation is leakage, which does not have to be addressed as a simple operational error, since designing robust manufacturing processes is essential to minimize failure rates. Due to the manual nature of VI, the appearance of leaks in the sealing contour is attributed to labour mistakes; however, sealing of the bagging film must be well thought to facilitate labour operation.

Void volume fraction, v_0 , can be minimized by optimizing flowing conditions in RTM as shown in Figure 2.11 [198,214]. Besides, another usual practice in RTM is to increase fluid pressure, P , after preform filling to force compression of voids, and increase resin capacity to dissolve air according Henry's law and, thus, the voids formed during preform impregnation [202,215,216]. If preform filling is assisted by vacuum venting (VARTM), this effect is even enhanced since the compressed volume ratio is inversely proportional to the ratio of pressures [207,217].

Nevertheless, in VI, P and σ_f are coupled through Terzaghi's relation [187], and a counter-productive reduction in v_f should result if P was increased during post-filling to enhance void collapse and resin capacity to dissolve voids. Attempts to minimize void content in VI are usually based on previously degassing the resin [205,218]. In an alternative approach patented by Airbus, the Vacuum Assisted Process (VAP), it is taken advantage of an air-permeable layer that is placed over the preform to allow continuous degassing of the resin while assuring the full impregnation of the preform [43].

2.3.2. Vacuum Infusion (VI)

VI is a complex multi-step manufacturing process whose main steps are governed by pressure, temperature and time parameters (Figure 2.12). The focus of LCM manufacturing is sometimes wrongly reduced to the filling stage, underestimating the rest of main manufacturing steps. This attitude is even more pronounced in VI, whose manufactured parts are not usually pushed to their limits. However, all degassing, debulking, filling, post-filling and curing steps are crucial to realize the full potential of composite materials.

2.3.2.1. Degassing

Although final porosity depends on the whole manufacturing process and materials involved [202,219,220], resin outgassing may be reduced or even avoided by carrying out a proper resin degassing procedure before preform impregnation. Conventional degassing approaches applied in the FRP field consist on exposing a volume of resin to high vacuum levels for a specific amount of time. Nevertheless, degassing efficacy of this procedure is suspicious if physics involved in the process is considered; since air is initially dispersed as molecules into the resin and molecules are removed very slowly from the solution via diffusion through the resin free surface.

Vacuum degassing can be speeded up by creating bubbles which can be removed faster. Therefore, improving attempts are usually based on enhancing heterogeneous bubble nucleation by adding a nucleation medium or sparging (injecting air at the bottom of a resin container) [205,218]. Air molecules diffuse to bubbles, reaching a saturated solution, but no longer over-saturated. However, different problems may arise since some micro-bubbles keep trapped near resin surface after degassing. The combination of a nucleation medium and a system of capillary separation results useful at filtrating these micro-bubbles [218].

In polymer manufacturing, in order to improve efficacy, degassing under vacuum pressures is often combined with assistance systems such as mixing, rotation or sonication which also help bubble formation through rupturing liquid polymers by cavitation [221].

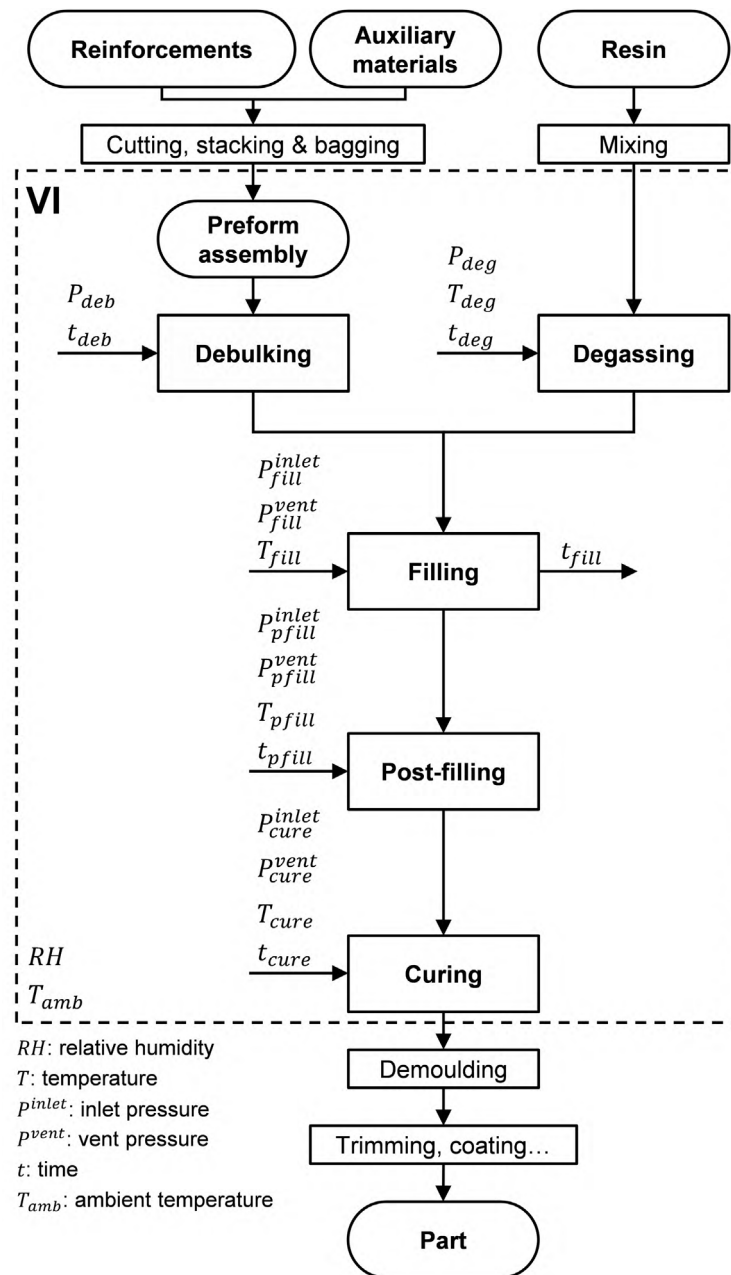


Figure 2.12. Typical flow chart of VI process.

2.3.2.2. Debulking

In the debulking step, preform thickness is reduced through rearranging fibre distribution by applying a compaction pressure once preform is placed onto the mould.

Achieving small thickness tolerances in VI is challenging because part thickness depends on the compressive pressure history exerted on the preform along all manufacturing steps: debulking, filling and post-filling [129–131].

Typical debulking procedures consist on carrying out a single loading step once vacuum is applied into the preform cavity, $P_{deb} = P_{vac}$. However, through multiple loading-unloading cycles, higher v_f can be reached due to the compressive stress-strain hysteresis shown by textile preforms [18,121]. Deformation achieved for a constant compaction pressure increases in successive compaction cycles, while most of fibre rearrangement occurs in the first compaction cycles. Besides, the magnitude of thickness gradient trapped into the preform during rectilinear flow filling is reduced after multi-cycle debulking, since the effect of preform relaxation is smaller [18].

An increment in v_f also affects preform permeability. It is worth noting that an increment of 5% in v_f could involve a decrement of almost one order of magnitude in in-plane and through-thickness permeabilities [148].

2.3.2.3. Filling

Darcy's law points out that flow through porous media is driven by a gradient of pressure, ∇P (Equation (1)). In dual-scale porous preforms, this statement is valid when being applied to inter-tow flow and it is still appropriate in case of taking the approach of unsaturated and saturated flows.

In RTM, fluid pressure, P , along the preform is a linear function of the distance from the inlet since preform thickness is independent from P . Nevertheless, in VI, due to the upper flexible half mould, P is not linear anymore since the compaction pressure, σ_f , that determines preform thickness, is linked to P through Terzaghi's relation [187]. Figure 2.13 shows representative pressure evolutions for both RTM and VI.

The reduction of σ_f from the flow front causes an increment in preform thickness, although this thickness increment caused by preform relaxation is often only significant in areas which are close to the resin inlet regions, where P is close to P_{atm} [129,132,134]. Actually, if resin pot is held at partial vacuum, preform thickness remained almost invariable throughout all the filling step [18,222].

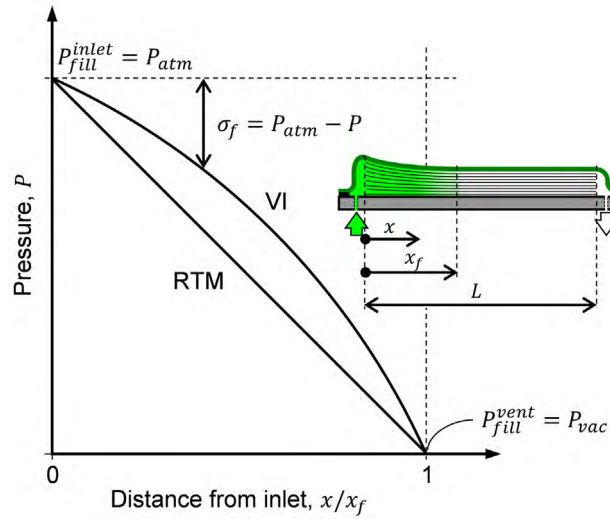


Figure 2.13. Characteristic gradient of pressure during preform filling.

The pressure distribution shown in Figure 2.13 corresponds to a rectilinear filling pattern. Fluid pressure and distributions along the filling direction depend on the filling pattern: rectilinear[132], radial and peripheral [133]. All three basic filling patterns configurations are depicted in Figure 2.14.a. Peripheral filling allows achieving shorter filling times than rectilinear filling; although preform relaxation is also more severe since the area close to the inlet regions is larger and, thus, more resin quantity is necessary to impregnated the whole preform. Conversely, in case of radial filling, filling times are longer and resin consumption is lower than rectilinear filling. Preform relaxation and the excess of resin required to fill the whole preform is a key issue in the post-filling state, as will be discussed later on.

Simulation of VI is a complex task not only due to the dual-scale porous nature of textile preforms used in high performance composites, but because of the large amount of input data which is required [44,223–225]. Permeability must be provided for each stacking sequence present in the preform along the full range of v_f occurring during the filling step [130,131]. Moreover, predicting v_f is not trivial due to the complex compressive behaviour of textile preforms [119,120] and the successive loading-unloading cycles carried out in VI. In case of being present a HPDM, its in-plane permeability is also necessary and through-thickness preform permeability becomes crucial [160,161]. Consequently, performing an accurate simulation of the filling stage in conventional VI is complex and time-consuming; however, it is sometimes necessary to have a fast form of computing filling time, t_{fill} , in the early stages of design. In case of RTM, t_{fill} in in-plane, rectilinear filling patterns can be directly derived from the following analytical expression, assuming complete flow saturation:

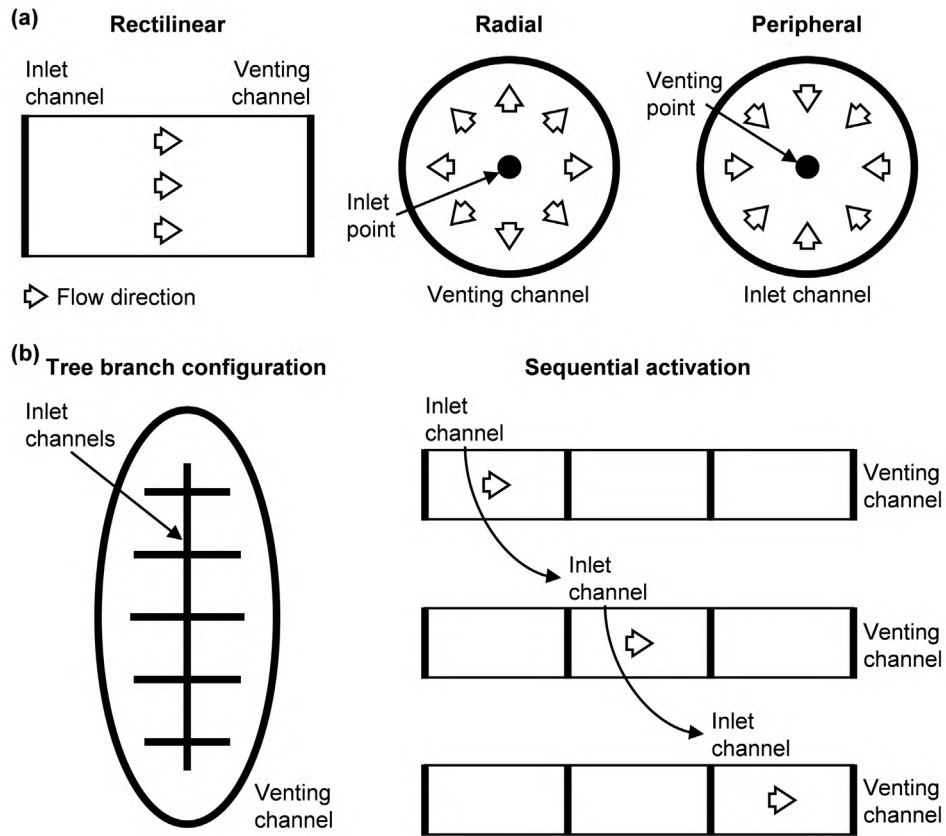


Figure 2.14. Filling patterns: (a) simple and (b) advanced.

$$t_{fill}(RTM) = -\frac{\phi\mu L^2}{2K\Delta P} \quad (6)$$

where μ is the dynamic viscosity, ϕ is the preform porosity ($\phi = 1 - v_f$), K is the permeability in the filling direction and L is the filling length.

In case of VI, other closed analytical solutions have been proposed [226–228]. These approaches require additional assumptions on P distribution along the filled region of the preform. A similar expression to that introduced in Equation (6) can be found in the literature [226]:

$$t_{fill}(VI) = -\frac{\mu}{2} \frac{L^2}{\left(\frac{K dP}{\phi d\alpha}\right)_{\alpha=1}} \quad (7)$$

where α is the relative position ($\alpha = x/x_f$). At the flow front $\alpha = 1$.

In general, these expressions provide accurate enough results considering the early stage in the process design at which they are used. More accurate predictions of t_{fill} require the whole simulation of the filling step.

In both expressions, it can be seen that t_{fill} is proportional to the square of the filling length, L^2 . Therefore, large parts require different filling patterns to achieve reasonable t_{fill} . In Figure 2.14.b, two more sophisticated approaches are shown: inlet channelling in a tree branch configuration [229–231], and sequential activation of inlet and venting channels [232,233]. The objective of both filling patterns is to reduce the effective filling length, L .

Nevertheless, achieving competitive processing times requires the combination of the above-mentioned filling patterns with through-thickness preform impregnation, often forced by placing a HPDM over the preform as in SCRIMP. Although through-thickness impregnation may be an order of magnitude lower than in-plane permeability [148,158]; through-thickness filling length is several orders of magnitude smaller than in-plane filling lengths, speeding up the filling step. A negative effect of through-thickness flow is that it is a proved cause of void entrapment near the mould surface [219], causing a detrimental effect on mechanical performance [234].

Closed form solutions for the case that HPDM is present over the preform have also been developed [235]. More complex expressions were obtained showing good agreement with t_{fill} for large parts, although preform relaxation was not considered [236]. A later study of different authors included preform compaction, also showing promising results [237].

High variability of textile preforms [135–137] and external flow disturbances such as race-tracking can cause incomplete preform impregnation and, thus, part discarding. Through *in situ* control techniques complete preform impregnation can be guaranteed by opening and closing strategically placed injection points [238–240], inducing preform relaxation based on VIPR [48], or locally heating specific areas to reduce resin viscosity [241]. Most of VI-like processes include an upper transparent bagging film which considerably facilitates flow monitoring through image recording [239].

During preform filling, air bubbles (voids) are formed at the flow front due to the heterogeneous architecture of reinforcements fabrics used in high performance composites. Inter-tow or intra-tow voids are formed according to Ca^* and for a specific range of values void content is minimized (Figure 2.11). It has been reported that optimal u_f at which void formation is minimized varies between 0,1–1 mm/s [197]. In RTM and at the onset of VI processes, u_f is usually higher; whereas, at the end of the filling stage of VI, u_f is lower.

After being formed, inter-tow voids mobilization occurs in the direction of the gradient of pressure at high u_f and, thus, high Ca^* [214,242]. Under a critical fluid velocity, no void movement happens; while voids move even faster than the fluid at very high u_f [214].

Mobilization of intra-tow voids is assumed as inexistent into the tow region; however, different hypotheses suggest that intra-tow voids merge into larger ones while migrating to gaps between tows [243] or, conversely, that intra-tow voids removal is only performed by air-compression and diffusion [244].

Resin bleeding is an usual practice to remove residual air voids by allowing bubble void mobilization, although it involves material waste; however, if bleeding time is not high enough, voids may keep trapped near venting regions [219].

2.3.2.4. *Post-filling*

At the end of the filling stage in VI, preform thickness is not homogeneous because of preform relaxation caused by the non-uniform pressure field and the flexible half mould. Resin flow continues after the filling stage until preform thickness becomes uniform.

The typical post-filling procedure involves clamping resin inlets once preform is considered to be completely filled, allowing the excess of resin to flow slowly towards the venting points/channels. Resin flow happens into the inter-tow regions [148,149] and can be represented again by Darcy's law (Equation (1)). While resin flow is driven by the pressure difference between inlet and vent in the filling step; the gradient of pressure trapped into the preform after clamping inlets drives post-filling flow.

As resin flows from preform areas with higher pressure, thickness and pressure decrease, leading to homogeneous thickness and pressure fields. Thickness stabilizes faster than pressure along the preform as a consequence of the strain-stress hysteresis behaviour of textile preforms [57,121–123]. From the point of view of part quality, interest lies in thickness since it is inversely proportional to v_f .

The required time to equilibrate preform thickness during this post-filling period is far from being negligible, actually it can exceed filling time in case of in-plane, rectilinear filling [132,134,245]. Pressure stabilization is normally obviated to avoid excessive process prolongation. In the previous section, it has been commented that filling time in radial filling is longer than in peripheral filling; however, post-filling time is also shorter, resulting in similar cumulative time [133].

Although preform filling is speeded-up by forcing through-thickness preform impregnation with a HPDM; the presence of a HPDM does not shorten time required to equilibrate thickness and pressure after inlet clamping, in spite of completely altering both profiles along the preform

[132]. Once inlet is clamped, thickness and pressure gradually drop after a sharp beginning to minimum levels in case of in-plane flow. In case of using a HPDM, thickness and pressure tend to initially equalise in the area covered by the HPDM, and then gradually drop to similar thickness and pressure values.

The two most effective methods for minimizing time required to equalize thickness and pressure are minimizing preform relaxation during filling [18] and turning inlet into vents after full preform impregnation [134,222].

The application of successive debulking cycles and/or keeping inlet at partial vacuum have been proved to reduce preform relaxation [18]. Consequently, resin consumption is also lower, although filling time, t_{fill} , increases. In case of successive debulking cycle is worth recalling that higher final v_f can be obtained.

Turning inlet into vent results in a fast equalization of thickness and pressure, and does not have any detrimental effect on t_{fill} ; however, it may also result in more porous parts. Since the outgassing behaviour of the resin is a function of the outgassing conditions, pressure and temperature [202–204], resin outgassing depends on pressure distribution along the laminate [207]; therefore, equalizing pressure into the preform to a vent pressure which is close to vacuum pressure, as guaranteed in case of turning inlets into vents, may result in an increment of v_0 with respect to specimens in which a pressure is not stabilized [134,222].

An slight increment of vent pressure after preform filling can help to reduce v_0 without affecting considerably v_f , since voids are formed due to flow through dual-scale porous media at a lower pressure than final gelation pressure [246]. Nevertheless, there exist a risk of drawing air into the resin at rising vent pressure [222].

Although through-thickness flow forced by HPDM causes void entrapment near mould surface [219]; some authors state that preform re-compaction and bagging film collapse during post-filling helps to dissolved trapped voids [219,247]. HPDM acts as a resin reservoir. When pressure is reduced into the laminate during post-filling, thickness of HPDM decreases enhancing resin flow towards the preform. Furthermore, depending on the flexibility of the vacuum bag, it also collapses over the HPDM and increases the forced flow of resin towards the preform.

Apart from HPDM, the placement of a flow resistance between the preform and the venting points/channels also alters thickness and pressure fields [134]. This brake is usually implemented by connecting the preform edges to the vent by means of peel-ply, whose permeability is considerably lower than preform permeability. At reaching the peel-ply during filling, the gradient

of pressure driving resin advance quickly moves to the peel-ply due to its considerably lower permeability. As a result, thickness and pressure differences into the laminates are narrowed; although later thickness and pressure stabilization is longer and, thus, it is difficult to control final thickness [134,222].

While simulation of the filling step is a recurrent topic in the literature; simulation of the post-filling step is not as usual [44,247,248].

2.3.2.5. Curing

During the curing step, the polymerization of the polymeric matrix occurs, a monomer or a mixture of monomers are turned to a polymer. It is worth noting that the polymerization mechanisms of TS and TP are different.

Polymerization of TS polymers involves the formation of cross-linked structures (polymers chains are connected to others by chemical bonds). Cross-linking reactions are usually initiated after adding the corresponding catalyst or hardener to the resin system. Temperature is an accelerator of the polymerization reaction. The main objective of the curing step is to maximize the cross-linking degree, since mechanical properties of the resins depend on the cross-linking between the small molecules which formed the TS polymer.

Conversely, mechanical properties of TP polymers depend on size of the molecules. TP matrices used in LCM *in situ* polymerize from mono- or oligomeric precursors, after initiating the polymerization reaction by heating or adding a catalyst system to the precursor prior to impregnation.

In any case, polymerization is started before preform filling, and continues during post-filling; but most of the polymerization reaction takes place during the curing step, which, if possible, is carried out at higher than ambient temperature to minimize processing time.

As the polymerization reaction advances, resin viscosity, μ , increases; hence, degassing, filling and post-filling steps must be carried out while resins are in a low viscosity state and the reaction is still dawning. The term “gel time” refers to the time it takes to a resin to become a gel, no longer in liquid state, and it is often taken as a good indication of the working time of the matrix. Although not being explicitly mentioned in the immediate previous sections, degassing, filling and post-filling may be conducted at higher than ambient temperature to decrease μ ; however, higher temperature involves shorter working times.

Furthermore, outgassing behaviour of resins is a function of the outgassing conditions, pressure and temperature [202–204]. It is assumed that once reached the gel time, outgassing is prevented; therefore, gelation temperature should affect part porosity. Higher gelation temperatures cause higher v_0 [72,220]. In order to achieve a high degree of cure as quick as possible, while not negatively affecting resin outgassing, two-step cure cycles are conducting. During the first isothermal step, gelation happens, and the final cross-linking degree is achieved in the second isothermal step [249,250]. Besides, more complex curing cycles can be designed to minimize part porosity, and maximize working time and cross-linking [251,252].

2.3.3. Hybrid VI-forming

In hybrid VI-forming processes, a flat preform of a stack of reinforcement fabrics is firstly impregnated with a low viscosity resin and, then, formed over a mould while the resin is still in the low viscosity state. This manufacturing strategy reduces the necessary preparation time and processing cost; meanwhile increasing repeatability. A flat preform assembly eliminates intensive labour work typically associated with 3D preforming, simplifies preforming automation, and reduces cycle time and final part quality dependence on labour skills. The main hybrid VI-forming variants that have been developed are based on double diaphragm forming: Flexible Resin Transfer Moulding (FRTM) [27] and Resin Infusion between Double Flexible Tooling (RIDFT) [33–37].

In FRTM, separate sheets of solid resin and dry fibre fabrics are placed together between the two elastomeric diaphragms (forming an air-tight cavity) and heated to liquefy the resin. As resin reaches a low viscosity state, vacuum is drawn out into the cavity exerting a compaction pressure between both diaphragms which forces through-thickness impregnation of the stack of dry fibre fabrics. Finally, the double diaphragm is formed over a hard tool by an external action as in vacuum forming or matched mould stamping. Figure 2.15.a shows a schematic of the FRTM process.

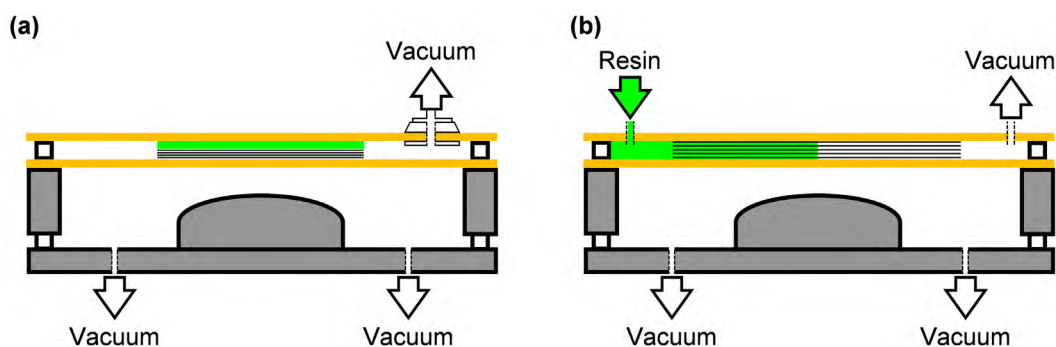


Figure 2.15. Hybrid VI-forming techniques: (a) FRTM and (b) RIDFT.

In RIDFT, a stack of dry fabrics is placed between two elastomeric diaphragms, forming an airtight cavity, and compacted by pulling out the air from the cavity. The same vacuum is responsible of preform impregnation by pulling a low viscosity resin from an outer deposit. After resin infusion, the double diaphragm and the infused preform is formed over a hard tool by vacuum. Low viscosity resin acts as a lubricant, increasing preform formability. A schematic of the RIDFT process is shown in Figure 2.15.b.

This page intentionally left blank

Chapter 3

***In Situ* Forming of a Liquid Infused Preform (ISFLIP)**

Recalling the description of ISFLIP previously provided, it is a hybrid process between VI and diaphragm forming, in which a flat preform of a stack of reinforcement fabrics is firstly impregnated with a low viscosity matrix and, then, formed over a mould while the matrix is still in the low viscosity state. This process sequence is possible because the preform assembly (preform and auxiliary materials which are air-tightly sealed by bagging films) is clamped between a couple of elastic diaphragms, which keep the preform flat during the infusion stage and allow its subsequent vacuum forming. Shell components, from simple to complex double curvature shapes, can be achieved.

ISFLIP was conceived with the purpose of manufacturing high quality FRP parts while still being competitive in lead time. The introduction of ISFLIP presented in this chapter was not arbitrarily addressed; but through the Manufacturing Triangle (MT), a knowledge management tool proposed by Tempelman, Shercliff and van Eyben and referred to industrial manufacturing [253]. After analysing ISFLIP through the MT, a SWOT analysis was performed from the information extracted, pointing out the research paths to be followed, and, specifically, the research activities to be addressed and presented in this dissertation. Finally, a functional prototype was designed considering the conclusions drawn from the SWOT analysis, the research objectives of this work, and previous knowledge of VI and diaphragm forming.

The very first result obtained from this chapter was a Spanish patent containing ISFLIP processing sequence and the main tooling systems [1].

3.1. Manufacturing method

A flow chart of the complete fabrication process that would be followed to manufacture a ‘C’ cross-section profile via ISFLIP is shown in Figure 3.1.

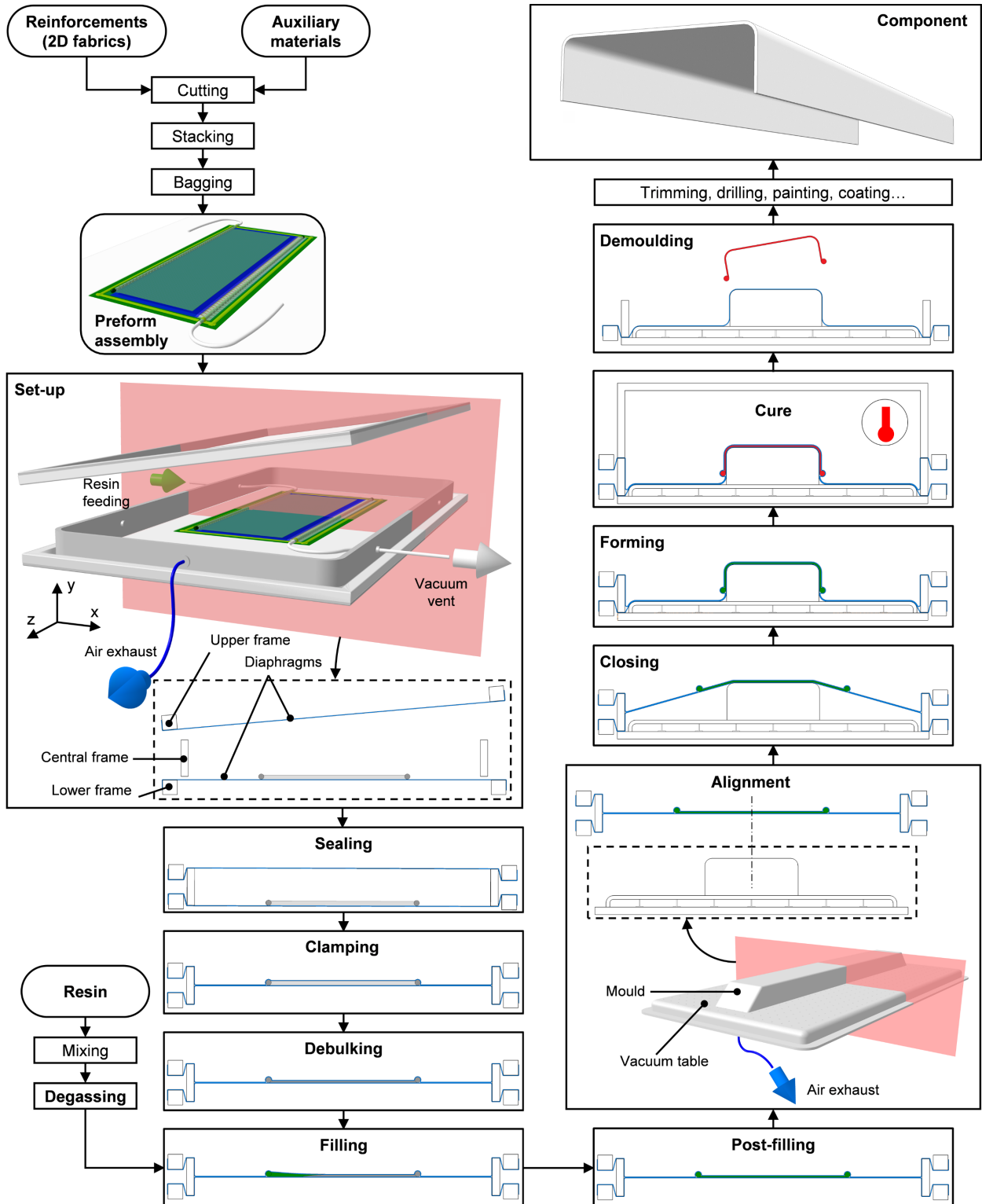


Figure 3.1. Flow chart of ISFLIP process (only curing step carried out at higher than ambient temperature).

VI is a complex multi-step manufacturing process whose main steps are governed by pressure, temperature and time parameters., as ISFLIP. The main manufacturing steps of VI are degassing, debulking, filling, post-filling and curing.

With respect to conventional VI, in which any forming step would be carried out before preform impregnation during preforming, in ISFLIP, this forming step is conducted between post-filling and curing steps.

Figure 3.2 shows a more detailed schematic of the preform assembly depicted in Figure 3.1. The main difference between ISFLIP and VI preform assemblies is that the preform is entirely enclosed by bagging films in case of ISFLIP.

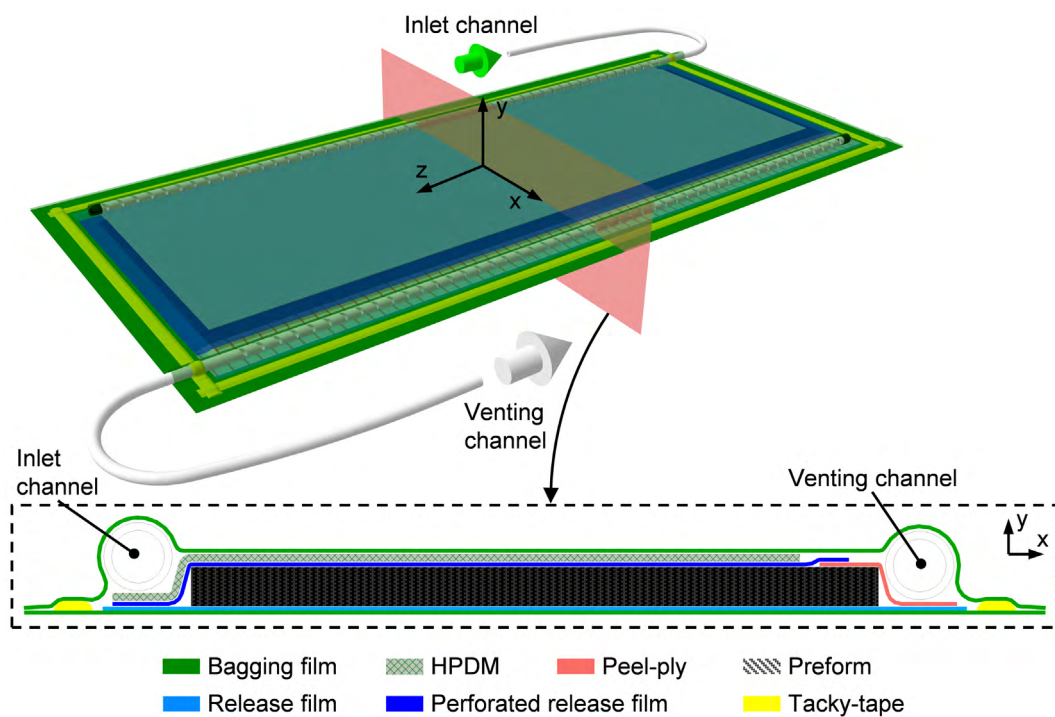


Figure 3.2. Representative ISFLIP preform assembly.

As in VI, HPDM is normally placed over the preform side which is opposite to the mould in order to avoid leaving any mark on parts. Preform assembly must be completely air-tightly sealed and accessible only by resin feed and venting ports. The specific configuration of a preform assembly for ISFLIP will finally depend on the size and shape of the part, and the chosen flow pattern.

The four main stages that ISFLIP is considered to consist on are set-up, infusion, forming and curing.

3.1.1. Set-up

Once prepared, the preform assembly is placed between two elastic diaphragms supported by rigid frames, and clamped by exhausting air from the air-tight cavity formed by both diaphragms and a central rigid frame. The vacuum pressure held between diaphragms is P_{diaph} . Stretching of diaphragms increases their bending rigidity, which allows to keep the preform assembly flat during subsequent preform filling.

Inlet and venting channels are connected to a resin reservoir and a vacuum generator (through a resin trap) by flexible hoses, since they must adapt to diaphragm deformation during the forming stage. Hoses pass through the preform assembly contour, not through the bagging films to avoid sealing problems when the assembly is clamped between the double diaphragm. Moreover, hoses can pass through the diaphragms or the central rigid frame; however, the later would not restrain the diaphragms to specific shapes.

3.1.2. Infusion

High performance FRP parts are associated with high fibre volume fractions, v_f , and negligible void volume fractions, v_0 (porosity). Besides, achieving tight thickness tolerances in VI is often challenging and time consuming [132–134]. A rigorous and well thought out design of the whole infusion process is necessary to guarantee high quality levels and to overcome the trade-offs usually presented between the mentioned quality attributes. Vacuum level into the preform assembly, P , is independently regulated from P_{diaph} , allowing the implementation of non-conventional filling and post-filling strategies to improve part quality while reducing processing time, and supposing a great advantage with respect to other hybrid VI-forming techniques [27,33].

P_{diaph} does not have any influence in the compaction pressure exerted over the preform due to the air-tightness of the preform assembly cavity. Compaction pressure applied to the preform, σ_f , is given by the pressure difference between the cavity formed by both diaphragms and the interior of the preform assembly, and the contact pressure between diaphragms and bagging films, P_{cont} , such that,

$$P_{cont} = P_{atm} - P_{diaph} \quad (8)$$

$$\sigma_f = P_{diaph} - P + P_{cont} = P_{atm} - P \quad (9)$$

However, it is convenient that $P_{diaph} > P$ to guarantee bagging film collapse on the irregular surface of HPDM (Figure 3.3), which has been reported by some authors to help dissolving trapped voids [219,247].

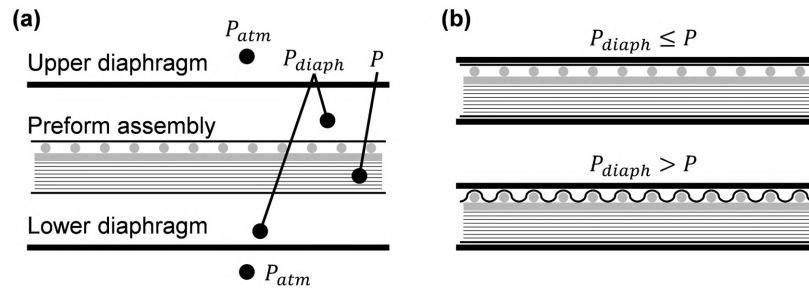


Figure 3.3. Pressure diagrams for preform clamping during the infusion stage: (a) pressure levels and (b) bagging film collapse on HPDM according to pressure levels.

Furthermore, the texturized surface of the preform assembly given by the irregular pattern on HPDM acts as a medium to achieve a homogeneous vacuum distribution, P_{diaph} , over the preform assembly.

Depending on matrix system requirements, degassing, debulking, filling and post-filling may be carried out at higher than the ambient temperature to guarantee the low viscosity state of the matrix. Flat preform impregnation favoured by ISFLIP considerably facilitates keeping a controlled preform temperature and, thus, guaranteeing constant processing conditions. Any conventional heating system (convection or radiation) could be used for this purpose, although heating time for radiation is considerably shorter than for convection [185].

3.1.3. Forming

The forming stage begins after post-filling end. Forming cycle is split in two steps: mould cavity closing and vacuum forming. Before forming, the mould is placed over a supporting tool and aligned with respect to the preform position between the diaphragms.

This first step consists on a guided vertical movement of the double diaphragm assembly with small deformations of the preform assembly. The purpose of this step is to close an air-tight cavity between the lower diaphragm and the supporting tool. Then, air is exhausted, and both diaphragms and the assembly preform are formed over the mould.

The vacuum pressure reached into the mould cavity is P_{mould} . Diaphragms separation and assembly preform releasing would only occur in case of $P_{mould} < P_{diaph}$ and under certain conditions. In Figure 3.4 it is shown how, in the limit situation in which no contact pressure is

transmitted between diaphragms, the ratio of pressure differences acting on both diaphragms, $\Delta P_{low}/\Delta P_{up}$, is a function of the radii of curvature (ΔR accounting for radius difference caused by diaphragms thickness and mainly by preform assembly thickness). Larger ratios would imply the separation of diaphragms; however, it must be noted that P_{diaph} should be close to full vacuum, P_{vac} , and thus away from P_{atm} , and $P_{atm} - P_{diaph}$ near an order of magnitude larger than $P_{diaph} - P_{mould}$ even if $P_{mould} \approx P_{vac}$. Therefore, diaphragms separation is not likely to happen.

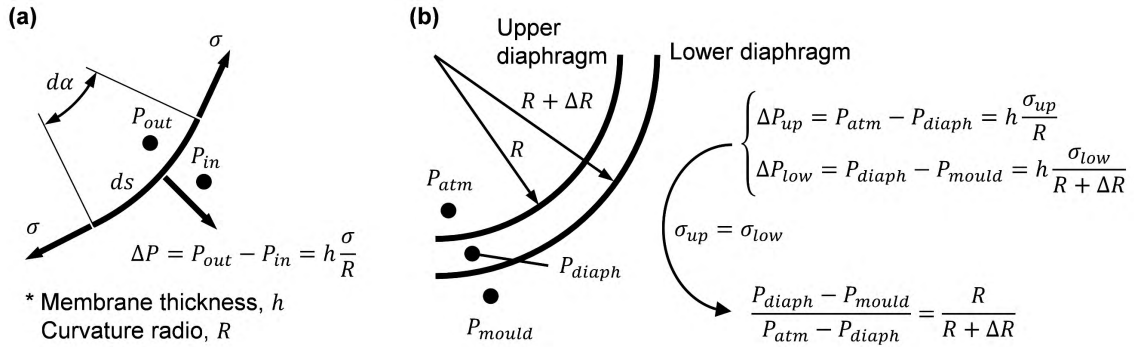


Figure 3.4. Pressure diagrams of semi-infinite membranes: (a) equilibrium of stresses in an infinitesimal portion of a curved diaphragm and (b) limit conditions for separation of diaphragms (assuming the worst case with equal stretching of both diagrams).

The primary deformation mechanisms involved in the forming stage are intra-ply shear and ply-ply shear. In multi-layer forming attempts, deformation rates are crucial due to the presence of highly viscous matrices [106,109,254]; however, in ISFLIP, matrixes are still in a low viscosity state, and act as a lubricant which enhances yarn rotation and ply sliding. In case of being necessary, forming rate could be controlled through regulating the exhausting flow via a proportional control system of P_{mould} . Vacuum forming is fast enough to preserve the temperature of the preform if non-isothermal forming at higher than ambient temperature is required, and then continue with the cure process at high temperature.

3.1.4. Curing

The applied cure temperature cycle is determined by matrix system needs. As listed in [4], a number of OOA technologies at industrial and lab scales are available. High temperature cure process in ISFLIP may be performed by heating the complete ISFLIP assembly in an oven (convention, infrared or microwave ovens) or by heating only the mould (liquid or induction heating).

After finishing the cure stage, part is demoulded by first releasing vacuum between diaphragms, while vacuum between the lower diaphragm and the mould is still applied to avoid any damage in the part or in the diaphragms.

3.2. Manufacturing Triangle (MT)

The MT is a structured approach in which the main attributes related to the applicability of a product (or component) are arranged in an ordered way [253]; thus, the main goal of the MT is to offer an ordered way of thinking to facilitate the analysis of product (or component) manufacturing. It is focussed from the point of view of mechanical design. Besides, its focus is on shaping processes more than in joining or finishing. Consequently, the emphasis of the MT is on specific parts rather than on bought-in components and semi-finished stock material.

As a knowledge management tool, the MT offers a structured way of thinking. It is not the only one nor the best one, but it is a useful way of thinking. In the MT, attributes are classified under three main categories which are considered the vertexes of the MT: function, quality and cost. For each vertex, a total of five attributes are defined and arranged around vertexes forming a hierarchical structure (Figure 3.5).

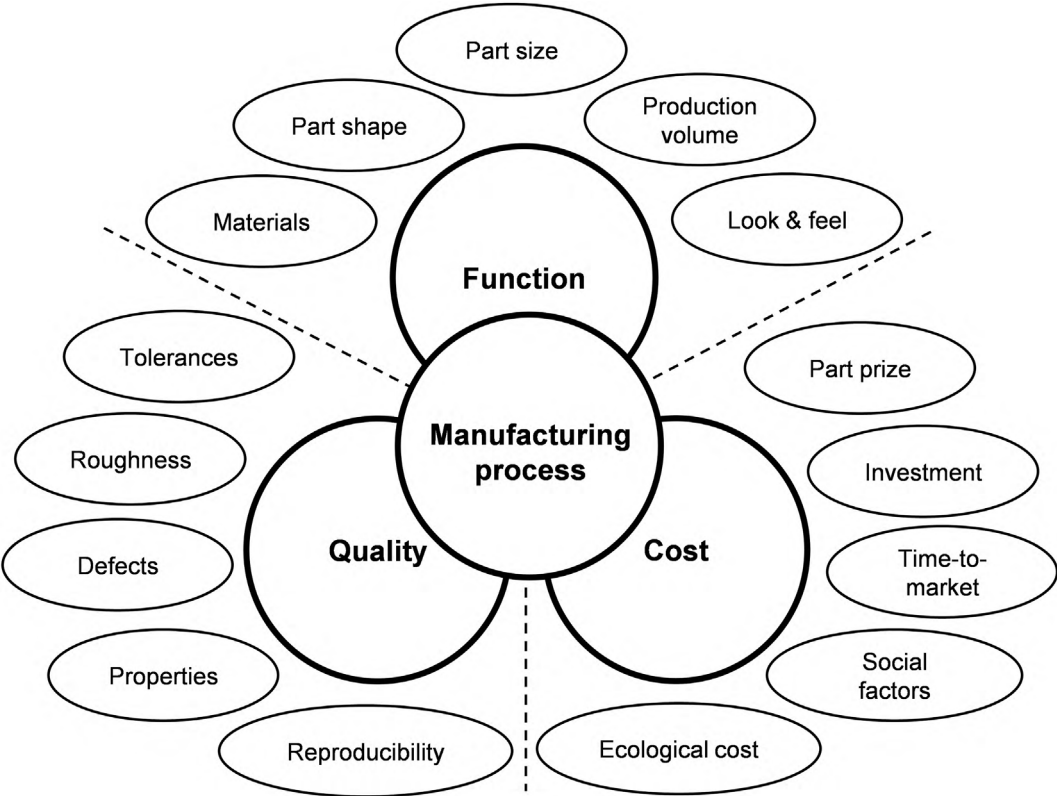


Figure 3.5. Hierarchical structure of the Manufacturing Triangle (extracted from [253]).

Every process has certain characteristic capabilities, which may be captured as numerical data ranges or lists of qualitative parameters. Matching the requirements of a design to suitable processes is the main goal of design for manufacture. It is crucial to recognize that process attributes are not fixed quantities but combinations of variables, with important couplings and trade-offs between them. Besides, it is worth emphasizing that most processes cannot address all attributes in only one manufacturing step.

All different manufacturing methods provided in Table 1.1 can be included in the category of shaping processes, just as ISFLIP, which share the same manufacturing principle, LCM. Since ISFLIP is still in an early stage of development, assessment of ISFLIP along the different attributes is performed by referencing both VI and diaphragm forming features, even RTM and other LCM variants. Therefore, in many cases, ISFLIP features has not been evaluated, but its potential features.

Time-to-market, social factors and ecological costs are not addressed in depth due to the mentioned early stage of development of ISFLIP, since these attributes are associated to end applications with well-established manufacturing processes. Only a couple comments in this respect are made.

ISFLIP can evolve in a completely automated manufacturing process in which investment is not massive; therefore, time-to-market could be lower than other LCM alternatives. Nevertheless, more knowledge and understanding of the process would be necessary. On the other hand, as an OOA manufacturing method, ISFLIP can provide considerable savings in energy consumption with respect to prepreg-based FRP manufactured in autoclave.

3.2.1. Materials and properties

As a hybrid VI-forming process, material restrictions are imposed in ISFLIP by both VI and diaphragm forming. VI requires the use of low viscosity matrixes and, during diaphragm forming, preform must allow intra-ply shear and ply-ply shear to accommodate to 3D shapes, which is accomplished by stacks of 2D fabrics.

One of the main advantages of ISFLIP is that debulking, filling and post-filling can be carried out with no additional constraint with respect to conventional VI. Therefore, the collection of appropriate matrices is not restricted. As introduced in the literature review section, it is available nowadays a broad range of both TS and TP matrix systems which are suitable to LCM processing, some of them requiring preform filling at high temperature. Besides, if TP tougheners are present

into the preform, a temperature raise is also needed to dissolve them into the matrix. Flat preform impregnation favoured by ISFLIP considerably facilitates keeping a controlled preform temperature and, thus, guaranteeing constant filling and post-filling conditions, and/or tougheners dissolution. Any conventional heating system (convection or radiation) could be used for this purpose.

Although ISFLIP is compatible with any 2D fabric architecture; logic dictates that added value textiles associated to high performance composites should be used to outweigh the cost increment with respect to common VI of auxiliary materials (showing high drapeability or formability) and additional equipment (diaphragm forming equipment). Fabric drapeability is crucial in double curvature shapes, being twill and satin weave fabrics the most appropriate for these conditions.

FRPs are special because the material is created not before, but during the manufacture of a part. Recalling the definition of a composite material provided in Chapter 2, it is the combination of two or more constituent materials which presents characteristics different from the individual components. Unlike metal alloys, each constituent material preserves its chemical, physical and mechanical properties.

Properties of manufactured parts will depend on properties of their constitutive materials. New reinforcement architectures such as spread tow fabrics, advance high temperature resin systems and the possibility of adding tougheners to preforms are bridging the gap between prepreg-based and dry fibre-based parts.

The main goal of FRP manufacturing is generally maximizing the reinforcement phase, v_f . In case of 2D fabric stacks, this is accomplished by exerting large compaction pressures over the preform. In ISFLIP, like in VI, compaction pressure, σ_f , is limited to the atmospheric pressure, P_{atm} , as stated by Terzaghi's relation [187]. Taking advantage of the compressive stress-strain hysteresis shown by textile preforms, v_f can be increased through a multiple-cycle debulking prior to proceed with preform impregnation [18,121]. Nevertheless, VI-like processes lack behind RTM-like counterparts in terms of v_f due to the lower pressure levels usually involved.

Trade-offs between component quality attributes, usually addressed through v_f and v_0 , and processing time are constant in VI processing. Unfortunately, improvements in one direction often requires deterioration of other quality attribute or increment of the overall processing time. More research on advance strategies of VI manufacturing is still required to find standard manufacturing procedures which can overcome the challenge of obtaining VI parts with high v_f , tight tolerances and negligible v_0 in a competitive scenario.

3.2.2. Part shape

One of the most widespread benefits of VI is shape flexibility and its ability to conform integrated multi-component parts. Achievable shapes in prepreg-based composites is fairly limited by intra-ply shear and ply-ply shear. The presence of high viscous matrices causes considerable difficulties to fibre rotation and movement. Dry fibre reinforcements do not present this inconvenient, being able to adapt to more complex shapes. In ISFLIP, resins may act as a lubricant and enhance forming, but combined compaction-shear loading is a proved cause of intra-ply shear limitation [104,105], restricting the range of feasible shapes.

A series of a priori ISFLIP formable shapes is highlighted in Figure 3.6. Flat shell shapes account for non-curved and single curvature shapes, while dished shell shapes refer to those geometries including double curvature.

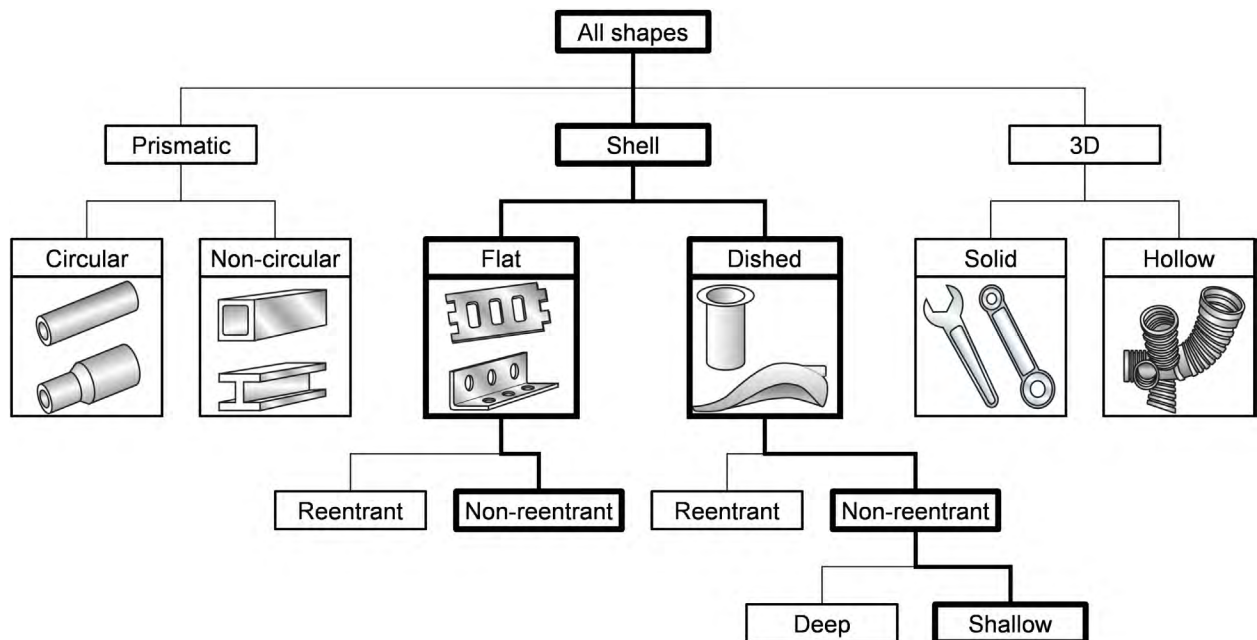


Figure 3.6. Taxonomy of shapes for shaping processes: appropriate shapes for ISFLIP (adapted from [255]).

Highlighted shapes, flat and dished shell shapes, are common to all forming processes in composite manufacturing. Removable moulds could be assembled to form reentrant shapes which can be later demoulded in stamping; however, in double diaphragm forming, mould cavity cannot be accessed before part demoulding. Therefore, reentrant shapes are discarded.

In single curvature shell shapes, minimum forming radius is given by ply-ply shear, slipping between consecutive layers is necessary to avoid the appearance of wrinkles. It must be pointed out that in ISFLIP, due to the low viscosity state of the matrix during the forming stage, preform layers are lubricated, being the friction between plies reduced with respect to conventional forming

attempts of dry fibre fabrics. As preform thickness increases, large displacements between the top and bottom layers of the preform are required. In case of high temperature preform impregnation and/or stabilized fabrics, forming would be carried out at high temperature to guarantee minimum matrix viscosity.

Moreover, if moulds are concave, an additional limitation is imposed on the minimum outer radius; since the minimum concave radius diaphragms can reach depends on diaphragm and preform thicknesses, vacuum level and diaphragm/mould slipping. Outer curvature radii smaller than 20 mm are not expected.

Experience dictates that realisable shapes in multi-layer forming are limited to shallow geometries in case of double curvature shapes. Apart from intra-ply shear and ply-ply shear, combination of fabrics with different fibre orientations are the main limiting factor in this respect [111,112]. It is worth recalling that auxiliary materials in ISFLIP are formed along with the preform, adding complexity to the overall formability performance. Although individual components of the preform assembly should be chosen to show high formability or drapeability; involved polymeric meshes, fabrics and films present different deformation mechanisms. The primary deformation mechanism in textile fabrics is intra-ply shear; while in a polymeric film, in-plane deformation is governed by tensile loading. Besides, in-plane shear behaviour in woven fabric significantly differs from knitted meshes usually used as HPDM [55].

Because of the impossibility of defining a specific range of viable shapes due to the high forming uncertainty, a set of potential applications to which ISFLIP could be applied is provided in Figure 3.7. In Figure 3.7.e, it must be noted that among the three components of the 'B' pillar, (inner shell, omega profile and shell outer) the outer shell has a reentrant section which would impede its demoulding. Depending of the real geometry of floor pans as that shown in Figure 3.7.g, a subdivision of the complete shape would be necessary to form more pronounced transmission tunnels [256].

In Figure 3.8, some examples of components which could not be obtained through ISFLIP are also provided. Figure 3.8.a shows a deep, non-reentrant, dished shell shape. Figure 3.8.b and Figure 3.8.c show shallow, non-reentrant, dished shell shapes, but they are too intricate to be produced via ISFLIP. Although textiles can adapt to non-flat surfaces; obtaining this kind of shapes with too marked details is not feasible in a single forming step from a flat preform, softer shapes are preferred. Finally, Figure 3.8.d depicts a reentrant, dished shell shape.

ISFLIP parts could also contain cores such as foams, provided that they are formable to the desired shape and compactible with VI (the quantity of absorbed matrix must be minimal).



Figure 3.7. Potential applications of ISFLIP: (a) leaf spring [257], (b) double-curved “C” spar [258], (c) single beam composite beam [259], (d) leading edge spar [260], (e) car “B” pillar structure [261], (f) Gaudi chair [262], (g) simple car floor pan , (h) bottom a bicycle trailer [263], (i) shells of wind turbine blades [264], (j) radiotherapy boards [265], and (k) kayak deck and hull [266].

3.2.3. Part size

It is common to address part size analyses in terms of part mass; however, due to the shell type shapes appropriated to ISFLIP, it is addressed part size through part thickness and surface area. Figure 3.7 also gives an insight of reachable part size, from thin to thick, and from small to large parts.

ISFLIP part size range can be extrapolated from VI. The required consumable materials in VI (or in ISFLIP) do not depend on component thickness; hence, in thin preforms, the cost associated to these auxiliary materials can even exceed the cost of the constitutive materials.

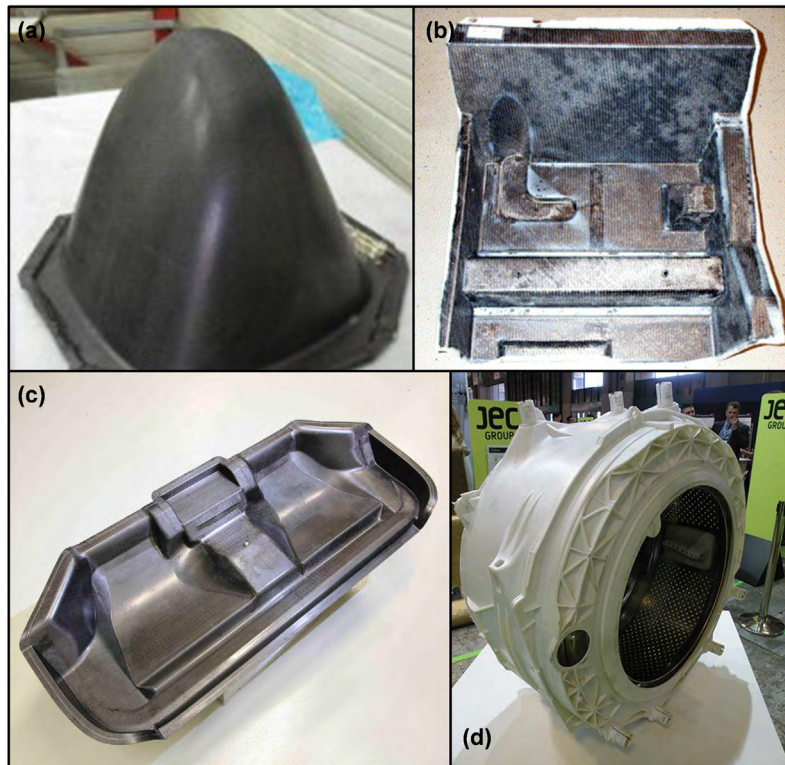


Figure 3.8. Inappropriate applications for ISFLIP: (a) elongated helicopter canopy [186], (b) complex auto floor pan [7], (c) complex auto part [267], and (d) reentrant washing machine tube [267].

On the other hand, in LCM, large thicknesses are limited by the long filling times required to impregnate thick preforms and the exothermic cure reaction of TS resins. In VI, resin flow is usually forced through preform thickness. Infusion time can take more than 40 h to fill preforms of length 90 cm and thickness 10 cm due to the low permeability of these preforms [268]. It is worth underlying that through-thickness preform permeability is usually at least one order of magnitude smaller than in-plane permeability [148,158]. In RTM, this thickness magnitude is not common, since RTM is often focused on short cycle times, which are incompatible with large thickness. Besides, race-tracking may arise as a big problem as cavity thickness increases [269].

Exothermic cure reactions of TS resins can cause degradation of the mechanical properties due to the excessive heat generated in the middle section of the components [270–272]. This peak of temperature is more exaggerated as thickness and cure temperature increase. Additionally, due to heterogeneous through-thickness temperature distribution, residual stresses can keep trapped into the parts. Most cure cycles recommended by resin suppliers are only suitable for thin laminates with thickness below 5 mm.

In respect of part surface area, common applications to VI, RTM and diaphragm forming are addressed to estimate the maximum part area ISFLIP could reach. VI is the predominant manufacturing process used in wind turbine blade shell manufacturing. Blade shells of large scale

wind turbines can exceed lengths of 50 m (maximum width > 5 m), resulting in surface areas larger than 200 m^2 . In contrast, RTM parts are limited to few meters due to span limitations of conventional milling machines during mould machining. Moreover, compaction loads are proportional to projected part area, thus high pressures require high capacity presses. Projected areas are often below 5 m^2 .

Since ISFLIP does not involve any special resin flow restriction over common VI conditions, achievable surface area should be limited by the elastic diaphragms and its supporting tooling. In the aeronautic industry, it can be found massive hot drape formers (based on diaphragm forming) with forming beds up to $20 \times 2,5$ m. Therefore, maximum part areas of this magnitude could be expected from ISLFIIP.

3.2.4. Tolerances

Tolerances are inevitable deviations to the part size and shape that the process delivers, which can be large (wide tolerances) or small (narrow tolerances).

Part shape tolerance in FRP parts is a challenging issue, and even more if manufacturing is carried out at higher than ambient temperatures [273]. Part distortion occurs when residual stresses keep trapped into the parts. The main mechanisms causing part distortion are different CTE of fibres and matrices, different CTE of the resulting composite and tool materials, and resin shrinkage during cure. As a result of the involved distortion mechanisms, asymmetric layups, heterogeneous volume fractions of each constituent material and large thermal gradients can cause even the distortion of flat parts.

A curious phenomenon in FRP is spring-in of curved parts. In stacks of 2D fabrics, through-thickness CTE is considerably higher than in-plane CTE, causing a more severe curvature to compensate the larger thickness reduction. Resin shrinkage, which is more prominent through the thickness, enhances spring-in.

In more intricate parts, these mechanisms can cause more complex distortions; however, since ISFLIP is not adding any special concern in this respect, it has not gone further on this topic.

VI is particularly sensitive to thickness tolerance since achieving narrow tolerances is time-consuming [132–134]. In RTM, part thickness is given by the rigid mould cavity; while, in VI, it is given by the compressive pressure history exerted on the preform during the whole manufacturing process [129–131].

Guaranteeing narrow thickness tolerances is crucial to offer high quality ISFLIP parts. This issue can be addressed through various non-conventional filling and post-filling procedures, but accounting for the trade-offs between component quality attributes that VI manufacturing usually involves.

3.2.5. Look & feel and roughness

Look & feel captures part colour, texture and expression, and is closely related to surface roughness. Although ISFLIP is not planned to directly produce cosmetic components; look and feel is essential, since no direct contact exists between manufactured components and moulds. ISFLIP could raise concerns in terms of the expected quality of the mould face, concerns that could lead to process discarding. Therefore, it is important to guarantee an even and smooth surface finish.

VI techniques only present one mould surface finish face. In shell-like parts, the opposite face may show an irregular, due to different preform thickness, and texturized, due to the use of peel-plies and HPDM, surface.

Roughness can be thought as an equivalent attribute to tolerance, but, instead of focusing on part shape and thickness, referring to part surface. It is several orders of magnitude smaller than geometric tolerances.

Quantitative assessment of surface quality is based on surface profile, which could be split up in roughness profile ($\lambda < 0,25$ mm), short-term waviness ($0,3$ mm $< \lambda < 1,2$ mm) and long-term waviness (3 mm $< \lambda < 30$ mm) [208,209,274]. However, in cosmetic applications, even in the automotive sector, surface quality is qualitatively assessed since it does not exist any standard method to characterize Class A surfaces in FRP parts. These inspections are carried by experts highly training in the matter. In spite of this subjective evaluation of surface quality, in the literature some evidences relating surface quality with the previously listed surface attributes can be found [13,208,275].

In painted components, highly polished moulds are not necessary to achieve a good quality cosmetic finish, since successive layers of coating and paint mask roughness and short-term waviness [195,208,209]. Surface roughness is given by mould roughness, since mould surface is directly printed on moulded components.

Waviness is dominated by fibre readout, which depends on matrix shrinkage, due to resin cure and/or different CTE between fibres and matrix, and yarn size [195,208,209]. Large yarns

favoured the formation of big resin rich areas trapped between fabrics and moulds that lead to the mentioned fibre readout, which is magnified at higher polymerization temperatures. In order to achieve a high quality Class A surface, it must be combined low shrinkage matrixes [208–210] and tight fabrics [275–277]. Surface veils, UD non-crimped textiles and even chopped strand mats are helpful in masking waviness of coarse fabric reinforcements.

In ISFLIP, surface finish is given by release films or directly through the bagging film if it is coated with any release agent, but no deterioration of the surface finish is expected [278]. Nevertheless, scratches caused on part surface due to film folds or irregular spots might cause an improper result in a later coating and/or paint stage.

Trapped surface porosity also affects surface finish, not only in the obvious case of bare laminates, but also in coated or painted surfaces. Surface porosity is a proved precursor of singular defects such as pinholes and blisters [195,276].

Apart from conventional coating or painting a component after being moulded, other alternatives of coating include applying the corresponding coat onto the mould before placing the preform [275], injecting the coat between the mould and the components after being moulded [279], placing a thermoformable film between the preform and the mould [280,281], and co-infusing the coat and the matrix [282–284]. The last three listed procedures would be compatible with ISFLIP, being the thermoformable film method a specially interesting technology to be combined with.

Furthermore, it can also be interesting to prepare bare surfaces for later bonding. In case of VI, it can be achieved by using peel-ply fabrics which leave a texturized surface in the laminate and can replace any abrasive preparation of the surface [196]. Peel-plyes are usually polyamide or polyester tight plain weave fabrics. Although the ISFLIP preform assembly shown Figure 3.2 does not contain any peel-ply, peel-ply layers could also be used to separate moulded parts from the rest of consumable materials; however, peel-ply drapeability is in general low due to the dense weave pattern and, thus, achievable shapes would be presumably limited.

3.2.6. Defects and reproducibility

Reproducibility captures the variability of the other quality attributes: tolerance, roughness, defects and properties. It refers to ensuring that parts are produced with consistent quality, which means that parts are produced into acceptance intervals defined around quality attributes. Defects and reproducibility are related through their influence on part rejection. Excessive variability does not

only lead to lack of reproducibility, but also to the appearance of defects. Along the manufacturing process, uncertainties in each process step can affect subsequent steps, leading to the formation of process-induced defects.

It is worth noting that not all defects cause part rejection. For example, it is usual in VI to manufacture components with significant levels of porosity, considering this material deterioration as an inevitable characteristic of VI processing. However, taking advantage of the full potential of composite materials, required in high performance applications, involves avoiding any material defect.

Intrinsic preform variability is one of the great challenges to deal with in LCM processes [135–137], from uncertainties of fabric architecture to uncertainties of fabric layups [137]. These intrinsic variability results in considerable changes in manufacturing steps involving resin flow through textile preforms [285,286] and forming of multi-layer preforms [287].

Manual handling and layup are important sources of fibre misalignments and defects, whose magnitude increases as geometry complexity increases. Therefore, ISFLIP approach, starting from a flat stack of 2D fabrics, facilitates manual preforming, reducing associated risks, and enhances implementation of automated preforming strategies. Besides, impregnation of flat preforms also facilitates prediction of resin flow through preforms, since there are no flow distortions caused by fabric shearing, uneven preform compaction due to complex geometries and race-tracking.

There are numerous sources of defects in FRP parts [135,136]; however, ISFLIP, as a hybrid VI-forming manufacturing technique, is especially sensitive to final part porosity, wrinkling and thinning/thickening.

In VI-like techniques, ISFLIP is not an exception, resin is prone to outgas at vacuum pressures due to its minimum air solubility as stated by Henry's law; hence, final part porosity is a major concern. Independent vacuum control into the preform assembly and between elastic diaphragms allows to take different actions in ISFLIP to minimize or even remove part porosity and, thus, achieving null void volume fraction, v_0 . Various measures to limit final v_0 are optimizing flow regime to minimize void formation caused by resin flow through dual-scale porous media [198,214] and altering outgassing conditions (pressure and temperature) to increase air solubility [202–204]. Nevertheless, as previously mentioned, trade-offs between quality attributes and processing time are usual in VI manufacturing; thus, special care must be taken to avoid causing any collateral damage.

The two main causes of wrinkle formation are shear deformation beyond the locking angle and in-plane compression due to geometry recess [180,181]. In ISFLIP, preforms are formed with a

significant compaction pressure, σ_f . Unlike combined tension-shear loading, which resulted in larger locking angles [106–108], combined compaction-shear loading results in smaller locking angles at which wrinkling occurs [104,105]. Besides, applying corrective measures in diaphragm forming are difficult to avoid geometry recess during forming. However, out-of-plane bending behavior also play an important role in wrinkling, and stretched diaphragms create an out-of-plane support to the preform which counteract wrinkle appearance. Ply-ply shear can also lead to transferring compression loads which can cause tow buckling and, thus, wrinkling [109,110]. This is an important limiting factor in forming of multi-layer preforms; but, in ISFLIP, due to the low viscosity state of the matrix during the forming stage, preform layers are lubricated, which may help to avoid tow buckling.

Finally, thinning or thickening are inevitable effects of forming a stack of textile fabrics over severe convex or concave curvature shapes, respectively [183,288]. Pressure concentration (convex) or relaxation (concave) are the causes behind these thickness alterations. In case of ISFLIP, stretching of diaphragms even boosts thickness variation. Since minimum outer radius in concave shapes is limited in ISFLIP by elastic diaphragms, thickening is not expected to be as critical as thinning.

3.2.7. Production volume, part price and investment

Production volume, also known as batch size, depends of process economics, but experience and historical data allow to define a characteristic economical production volume as a separate attribute without going further into the economic analysis. This economical batch size allows to check if a manufacturing process fits the requirements of a specific application. Beyond the obvious dependence of production volume for a particular application on involved materials, part size and part shape, this attribute refers to typical production volumes associated to a manufacturing process.

Performing a cost analysis of any LCM technique without accounting for the preforming step and the chosen equipment is not possible. Preforming for VI is often carried out manually by labours, involving low initial investment but high labour costs. On the other hand, it is usual to combine non-isothermal stamping with RTM-like processes to achieve short processing times.

Apart from the production volume, n (the total number of parts to be made), cycle time (inverse production rate, \dot{n}) also plays a key role at defining the production needs of an application; since for a specific annual production volume, multiple production lines might be necessary according to the cycle time.

Production volume and cycle time are connected to part price, C , which can be computed from a series of costs associated to material, C_1 (constitutive and consumable materials), dedicated tooling, C_2 (dies, moulds, fixtures and jigs), non-dedicated equipment, C_3 (e.g. press or oven), and overheads, C_4 (labour, administration, general plant costs, energy and know-how) [289]:

$$C = C_1 + C_2 + C_3 + C_4 = \frac{MC_m}{(1-f)} + \frac{C_t}{n} \left[\text{Int} \left(\frac{n}{n_t} + 0,51 \right) \right] + \frac{1}{\dot{n}} \frac{C_c}{Lt_{wo}} + \frac{\dot{C}_{oh}}{\dot{n}} \quad (10)$$

where M is component mass [kg/u], C_m is material cost [€/kg], f is scrap fraction, C_t is the tooling cost [€], n is production volume [u], n_t is tool life in units of production [u], \dot{n} is production rate [u/hour], C_c is capital cost of equipment [€], L is time fraction for which equipment is productive, t_{wo} is capital write-off time [hour] and \dot{C}_{oh} is overhead rate [€/hour]. t_{wo} is normally expressed in [year], although it must be converted to [hour] to match the units of rest of variables.

Terms of Equation (10) can be rearranged to obtain a cost quantity that is independent of batch size and rate, a dedicated cost that is proportional to the reciprocal of the batch size, $1/n$, and a gross overhead that is proportional to the reciprocal of the production rate $1/\dot{n}$,

$$C = \frac{MC_m}{(1-f)} + C_t \left[\text{Int} \left(\frac{n}{n_t} + 0,51 \right) \right] \frac{1}{n} + \left(\frac{C_c}{Lt_{wo}} + \dot{C}_{oh} \right) \frac{1}{\dot{n}} \quad (11)$$

At low n , part price is governed by investment ($C_2 + C_3$); while at high n , part price is governed by materials cost, C_1 . In massive production volumes, VI-like processes cannot compete with RTM-like processes since consumable materials used in VI, apart from the ecological cost, involve an additional cost to the own cost of the constitutive materials, C_m [30].

Although it exists the thought that FRP parts are expensive because of the high cost of constituent materials; manufacturing costs are in most cases comparable or even exceed material costs when labour intensive work is needed [163,290,291].

Tooling cost, C_t , regardless part size and shape, depend on service pressure and temperature, and incorporation or not of internal heating and/or cooling [292]. Involved pressures in RTM and autoclave manufacturing are larger than in ISFLIP (< 1 atm), which should imply lower C_t . Soft tool materials (non-metallic materials such as epoxy or FRP) could be used in ISFLIP instead of conventional hard tool materials (metallic materials such as aluminium, nickel or steel) in the production of relatively large production volumes, since no direct contact between the FRP part and the mould avoids mould abrasion.

Another important factor affecting C_2 in ISFLIP is the cost of elastic diaphragms, C_t , and their usage life, n_t . Typical usage life of elastic diaphragms is under a thousand cycles, 200-1000 u. Again, absence of abrasion (no direct contact between FRP and diaphragm) could reduce diaphragm damage due to successive loading.

Nevertheless, it is in costs associated to non-dedicated equipment, C_3 , in which ISFLIP shows a promising potential to reduce part cost. ISFLIP would allow achieving short cycle times ($1/\dot{n}$) without requiring massive investment.

Equipment usually used in VI and RTM, and that would be used in ISFLIP is listed in Table 3.1, as well as a representative industrial cost of each element for manufacturing of a medium size part (large size part according to RTM usual size range). Equipment selection for each process accounted for the typical manual production adopted in VI and a fully automated production cell in case of RTM:

- In case of VI, it was considered manual cutting, preforming and bagging (assisted by appropriate tools and jigs); and a vacuum unit and a convection oven to complete VI.
- In case of ISFLIP, it was considered a fully automated cutting table system; manual preforming and bagging (assisted by appropriate tools and jigs); three vacuum units for degassing, VI and forming; non-isothermal double diaphragm forming with radiation heating; and a convection oven to complete VI.
- In case of RTM, it was considered a fully automated cutting table system, industrial robots for flat preform layup and transferring between forming and RTM stations, non-isothermal stamping with radiation heating, injection and vacuum units to conduct moulding steps, and one press for the forming station and one press for the RTM station. It must be noted that additional cost associated to more expensive moulds (including heating and cooling) was not considered.

Table 3.1 also shows the total equipment cost associated to each process; although it is only provided for establishing a qualitative comparison between processes, since not all equipment would have to be productive for the same fraction of time or fully dedicated to the same production line. ISFLIP investment is considerably higher than in VI; but, if the cost of the fully automated cutting table is deducted, cost difference is reduced (400 k€). RTM equipment is in turn more than double than ISFLIP, even if a transfer robot would be used to automate preform layup (590 k€). Equipment cost in RTM is clearly dominated by the cost of both presses. Stamping was included

to put at the same level RTM and ISFLIP, since processing would start from a flat stack of textiles in both scenarios.

Table 3.1. Equipment costs for VI, ISFLIP and RTM.

Equipment	Cost [k€]*	VI	ISFLIP	RTM
Cutting table	150	-	1	1
Tools and jigs to assist cutting	30	1	-	-
Tools and jigs to assist preforming and bagging	30	1	1	-
Transfer robot	100	-	-	2
Injection unit	150	-	-	1
Vacuum unit	30	1	3	
Convection heater	60	1	1	-
Radiation heater	70	-	1	1
Double diaphragm forming tooling and vacuum table	120	-	1	-
Low pressure press	350	-	-	1
High pressure press	450	-	-	1
Total cost [k€]		150	520	1370

* Equipment costs extracted from [7,163,293,294].

Achieving shorter cycle times usually involves higher investment. CRTM and HP-RTM are RTM variants which were conceived to speed-up the process and reduce cycle time. While CRTM starts from slightly different process conception, HP-RTM takes use of larger and more expensive equipment, increasing the required investment. Due to the higher pressures involved in HP-RTM, resulting press cost could be almost twice the cost of a conventional RTM press [293]. Both technologies were adopted by BMW to manufacture different structural components, since CRTM presents some part shape limitations.

In multi-stage processes, cycle time depends on the level of parallelization of the different manufacturing steps. In a sequential approach, cycle time is calculated as the sum of processing time of each step. If the manufacturing process is carried out in different workstations that can operate in parallel, cycle time is the longer time to complete all the manufacturing steps in each workstation. In LCM, cycle time normally coincides with mould utilization time, referred as “in-mould cycle time”.

Figure 3.9 shows the main manufacturing steps in VI, ISFLIP and RTM contributing to cycle time computation. No heating up and cooling down steps are shown in Figure 3.9; although

forming, filling, post-filling and curing steps, which are those that could be conducted at higher than ambient temperature, may include heating and/or cooling rates as substeps. Mould utilisation in VI is not only limited to those stages really associated to VI, but also time-consuming steps such as stacking and bagging. On the other hand, filling, curing and demoulding are the main steps contributing to cycle time in RTM; while, in ISFLIP, since debulking, filling and post-filling are conducted out of the mould, in-mould cycle time is given by forming, curing and demoulding times. Potentially, cycle times of ISFLIP could be even shorter than RTM, expecting shorter forming than filling (in RTM) times.

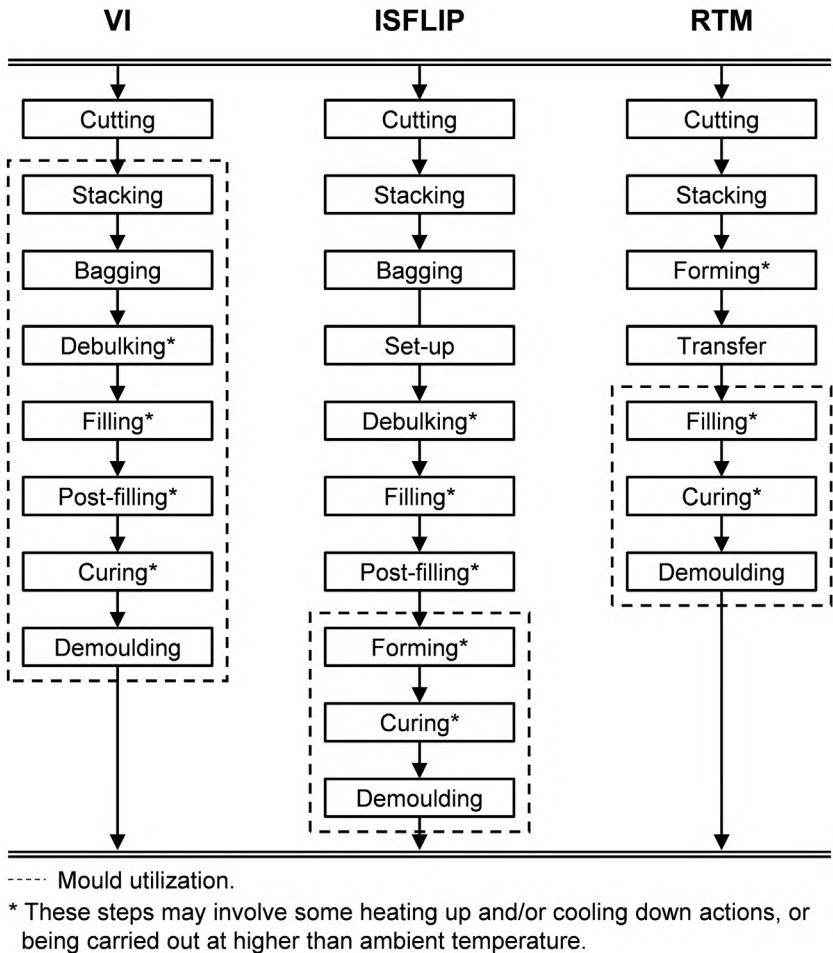


Figure 3.9. Flow charts of VI, ISFLIP and RTM (only steps which can significantly affect cycle time are shown).

ISFLIP potential to achieve short cycle times resides in uncoupling of debulking, filling and post-filling, from forming and curing (steps involving mould utilisation); however, this competitive advantage could be lost if filling and post-filling time exceeded in-mould cycle time. Therefore, it is crucial to achieve short filling and post-filling times. At this point, the trade-offs between part quality and VI processing time arise again as a key challenge to overcome in the manufacturing of high performance FRP parts with shorter processing times.

Furthermore, it should not be underestimated the importance of not needing mould cleaning and preparation between units, and beginning from a flat preform, simplifying its elaboration and enhancing preforming automation, which lead to shorter preforming times

Economical production volumes are not fixed ranges. Variations are found between different sources of information [163,269]. Around 100-1000 u/year can be obtained in VI, and 400-15000 u/year in case of RTM adoption. Annual production volumes of conventional RTM can be doubled or tripled in case of CRTM and HP-RTM. These high annual production volumes require the use of fast polymerization matrices to achieve short cycle times [7,9,84].

Economic batch size of ISFLIP should lie between VI and RTM. Production volume of single diaphragm isothermal forming lies between 300-4000 u/year. Isothermal forming attempts of TS and TP prepregs, and stabilized preforms need previous material heating to achieve a matrix low viscosity state and subsequent cooling to allow demoulding. However, assuming that, in ISFLIP, cycle time is given by cumulative time of forming, curing and demoulding steps, and preform heating can be carried out previously and cooling should not be necessary for TS and most TP matrices; then, resulting production volume could be higher than 4000 u/year. If one 8 hour work shift and 250 workdays per year were considered, achieving 8000 u/year would need a 15 min cycle time, which is perfectly feasible with an appropriate resin system and the right level of automation.

ISFLIP is able to achieve economic short cycle times, unattainable for VI, and manufacture large size parts, which cannot be manufactured through RTM, and, thus, filling a gap that VI and RTM cannot cover (Figure 3.10).

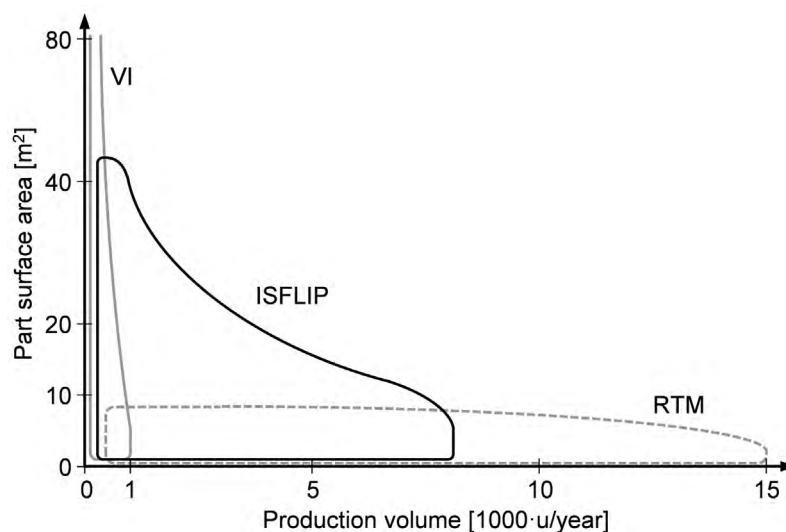


Figure 3.10. Representative part size and economic production volume for VI, ISFLIP and RTM.

Additionally, the flexibility of double diaphragm forming equipment in terms of part shape and size, relatively low compressive pressures exerted onto moulds that allow the use of soft tool materials, and no mould surface preparation make ISFLIP ideal for prototype parts which require very short time-to-market.

3.3. SWOT analysis

ISFLIP was conceived as a real alternative to manufacture high performance FRP parts with shorter processing times and higher reproducibility than other conventional VI variants. Through the MT, a series of factors affecting ISFLIP function, quality and cost attributes were identified and now arranged in form of a SWOT analysis. Table 3.2 and Table 3.3 show the internal and external factors of the SWOT analysis of ISFLIP.

Table 3.2. Strengths and weaknesses of the SWOT analysis of ISFLIP.

Strengths	Weaknesses
<p>Materials Suitable to all kind of 2D fabric reinforcements, even chemically stabilized such as spread tow fabrics.</p> <p>Suitable to TS and TP matrices appropriate to LCM, even if high temperature processing is required.</p> <p>Part size Large parts. Parts with surface area up to 50 m² are expected.</p> <p>Part shape Resin in a low viscosity state may act as a lubricant and enhance intra-ply and ply-ply shear deformation.</p> <p>Production volume Preparation of flat preform assemblies is simple and fast.</p> <p>Mould utilization is limited to forming, curing and demoulding.</p> <p>Production volume and investment Large production volumes are achievable without massive investment.</p> <p>Tolerances, properties and defects Compatible with non-conventional, debulking, filling and post-filling strategies.</p> <p>Defects Low risk of vacuum leaks (double sealing level).</p> <p>Risk of wrinkling in double diaphragm forming attempts is significantly lower than in single diaphragm forming.</p>	<p>Materials Unsuitable to 3D fabric reinforcements.</p> <p>Suitable to low viscosity state resins.</p> <p>Part shape Limited to non-reentrant, flat shell shapes and shallow, non-reentrant, dished shell shapes.</p> <p>Minimum outer radius of 20 mm is expected in concave shapes.</p> <p>Formability is restricted due to the simultaneous forming of preform and consumables.</p> <p>Part shape and defects Formability is restricted due to the combined compaction-shear loading, promoting wrinkle formation due to reduction of locking angle.</p> <p>Production volume Short cycle times require short filling and post-filling steps, which is not the norm in VI manufacturing.</p> <p>Look & feel Only one face with smooth surface finish (mould side).</p> <p>Tolerances Achieving homogeneous thickness and thus, narrow v_f tolerances is very time-consuming in conventional VI-like production.</p> <p>Tolerances, properties and defects Typical VI trade-offs between part quality, such as v_f, thickness tolerance and v_0, and processing time.</p>

Table 3.2. Strengths and weaknesses of the SWOT analysis of ISFLIP (continuation).

Strengths	Weaknesses
<p>Reproducibility Influence of operators on final product quality is minimized, since preforming of flat layups is simpler.</p> <p>Predictable resin flow through preform during filling and post-filling due to the flat preform configuration.</p> <p>Part price Mould surface maintenance is not necessary.</p> <p>Investment Soft tool materials can be used in moulds, since no abrasion occurs.</p> <p>Highly flexible equipment and tooling, appropriate to different part size and shape.</p> <p>Time-to-market Short time-to-market for prototype parts.</p> <p>Ecological cost Low emission of volatile organic compounds.</p>	<p>Defects Risk of surface finish deterioration by scratching due to film folds.</p> <p>Porosity is a major concern in VI-like processes, since resin is prone to outgas at vacuum pressures.</p> <p>Difficult implementation of correcting measures to avoid wrinkle formation due to geometry recess.</p> <p>Lubrication between plies caused by low viscosity resins may boost thinning/thickening.</p> <p>Properties Achievable v_f in VI-like processes is lower than in RTM-like processes.</p> <p>Part price Usage life of elastic diaphragms is under a thousand cycles.</p> <p>Part price and ecological cost High consumption of disposable auxiliary materials.</p> <p>Time-to-market Lack of technological maturity. Complex modelling and simulation of forming stage.</p>

Table 3.3. Opportunities and threats of the SWOT analysis of ISFLIP.

Opportunities	Threats
<p>Materials Processing at high temperature is feasible because of flat preform impregnation and the possibility of non-isothermal forming.</p> <p>Suitable to nano-reinforced resins. As a VI variant, ISFLIP is more appropriate than RTM to work with nano-reinforced resins.</p> <p>Part size and production volume Wide range of part sizes and production volumes, filling a gap that VI and RTM cannot cover.</p> <p>Part shape Shell shapes are common in FRP applications, since non-local loading of parts is promoted.</p> <p>Production volume and reproducibility High potential of preforming automation due to the flat preform configuration.</p> <p>Reproducibility Dependence on operator skills is minimized. There exists an industry trend to avoid dependence on operator skills.</p> <p>Investment Lower equipment and tooling costs than autoclave manufacturing and RTM-like processes.</p> <p>Social factors Many VI variants have emerged in the last decade.</p>	<p>Part shape Unsuitable to highly complex integrated structures usually associated to LCM.</p> <p>Tolerances Mistrust of shape accuracy due to the non-direct contact between part and mould.</p> <p>Roughness Mistrust of surface finish due to the non-direct contact between part and mould.</p> <p>Properties Mistrust of material properties since VI-like processes are still far away from major acceptance in high performance applications.</p> <p>Investment Higher equipment and tooling cost than in conventional VI.</p> <p>Social factors Similar hybrid VI-forming techniques are not spread in industry.</p>

3.4. Prototype

A functional prototype to carry out ISFLIP test campaigns was designed and built. The prototype was based on a conventional double diaphragm forming machine design and adapted to allow filling, post-filling and curing of the preform assembly between the double diaphragm. The prototype was split into three main tooling assemblies: vacuum table, double diaphragm tooling and heating chamber.

3.4.1. Requirements

A series of design requirements that the prototype must meet are listed in Table 3.4.

Table 3.4. Design requirements for ISFLIP prototype.

Code	Requirements
0.1.	Independent main tooling assemblies.
0.2.	Minimum service temperature of 120°C for elements subjected to heating.
0.3.	Working area around 2000x1000 mm.
Vacuum table	
1.1.	Movable.
1.2.	Air evacuation from all table surface.
1.3.	Stable support of moulds.
1.4.	Diaphragm friendly to avoid tear.
1.5.	Base support of the other two main tooling assemblies.
Double diaphragm tooling	
Diaphragms	
2.1.	Large elastic deformations, more than > 500%.
2.2.	Transparent or translucent.
Supporting structure of diaphragms	
2.3.	Based on independent rigid frames.
2.4.	Easy and fast manual assembly and removal of diaphragms.
2.5.	Self-stretching of diaphragms.
2.6.	Inclusion of vacuum ports and pass-through connectors for flexible hoses.
2.7.	Easy, fast and comfortable mounting of pass-through connections.
2.8.	Easy, fast and comfortable placement of the preform assembly over the diaphragm.
Diaphragms and support structure	
2.9.	Able to create an air-tight cavity to introduce preform assembly.
2.10.	Able to be aligned with respect to the vacuum table.
2.11.	Able to create an air-tight cavity with the vacuum table.
Heating chamber	
Heating system	
3.1.	Infrared Radiation (IR).
3.2.	Heating power to reach 100°C.
3.3.	Adjustable position of IR panels.
3.4.	Homogeneous heating of different shapes.
Enclosure	
3.5.	Manually removable by two operators.
3.6.	Thermal insulation.

3.4.2. Design

A general view of ISFLIP prototype design is provided in Figure 3.11. The prototype was designed in CATIA V5. Relevant decision making, design details and basic configurations of the three independent main tooling assemblies (requirement 0.1) are commented in the following subsections.

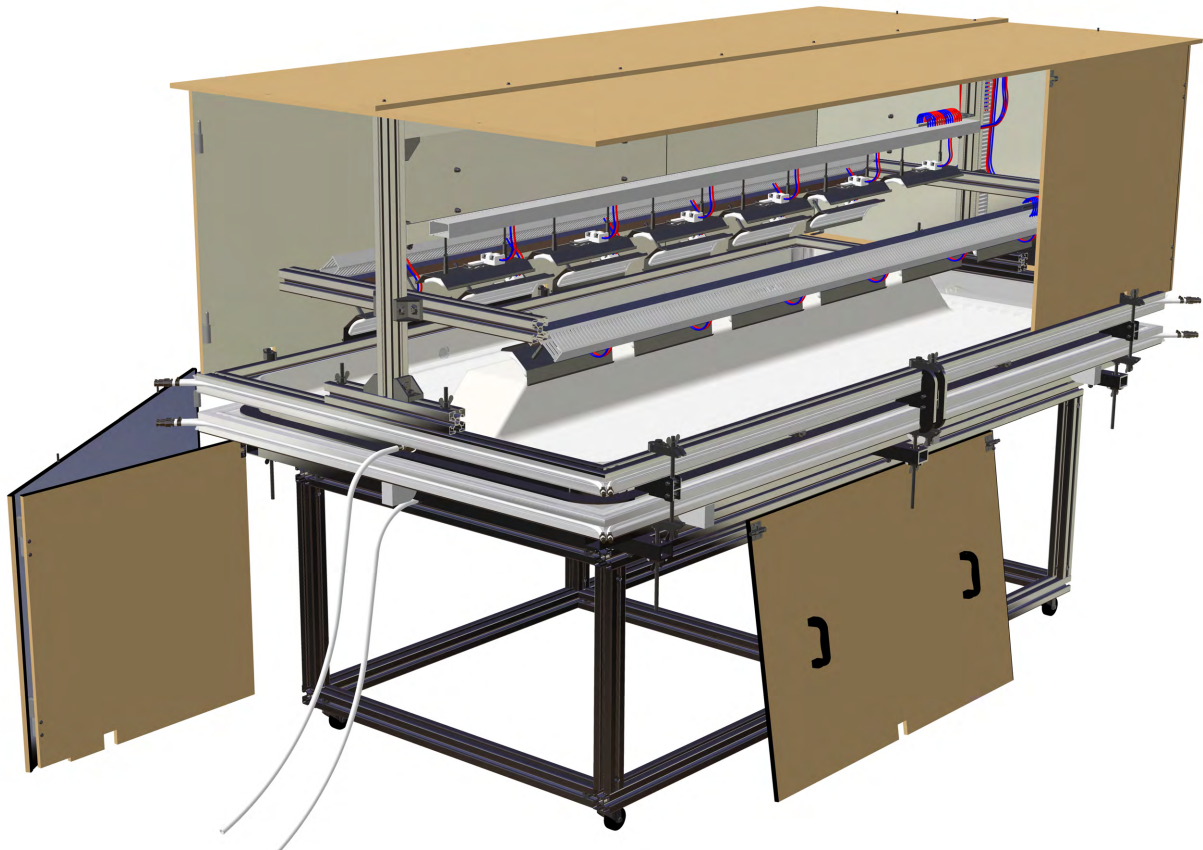


Figure 3.11. Design of ISFLIP prototype.

It was not expected to exceed 80°C during test campaigns; however, in anticipation of undesired and sudden heat peaks, a minimum service temperature of 120°C was set for all those elements subjected to heating. This temperature level could be critical for elastic diaphragms, plastic components, rubber seals and adhesives; therefore, their selection was done accounting for this requirement (req. 0.2).

3.4.2.1. Vacuum table

The vacuum table is depicted in Figure 3.12.a. It was supported over a structure of modular aluminium profiles equipped with conventional wheels (req. 1.1).

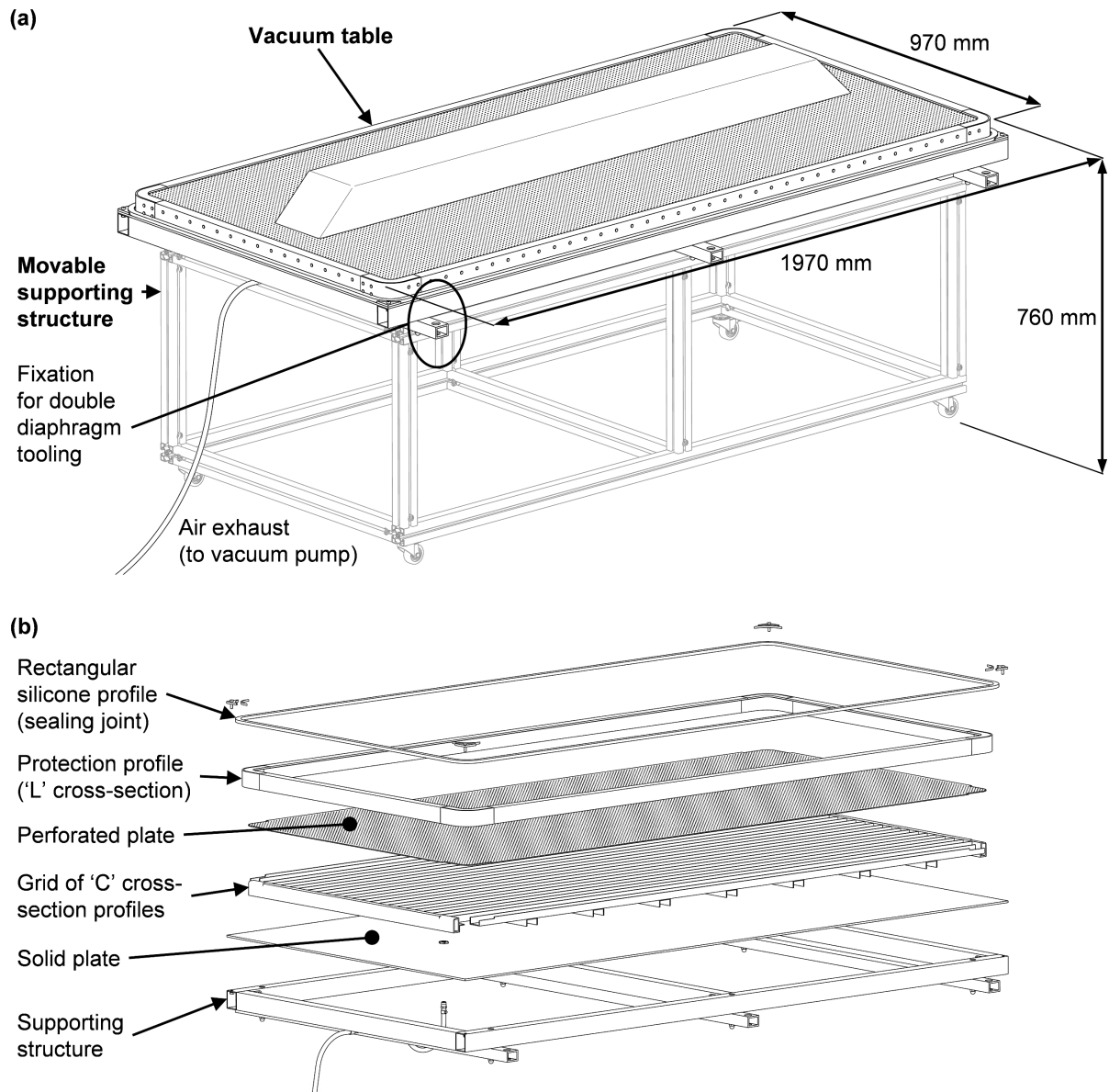


Figure 3.12. Vacuum table design: (a) vacuum table and supporting structure , (b) exploded view of vacuum table.

Elements forming the vacuum table are shown in Figure 3.12.b. A perforated aluminium plate of thickness 2 mm was placed over a grid of aluminium profiles which supported the perforated plate and allowed complete air evacuation from a single vacuum port (req. 1.2). The grid was placed over a 5 mm thickness non-perforated aluminium plate which provided stability to the vacuum table (req. 1.3). The contour of the perforated plate was covered by a continuous 'L' cross-section profile to protect elastic diaphragms from damage (req. 1.4). The effective work area was 1970x970 mm (req. 0.3).

The non-perforated aluminium plate was mounted over a structure of rectangular aluminium profiles which, apart from supporting the vacuum table, allowed the later coupling of the double diaphragm tooling (req. 1.5). A rectangular 15x10 mm silicone profile was placed around the 'L' cross-section aluminium contour to guarantee the closing of the air-tight mould cavity (req. 2.11).

3.4.2.2. Double diaphragm tooling

The most usual materials for elastic diaphragms are latex and silicone, but only silicone offers a service temperature higher than 120°C (req. 0.2). Therefore, silicone sheets of 0,5 mm, 1 mm and 2 mm were considered and proved. Thicker sheets have higher tear resistance, but the minimum outer radius in concave shapes is also larger. Silicone sheets of thickness 1 mm were chosen because of the good compromise between both features. Acquired silicone sheets showed elastic deformations over 500% (req. 2.1) and were translucent (req. 2.2), thus allowing visual inspection of preform filling.

After being assembled for the first time, each silicone diaphragm was stretched twenty times from the upper diaphragm position with no mould tooling over the vacuum table and, then, reassembled on their respective rigids frames to compensate Mullins effect.

A three rigid frames configuration, shown in Figure 3.13.a, was preferred to facilitate silicone diaphragm mounting and stretching (req. 2.3). Diaphragms were directly supported on identical T-slotted aluminium frames and clamped by pressurizing silicone hoses into the slots of the aluminium profiles, which allow a fast and secure diaphragm replacement (req. 2.4). When being coupled to the central aluminium frame, both upper and lower diaphragms result stretched (req. 2.5). If a preform were placed over a loose diaphragm, at clamping the preform by evacuating the air from the cavity between diaphragms, undesired preform displacements could occur. Details of diaphragm clamping on frames and sealing of both air-tight cavities are shown in Figure 3.13.b and Figure 3.13.c, respectively.

Upper and lower diaphragm bending over the interior plate of the central frame created a double sealing contour which allowed to form the air-tight cavity containing the preform assembly (req. 2.9). Straight sections of the interior plate of the central frame were welded to bended sections to create a hermetic contour, while protecting diaphragms from tearing in the corners. Besides, the central frame was reinforced with a 'U' cross-section profile to resist loads exerted by the diaphragms, and pressure difference between interior and exterior of the air-tight cavity. Applied loads could lead to considerable deformation due to flexural stresses along frame sides.

Two couples of hermetic pass-through connectors were installed in each long side of the central frame, as well as a single vacuum port in each short side of the central frame (req. 2.6). Chosen pass-through connectors, apart from having a maximum service temperature of 200°C (req. 0.2), allowed an easy and fast assembly of the flexible hoses (req. 2.7). Both pass-through connections and preform assembly positioning was facilitated by the three-individual frame configuration (req. 2.7 and 2.8), because operators could access diaphragms without obstacles.

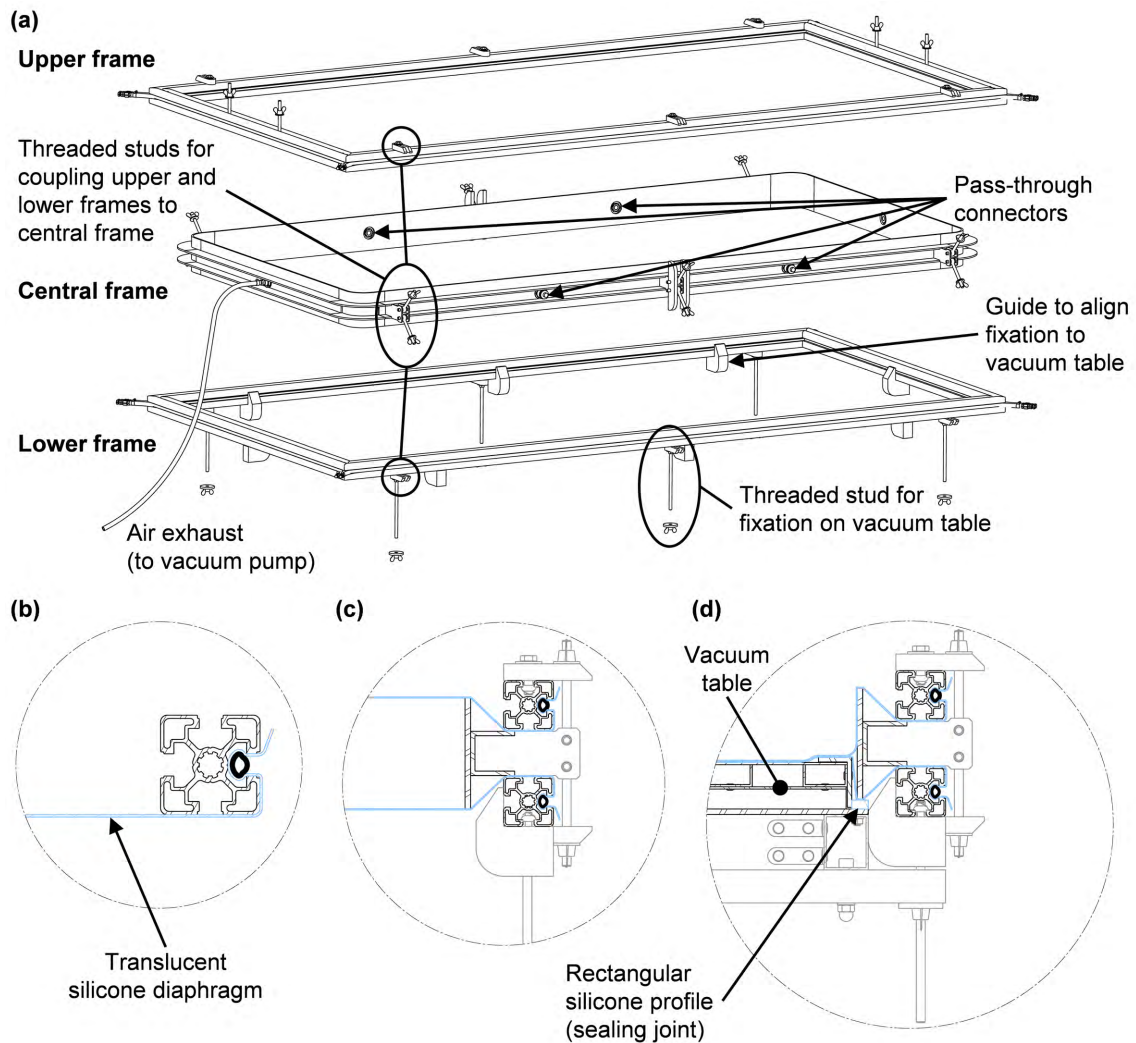


Figure 3.13. Double diaphragm tooling design: (a) expanded view of the three frames (without silicone diaphragms), (b) cross-section of a single diaphragm frame, (c) cross-section of the uncoupled double diaphragm tooling, and (d) cross-section of the coupled double diaphragm tooling and the vacuum table.

The frame of the lower diaphragm was equipped with a series of long threaded rods and PA guides to join the double diaphragm tooling and the vacuum table, and guarantee an accurate alignment between assemblies (req. 2.10). Mould cavity sealed was achieved by supporting the double diaphragm tooling through the interior plate of the central frame on the silicone profile placed over the non-perforated aluminium plate (req. 2.11). The interior plate of the central frame pressed the lower diaphragm against the silicone profile, constituting an air-tight cavity with the aluminium plate. Size of the supporting frames and the central frame were determined to fit the size of the vacuum table.

All metallic components used in the double diaphragm tooling were of aluminium. The total weight of the double diaphragm tooling was ~50 kg.

3.4.2.3. Heating chamber

Although convection heating would have been a better option to only proceed with resin cure, IR was chosen because it could also be used in any non-isothermal forming experiment (req. 3.1). A total of eighteen IR panels of power 600 W, which previous experience showed that it was enough power to guarantee mould temperatures over 100°C (req. 3.2), were distributed in three rows, adaptable in directions x and y (height), and orientation z (req. 3.3). A general view of the supporting structure of the IR grid is shown in Figure 3.14.a.

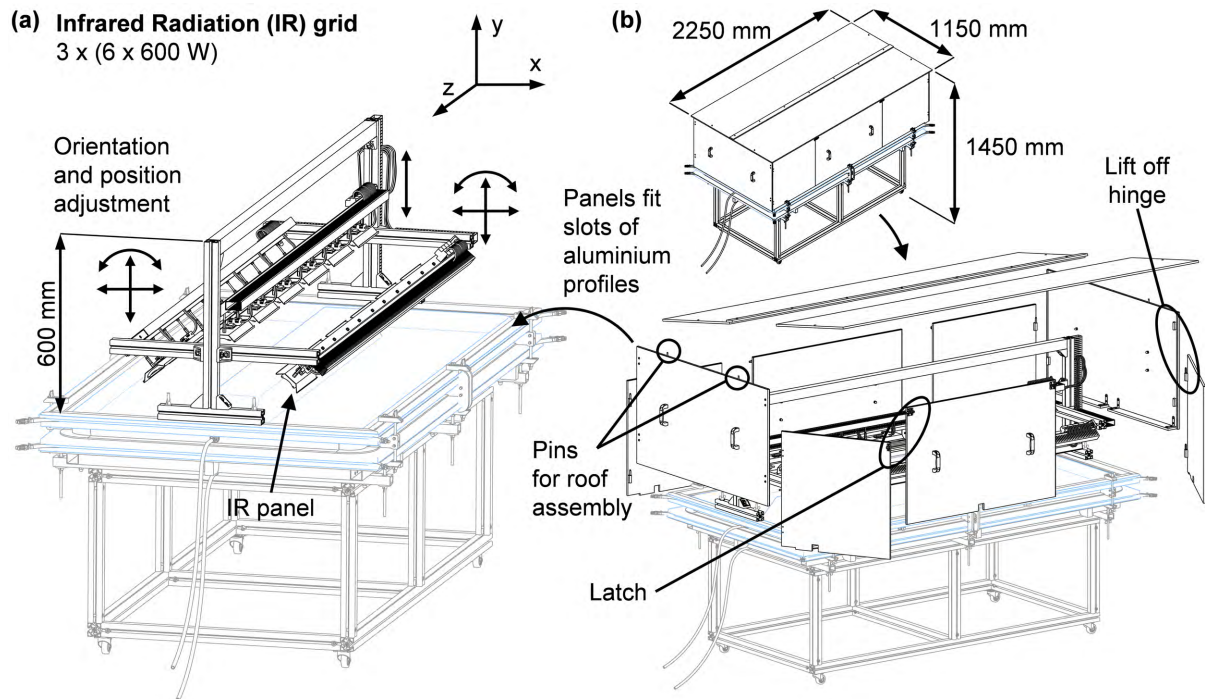


Figure 3.14. Heating chamber: (a) supporting structure of IR panels and (b) enclosure details.

Furthermore, IR panels were connected in pairs that could be later assigned to different heating sectors. Combination of adjustable panels positions and flexibility of the tailored control system made possible the adaption of the IR grid to different geometries (req. 3.4).

Heating power was governed through closed-loop PID controllers that monitored upper diaphragm temperature through 'J' type thermocouples. It was experimentally checked that under constant target temperatures, temperature difference with respect to between diaphragms fell under 3°C in less than 10 min.

For each processed geometry, position adjustment of each row of IR panels, as well as grouping into each heating sector, was carried out through successive trial and error tests without preform assembly inclusion.

The enclosure of the heating chamber was built with Medium Density (MD) fibreboard panels of thickness 10 mm. A total of eight lateral MD panels and a two-pieces MD fibreboard roof allowed assembly and removal of the enclosure over the upper diaphragm supporting frame, which also held the supporting structure of the IR panels (req. 3.5). MD panels perfectly fitted the slots of the aluminium frames and were joint together through various lift off hinges and latches. EPDM foam seals were placed between panels to reduce hot air losses. Some enclosure details are presented in Figure 3.14.b.

Interior of MD panels were covered with aluminium foil, glued with a high temperature adhesive (service temperature $> 180^{\circ}\text{C}$, req. 0.2) to maximize IR reflectivity and minimize heating absorption, thus minimizing heat losses. Although not being a perfect insulation solution, insulation level was enough for protecting operators from working temperatures (req. 3.6).

3.4.3. Built

According to the design of the ISFLIP prototype detailed in the previous section, a successful construction of the prototype was carried out to conduct the corresponding testing campaigns (Figure 3.15).

3.5. Research strategy

In the context of manufacturing high performance FRP parts, ISFLIP was conceived to exploit the opportunity of manufacturing bigger parts at higher production rates, and the benefits of flat preforming to facilitate preforming automation and minimize labour dependence, and gain reproducibility due to flat preform filling and fully controlled forming. However, a deeper and more rigorous analysis through the MT let identifying a wider range of internal and external factors affecting consecution of ISFLIP main goal. From this analysis, a series of challenges and uncertainties were identified to mark the research paths to be followed.

The first challenge only referred to the infusion stage of ISFLIP, focusing on achieving high v_f , narrow thickness tolerance and null porosity while keeping short filling and post-filling times. The trade-offs between component quality and processing time in VI required a new and fresh approach to deconstruct VI, and determine how processing conditions of each main step affected quality attributes in order to reconstruct VI from the objectives of maximizing part quality and minimizing manufacturing time.

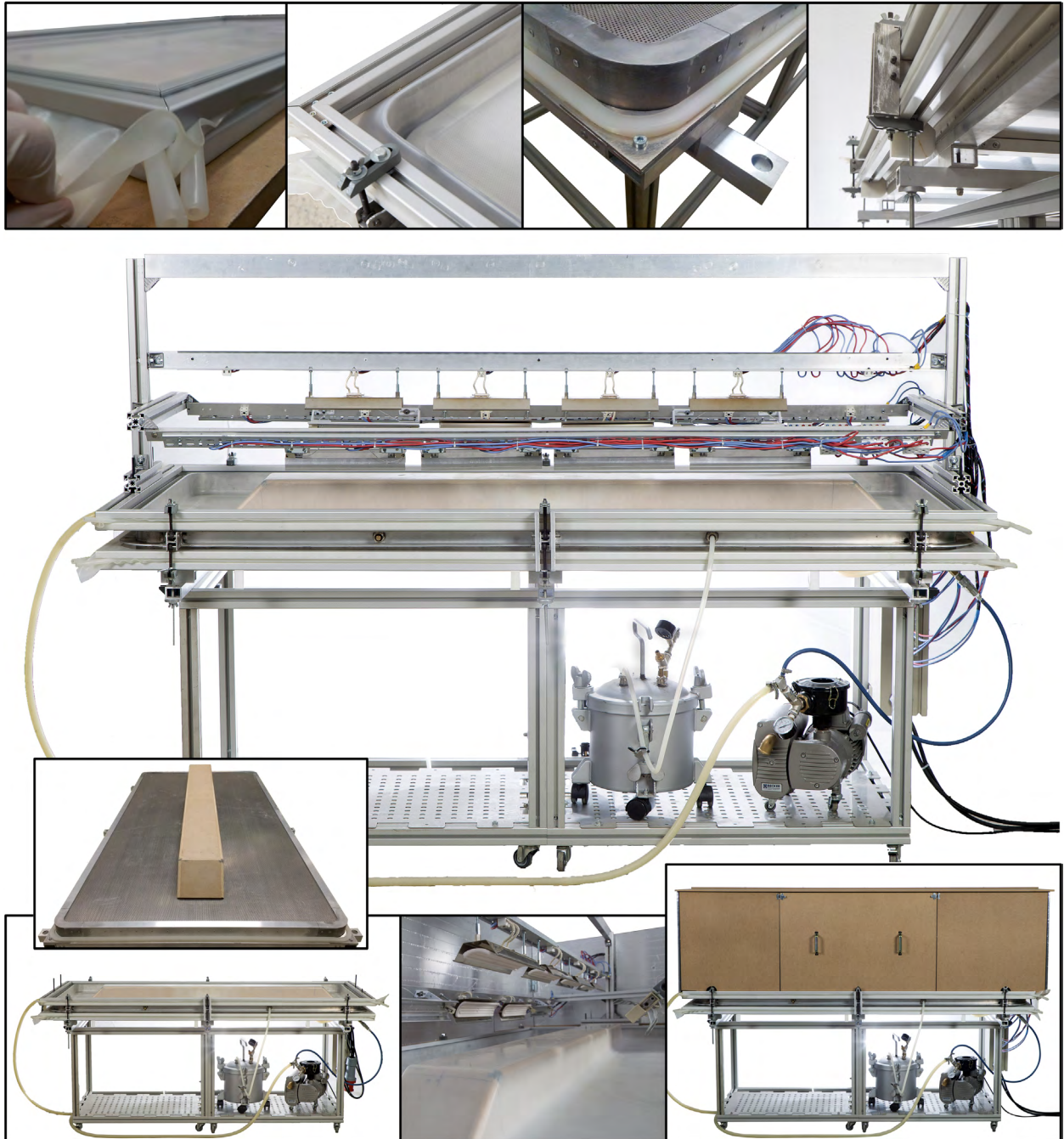


Figure 3.15. Built prototype.

As a new manufacturing technique in an early stage of development, ISFLIP presented some uncertainties which should be clarified before defining a more focused research path. These uncertainties mainly originated in the forming stage, but not only referring to preform formability. It was unclear how forming after preform impregnation could affect void formation, and how local folding of thin films covering the preform could create defects in form of scratches on the surface of manufactured parts. However, most of doubts arose from the forming behaviour of a lubricated preform that interacts with different consumable materials and elastic diaphragms, each element presenting different deformation mechanisms. Besides, it was necessary to evaluate the magnitude

of the negative effect on preform drapability of two known factors such as combined compaction-shear loading and geometry recesses. A first insight on these uncertainties was crucial to define more concrete research activities.

Apart from forming uncertainties, mistrusts of cosmetic surface finish and shape tolerances should be cleared up to avoid any unfounded preconception of ISFLIP. Both mistrusts come from the non-direct contact between part and mould. The capacity of ISFLIP to manufacture parts that can achieve a cosmetic finish after an appropriate coating procedure must be proved, as well as its ability to reproduce mould geometries (accounting for the thickness of the lower diaphragm) without adding any special concern in this respect.

Finally, simulation of the forming stage should be addressed. Nowadays, simulation of manufacturing processes is fundamental in design for manufacturing approaches to reduce development cost and time. Flat preform impregnation facilitates preform modelling and filling simulation; but forming of a stack of dry fabrics embedded in a low viscosity matrix and in contact with materials with different deformation mechanics entails a massive effort in characterising and modelling all materials, and simulating physics involved in the process.

In essence, four research paths have been introduced: trade-offs in VI, forming uncertainties, mistrusts of surface finish and shape tolerance, and simulation of the forming stage. The research project presented in this dissertation deals with the challenge of solving trade-offs of component quality and processing time in VI (Chapter 4 and 5) and evaluation of forming uncertainties in ISFLIP (Chapter 6).

3.6. Conclusions

This chapter has introduced ISFLIP as a promising manufacturing process, laying the foundations that should support its progression. It is worth recalling ISFLIP primary goal, manufacturing high performance FRP parts with shorter processing times and higher reproducibility than other conventional VI variants.

From the initial conception of combining VI and forming, a detailed manufacturing methodology was defined from which process prospects could be assessed and a functional prototype built.

ISFLIP was analysed from the point of view of the applicability of a manufactured component through the MT; thus, very focused on a future adoption in industry. Both positive and negative, internal and external factors affecting ISFLIP performance were arranged in form of a SWOT

analysis in order to facilitate the planning of the research tasks, some of them addressed in the present dissertation, to be carried out along ISFLIP development.

Furthermore, findings from the MT support the idea that ISFLIP is a feasible process with a great potential. Aiming at shell shapes (flat or shallow dished non-reentrant shell shapes), ISFLIP enables the possibility of manufacturing components whose size and economic batch cannot be covered by VI and RTM.

A functional prototype was successfully designed and constructed to meet a series of requirements set from previous experience, the defined processing sequence and the SWOT analysis. Once the processing sequence was detailed and an ISFLIP prototype implemented, a proof-of-concept of ISFLIP was able to be performed, continuing with the challenges, uncertainties and mistrusts on which ISFLIP development should be focussed.

This page intentionally left blank

Chapter 4

Void content minimization via effective degassing

In order to bridge the gap between VI and RTM in terms of component quality through minimizing void content, this chapter addresses the efficacy of conventional vacuum degassing and the benefits of additional assistance systems which enhance bubble formation during degassing and dissolution of the remaining micro-bubbles in the volume of resin.

A straight and reliable way of characterizing resin outgassing behaviour in VI manufacturing is unknown nowadays; since it depends not only on the quantity of dissolved air into the resin, but in manufacturing conditions and materials involved. Consequently, degassing effectiveness has been assessed by means of the resin outgassing behaviour during VI manufacturing of glass-epoxy specimens, through the final specimen porosity content and after isolating outgassing effects from the rest of porosity causes.

After characterizing manufactured specimens, a screening experiment, based on a fractional factorial design, was conducted to analyse the effects on specimen porosity of degassing time, addition of a nucleation medium in the volume of resin, stirring the resin at High Speed (HS) while degassing and later pressurization of the resin.

4.1. VI manufacturing: decision-making

The conducted VI process was designed to minimize differences between specimens in void formation due to flow through dual-scale porous media, and to promote a gradient of resin pressure into preforms when gelation occurred. Since epoxy resin evaporation of volatile components and shrinkage at cure are negligible in comparison with other resin systems such as unsaturated polyester and vinyl ester [210–213], and special attention was kept during manufacturing experiments to detect any undesired leak; the two predominant causes of void formation were resin flow through heterogeneous dual-scale porous media and outgassing of air dissolved into the resin, which is the object of this study.

In-plane filling of preforms, in combination with short post-filling times, should result in specimens containing decreasing gradients of thickness and pressure between inlet and venting channels. Besides, according to Henry's law, this gradient of pressure should result in a gradient of void content into each specimen due to different outgassing conditions. Outgassing is enhanced as resin pressure decreases. Furthermore, from a specific pressure level, outgassing should not occur and free-porosity regions close to inlet channels should appear; while porosity accumulates near venting channels.

VI is a complex multi-step manufacturing process whose main steps are governed by pressure, temperature and time parameters. Processing parameters governing specimen manufacturing in the experiments are provided in Figure 4.1. The degassing parameters which were focus of this study were degassing time, t_{deg} , and degassing assistance systems. As will be lay out further on, in the eight conducted experiments, a total of four different vacuum degassing configurations were adopted: conventional (Figure 4.2.a), assisted by adding a nucleation medium over the base of the resin pot (Figure 4.2.b), assisted by HS resin stirring (Figure 4.2.c), and assisted by both adding a nucleation medium and HS resin stirring (Figure 4.2.d). These vacuum configurations were then combined with different t_{deg} and the possibility of later resin pressurization prior to the filling stage. Degassing was carried out at $P_{deg} = -98 \pm 1$ kPa. The nominal ultimate pressure able to be held by the vacuum pump was 0,1 kPa (absolute pressure).

Preforms were enclosed in an ordinary assembly with peel-ply layers covering preform top and bottom surfaces (Figure 4.3). Inlet and venting channels were placed parallel to preform edges (direction z) to force a rectilinear flow front progression and in-plane preform impregnation (dir. x). No separation was allowed between channels and preform edges to avoid unnecessary flow resistance; since it is a proved cause of pressure equalization into the preform [222].

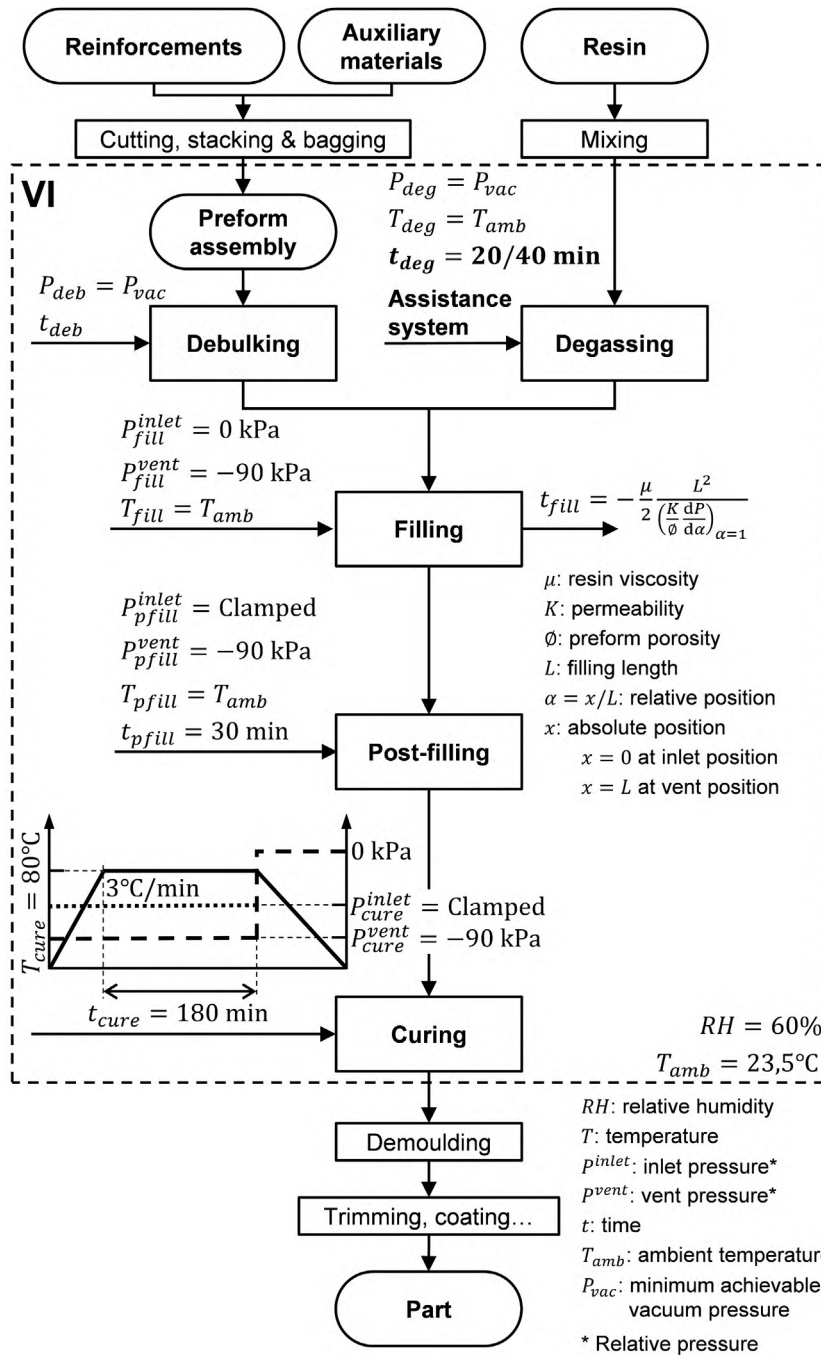


Figure 4.1 Flow chart and governing parameters of VI process.

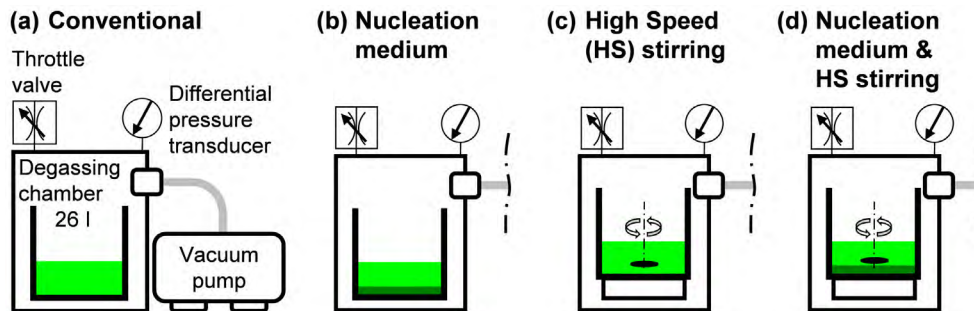


Figure 4.2. Vacuum degassing configurations.

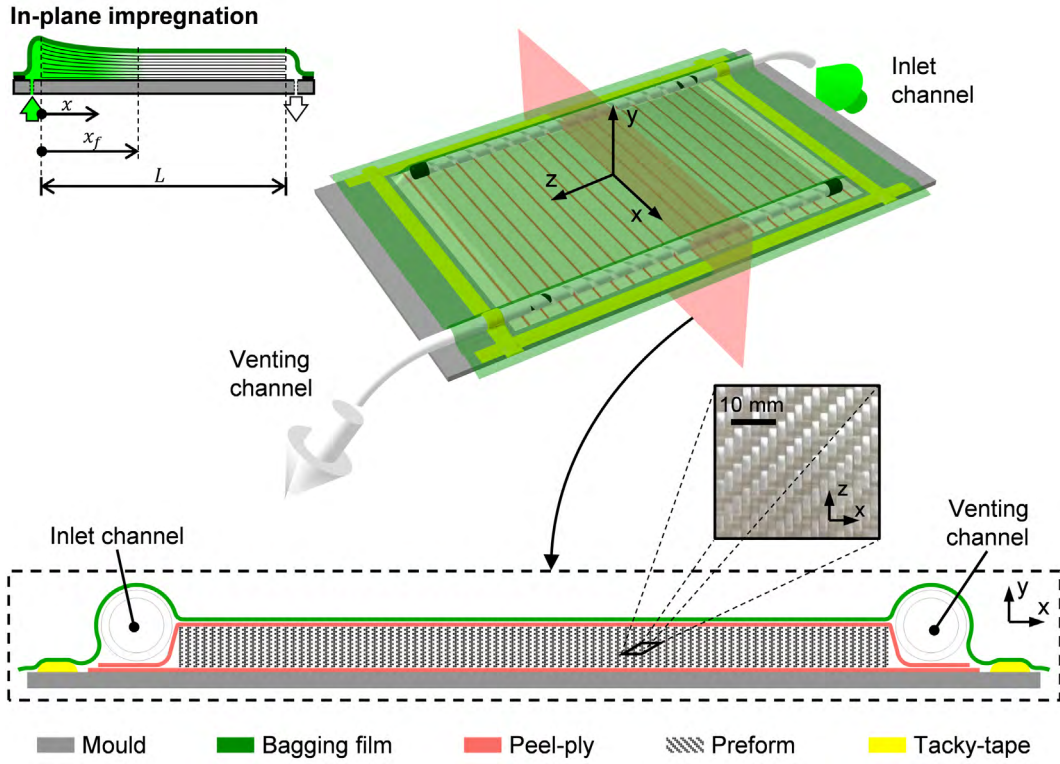


Figure 4.3. VI preform assembly (schematic dimensions are only representative).

Void formation at the flow front through dual-scale porous preforms is addressed in the literature by the modified capillary number, Ca^* [200,201]. It is worth recalling Equation (4), that expresses Ca^* as

$$Ca^* = \frac{\mu \cdot u_f}{\gamma \cdot \cos \theta} \quad (4)$$

where u_f is the macroscopic resin velocity at the flow front, μ is the resin dynamic viscosity, γ is the resin surface tension and θ is the contact angle between resin and reinforcement. Besides, in case of 1D rectilinear flow (direction x), macroscopic resin velocity, u , is given by a simplified version of Darcy's law introduced in Equation (1),

$$u = -\frac{K}{\mu} \frac{dP}{dx} \quad (12)$$

where K is the preform permeability in the flow direction and dP/dx is the pressure gradient along the filled region of the preform.

Void formation is negligible in a specific range of Ca^* ; while intra-tow and inter-tow voids are formed at higher and lower values of Ca^* , respectively (Figure 2.11). Therefore, void formation

differences between manufactured specimens may arise from μ and u , which in turn may also vary because of changes in K and/or dP/dx .

Resin viscosity, μ , is a function of temperature and time elapsed from the onset of the reaction of polymerization. As the reaction progresses, the degree of crosslinking increases, involving a raise in μ and making it more difficult for the resin to flow through the preform. Initially, the crosslinking reaction advances slowly; but large variations in reaction times may cause substantial changes in μ . Not all degassing procedures took the same time; hence, although resin was kept at ambient temperature, T_{amb} , flow differences could arise due to different values of μ during preform filling. In spite of not directly monitoring μ along the VI process, times elapsed from resin mixing until the onset of the filling stage, $t_{0 \rightarrow fill_0}$, and until the end of the filling stage, $t_{0 \rightarrow fill_{end}}$, were recorded to account for the effects caused by μ variations.

Preform permeability, K , depends on the compressive pressure history exerted on the preform along all the successive manufacturing steps (debulking, filling and post-filling) [129–131,248] and, thus, is also closely connected to dP/dx . However, characterizing K during the different VI steps is a challenging task, since multi-layer textile preforms exhibit highly complex inelastic compressive phenomena such as dependence on compaction velocity, stress relaxation and stress-strain hysteresis [119,120].

Furthermore, in VI, compaction and resin pressures are coupled due to the flexibility of one mould half, as pointed out in Terzaghi's relation [187], in which it is decomposed the normal pressure applied to the fibre-matrix system, P_{atm} , into the sum of resin pressure, P , and fibre compaction stress, σ_f .

Since specimen materials and size were kept constant along the research, and governing pressure controlled along the test campaign; main variations in K and dP/dx could have appeared due to different debulking times, t_{deb} . Because debulking and degassing steps were carried out in parallel, different t_{deg} involved variations in t_{deb} . However, debulking was planned to include a single loading step to the minimum attainable vacuum pressure, P_{deb} , for $t_{deb} > 75$ min, which was considerably longer than time required to fibre settling occur (< 30 min for preforms later introduced). Therefore, expected K and dP/dx variations between specimens would be caused by inherent preform variability more than by processing conditions.

Variations in u could be also evaluated through monitoring filling time, t_{fill} . Correlation between both variables becomes clear once making use of an analytical expression to determine t_{fill} , such as the one provided below and previously introduced in Equation (7),

$$t_{fill} = -\frac{\mu}{2} \frac{L^2}{\left(\frac{K}{\phi} \frac{dP}{d\alpha}\right)_{\alpha=1}} \quad (7)$$

where L is the filling length, α is the relative position such as $\alpha = x/x_f$, x_f is the flow front position and ϕ is preform porosity (distinct from specimen porosity associated to void content). It must be noted how an alternative version of Equation (12) takes part in t_{fill} calculation. Equation (7) provides t_{fill} when the preform is fully filled, $x_f = L$.

On the other hand, resin outgassing depends on both the quantity of dissolved air into the resin and the resin capacity of dissolving air. The above listed degassing procedures tried to minimize air content into the resin; while, recalling the expression of Henry's law given in Equation (5), air solubility in equilibrium at a fixed temperature, C_{air} , is a function of the partial pressure of air, P_{air} , such that

$$C_{air} = H \cdot P_{air} \quad (5)$$

where H is the Henry's law solubility constant, which depends on temperature (decreasing with rising temperatures) and the resin.

In equilibrium, P_{air} equals the resin pressure, $P = P_{air}$; hence, air solubility into the preform would be a function of the position, $P(x)$. Forcing the existence of a gradient of pressure into the specimen between inlet and venting channels at resin gelation would allow to capture a continuous distribution of air solubility conditions. After preform filling, inlet channel was clamped while vent pressure was kept constant. Achieving homogeneous distributions of thickness and pressure along specimens would have required even a longer post-filling time, t_{pfill} , than t_{fill} [132–134]; however, $t_{pfill} = 30$ min was set to only about half of t_{fill} , resulting in the expected gradients of thickness and pressure between inlet and venting channels. Post-filling was monitored through preform thickness measurement with two laser displacement sensors at approx. 30 mm from the inlet and venting channels. Specimen manufacturing was carried out in the workbench described in Appendix B.

Resin cure was carried out in a single cure cycle at $T_{cure} = 80^\circ\text{C}$ to assure a rapid gelation of the resin after the post-filling step and avoid pressure homogenization into the preform; although it implied a reduction in air solubility.

It is worth noting that filling, post-filling and curing steps were conducted at pressures higher than P_{deg} in order to increase resin capacity of dissolving bubbles formed during preform impregnation.

4.2. Materials and methods

4.2.1. Specimens

Constituent materials used in the experimentation were the E-Glass 2/2 Twill-Weave Fabric (GTWF) Angeloni VV 320 T (Table 4.1) and the epoxy system Sicomin SR 8100 (bisphenol A diglycidylether, DGEBA) – SD 8822 (isophorone diamin). This epoxy system exhibits low viscosity, 340-390 mPa·s, and a working time longer than 200 min at ambient temperature [295].

Table 4.1. Textile properties of E-Glass 2/2 Twill-Weave Fabric (GTWF).

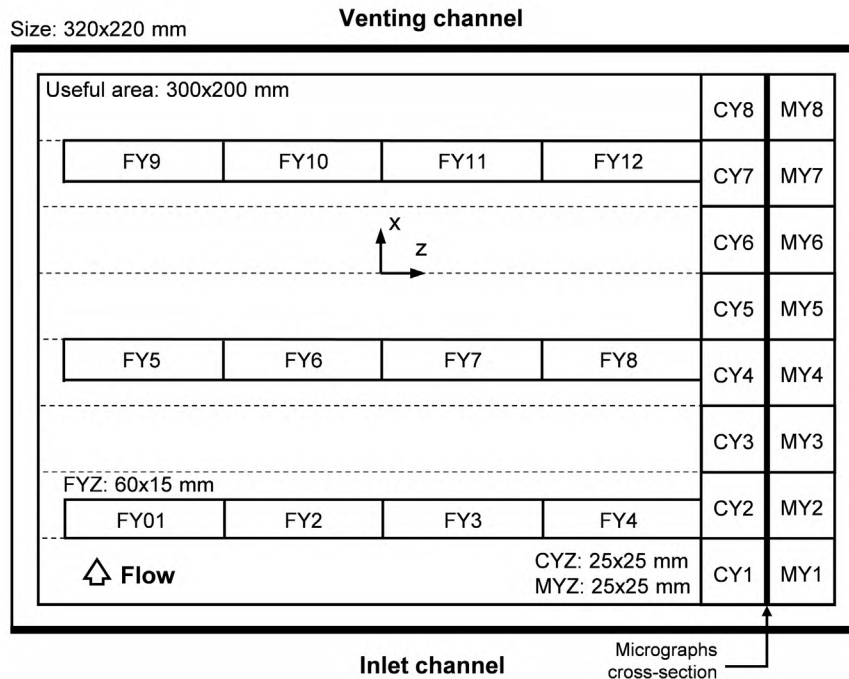
Reference	Weave style	Yarn	Areal density [g/m ²]	Thickness [mm]	Ends count [cm ⁻¹]	
					Warp	Weft
VV 320 T	2/2 twill	E-glass	320	0,281	5	5

A total of 9 GTWF layers of 320x220 mm with two orientations, (0/90) and (+45/−45), were alternately stacked over a flat aluminium mould resulting in quasi-isotropic preforms [(0/90), (+45/−45)]₂, (0/90), [(+45/−45), (0/90)]₂. Due to the irregular free-edge thickness, specimens were trimmed to a useful area, S_{useful} , of 300x200 mm.

4.2.2. Test procedures

Specimen characterization was not limited to porosity-related attributes such as void volume fraction, v_0 ; but, specimen quality was also addressed in terms of fibre volume fraction, v_f . Besides, morphology and distribution of trapped pores, and their effects on the flexural response of the specimens were also studied in order to give a clear picture of the problem caused by trapped porosity.

A series of samples were systematically distributed to capture the intentionally caused gradients of fibre and void content into each specimen (Figure 4.4): two rows of samples parallel to the flow direction (direction x) to measure constituent contents (CYZ) and pore morphology (MYZ), and three rows of samples perpendicular to the flow direction (direction z) to capture flexural properties along specimens (FYZ).



Sample codification (1) Test: flexural test (F), loss on ignition method (C) or light microscopy (M).

XYZ

(1) (2) (3)

(2) Specimen: 1, 2, 3, 4, 5, 6, 7 or 8.

(3) Sample number of test (1): 1, 2, 3...

Figure 4.4. Generic pattern of samples: size, distribution and codification rules.

More detailed descriptions of the testing procedures followed, as well as supplementary data to that provided later on the results section, can be consulted in Appendix D for visual inspection, loss on ignition and three-point flexure methods, and in Appendix E in case of light microscopy.

4.2.2.1. Visual inspection

The translucent nature of the GTWF-epoxy specimens allowed to identify the specimen areas in which porosity was present. For each specimen, porous area fraction, s_0 , was computed as the ratio of porous area, S_0 , and specimen useful area, S_{useful} :

$$s_0 = \frac{S_0}{S_{useful}} \quad (13)$$

The open-source image processing package Fiji, based on ImageJ, was used to scan the top view pictures of the manufactured specimens.

4.2.2.2. Loss on ignition method

Samples coded as CYZ in Figure 4.4 were tested via the loss on ignition method, according to the procedure stated in the standards UNE-EN ISO 1172:1999 and UNE-EN ISO 7822:2001, in order to determine v_f and v_0 .

Initially, constituent materials volume fractions were computed from the mass fractions and the sample volume, V_{sample} , such that

$$v_f = \frac{m_f/\rho_f}{V_{sample}}, \quad v_r = \frac{m_r/\rho_r}{V_{sample}} \quad (14)$$

where m_f and m_r are the fibre and resin mass fractions, v_f and v_r are the fibre and resin volume fractions, and $\rho_f = 2544 \text{ kg/m}^3$ and $\rho_r = 1095 \text{ kg/m}^3$ are the fibre and resin densities [296]. Then, v_0 was estimated for each sample by applying the balance of component fractions:

$$v_0 = 1 - v_f - v_r \quad (15)$$

The determination of v_0 presented two limitations: 25x25 mm samples resulted in a range of volumes $\sim 1,4 \text{ cm}^3$ lower than the minimum 2 cm^3 recommended in the standards; and the texturized surface created by the peel-ply caused an over-estimation of sample volumes and, thus, $v_0 > 0\%$ were obtained even in samples with no porosity expectation.

Since translucent specimens allowed to identify which samples contained trapped pores, those n samples with expectation of no porosity were used to compute an average surface void volume, \bar{V}_0^{surf} , as

$$\bar{V}_0^{surf} = \frac{1}{n} \sum (v_0 \cdot V_{sample}) \quad (16)$$

Then, updated fibre and resin volume fractions, v'_f and v'_r respectively, were calculated considering an adjusted volume according to \bar{V}_0^{surf} such that

$$v'_f = \frac{m_f/\rho_f}{V_{sample} - \bar{V}_0^{surf}}, \quad v'_r = \frac{m_r/\rho_r}{V_{sample} - \bar{V}_0^{surf}} \quad (17)$$

Finally, v'_0 was estimated for each sample by applying the balance of component fractions:

$$v'_0 = 1 - v'_f - v'_r \quad (18)$$

4.2.2.3. Light microscopy

Samples coded as MYZ in Figure 4.4 were used to measure void content and characterize void morphology through digital image processing. Micrographs were taken from cross-sections underlined in the referred figure.

Micrographic samples were casted in polyester resin round micrographic specimens, grinded with diamond discs and finally polished in two steps, with a two-in-one suspension of 6 μm diamond and lubricant, and with a silica suspension. A number of fourteen to sixteen micrographs per sample were taken at 50X magnification and stitched to get a picture covering the full sample length. The open-source image processing package Fiji, based on ImageJ, was used to process the micrographs.

Total void content, a_0 , intra-tow void content, a_0^{intra} , and inter-tow void content, a_0^{inter} , were calculated in the set of stitched micrographs as the ratio of the area occupied by all voids of each void type, A_0 , A_0^{intra} and A_0^{inter} respectively, and the area occupied by the sample, A_{sample} , as

$$a_0 = \frac{\sum A_0}{A_{sample}}, \quad a_0^{intra} = \frac{\sum A_0^{intra}}{A_{sample}}, \quad a_0^{inter} = \frac{\sum A_0^{inter}}{A_{sample}} \quad (19)$$

Additionally, Feret's diameter, ϕ_{Feret} (maximum distance between any two points belonging to a pore), Feret's angle, φ_{Feret} (angle formed by the Feret's diameter and the horizontal axis), and aspect ratio, AR , were also computed for all the voids belonging to each sample. AR was defined as the ratio of the two second moments of area of a pore around its principal axes, i_1 and i_2 (AR of a circle and a square is 1) such that

$$AR = \frac{i_1}{i_2} \leq 1 \quad (20)$$

4.2.2.4. Three-point flexure test

Flexural properties of samples coded as FYZ in Figure 4.4 were obtained through a three-point flexure test according to the procedure stated in the standard UNE-EN ISO 14125:1999.

Flexure stress, σ_f , vs. strain, ε_f , response was calculated from the crosshead load, F , and deflection at the mid-point, s , by applying corrections due to large deflections; since final deflection was larger than 10% of the span between supports, l' :

$$\sigma_f = \frac{3Fl'}{2bh^2} \left\{ 1 + \left(\frac{s}{l'} \right)^2 - 3 \left(\frac{sh}{l'^2} \right) \right\} \quad (21)$$

$$\varepsilon_f = \frac{h}{l'} \left\{ 6,00 \frac{s}{l'} - 24,37 \left(\frac{s}{l'} \right)^3 + 62,17 \left(\frac{s}{l'} \right)^5 \right\} \quad (22)$$

where w and s are sample width and thickness, respectively.

Flexural strength, σ_{fM} , is determined as the flexural stress sustained by the sample at the maximum load. Flexural modulus, E_f , was estimated by applying a linear regression procedure to the curve σ_f vs. ε_f between $\varepsilon_f = 0,010$ and $\varepsilon_f = 0,014$, a section of the response curve in which slope kept stable after an initial instability that might have been caused by backlash in the spindles of the testing machine or by initial settling of the samples between the round supports. Samples were tested at 1 mm/min.

4.2.3. Fractional factorial design

Fractional factorial designs are particularly useful in early stages of experimental work, when it is likely that too many factors are investigated and some effects have little or no effect on the response variable. Consequently, these designs are widely used in screening experiments, in which an initially unreplicated experiment may become replicated after discarding some factors or high order interactions, and are later extendible to more complex fractional designs if necessary [297].

The effectiveness of a total of eight vacuum degassing procedures were compared through the analysis of their effects on the porosity of the corresponding VI manufactured specimens. Each degassing procedure was defined by the level adopted by a set of four factors previously introduced (Table 4.2): nucleation medium (N), HS stirring (S), pressurization (P), and degassing time (T).

Table 4.2. Design factors of the screening experiment of degassing procedures.

Factor	Level*1		Details	Motivation
	High (+)	Low (-)		
Nucleation medium (N)	On	Off	Scotch-Brite	Enhancing heterogeneous bubble formation
HS stirring (S)	On	Off	Magnetic stirrer at ≈ 300 rpm with a rod of 40 mm	Enhancing bubble formation due to cavitation
Pressurization (P)	On	Off	200 kPa*2 for 5 min	Collapse of micro-bubbles [218]
Degassing time (T)	40 min	20 min	-	-

*1 In regression models, high and low levels were considered +1 and -1, respectively.

*2 Relative pressure.

Factor levels were arranged according to the principal one-half fraction of a two-level fractional factorial design, 2_{IV}^{4-1} (Table 4.3). In two-level factors, the effect of a factor (or interaction) is expressed as the difference between the averages of a response variable at the high (+) and low (–) levels of the factor (or interaction). For example, in case of factor T, its effect, l_T , was given by

$$l_T = \bar{y}_{T+} - \bar{y}_{T-} \quad (23)$$

where \bar{y}_{T+} and \bar{y}_{T-} are the average of a response variable at high level (+) and low level (–), respectively.

Table 4.3. The 2_{IV}^{4-1} fractional factorial design, principal one-half fraction, applied to the screening experiment of degassing procedures.

Specimen	Run order	Basic design			T = NSP	Treatment
		N	S	P		
6	4	–	–	–	–	(1)
5	5	+	–	–	+	nt
3	2	–	+	–	+	st
7	8	+	+	–	–	ns
4	7	–	–	+	+	pt
1	1	+	–	+	–	np
8	6	–	+	+	–	sp
2	3	+	+	+	+	nspt

Only effects of main factors N, S, P and T, and two-factor interactions were considered in the analysis, neglecting the influence of higher order interactions. Besides, in 2^{4-1} factorial designs, effects of two-factor interactions are aliased with each other ($l_{NS} = l_{PT}$, $l_{NP} = l_{ST}$, $l_{NT} = l_{SP}$); therefore, interaction effects were carefully addressed to discern, according to main factor effects and experimental conditions, which was the predominant interaction.

Specimen porosity was characterized by different procedures, but only attributes which showed evident variation between specimens were taken as response variables of the factorial design. This variation was assessed by the coefficient of variation (or relative standard deviation), defined as the ratio between the standard deviation and the mean response.

Since the initial fractional factorial design was saturated (no available degree of freedom to compute error variance), effect significance was firstly qualitatively assessed through a half-normal probability plot of the effects. The largest effects which did not lie along the normal straight line were considered good candidates to be included in the later Analysis of Variance (ANOVA),

which statistically evaluated significance of factor or interaction effects on response variables. Backward elimination was performed to sequentially remove any factor or interaction from models with a significance level $p > 0,10$ ($\equiv 10\%$); although, actually, effect significance was set at $p \leq 0,05$ ($\equiv 5\%$).

From the rigorous analysis of the VI process previously presented, apart from the design factors considered in the fractional factorial design (N, S, P and T) and the held-constant factors (Figure 4.1), a set of nuisance factors (RH , T_{deg} , T_{fill} and T_{pfill}) and allow-to-vary factors (P_{deb} , t_{deb} , P_{deg} , $t_{0 \rightarrow fill_0}$, $t_{0 \rightarrow fill_{end}}$ and t_{fill}) that might affect the response variables were identified. These factors may be treated as covariates and analysed through a variation of ANOVA, an Analysis of Covariance (ANCOVA) [298]. Special attention was kept on filling-related times, which showed large variations depending on the degassing procedure and were directly connected to void formation due to flow through dual-scale porous media.

Statistical analyses were performed with Minitab Statistical Software.

4.3. Results

4.3.1. Porous area fraction

The eight manufactured specimens are shown in Figure 4.5, as well as corresponding porous area fractions and specimen thickness, measured at samples MYZ.

As planned, a porous area was formed near venting channels. In specimens 4 and 6, s_0 was considerably larger than in the rest of specimens. Furthermore, a decreasing gradient of thickness seemed to exist between the inlet and venting channels.

4.3.2. Fibre and void volume fractions

In Figure 4.6, it is depicted the results of the loss on ignition method for the adjusted fibre volume fraction, v_f' , and void volume fraction, v_0' . The average surface void volume, \bar{V}_0^{surf} , computed to correct the thickness overestimation caused by texturized surfaces was 66 mm^3 , which is equivalent to a reduction of $0,11 \text{ mm}$ in effective sample thickness.

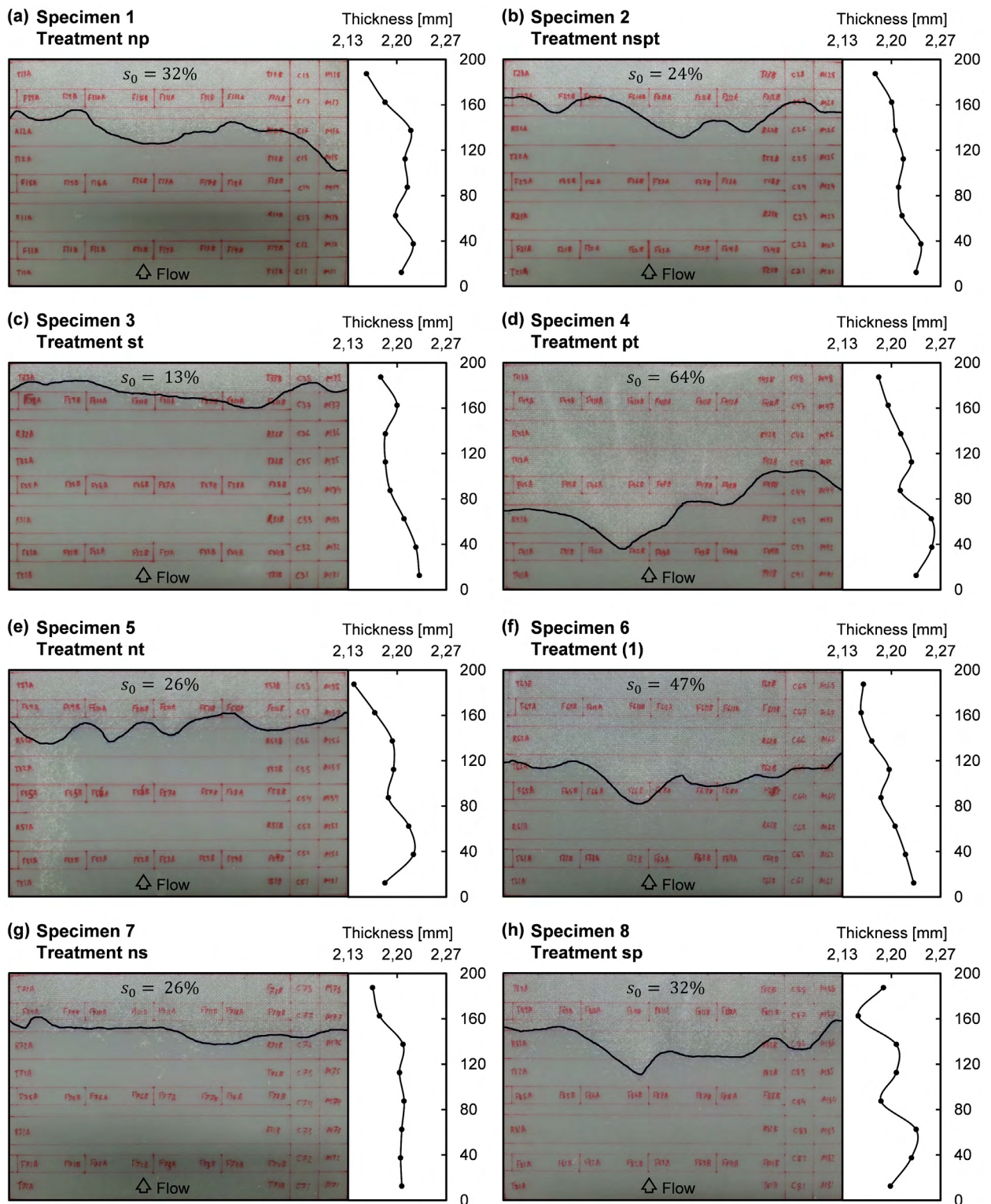


Figure 4.5. Manufactured specimens: porous area fraction, s_0 , and thickness measured at samples MYZ.

Only data of samples CY1, CY4 and CY8 is shown in Figure 4.6.a for clarity reasons, each sample representing conditions near inlet and venting channels, and in an intermediate position. It can be observed that the average per sample of v_f' and into each specimen increased at approaching the venting channels, involving an equivalent decreasing gradient of thickness along the specimens.

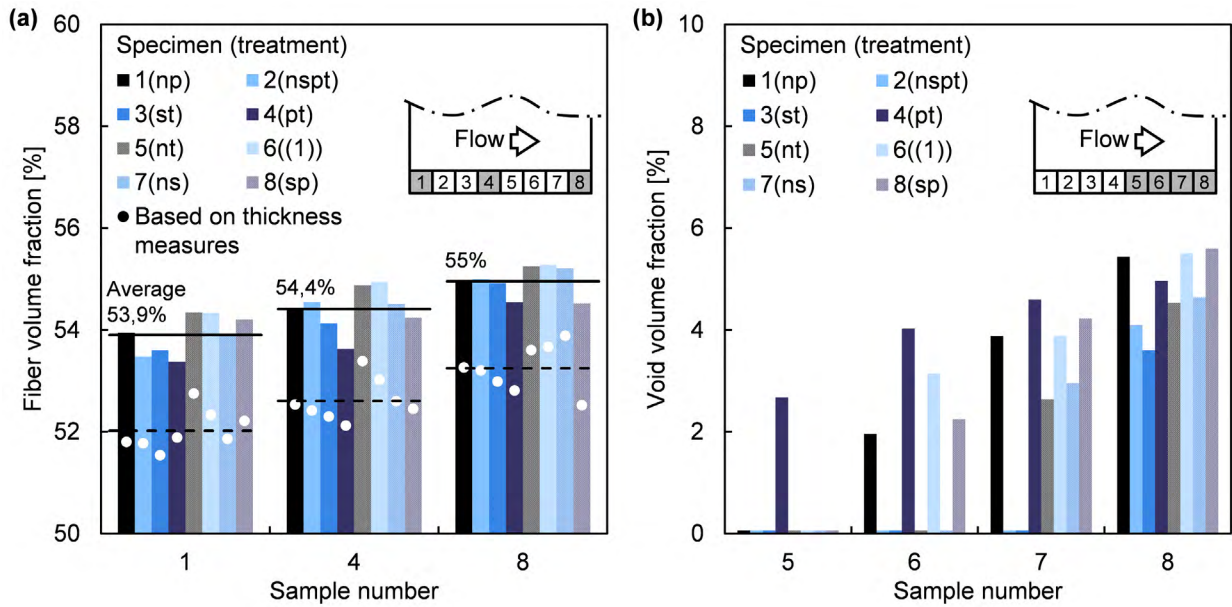


Figure 4.6. Results of the loss on ignition method: (a) Fibre volume fraction, v_f' , and (b) void volume fraction, v_0' .

In case of non-texturized samples (flat top and bottom specimen surfaces), the fibre volume fraction could have been computed through laminate thickness, h , as

$$v_f^h = \frac{n_l \cdot \rho_A}{\rho_f \cdot h} \quad (24)$$

where $n_l = 9$ is the number of layers, $\rho_A = 326 \text{ g/m}^2$ is the areal density of GTWF and $\rho_f = 2544 \text{ kg/m}^3$ is the E-glass fibre density [296].

However, the over-estimation of h due to the surface texture involved the underestimation of the results computed by Equation (24), as can be seen in Figure 4.6.a. Nevertheless, h could still be used as a good estimator of v_f' through a linear model adjusted with the experimental data such that

$$\hat{v}_f'[\%] = 14,9 + \frac{84,6}{h[\text{mm}]}, \quad R^2 = 73,8\% \quad (25)$$

Another gradient into each specimen of v_0' is also observable in Figure 4.6.b. All samples that are not included in Figure 4.6.b contain no porosity as can be checked in Figure 4.5. As expected, the maximum void content into each specimen occurred in the vent side, samples CY8. Besides, a considerable $v_0' > 2\%$ was measured even in the first sample belonging to the porous area into each specimen, reflecting a sudden accumulation of voids instead of a gradual increment of porosity from free-void samples.

4.3.3. Void size, shape and spatial distribution

Microscopy analysis was focused on samples MY8, which contained the highest void content into each specimen according to the results presented in the previous section. Since inter-tow voids were considerably larger than intra-tow voids, in order to automate their identification, a void area $A_0 = 3000 \mu\text{m}^2$ was set as the boundary between both void types.

Although intra-tow void occurrence was higher than inter-tow's in general; the huge difference in A_0 between both void types (Figure 4.7.a) involved that most of void area fraction, a_0 , belonged to inter-tow voids, as shown in Figure 4.7.b. Besides, it can be noticed that a_0 and void content measured through the loss on ignition method, v'_0 , differed significantly. The extrapolation of a_0 to a volumetric magnitude may arise some concern and, thus, it was preferred to focus the microscopy analysis on pore morphology more than on total void content.

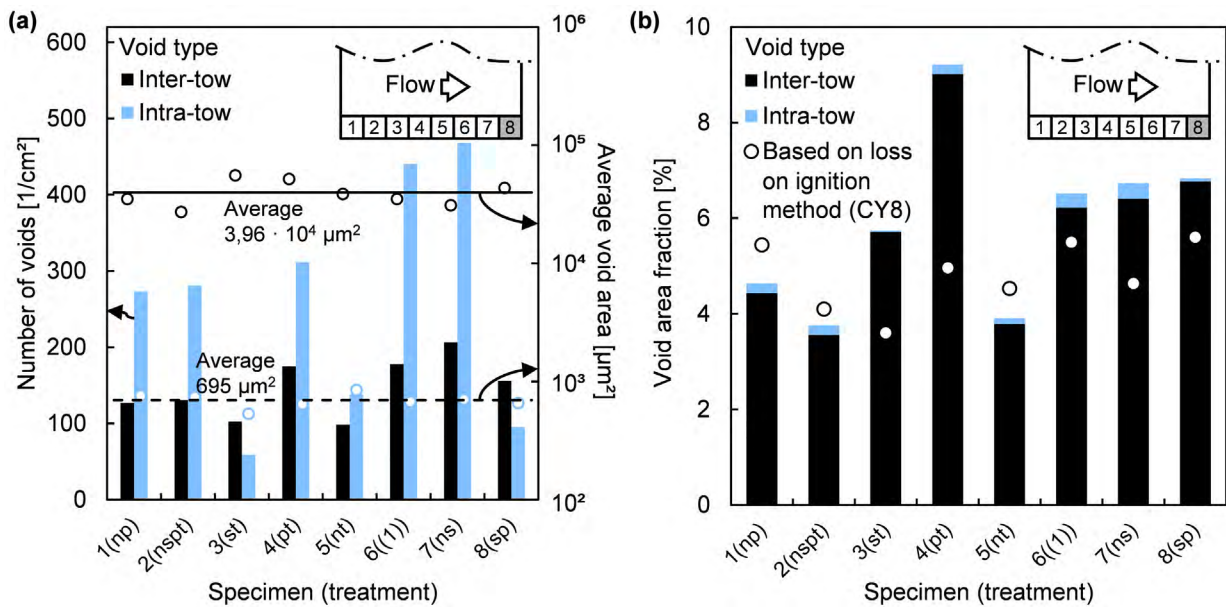


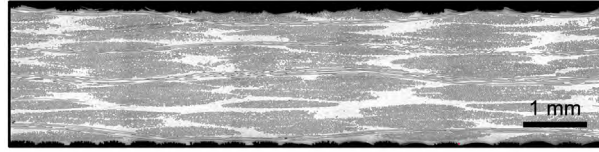
Figure 4.7. Size, occurrence and total content (void area fraction, a_0) of inter-tow and intra-tow voids.

The heterogeneous distribution of porosity into the laminates can be visually assessed in the micrographic samples of specimen 4 shown in Figure 4.8. Inter-tow voids were predominantly formed between fabric layers. Apparently, void size depended on the local nesting between layers in each analysed cross-section; hence, a_0 sensitivity with respect to small variations in cross-section location should be high. Microscopy analysis also allowed the observation of the fast transition between non-porous and porous areas. As can be seen in sample M45, the first sample belonging to the porous area in specimen 4 (Figure 4.8.b), the occurrence of a few inter-tow voids directly caused the accumulation of a significant void content.

Specimen 4 (treatment pt)

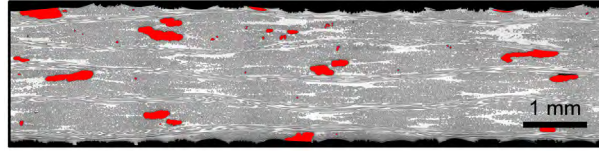
(a) Sample M41

$a_0 = 0,0\%$



(b) Sample M45

$a_0 = 3,6\%$



(c) Sample M48

$a_0 = 9,2\%$

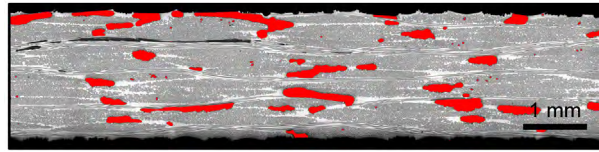


Figure 4.8. Detail views of micrographic samples belonging to specimen 4 and void area fraction, a_0 , of the corresponding whole sample (not only the partial cross-section depicted).

Once analysing inter-tow voids morphology in more depth, a significant correlation between Feret's diameter, Φ_{Feret} , and A_0^{inter} arose at representing the log transformation of both features, as seen in Figure 4.9.a. A similar trend can be noticed in Figure 4.9.b between Φ_{Feret} and the aspect ratio, AR ; although in this case, at increasing Φ_{Feret} , AR decreased. Obviously, inter-tow void tows were oriented according to the gaps between GTWF layers; therefore, at increasing Φ_{Feret} , inter-tow void orientation tended to 0° (direction x), as shown in Figure 4.9.c.

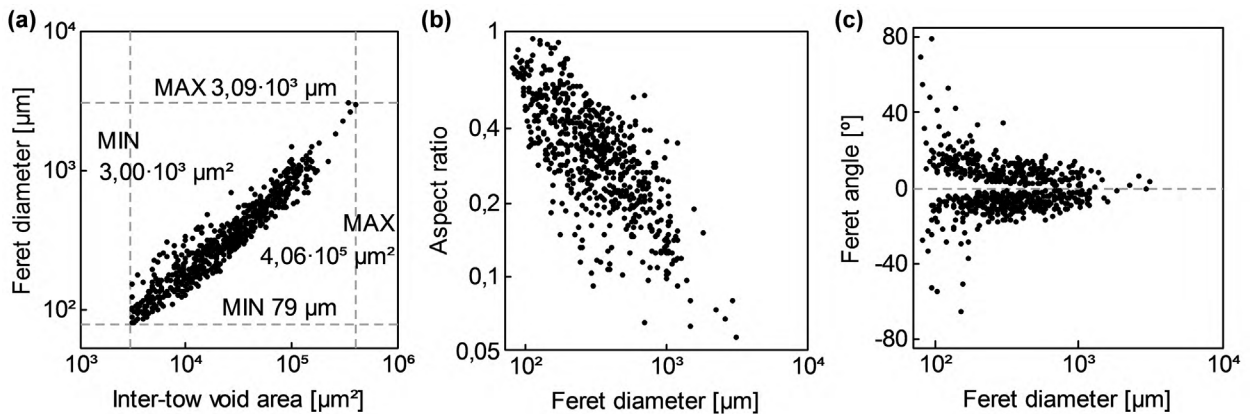


Figure 4.9. Shape descriptors of inter-tow voids: inter-tow void area, A_0^{inter} ; Feret's diameter, Φ_{Feret} ; Feret's angle, φ_{Feret} ; and aspect ratio, AR .

Pore size attributes, orientation and AR reflected the direct dependence of inter-tow void morphology on size and shape of resin rich areas between fabric layers in which inter-tow voids grew. Formation of resin rich areas depends in turn on preform properties, such as fabric architecture, relative orientation between consecutive fabric layers and nesting.

4.3.4. Flexure response

In Figure 4.10, it is depicted both flexural strength, σ_{fM} , and modulus, E_f , with respect to \hat{v}'_f , estimated through Equation (25), and v'_0 , at the corresponding sample CYZ (flexural sample FYZ and sample CYZ belonged to the same row of samples shown in Figure 4.4).

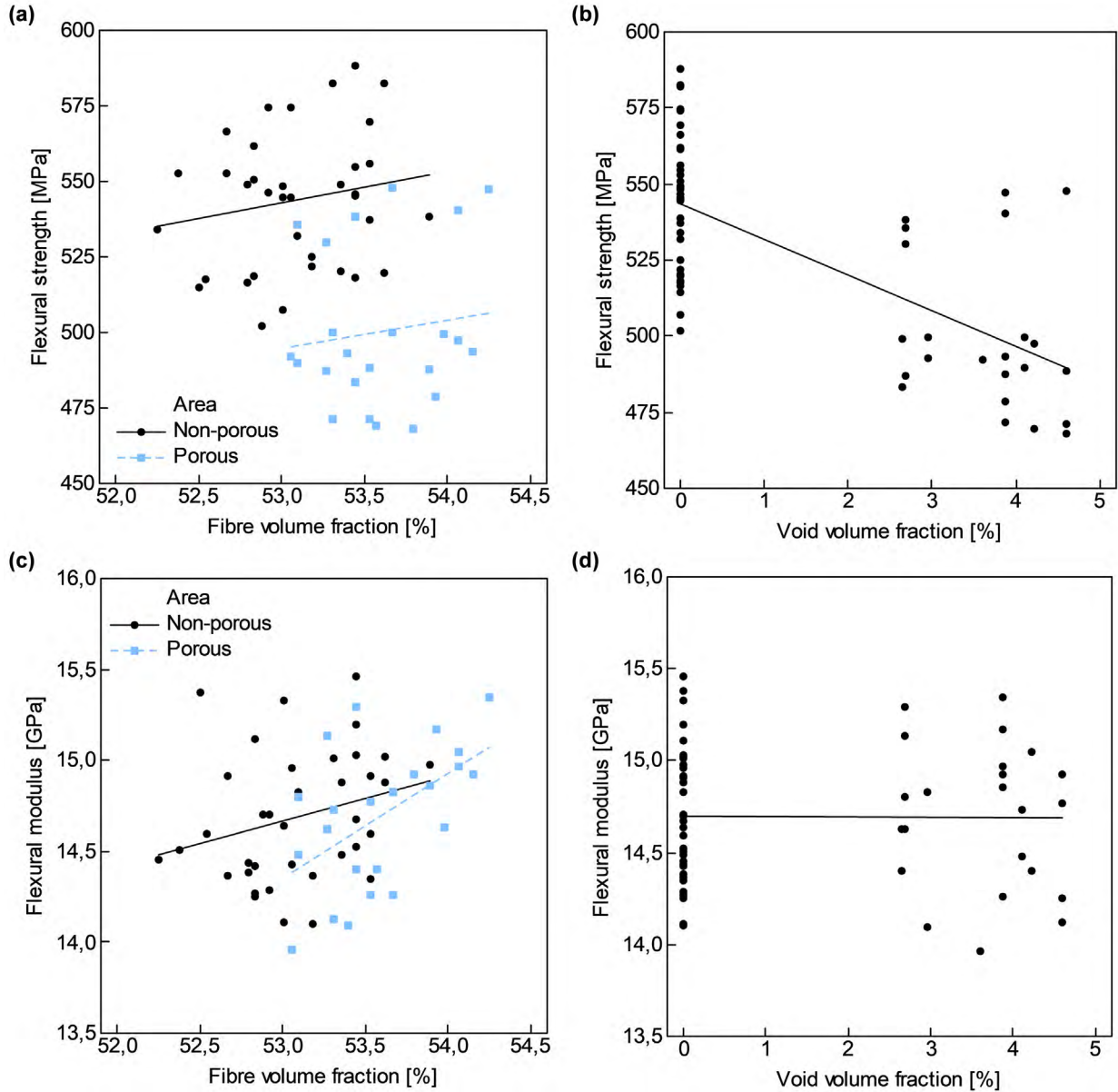


Figure 4.10. Flexural properties vs. estimated fibre volume fraction, \hat{v}'_f , and void volume fraction, v'_0 : (a-b) flexural strength, σ_{fM} , and (c-d) flexural modulus, E_f .

Although both σ_{fM} and E_f should depend on \hat{v}'_f , due to the reduced variation of \hat{v}'_f along samples, it was only shown a slight increment on both flexural properties as \hat{v}'_f increased. On the other hand, a significant dependence of σ_{fM} on v'_0 arose as shown in Figure 4.10; while no relation seemed to exist between E_f and v'_0 .

Two linear models were fitted with the experimental data to estimate σ_{fM} and E_f from material quality attributes, \hat{v}'_f and v'_0 :

$$\hat{\sigma}_{fM}[\text{MPa}] = -83 + 11,8\hat{v}'_f[\%] - 13,4v'_0[\%], \quad R^2 = 48,2\% \quad (26)$$

$$\hat{E}_f[\text{GPa}] = -5,55 + 0,381\hat{v}'_f[\%] - 0,0551v'_0[\%], \quad R^2 = 14,5\% \quad (27)$$

Nevertheless, experimental variability explained by both models did not reach even 50%. In case of E_f , a very low coefficient of determinations, R^2 , was obtained.

Reduction in σ_{fM} was slightly masked by some abnormally high values. Due to the heterogeneous porosity distribution, it is coherent to expect some samples which do not show any detrimental effect on flexural performance. Although it was identified a correlation between σ_{fM} and v'_0 , it was more appreciable the different performance between samples belonging to non-porous and porous areas, than between samples with different $v'_0 > 0\%$. The mean flexural strength, $\bar{\sigma}_{fM}$, in the non-porous area was 544 MPa ($\bar{v}'_f = 53,1\%$), while in the porous area it was 500 MPa ($\bar{v}'_f = 53,6\%$), a reduction of 8,1%. Subtracting the effect of \bar{v}'_f , the reduction in $\bar{\sigma}_{fM}$ increased to 9,1%. On the other hand, the mean flexural modulus, \bar{E}_f , was 14,7 GPa ($\bar{v}'_f = 53,3\%$).

4.3.5. Screening of degassing procedures

The fractional factorial design was analysed with respect to porosity-related attributes which showed significantly higher variability than the rest of quality-related attributes presented (Figure 4.11): porous area fraction, s_0 , and updated void volume fraction, v'_0 , (only corresponding to samples CY8). In addition, time-related factors also showed significant variability. Special attention was kept on time until filling onset, $t_{0 \rightarrow fill_0}$, time until filling end, $t_{0 \rightarrow fill_{end}}$, and filling time, t_{fill} ; because of their connection with void formation due to flow through dual-scale porous media.

At representing s_0 vs. v'_0 , it can be observed some kind of connection between both attributes as shown in Figure 4.12.a. Actually, if only specimens whose degassing treatments included at least one of the factors N (nucleation medium) or S (HS stirring) were considered, the trend would show a quite linear behaviour; hence, although both attributes were studied individually, it was expected a similar result.

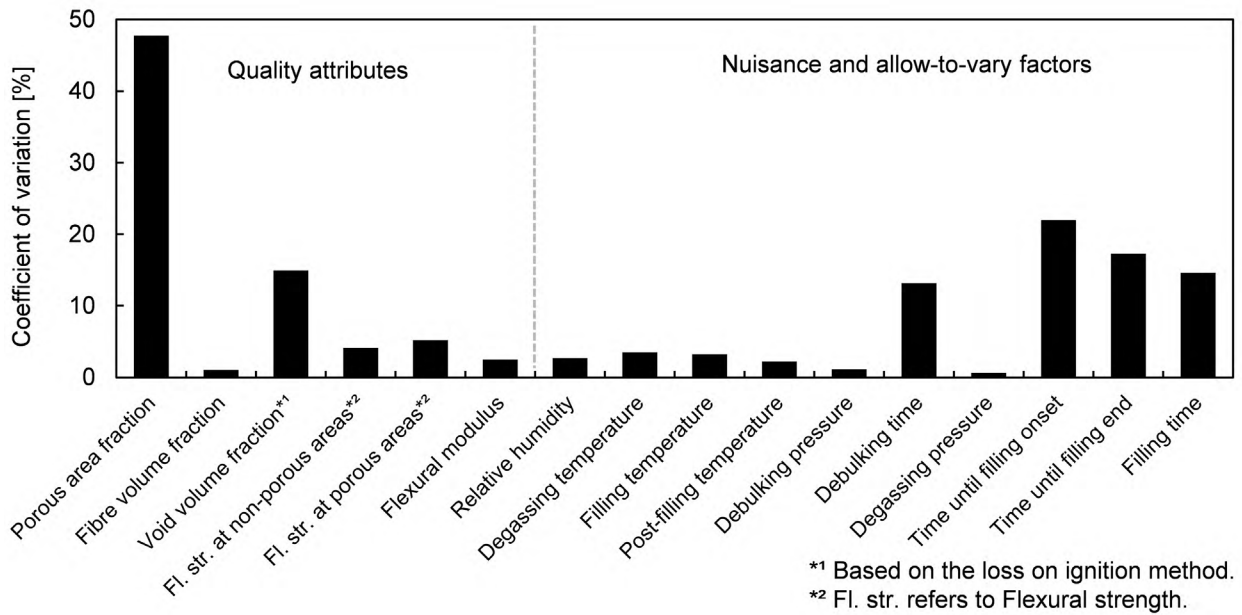


Figure 4.11. Coefficients of variation of measured quality attributes, and monitored nuisance and allow-to-vary factors.

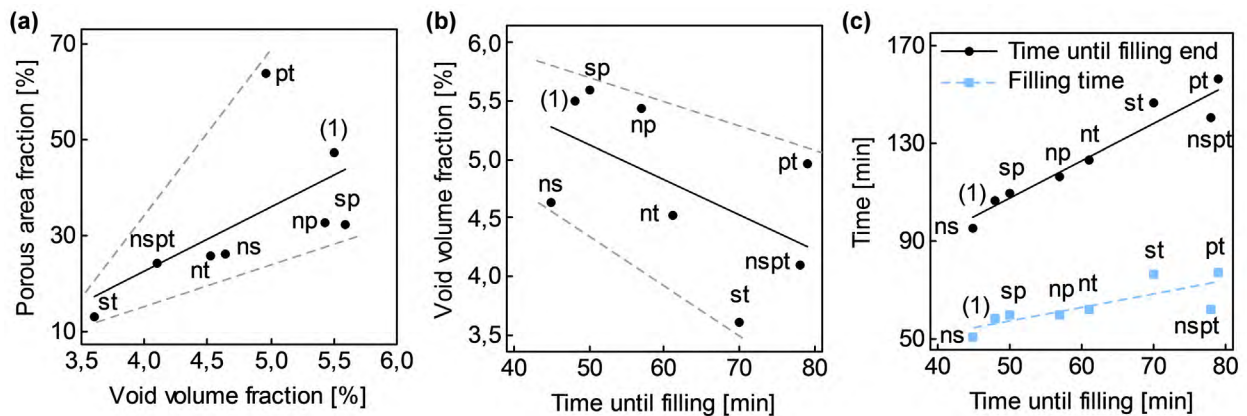


Figure 4.12. Noteworthy dependencies between response variables (porous area fraction, s_0 , and void volume fraction, v'_0) and covariates (time until filling, $t_{0 \rightarrow fill_0}$; time until filling end, $t_{0 \rightarrow fill_{end}}$; and filling time, t_{fill}).

No correlation seemed to exist between s_0 and any covariate; but at confronting v'_0 vs. $t_{0 \rightarrow fill_0}$, a connection between them was observed (Figure 4.12.b). v'_0 decreased as $t_{0 \rightarrow fill_0}$ increased. Similar trends arose between v'_0 , and $t_{0 \rightarrow fill_{end}}$ and t_{fill} ; however, $t_{0 \rightarrow fill_0}$ seemed to be the real cause behind these connections, since changes in resin viscosity, μ , at the onset of the filling step caused by different $t_{0 \rightarrow fill_0}$, beyond inherent preform variability, seemed to be the real cause behind $t_{0 \rightarrow fill_{end}}$ and t_{fill} scatter (Figure 4.12.c). Degassing procedures that included pressurization, factor P, implied an average increment of 10 min in $t_{0 \rightarrow fill_0}$; while different degassing times, factor T, implied an average increment of 22 min between the high level (40 min) and the low level (20 min). Therefore, both factors were partially aliased with $t_{0 \rightarrow fill_0}$. Effects of $t_{0 \rightarrow fill_0}$ on v'_0 was later analysed through ANCOVA.

The described statistical procedure was applied to the experimental data gathered in Figure 4.13. In Figure 4.14.a and Figure 4.14.b, it can be seen how main factor effects l_N , l_S and l_P behaved similarly in both response variables; while l_T was considerably larger in case of v'_0 , which could have been caused by the correlation found between v'_0 and $t_{0 \rightarrow fill_0}$, and the coupling between T and $t_{0 \rightarrow fill_0}$. Besides, interaction NS in case of s_0 (Figure 4.14.a) stood out from the rest of two-factor interactions. Factors N, S and T at high level (+) appeared to enhance void minimization, while factor P was negatively affecting specimen porosity.

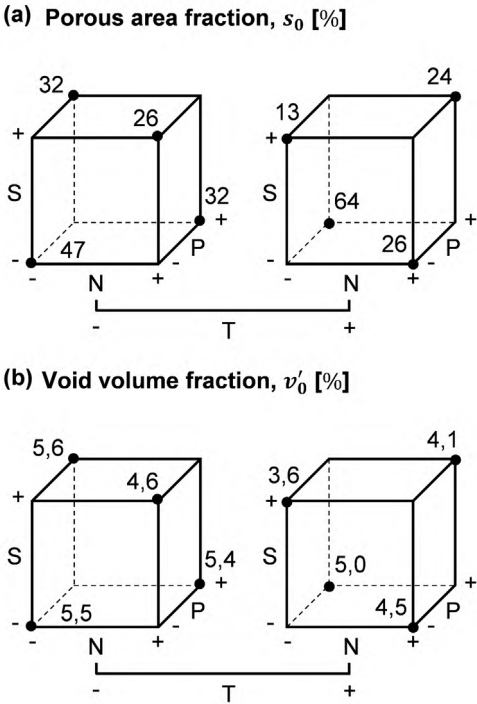


Figure 4.13. Cube plots of the input data of the screening experiment.

Highlighted effects shown in Figure 4.15.a and Figure 4.15.c were addressed through the ANOVA, performing the backward elimination until reaching the two models depicted in Table 4.4. Although initially unreplicated, both models evolved to replicated designs with an enough number of degrees of freedom to reliably compute error variance. It must be pointed out that, in both models, factor P was added after performing the corresponding analyses; since it appeared a strong dependence of the residuals on it.

In both models only appeared one significant term ($p \leq 0,05$), factor S in case of s_0 and T in case of v'_0 ; although interaction NS and factor S were very close to the limit of significance in case of s_0 and v'_0 , respectively. In order to address the aliasing between T and $t_{0 \rightarrow fill_0}$, an ANCOVA procedure was applied to the same model included in Table 4.4, substituting factor T by $t_{0 \rightarrow fill_0}$. The resulting model showed even a higher adjusted coefficient of determination, $R^2_{adj} = 87\%$,

than the presented model; however, the analysis of residuals showed an improper distribution vs. fitted values, hence it was preferred to present only the model including main factors S, P and T.

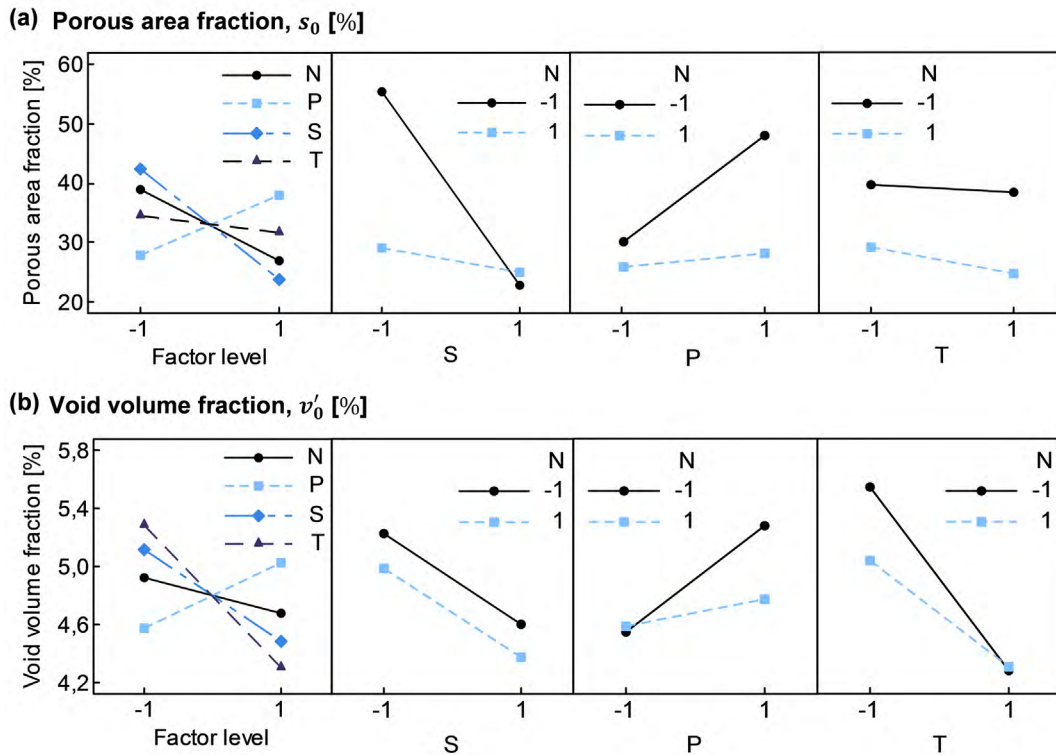


Figure 4.14. Effects of main factors and two-factor interactions (interaction effects are aliased according to $l_{NS} = l_{PT}$, $l_{NP} = l_{ST}$, $l_{NT} = l_{SP}$).

The apparent relation between v'_0 and $t_{0 \rightarrow fill_0}$, the aliasing between T and $t_{0 \rightarrow fill_0}$, the fact that T is the only main factor whose influence considerably changed between both response variables and, finally, conducted ANOVA and ANCOVA suggested that variations in $t_{0 \rightarrow fill_0}$ affected resulting v'_0 more than different degassing times. However, it was not possible to isolate effects of T and $t_{0 \rightarrow fill_0}$ from each other.

In the models presented in Table 4.4, interest lies more on the terms included than in the estimated response variables, because developed models are only applicable to the materials and processing conditions previously defined. Figure 16.b and Figure 16.d show the fitted values for the proposed models. The best performance in both cases was achieved when resin was stirred while being degassed, factor S. Besides, when none of factors N and S were included in the degassing procedure, obtained results were considerably worse.

Analyses of residuals were not included to avoid a saturation of statistical graphs which do not provide any additional information from the point of view of the manufacturing process; however, extended statistical analyses are provided in Appendix F.

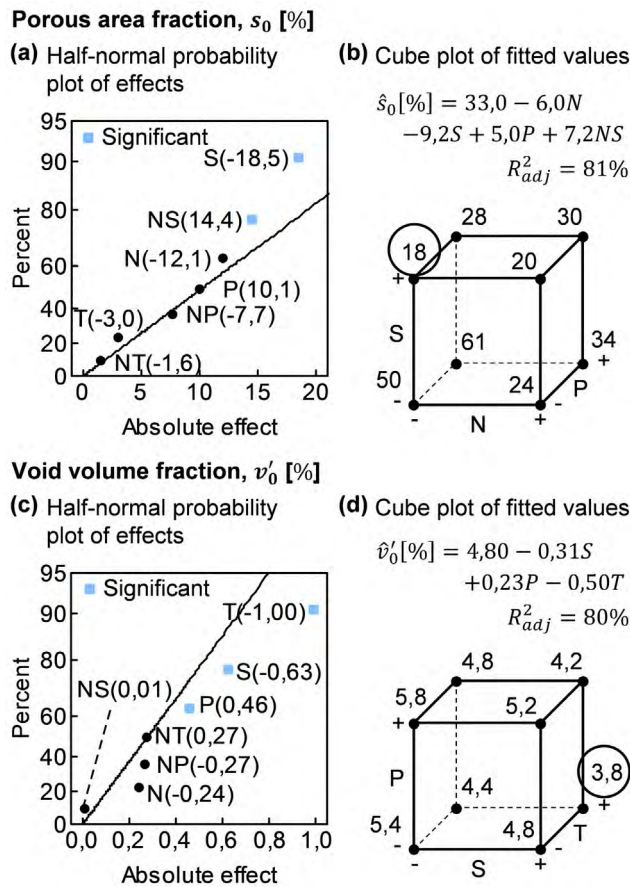


Figure 4.15. Initial qualitative evaluation of effect significance before conducting the ANOVA and resultant models from the ANOVA.

Table 4.4. ANOVA tables including Sum of Squares (SS); Degrees of Freedom (DF); Mean Squares (MS); F-statistic, F_0 , associated to each term; and level of significance, p , associated to each F-statistic.

Source	SS	DF	MS	F_0	p
Porous area fraction, s_0 [%]				$R^2_{adj} = 81\%$	
N	291,6	1	291,6	6,19	0,089
S	683,1	1	683,1	14,5	0,032
P	203,3	1	203,3	4,32	0,129
NS	416,4	1	416,4	8,84	0,059
Error	141,3	3	47,1		
Total	1736	7			
Void volume fraction, v'_0 [%]				$R^2_{adj} = 80\%$	
S	0,78	1	0,78	7,60	0,051
P	0,42	1	0,42	4,04	0,115
T	1,98	1	1,98	19,2	0,012
Error	0,41	4	0,10		
Total	3,59	7			

* Adjusted coefficient of determination, R^2_{adj} , is appropriate when available DF to compute error variance is small.

4.4. Discussion

Although not being a major topic of research, previous studies have already been focused on the importance of resin degassing in VI manufacturing, while rising some concern about conventional vacuum degassing [205,218,230]. Air solubility can be determined at different pressure and temperature conditions; however, resin outgassing after preform filling also depends on impregnation conditions, and the interaction between resin and reinforcements [203–205]. Therefore, it was proposed a rigorous VI processing methodology which allowed the outgassing assessment through the final porosity content of a series of specimens manufactured for that purpose.

In the present research, this methodology was applied to analyse the efficacy of different degassing procedures directly through the outgassing behaviour of the resin. The proposed manufacturing methodology do not have to be considered as a proposal to fabricate null void components, but only a proposal to allow the comparison of different outgassing behaviours. Actually, if resin pressure along the preform had become equal to the vent pressure at resin gelation, $P_{cure}^{vent} = -90$ kPa, a specimen completely covered by porosity would have occurred.

The conducted manufacturing procedure was based on inducing a decreasing gradient of pressure into the VI specimens, which should result in different outgassing conditions across the filling length, L . At characterizing specimens by the loss on ignition method, gradients of fibre volume fraction, v'_f , and void volume fraction, v'_0 , appeared into each specimen. As reported in previous studies, trapped gradients of pressure and thickness ($\propto v'_f$) into laminates are closely related, requiring the former even more time to equalize into specimens during post-filling steps [132,134,248]. Furthermore, the increasing gradient of v'_0 was an evidence of the presence of a continuous range of outgassing conditions into each specimen.

In all the manufactured specimens, critical conditions at which outgassing firstly happened were enclosed into L . Setting vent pressure to $P^{vent} = -90$ kPa along filling, post-filling and curing steps, played a key role to this end. A P^{vent} closer to vacuum pressure could have result in specimens whose useful area were completely covered by porosity. The porous area fraction, s_0 , can be understood as an indicator of the above mentioned critical outgassing conditions.

Although it was pretended to isolate outgassing effects on void formation from flow through dual-scale porous media; variations in resin viscosity, μ , significantly affected void formation. In a future implementation of the proposed manufacturing methodology, it would be recommended not to considerably alter time until filling, $t_{0 \rightarrow fill_0}$, between different tests.

Predominant formation of inter-tow voids resulted in a fast void content increment once entering porous areas due to the large size of these voids. As a consequence, flexural strength, σ_{fM} , did not suffer a continuous deterioration, but a sudden drop [193,194]. In Figure 4.10.a, two different behaviours in terms of σ_{fM} can be identified according to the presence or not of voids into the tested samples. A drop of 9,1% in σ_{fM} of porous samples (once effect of fibre content was subtracted) occurred even including the abnormally high values of some porous samples. Deterioration in σ_{fM} was more pronounced between non-porous and porous samples than into samples with $v'_0 > 0$ (Figure 4.10.b). It is worth noting that, in the literature, the detrimental effect of porosity on other matrix-dominated mechanical properties such as inter-laminar shear strength and fatigue behaviour is even more appreciable [191–193].

In spite of uncertainty at measuring v'_0 through the loss on ignition method due to surface texture corrections, these measurements were more realistic than those obtained by light microscopy. The heterogeneous pore distribution did not allow to capture in a single cross-section, despite the large area analysed, a representative picture to reliably determine the void content fraction. A more accurate quantification of void content through microscopy analysis would have required processing more cross-sections reflecting specific outgassing conditions or a volumetric measurement method [194,251,299].

After analysing micrographic samples, inter-tow void size, A_0^{inter} , seemed to be related to the gaps between tows into the preforms; hence, higher fibre content preforms should reduce A_0^{inter} and even may decrease the total trapped void content. A similar order of pore magnitude was found in other studies focused in components manufactured by RTM [201,300]. In order to be really aware of the problem importance, it deserves to be highlighted the maximum values of A_0^{inter} and Feret's diameter, \emptyset_{Feret} , found in the micrographic samples, 0,41 mm² and 3,09 mm, respectively (Figure 4.9.a). The maximum \emptyset_{Feret} was even larger than the thickness of the specimens.

The screening experiment confirmed the concern about traditional vacuum degassing. It has been proved that mechanisms to enhance bubble formation are fundamental to perform effective resin degassing. Assisting conventional vacuum degassing by adding of nucleation media and/or HS resin stirring has arisen as a real alternative to minimize outgassing in VI, and enhance dissolution of voids formed during preform filling. Furthermore, both involved degassing times, t_{deg} , were long enough to not affect resin outgassing; whereas, later resin pressurization, to remove micro-bubbles trapped near resin surface, counter-productively resulted in higher void contents.

The apparent degassing performance was similar in all degassing procedures. Initially, bubble clusters were formed at the free surface and the average bubble size increased due to bubble coalescence and diffusion of air molecules, resulting in the increment of the volume of resin. Then, the volume of resin reached a maximum level, but bubble continued increasing in size. After a short period of time, the volume diminished to its initial level as the average bubble size also decreased. Finally, non-clustered bubbles burst at the free surface of the resin, while the volume kept close to the initial level. The described process did not require more than 20 min in any case, and the quantity of bubbles trapped near the free surface did not significantly vary between experiments; therefore, a false impression could have been created if attention had been only paid to resin behaviour during degassing.

The best results in terms of porosity minimization were obtained when only HS resin stirring was involved in the degassing procedure. Apart from being an easily implementable degassing procedure, it did not involve waste of any additional material as in case of the nucleation medium. The combination of HS resin stirring and nucleation medium showed a worse result than when only stirring was involved in the degassing procedure. It may be explained by a higher rotation resistance at placing the magnetic rod over the nucleation medium, involving a reduction in the stirring speed.

Future work on this research should include the analysis of the effect of stirring speed and the influence of more stirring points on degassing efficacy. Furthermore, a pressure measurement system would be useful to monitor inlet pressure evolution after clamping the inlet; since preform thickness measurement during post-filling did not provide absolute data about the gradient of pressure, although it allowed a qualitative comparison between specimens.

4.5. Conclusions

The effects of some factors (addition of a nucleation medium, HS resin stirring, later pressurization and degassing time) on conventional vacuum degassing have been analysed through a screening experiment based on a fractional factorial design, with the aim of finding a really effective degassing procedure to minimize porosity in specimens manufactured by VI. A detailed VI process has been defined to allow the direct assessment of degassing efficacy by means of the resin outgassing behaviour through final specimen void content.

Specimen characterization revealed a large magnitude of inter-tow voids, finding pores even larger than specimen thickness which resulted in a sudden and significant drop in flexural strength.

The results of the screening experiment supported the idea that conventional vacuum degassing is not really effective and mechanisms to enhance bubble formation are fundamental. Stirring the resin while being degassed at ≈ 300 rpm arose as an easily implementable and significantly efficient procedure of reducing final specimen void content.

These findings are not only crucial to approach the final goal of manufacturing no porosity VI parts; but conducting a proper degassing procedure is fundamental in the analysis of matrix-dominated mechanical properties in VI samples, since the presence of undesired porosity avoids taking advantage of the full potential of FRPs.

Finally, it is worth pointing out that the results obtained and the conclusions drawn from the present study are only qualitatively applicable to other experimental conditions, because outgassing behaviour is closely related to materials involved and VI governing parameters. Moreover, further research is necessary to evaluate the effect of higher stirring speeds and more stirring points on degassing efficacy.

This page intentionally left blank

Chapter 5

High performance FRPs being competitive in time via control of filling and post-filling conditions

In order to bridge the gap between VI and RTM in terms of component quality, this chapter explores the viability of manufacturing VI specimens with short processing times without any detrimental effect on fibre and, especially, on void contents.

Two key points to reduce long processing times usually associated to VI are to force through-thickness impregnation by placing a HPDM over the preform, and to turn inlet into vent at the onset of the post-filling step. On the basis of these two manufacturing guidelines and using a preform assembly appropriate for ISFLIP, it was conducted a screening experiment whose first stage was focused on the additional benefits on component quality that different gradients of pressure during filling, and vent pressure increment between filling and post-filling might provide, expecting the minimization of specimen porosity.

Then, in the second stage of the screening experiment, the results of the first stage were compared to component quality associated to conventional VI manufacturing conditions: inlet clamping at the onset of the post-filling step and a common preform assembly.

Experimentation was arranged through factorial designs to screen those effects of the above-mentioned factors which significantly affect specimen quality in terms of fibre content and/or porosity. A set of glass-epoxy specimens were manufactured for this purpose.

5.1. VI manufacturing: decision-making

Along the experimentation, in one way or another, four pairwise comparisons were addressed: (I) inlet clamping/turning inlet into vent, (II) keeping constant/increasing vent pressure between filling and post-filling, (III) full/reduced filling gradient of pressure and (IV) VI/ISFLIP preform assemblies.

VI is a complex multi-step manufacturing process whose main steps are governed by pressure, temperature and time parameters; therefore, the pairwise comparisons related to inlet and vent pressures (I-III) substantially affected filling and post-filling performance. Processing parameters governing specimen manufacturing in the experiments are provided in Figure 5.1.

(I) At turning inlet into vent at the onset of the post-filling step, preform thickness rapidly equalizes; however, post-filling time was set to $t_{pfill} = 30$ min in all runs to guarantee that thickness equalizes even in case of clamping the inlet. Post-filling was monitored through preform thickness measurement with a system of laser displacement sensors at approx. 30 mm from inlet channels.

Furthermore, if resin pressure into the preform also reached equilibrium with venting channels, outgassing behaviour variations should not occur into the specimens. Since resin outgassing is a function of pressure and temperature [202–204], it depends on pressure distribution along the laminate [207]. Therefore, equalizing pressure into the preform to a vent pressure which is close to absolute vacuum may result in an increment of porosity with respect to specimens in which a gradient of pressure is trapped into the specimen when resin cures [134,222].

(II) It was chosen a vent pressure of $P^{vent} = -90$ kPa, higher than the degassing pressure, P_{deg} , in order to increase resin capacity of dissolving bubbles formed during preform impregnation. In runs in which vent pressure was increased between the filling and post-filling steps, in order not to alter outgassing behaviour, vent pressure in the filling stage was kept at $P_{fill}^{vent} = -95$ kPa to allow a later increment $\Delta P_{fill \rightarrow pfill}^{vent} = 5$ kPa and keep constant gelation conditions. This small pressure variations at pressure levels close to absolute vacuum were expected to not cause any variation in v_f due to preform relaxation.

(III) During filling, resin container was kept at atmospheric pressure, $P_{fill}^{inlet} = 0$ kPa, or exposed to partial vacuum, $P_{fill}^{inlet} = -40$ kPa, according to the experimental conditions defined for each run related to the gradient of pressure. In case of the full gradient of pressure, resin advance through the preform was governed by $\Delta P_{fill}^{inlet \rightarrow vent} = -90/-95$ kPa; while in case of

the reduced gradient of pressure, $\Delta P_{fill}^{inlet \rightarrow vent} = -50/-55$ kPa. Different P_{fill}^{vent} obviously altered the magnitude of $\Delta P_{fill}^{inlet \rightarrow vent}$; thus, special attention was kept on the effect of the interaction between different gradients of pressure and pressure increment, since void formation caused by resin flow through dual scale porous media might be affected in some way.

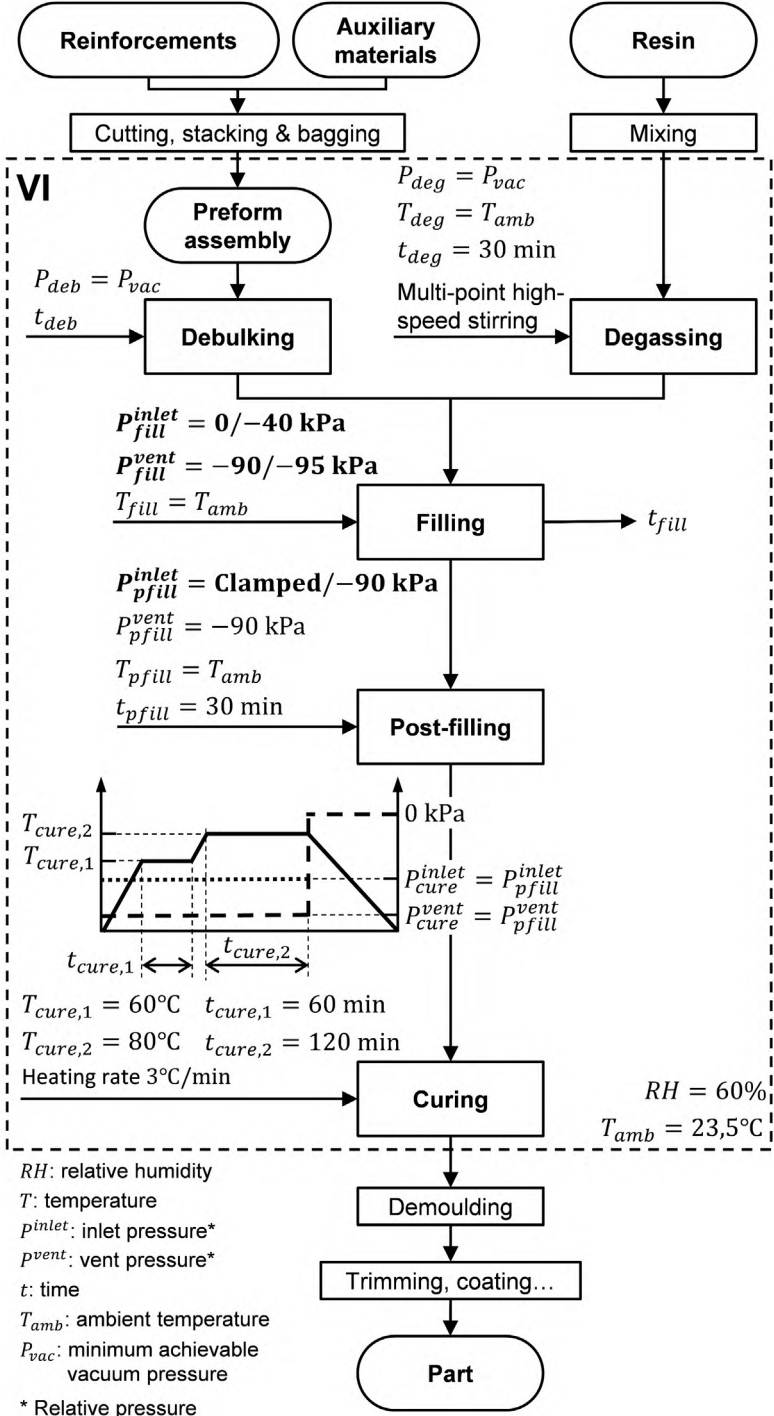


Figure 5.1. Flow chart and governing parameters of VI process.

Apart from the inlet state at curing, which was kept clamped or turned into vent depending on the defined post-filling conditions; debulking, degassing and curing steps remained unchanged along the experiments to avoid any interference on fibre and void contents.

Degassing was carried out at $P_{deg} = -98 \pm 0,5$ kPa for 30 min, being the nominal ultimate pressure able to be held by the vacuum pump 0,1 kPa (absolute pressure). Degassing was assisted by a multi-position magnetic stirrer (four magnetic rods of diameter 8 mm and length 40 mm) at 700 ± 25 rpm (Figure 5.2), system developed from the work presented in Chapter 4.

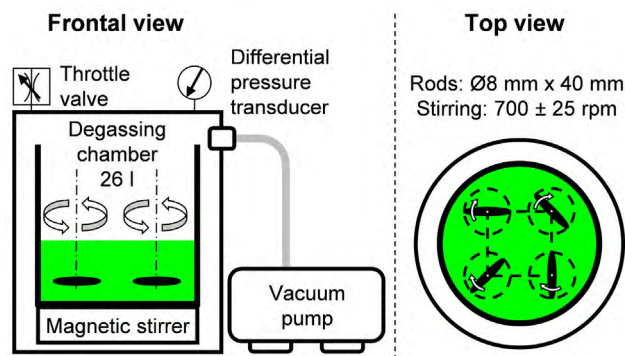


Figure 5.2. Vacuum degassing equipment.

The debulking step consisted on a single loading cycle to the minimum achievable vacuum pressure, P_{deb} . Vacuum was applied for $t_{deb} > 75$ min, considerably longer than time required to fibre settling occur (< 30 min for preforms later introduced). Therefore, it was not expected any effect on v_f due to deviations from target debulking conditions.

Finally, a two-step cure cycle was followed in which resin gelation occurred at $T_{cure,1} = 60^\circ\text{C}$ and the final crosslinking took place at $T_{cure,2} = 80^\circ\text{C}$. It was chosen a two-step cure cycle because it was noted that resin boiled-off at 80°C into the venting channels under the same P_{cure}^{vent} during manufacturing of the specimens presented in Chapter 4.

(IV) As previously mentioned, two preform assembly configurations were used in the experiments (Figure 5.3), referred from now on as “VI assembly” and “ISFLIP assembly”. In both assembly configurations, a HPDM was placed over the preform to force resin flow through preform thickness (direction y). Release film was used in ISFLIP assemblies instead of the peel-ply used in VI assemblies, including the upper release film a staggered pattern of perforations ($\varnothing 0,4$ mm at 3 mm and staggered 60°) to allow resin pass-through.

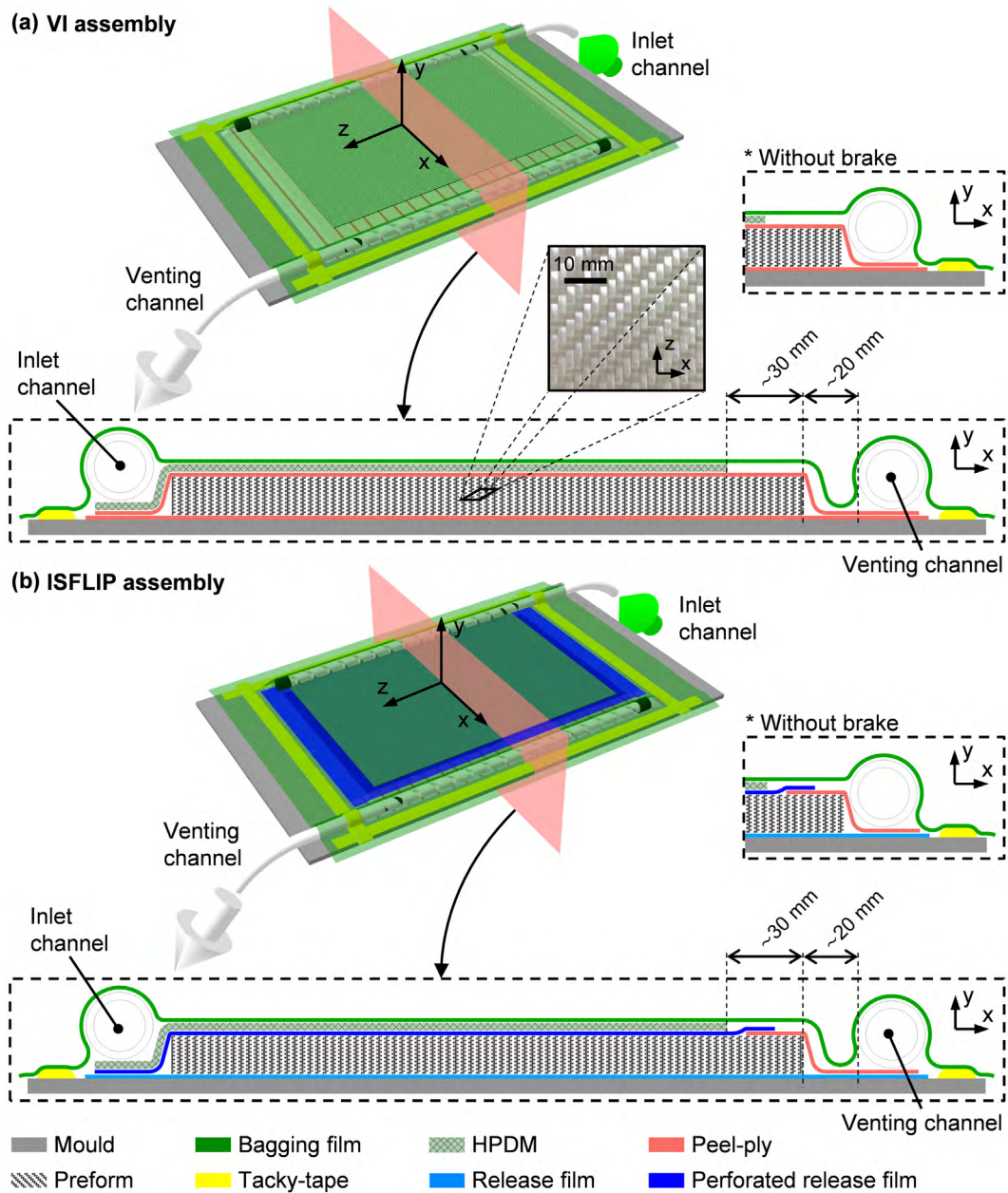


Figure 5.3. Preform assemblies (schematic dimensions are only representative).

The presence of a perforated layer involves a change in flow conditions. Each perforation works as an independent point source of resin which initially includes in-plane (directions x and z) and through-thickness (direction y) resin flow components [301], until flow fronts created at different source points converge to form one only flow front which advances through the preform thickness (direction y).

Importance of flow direction through preforms cannot be underestimated, since considerable difference between in-plane and through-thickness permeability might significantly affect void formation due to resin flow through a dual-scale porous medium. Besides, some authors have reported the formation of a discontinuous flow front in the mould surface, caused by the

incomplete convergence of multi-point flows, which lead to dry spots in manufactured specimens [302,303].

In those specimens in which inlet was clamped after filling the preform, no separation was allowed between channels and preform edges to avoid unnecessary flow resistance, that would slow down pressure and thickness equalization during the post-filling and may cause an increment in P_{cure}^{vent} into the preform. However, in specimens in which inlet was turned into vent, venting channels were connected to preform edges by a ≈ 20 mm peel-ply layer, avoiding air recirculation from vent to preform in those runs with $\Delta P_{fill \rightarrow pfill}^{vent} = 5$ kPa. Vent pressure was raised before turning the inlet into a vent. At reaching the peel-ply, the gradient of pressure governing resin advance quickly moves to the peel-ply due to its considerably lower permeability; hence, at increasing vent pressure, resin pressure into the preform is still higher and no air recirculation occurs [134,222].

Specimen were manufactured in the workbench described in Appendix B.

5.2. Materials and methods

5.2.1. Specimens

Constituent materials used in the experimentation were the E-Glass 2/2 Twill-Weave Fabric (GTWF) Angeloni VV 320 T (Table 4.1) and the epoxy system Sicomin SR 8100 (bisphenol A diglycidylether, DGEBA) – SD 8822 (isophorone diamin). This epoxy system exhibits low viscosity, 340-390 mPa·s, and a working time longer than 200 min at ambient temperature [295].

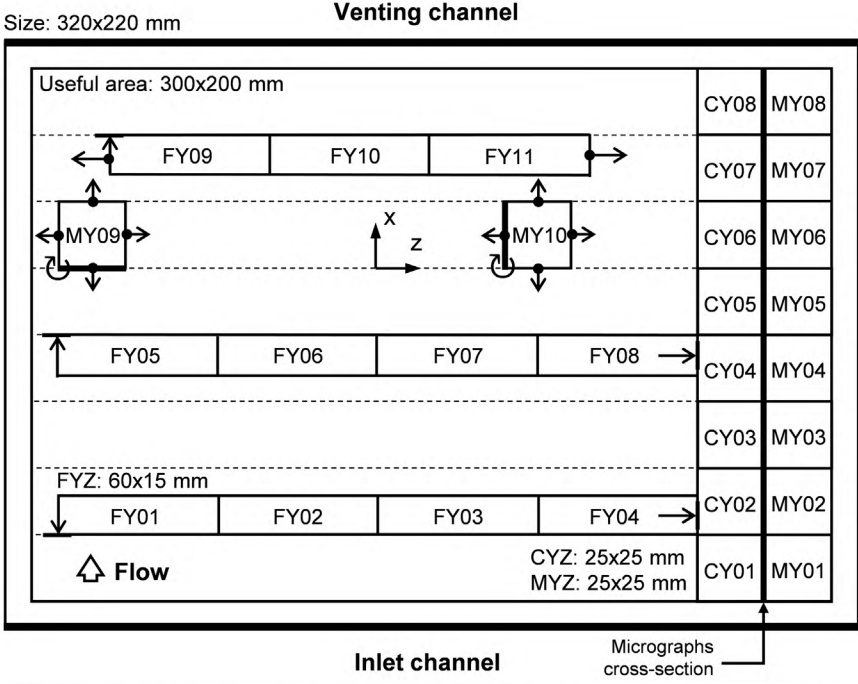
A total of 9 GTWF layers of 320x220 mm [(0/90)]₉ were stacked over a flat aluminum mould, resulting in orthotropic preforms. Due to the irregular free-edge thickness, specimens were trimmed to a useful area, S_{useful} , of 300x200 mm.

5.2.2. Test procedures

Specimen characterization was not limited to material-related attributes associated with fibre and void contents. Morphology and distribution of trapped pores and their effects on flexural response of the specimens were also studied in order to give a clear picture of the problem caused by trapped porosity.

Due to the random and heterogeneous porosity distribution, it was not possible to obtain a realistic quantitative measure per specimen of the characteristic void content with available means (loss on ignition method and light microscopy). Therefore, porosity was semi-quantitatively assessed by means of the specimen area containing voids.

A series of samples were systematically distributed in each specimen as shown in Figure 5.4: two rows of samples parallel to the flow direction through the HPDM (direction x) to measure constituent contents (CYZ) and pore morphology (MYZ), and a series of samples perpendicular to the flow direction (direction z) to capture flexural properties along specimens (FYZ). Rows of samples FYZ were placed according to the random appearance of porous areas, always aligned to the rectangular pattern defined in Figure 5.4. Besides, some samples MYZ had to be also placed in the region initially allocated to samples FYZ to capture all different porosity distributions.



Sample codification (1) Test: flexural test (F), loss on ignition method (C) or light microscopy (M).
 \overline{XYZ} (2) Specimen: A1, A2, A3, A4, B1, B1', B2, B3
 (1) (2) (3) (3) Sample number of test (1): 01, 02, 03...

Figure 5.4. Generic pattern of samples: size, distribution and codification rules.

More detailed descriptions of the testing procedures followed, as well as supplementary data to that provided later on the results section, can be consulted in Appendix D for visual inspection, loss on ignition and three-point flexure methods, and in Appendix E in case of light microscopy.

5.2.2.1. Visual inspection

The translucent nature of the GTWF-epoxy specimens allowed to identify specimen areas in which porosity was present. For each specimen, porous area fraction, s_0 , was computed as the ratio of porous area, S_0 , and specimen useful area, S_{useful} . The open-source image processing package Fiji, based on ImageJ, was used to scan top view pictures of the manufactured specimens.

5.2.2.2. Loss on ignition method

Samples coded as CYZ in Figure 5.4 were tested via the loss on ignition method according to the procedure stated in the standards UNE-EN ISO 1172:1999 and UNE-EN ISO 7822:2001 in order to determine v_f . It was not addressed the determination of v_0 due to the random and discontinuous distribution of porosity into the specimens, which, in most cases, covered only a volume considerably lower than the minimum sample volume of 2 cm³ recommended in the standard UNE-EN ISO 7822:2001.

Recalling the procedure followed in Chapter 4, constituent materials volume fractions were computed from the mass fractions and the volume sample, V_{sample} , as

$$v_f = \frac{m_f / \rho_f}{V_{sample}}, \quad v_r = \frac{m_r / \rho_r}{V_{sample}} \quad (14)$$

where m_f and m_r are the fibre and resin mass fractions, v_f and v_r are the fibre and resin volume fractions, and $\rho_f = 2544 \text{ kg/m}^3$ and $\rho_r = 1095 \text{ kg/m}^3$ are the fibre and resin densities [296].

Due to the texturized surface of specimens, V_{sample} was over-estimated, hence underestimating constituent contents. Since translucent specimens allowed to identify which samples contained trapped pores, those n samples with expectation of no porosity were used to compute an average surface void volume, \bar{V}_0^{surf} , as

$$\bar{V}_0^{surf} = \frac{1}{n} \sum (v_0 \cdot V_{sample}) \quad (16)$$

where

$$v_0 = 1 - v_f - v_r \quad (15)$$

Then, updated fibre volume fraction, v_f' , was calculated considering volume adjustment such that

$$v_f' = \frac{m_f / \rho_f}{V_{sample} - \bar{V}_0^{surf}} \quad (28)$$

5.2.2.3. Light microscopy

Samples coded as MYZ in Figure 5.4 were used to characterize void morphology through digital image processing, although void content of analysed samples was also measured. Micrographs were taken from cross-sections underlined in Figure 5.4. Preparation of micrographic samples and microscopy analysis were identical to those followed in Chapter 4.

Micrographic samples were casted in polyester resin round micrographic specimens, grinded with diamond discs and finally polished in two steps, with a two-in-one suspension of 6 μm diamond and lubricant, and with a silica suspension. A number of fourteen to sixteen micrographs per sample were taken at 50X magnification and stitched to get a picture covering the full sample length. The open-source image processing package Fiji, based on ImageJ, was used to process the micrographs.

Total void content, a_0 , intra-tow void content, a_0^{intra} , and inter-tow void content, a_0^{inter} , were calculated in the set of stitched micrographs as the ratio of the area occupied by all voids of each void type, A_0 , A_0^{intra} and A_0^{inter} respectively, and the area occupied by the sample, A_{sample} , as

$$a_0 = \frac{\sum A_0}{A_{sample}}, \quad a_0^{intra} = \frac{\sum A_0^{intra}}{A_{sample}}, \quad a_0^{inter} = \frac{\sum A_0^{inter}}{A_{sample}} \quad (19)$$

Additionally, Feret's diameter, Φ_{Feret} (maximum distance between any two points belonging to a pore), Feret's angle, φ_{Feret} (angle formed by the Feret's diameter and the horizontal axis), and aspect ratio, AR , were also computed for all the voids belonging to each sample. AR was defined as the ratio of the two second moments of a pore around its principal axes, i_1 and i_2 (AR of a circle and a square is 1) such that

$$AR = \frac{i_1}{i_2} \leq 1 \quad (20)$$

5.2.2.4. Three-point flexure test

Flexural properties of samples coded as FYZ in Figure 5.4 were obtained through a three-point flexure test according to the procedure stated in the standard UNE-EN ISO 14125:1999.

Recalling the procedure followed in Chapter 4, flexure stress, σ_f , vs. strain, ε_f , response was calculated from the crosshead load, F , and deflection at the mid-point, s , by applying corrections due to large deflections; since final deflection was larger than 10% of the span between supports, l' :

$$\sigma_f = \frac{3Fl'}{2wh^2} \left\{ 1 + \left(\frac{s}{l'}\right)^2 - 3 \left(\frac{sh}{l'^2}\right) \right\} \quad (21)$$

$$\varepsilon_f = \frac{h}{l'} \left\{ 6,00 \frac{s}{l'} - 24,37 \left(\frac{s}{l'}\right)^3 + 62,17 \left(\frac{s}{l'}\right)^5 \right\} \quad (22)$$

where w and s are sample width and thickness, respectively.

Flexural strength, σ_{fM} , is determined as the flexural stress sustained by the sample at the maximum load. Flexural modulus, E_f , was estimated by applying a linear regression procedure to the curve σ_f vs. ε_f between $\varepsilon_f = 0,010$ and $\varepsilon_f = 0,014$, a section of the response curve in which slope kept stable after an initial instability that might have been caused by backlash in the spindles of the testing machine or by initial settling of the samples between the round supports. Samples were tested at 1 mm/min.

5.2.3. Factorial designs

Design Of Experiments (DOE) plays a major role in engineering design activities. Factorial designs are more efficient than one-factor-at-a-time experiments and allow the effect of a factor to be estimated at several levels of the other factors, yielding conclusions that are valid over a range of experimental conditions. Two-level factorial designs are often used in screening experiments of process parameters in order to optimize a specific quality attribute, an early stage of the optimization experiment which is usually followed by successive stages that provide more precise results [304].

Designs were kept as simple as possible while satisfying the required level of scientific soundness. Effects on specimen quality attributes of different filling and post-filling pressure conditions, and preform assemblies were addressed through two simple two-level factorial designs, 2^2 . A total of four design factors were analysed (Table 5.1): pressure increment (P), gradient of pressure (G), preform assembly (A) and inlet condition (I).

In the first set of runs, four ISFLIP assembly-like specimens were manufactured in order to screen the effects of factors P and G in a manufacturing scenario in which resin inlet was turned

into vent after the filling step. Factor levels were arranged in a 2^2 factorial design as mentioned (Table 5.2).

Table 5.1. Design factors of the screening experiment of filling and post-filling conditions.

Factor	Level* ¹		Details	Motivation
	High (+)	Low (-)		
Pressure increment (P)	5 kPa	0 kPa	Between filling and post-filling steps	Enhancing air dissolution capacity and bubble collapse
Gradient of pressure (G)	Full	Reduced	Gradient of pressure is reduced by setting $p_{fill}^{inlet} = -40 \text{ kPa}^{*2}$	Altering void formation due to resin flow through dual-scale porous medium
Preform assembly (A)	ISFLIP	VI	Figure 5.3	Comparing conventional VI processing conditions
Inlet condition (I)	Turned into vent	Clamped	From post-filling onwards	

*¹ In regression models, high and low levels were considered +1 and -1, respectively.

*² Relative pressure.

Table 5.2. The 2^2 factorial design applied to the first stage of the screening experiment of filling and post-filling conditions.

Specimen	Run order	P	G	Treatment
A1	3	-	-	(1)
A2	2	+	-	p
A3	4	-	+	g
A4	1	+	+	pg

A combination of factor levels (P and G) was chosen from the first screening experiment according to the best performance of the analysed response variables and used in a second round of experimentation, in which the effects of factors A and I were considered. The arrangement of factor levels in this second set of runs is depicted in Table 5.3.

Table 5.3. The 2^2 factorial design applied to the second stage of the screening experiment of filling and post-filling conditions.

Specimen	Run order	P	G	Treatment
B1	3	-	-	(1)
B2	1	+	-	a
B3	4	-	+	i
B4*	2	+	+	ai

* It corresponds to the chosen experiment from previous factorial design (Table 5.2).

In specimens in which preform was clamped after preform filling (B1 and B2), a full gradient of pressure was applied to carry out preform impregnation, $\Delta P_{fill}^{inlet \rightarrow vent} = -90$ kPa, and no pressure increment between filling and post-filling steps was forced, $\Delta P_{fill \rightarrow pfill}^{vent} = 0$ kPa. These practices fit in with conventional VI manufacturing conditions. On the other hand, filling and post-filling pressure conditions of specimen B3 were determined according to the combination of levels chosen from the first factorial design (specimen B4). It is worth noting that the design factors of the first screening experiment became held-constant factors in the second one, and *vice versa*.

Specimen quality may be characterized by different quality attributes associated with fibre and void contents, but only attributes which showed an evident variation between specimens were taken as response variables of the factorial design. This variation was assessed by the coefficient of variation (or relative standard deviation), defined as the ratio between the standard deviation and the mean response. Significance of factor or interaction effects on response variables was addressed through a conventional Analysis of Variance (ANOVA).

Apart from the design factors considered in the factorial designs (P, G, A and I) and the held-constant factors set in Figure 5.1, a set of nuisance factors (RH , T_{deg} , T_{fill} and T_{pfill}) and allow-to-vary factors (P_{deb} , t_{deb} , P_{deg} and $t_{0 \rightarrow fill}$) that might affect the response variables were identified. These factors may be treated as covariates and analysed through a variation of the ANOVA, an Analysis of Covariance (ANCOVA) [298]. Special attention was kept on time elapsed from resin mixing until the onset of the filling stage, $t_{0 \rightarrow fill}$; since polymerization time may affect resin viscosity, μ , and, thus, flow through the preforms.

Since factorial designs were initially saturated (no available degree of freedom to compute error variance), effect significance was firstly qualitatively evaluated through a half-normal probability plot of the effects. The largest effects which did not lie along the normal straight line were considered good candidates to include in the later ANOVA. Backward elimination was then performed to sequentially remove any factor or interaction from models with a significance level $p > 0,10$ ($\equiv 10\%$); although, effect significance was actually set at $p \leq 0,05$ ($\equiv 5\%$).

Statistical analyses were performed with Minitab Statistical Software.

5.3. Results

A total of eight specimens were manufactured: seven specimens defined in the previous section, and a replica of specimen B1 which was referred as B1'. This new specimen was manufactured to provide enough experimental data for analysing VI assembly-like specimens.

5.3.1. Porous area fraction

Specimen porosity was classified according to its macroscopic aspect of pore distribution (Figure 5.5), discerning between three different Porous Area Types (PAT): scattered porosity (PAT I), isolated pore clusters (PAT II) and large pore clusters (PAT III). The manufactured specimens are shown in Figure 5.6, as well as the corresponding PAT fractions. Fractions of each PAT, s_0^i , were calculated as the ratio between the porous area corresponding to each type, S_0^i , and the specimen useful area, S_{useful} , such that

$$s_0^i = \frac{S_0^i}{S_{useful}}, \quad i = I, II, III \tag{29}$$

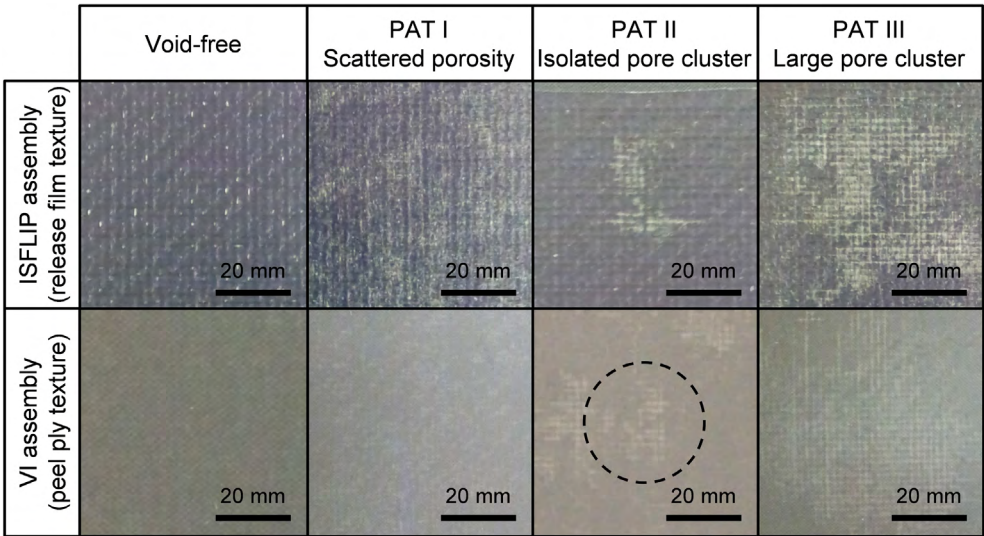


Figure 5.5. Detail views of each Porous Area Type (PAT).

Scattered porosity, PAT I, was only present in specimens A1 and B1'. Besides, it is worth noting that PAT II and III were mainly concentrated in specimen halves which were closer to the venting channels.

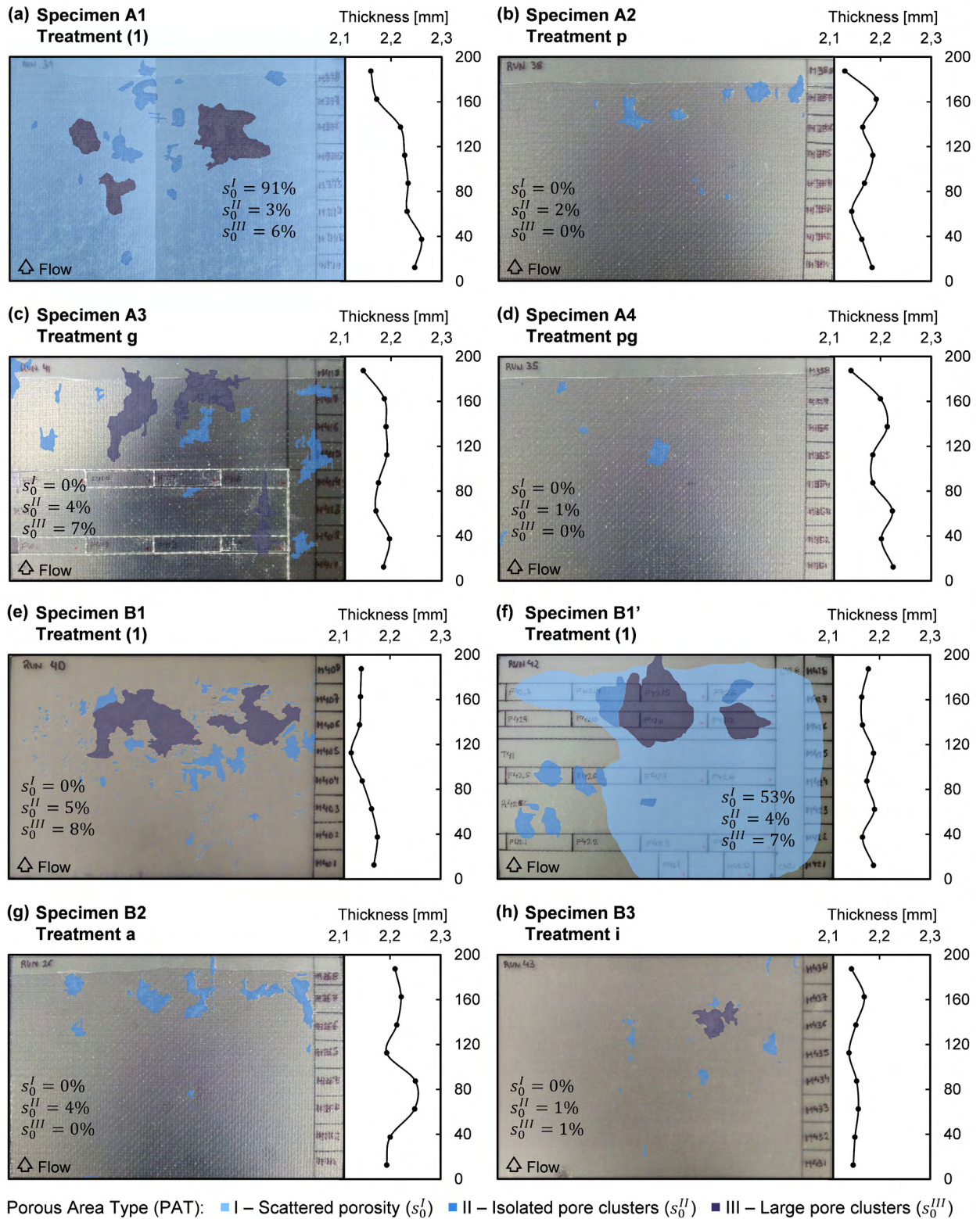


Figure 5.6. Manufactured specimens: porous area fraction, s_0 , according to each Porous Area Type (PAT), and thickness measured at samples MYZ.

5.3.2. Fibre volume fraction

In Figure 5.7, it is depicted the results of the loss on ignition method for v_f' . No general trend was observed in v_f' between samples into each specimen. However, specimens A1, A4 and B2, all

corresponding to ISFLIP assembly-like specimens, showed appreciable lower average fibre volume fraction per specimen, \bar{v}'_f , than the rest. This trend is also noticeable in the measured thickness of samples MYZ shown in Figure 5.6.

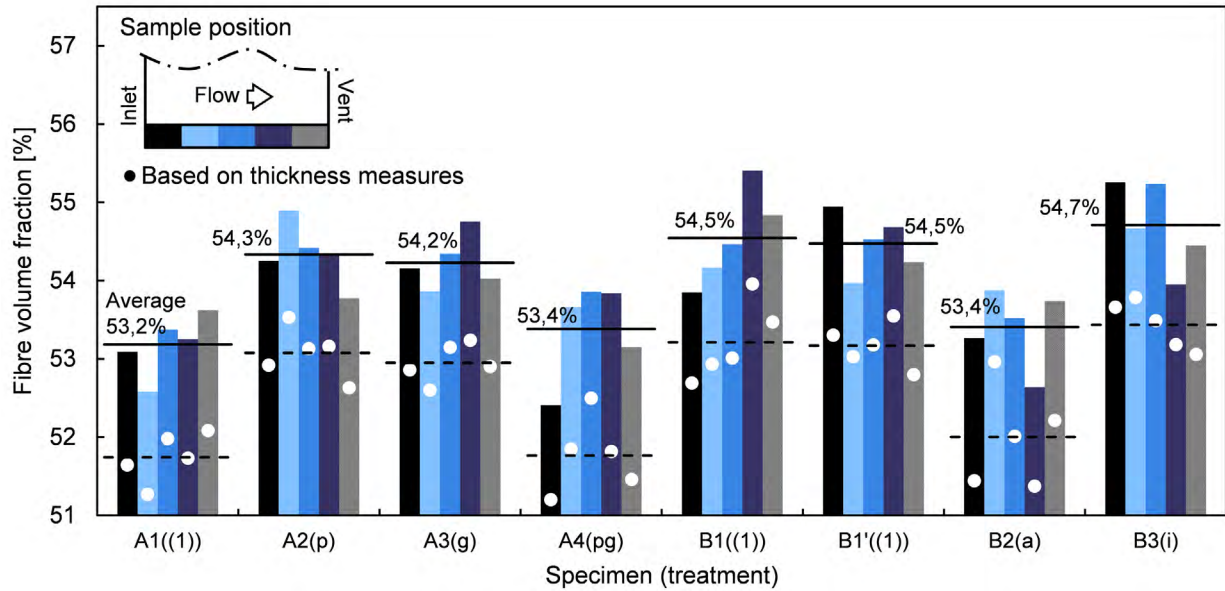


Figure 5.7. Fibre volume fraction, v'_f , obtained through the loss on ignition method (bars), and estimated fibre volume fraction from thickness measures, v_f^h (dots).

Texture corrections involved the determination of average surface void volumes $\bar{V}_0^{surf} = 69 \text{ mm}^3$ for ISFLIP assembly-like and $\bar{V}_0^{surf} = 66 \text{ mm}^3$ for VI assembly-like samples, equivalent in both cases to a reduction in effective sample thickness of 0,11 mm. It is worth noting that, despite the similar \bar{V}_0^{surf} of both assemblies, surface textures were completely different as will be pointed out in the next section. When estimating fibre volume fraction through thickness measures, v_f^h , over-estimation of h due to surface texture involved the underestimation of the results computed through Equation (24), as can be seen in Figure 5.7. Nevertheless, h could still be used as a good estimator of v'_f through a linear model adjusted with the experimental data:

$$\hat{v}'_f [\%] = 9,3 + \frac{98,0}{h[\text{mm}]}, \quad R^2 = 86,5\% \quad \text{for ISFILP assemblies} \quad (30)$$

$$\hat{v}'_f [\%] = -3,9 + \frac{126,6}{h[\text{mm}]}, \quad R^2 = 67,6\% \quad \text{for VI assemblies} \quad (31)$$

5.3.3. Void size, shape and spatial distribution

Samples MYZ were distributed among the specimens to capture void features into each PAT. Since inter-tow voids were considerably larger than intra-tow voids and in order to automate their identification, a void area of $A_0 = 3000 \mu\text{m}^2$ was set as the boundary between both void types.

Characteristic micrographs of each PAT are shown in Figure 5.8. Most of void content corresponded to inter-tow voids; even in samples PAT I, in which intra-tow void occurrence was considerably higher than inter-tow's. This fact is reflected in Figure 5.9.a, in which intra-tow and inter-tow void area fractions, a_0^{intra} and a_0^{inter} , were computed for a series of samples belonging to each PAT. Some problems arose at computing a_0^{intra} due to the occasional detachment of fibres parallel to the analysed cross-sections during grinding, making difficult to discern between intra-tow voids and prints of detached fibres.

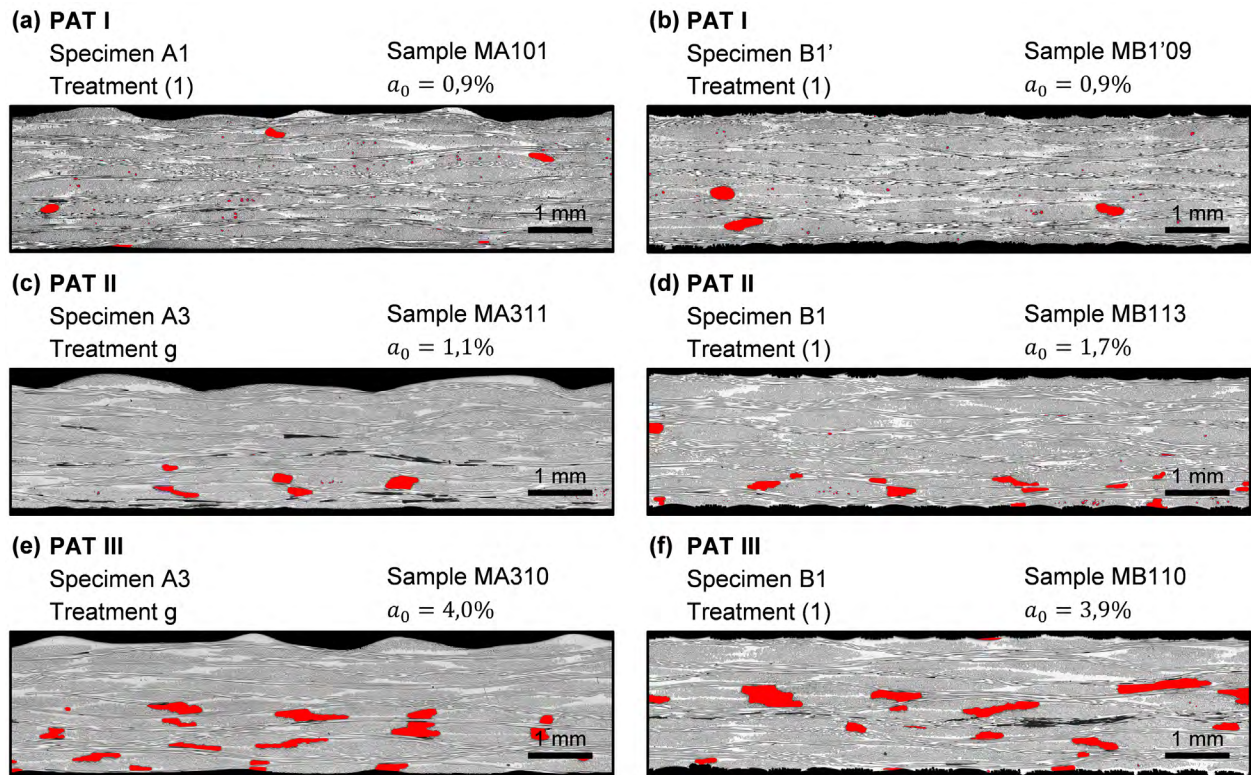


Figure 5.8. Detail views of micrographic samples for each Porous Area Type (PAT), and void area fraction, a_0 , of the corresponding whole sample (not only the partial cross-section depicted).

The heterogeneous distribution of porosity into the laminates involved a considerable variability between captured cross-sections. In samples PAT I, it was even difficult to capture a cross-section with significant void content. In samples PAT II and III, it was noticed that inter-tow voids accumulated in the lower sample half, on the opposite side in which HPDM was placed. The largest voids were found in samples corresponding to PAT III, while inter-tow voids in PAT II were

slightly larger than in PAT I. The main difference between pores in samples PAT I and II was pore concentration, larger in PAT II; although it was not as severe as in case of samples PAT III, resulting in a large increment in a_0 . It is worth noting that it is depicted the results of those samples PAT I which contained significant void content; that is why a_0 is similar in samples PAT I and II shown in Figure 5.9.a.

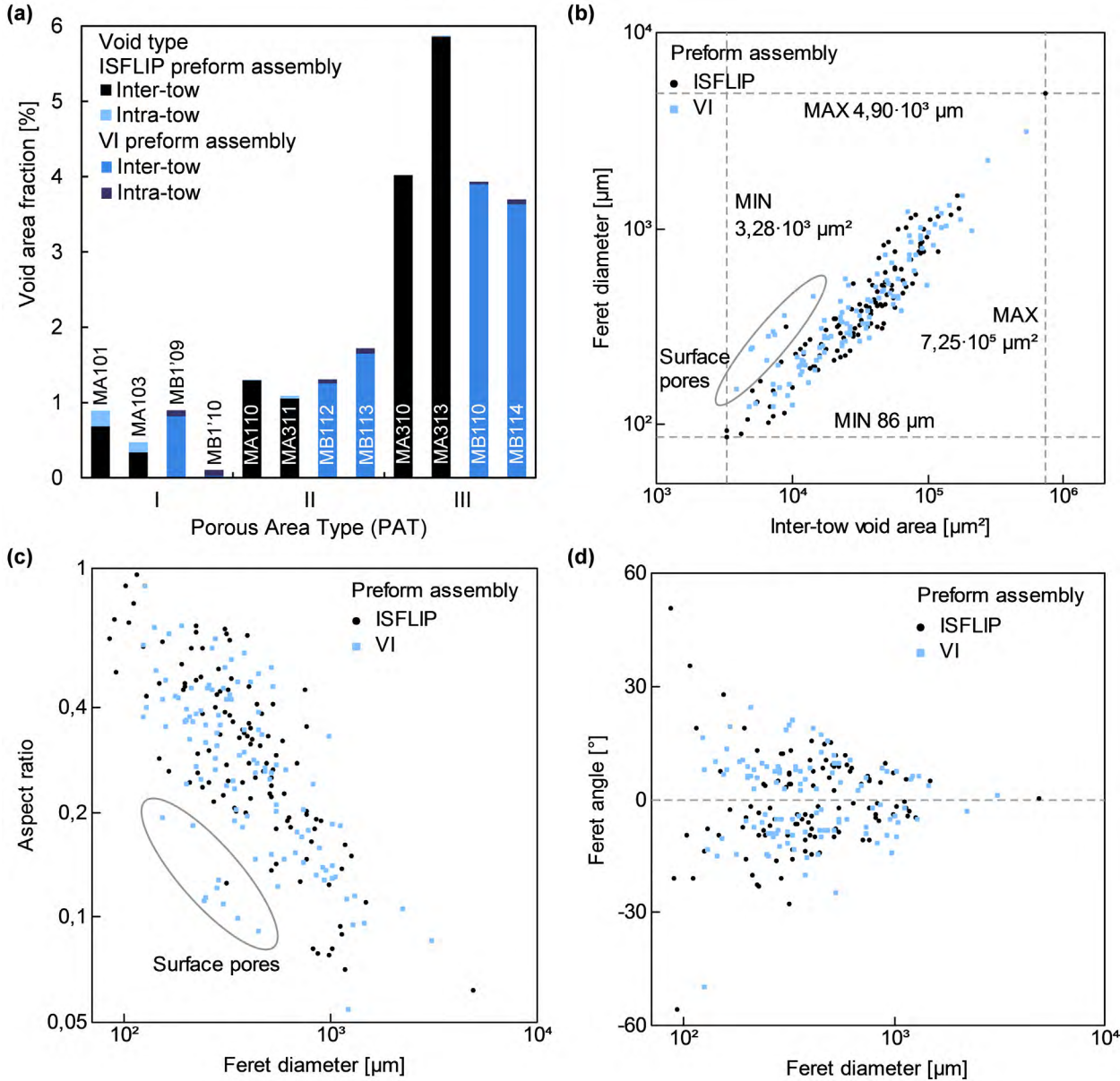


Figure 5.9. (a) Total content (void area fraction, a_0) of inter-tow and intra-tow voids, and (b-d) shape descriptors of inter-tow voids (inter-tow void area, A_0^{inter} ; Feret's diameter, ϕ_{Feret} ; Feret's angle, φ_{Feret} ; and aspect ratio, AR).

Furthermore, differences between each surface texture are clearly observable. In case of VI assembly-like specimens, peel-ply transfer their fabric architecture to the specimen surfaces; while, in case ISFLIP assembly-like specimens, release films transfer the HPDM and mould surface textures to the top and bottom faces, respectively.

Once the results of the different micrographic samples were gathered together, and the size and shape descriptors of inter-two voids analysed in more depth, significant linear correlations appeared between the log transformations of Feret's diameter, Φ_{Feret} , inter-tow void area, A_0^{inter} , and aspect ratio, AR , as shown in Figure 5.9.b and Figure 5.9.c. Besides, inter-tow voids orientation tended to 0° as Φ_{Feret} increased (Figure 5.9.d). It is worth noting that inter-tow voids formed between GTWF layers, and their size and shape seems to be connected as mentioned in Chapter 4 to fabric architecture and local nesting between layers.

5.3.4. Flexure response

In Figure 5.10, it is depicted both flexural strength, σ_{fM} , and modulus, E_f , with respect to \hat{v}'_f , estimated through Equations (30) and (31), and the PAT to which the testing region of the sample belonged. Samples FYZ were randomly tested upwards (compressive face corresponded to the HPDM face) and downwards (compressive face corresponded to the mould face) and at least eight samples per specimen (four upwards and four downwards) were tested in case of void-free samples and samples PAT I. Testing orientation helped to analyse the effect of inter-tow void accumulation near the lower specimen surface (mould face).

Although both σ_{fM} and E_f should depend on \hat{v}'_f , due to the reduced variation of \hat{v}'_f along samples, experimental variability was large in comparison with the slight increment on both flexural properties observed as \hat{v}'_f increased. Two linear models were fitted with the experimental data to estimate σ_{fM} and E_f from \hat{v}'_f in void-free samples:

$$\hat{\sigma}_{fM}[\text{MPa}] = -276 + 15,4 \cdot \hat{v}'_f[\%], \quad R^2 = 10,5\% \quad (32)$$

$$\hat{E}_f[\text{GPa}] = -12,0 + 0,576 \cdot \hat{v}'_f[\%], \quad R^2 = 38,1\% \quad (33)$$

In spite of different surface textures, in case of void-free samples, ISFLIP assembly-like and VI assembly-like specimens exhibited similar flexural behaviours. Difference in σ_{fM} was 11 MPa, and, in case of E_f , the difference was lower than 0,1 GPa.

The experimental variability was also large at representing both flexural properties vs. PAT; however, in Figure 5.10.b, it can be seen a continuous reduction in σ_{fM} when samples were tested downwards. Since compressive behavior is more severely affected by porosity than tensile behaviour, when pores were located close to the compressive face of the samples, a significant

detriment on σ_{fM} occurred. The predominant failure mode in tested samples was compressive fracture.

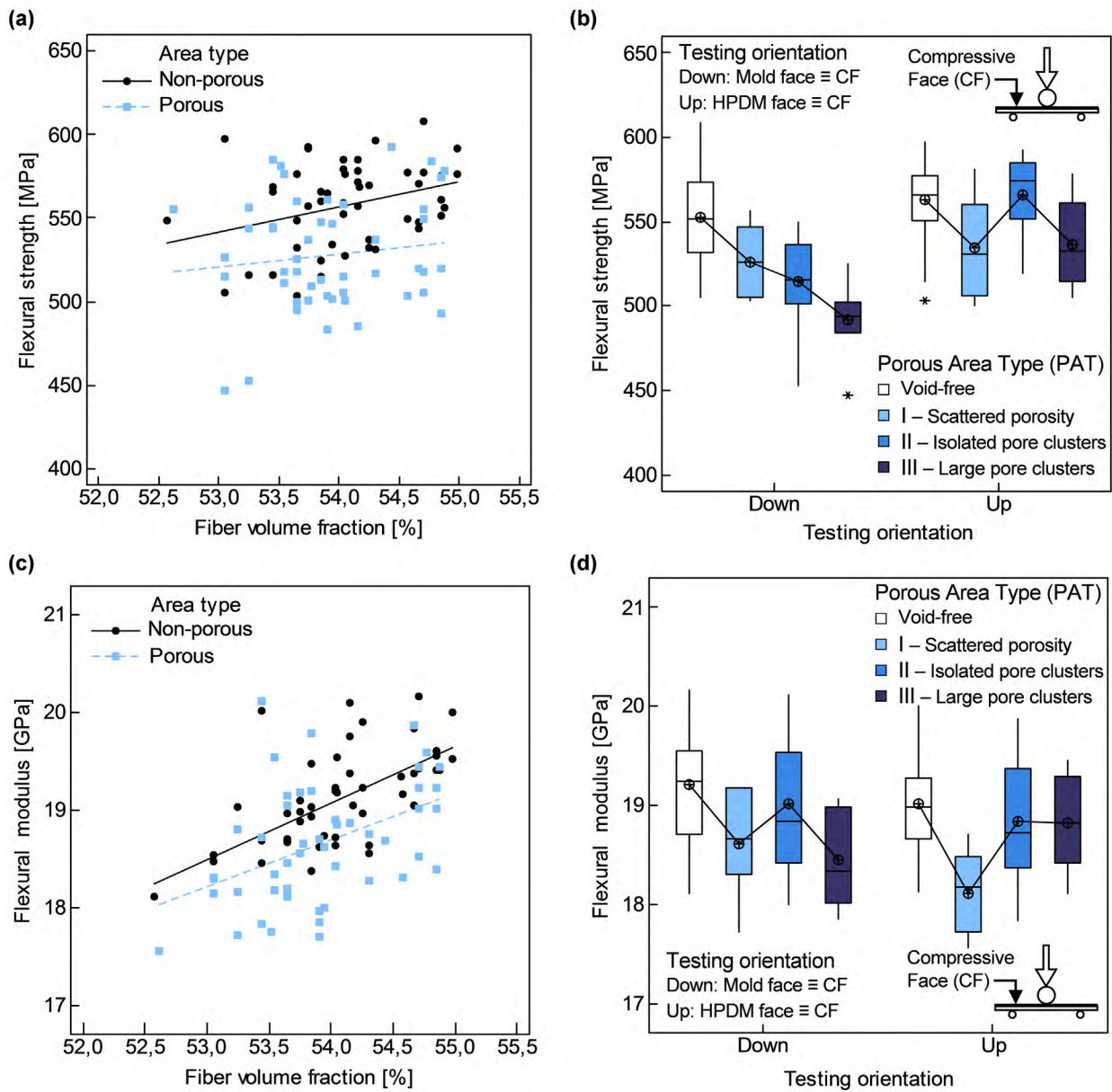


Figure 5.10. Flexural properties vs. estimated fibre volume fraction, \hat{v}_f' , Porous Area Type (PAT) and testing orientation: (a-b) flexural strength, σ_{fM} , and (c-d) flexural modulus, E_f .

No special trend was observed between E_f and PAT of tested samples; although, low E_f values obtained in three of the samples tested upwards of specimen B1' caused a considerable reduction of E_f in samples PAT I as can be seen in Figure 5.10.d.

In order to find if any level of the interaction between PAT and testing orientation was really causing a significant detriment on flexural performance, the Tukey's multiple comparison test was applied [305]. Tukey's method tests all pairwise mean comparisons, each interaction level mean

is compared against each other, accounting for the scatter of all the data to define a confidence interval to each difference of means. If the confidence interval includes the value zero, it is considered that the difference of means is not significant; otherwise, the difference is significant.

In the performed Tukey’s test, with a confidence level of 95% for the whole test (not for each pairwise comparison), only samples of PAT II and III tested downwards showed a significant difference in σ_{fM} with both void-free samples tested upwards and downwards as can be seen in Figure 5.11.a. In Figure 5.11.b, it is also depicted that samples of PAT I and III, tested upwards and downwards respectively, showed a significance difference in E_f with respect to void-free samples tested downwards, but not with respect to void-free samples tested upwards. Therefore, it should not be concluded that any of these PATs were causing any detrimental effect on E_f . In all the confidence intervals showed in Figure 5.11, effects of \hat{v}'_f were also included in the calculations.

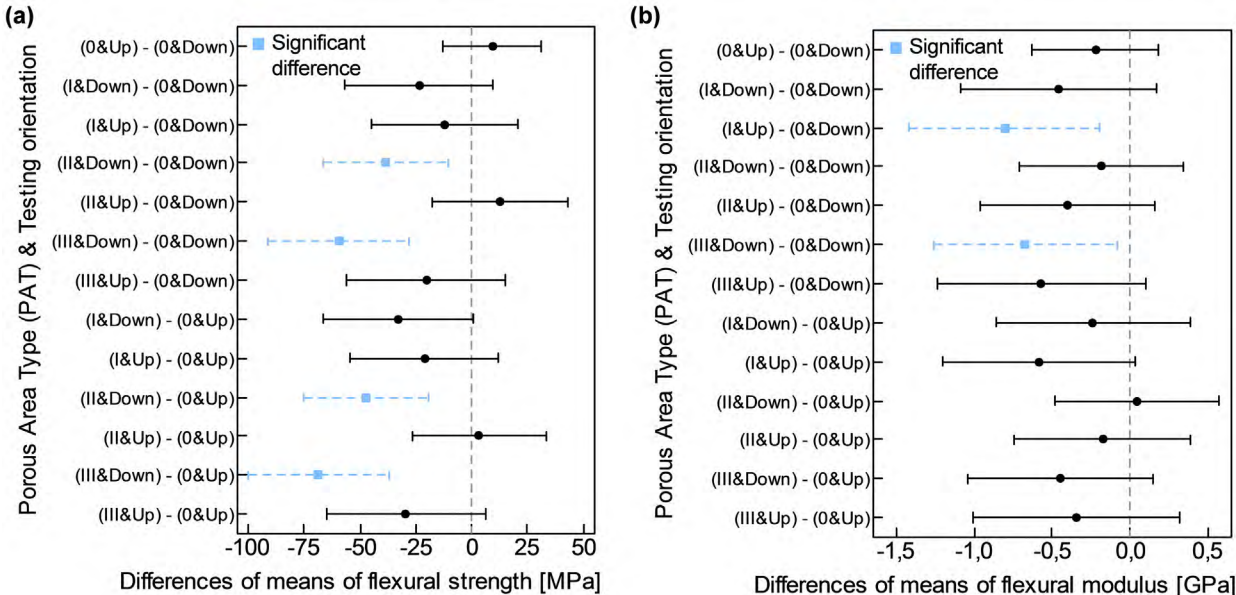


Figure 5.11. Interval plots of Tukey’s test (overall confidence level 95% and individual confidence level 99,7%): (a) flexural strength, σ_{fM} , and (b) flexural modulus, E_f .

As a summary, samples of PAT II and III tested downwards showed a mean flexural strength of $\bar{\sigma}_{fM} = 504$ MPa ($\bar{v}'_f = 54,0\%$), while in the remaining samples $\bar{\sigma}_{fM} = 552$ MPa ($\bar{v}'_f = 54,0\%$). A drop of in flexural strength of 8,7% occurred. On the other hand, the mean flexural modulus was $\bar{E}_f = 18,9$ GPa ($\bar{v}'_f = 54,0\%$).

See Appendix F for further detail on statistical analysis of the flexural results presented in this section.

5.3.5. Screening of filling and post-filling conditions

Among the coefficients of variation shown in Figure 5.12, those corresponding to porous area fraction stood out from the rest of analysed quality attributes, and the nuisance and allow-to-vary factors taken as covariates. In case of fibre volume fraction, v_f' , although three specimens (A1, A4 and B2) presented lower values, the difference between the specimen with the highest \bar{v}_f' (B3) and the specimen with the lowest \bar{v}_f' (A1) was only 1,5%. This variation was too small to be considered in the set of screening experiments proposed in the present analysis.

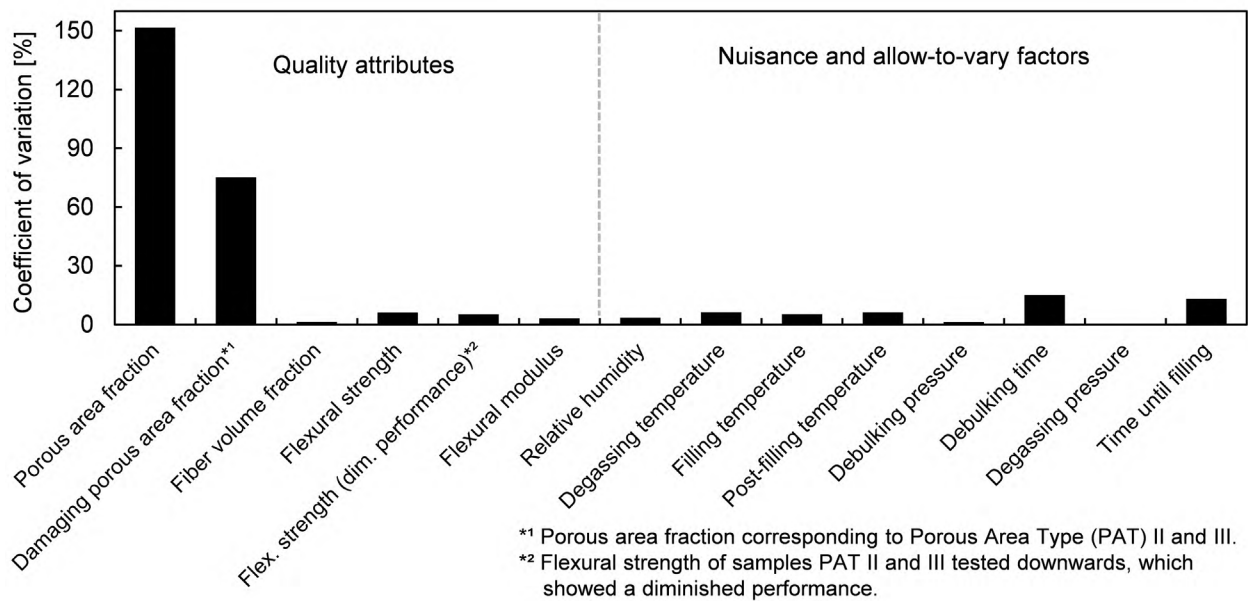


Figure 5.12. Coefficients of variation of measured quality attributes, and monitored nuisance and allow-to-vary factors.

The influence of the two specimens which contained PAT I (A1 and B1') was enormous at addressing the analysis of the whole porous area fraction, s_0 ; since s_0^I in those two specimens was considerably larger than s_0^{II+III} in the rest of specimens. Furthermore, although manufacturing conditions of specimen B1 and B1' were identical; PAT I only appeared in specimen B1', while sums of PAT II and III were similar in both specimens. No relation was noticed between PAT I and any design factor or covariate, and the real cause behind the appearance of PAT I remained unclear. Certainly, the only factor level at which it did not appeared was at high level of factor P ($\Delta P_{fill \rightarrow pfill}^{vent} = 5$ kPa).

Finally, the proposed factorial designs were analysed with respect to the porous area fraction which negatively affected flexure performance, s_0^{II+III} . Variability of s_0^{II+III} was still considerably larger than the rest of quality attributes and covariates (Figure 5.12). Besides, no apparent

correlation arose at confronting s_0^{II+III} versus any covariate; therefore, the analyses were focused only on the design factors, without considering any covariate.

The input data of the first stage of the screening experiment is shown in Figure 5.13.a. In Figure 5.13.b, it can be seen the effects of main factors P (pressure increment) and G (gradient of pressure), and its interaction. The magnitude of the effect of factor P, l_P , was considerably larger. Pressure increment between filling and post-filling steps apparently showed a positive effect on porous content, s_0^{II+III} decreased. In the half-normal probability plot of effects (Figure 5.13.c), l_P arose as a good candidate to be included in a single factor ANOVA, which is depicted in Table 5.4. It is worth emphasizing that the initially saturated factorial design became a fully replicated design. The ANOVA proved the significance of factor P ($p = 0,012 < 0,05$) and the later analysis of residuals did not show any abnormal behaviour.

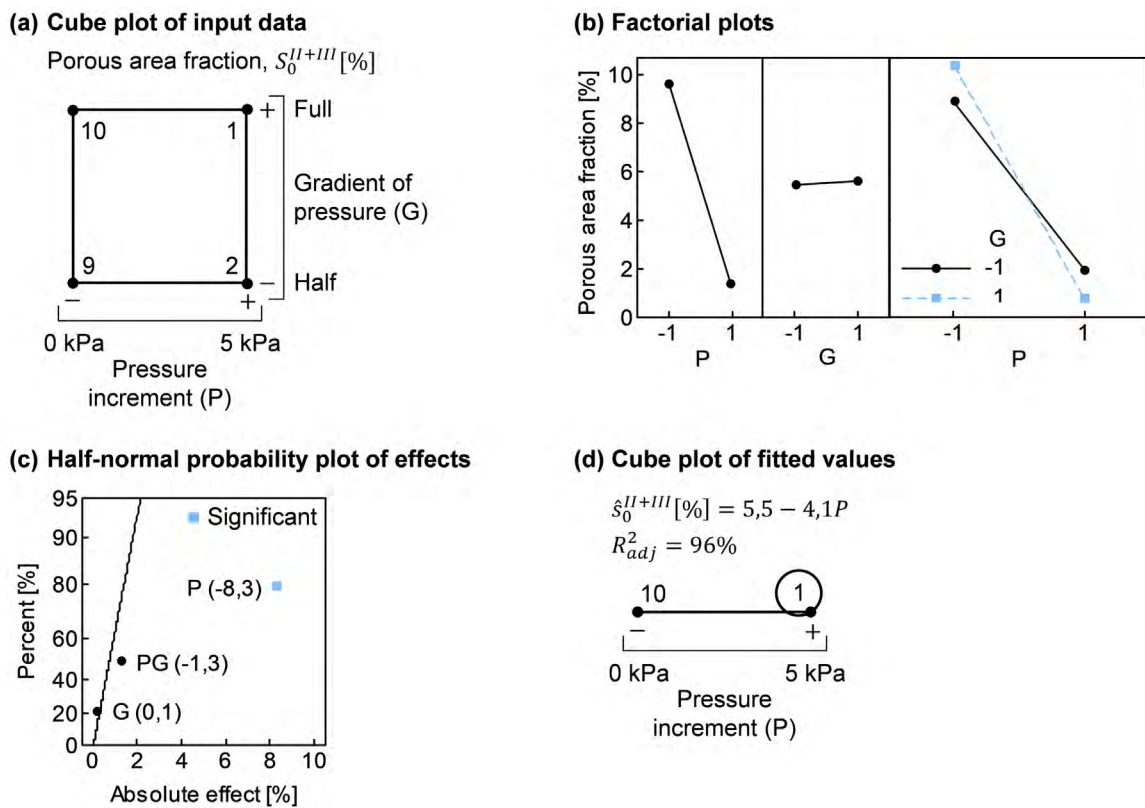


Figure 5.13. Plots of the statistical analysis of the first stage of the screening experiment of filling and post-filling conditions.

Since P was the only really significant factor affecting the response variable and s_0^{II+III} was minimized at high level of P (Figure 5.13.d); manufacturing conditions of specimen A4 were chosen for expanding the set of experiments to analyse the effects of factors A (preform assembly) and I (inlet condition after filling). It was preferred the manufacturing conditions of specimen A4 over A2 because of its shorter filling time ($t_{fill} = 114$ s in specimen A4 and $t_{fill} = 232$ s in

specimen A2), which came from the application of a full gradient of pressure. In bigger size real applications, in which involved t_{fill} is considerable longer, time savings of this magnitude may be crucial; although resin consumption is also higher due to more pronounced preform relaxation.

Table 5.4. ANOVA tables for analysis of porous area fraction, s_0^{II+III} [%], including Sum of Squares (SS); Degrees of Freedom (DF); Mean Squares (MS); F-statistic, F_0 , associated to each term; and level of significance, p , associated to each F-statistic.

Source	SS	DF	MS	F_0	p
First stage				$R_{adj}^2 = 96\%$	
P	68,7	1	68,7	80,4	0,012
Error	1,7	2	0,9		
Total	70,4	3			
Second stage				$R_{adj}^2 = 98\%$	
A	28,0	1	28,0	60,3	0,016
I	54,2	1	54,2	117	0,008
AI	21,2	1	21,2	45,8	0,021
Error	0,9	2	0,5		
Total	143,9	5			

* Adjusted coefficient of determination, R_{adj}^2 , is appropriate when available DF to compute error variance is small.

In the second set of runs, apart from the specimens initially manufactured for this purpose B1, B2, B3 and A4 (which would correspond to B4), specimens B1' (replica of B1) and A2 (replica of A4) were also considered in the analysis to gain some degrees of freedom to compute experimental variability. Specimen A2 could be included as a replica of A4 because only factor P significantly affected s_0^{II+III} in the previous stage of the screening experiment. The initially saturated factorial design became an unsaturated and unbalanced factorial design (partially replicated).

The input data of the second stage of the screening experiment is shown in Figure 5.14.a. In this case, the magnitude of the effects of both main factors and its interactions were comparable (Figure 5.14.b). In the half-normal probability plot of effects (Figure 5.14.c), all three effects arose as candidates to be included in the ANOVA, which is depicted in Table 5.4. The ANOVA proved the significance of all three factors ($p < 0,05$) and the later analysis of residuals did not show any abnormal behavior. Both replicas allowed to compute experimental variability, considerably smaller than variability associated with both factors and its interaction.

Minimization of s_0^{II+III} was achieved when combining high level of factor A (ISFLIP assembly) and high level of factor I (turning inlet into vent and pressure increment between filling and post-filling steps), which are the manufactured conditions resulting from the first stage of the screening experiment (Figure 5.14.d).

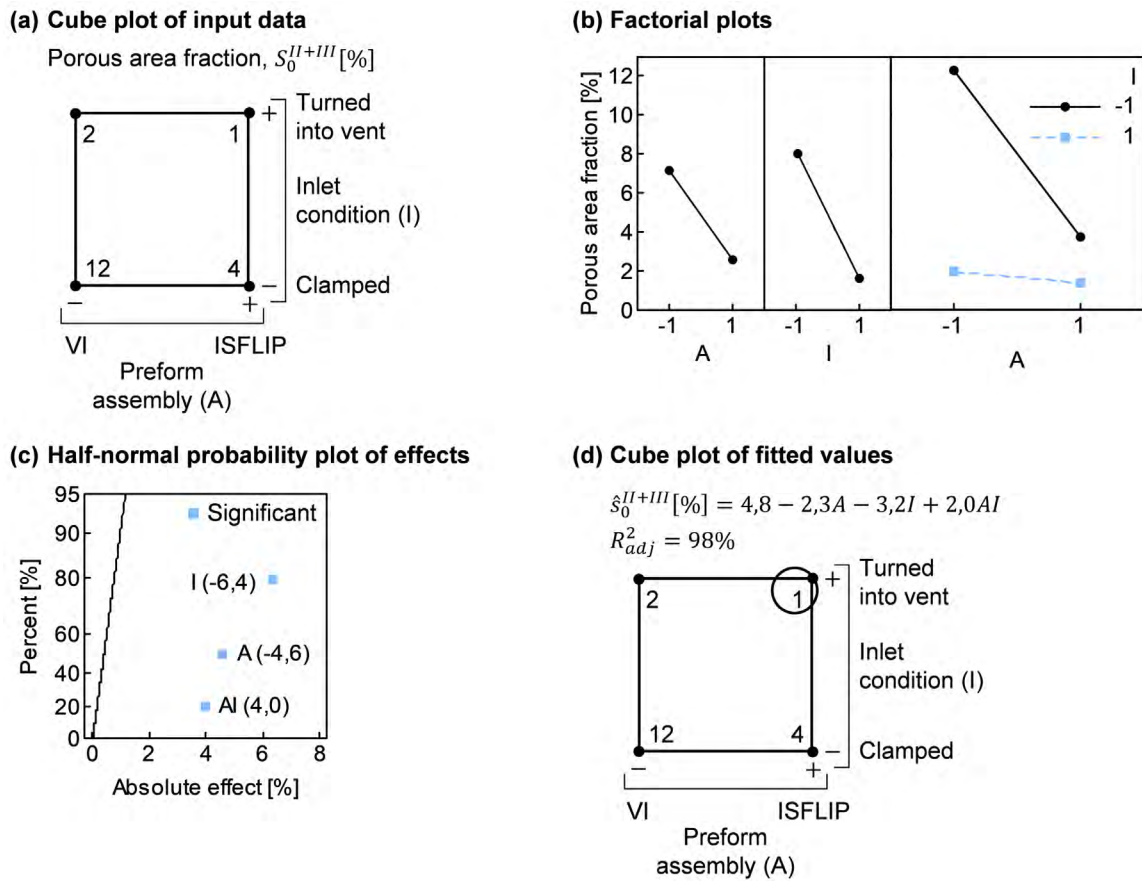


Figure 5.14. Plots of the statistical analysis of the second stage of the screening experiment of filling and post-filling conditions.

Analyses of residuals were not included to avoid a saturation of statistical graphs which do not provide any additional information from the point of view of the manufacturing process; however, extended statistical analyses are provided in Appendix F.

5.4. Discussion

Trade-offs between component quality attributes, usually addressed through v_f and v_0 , and processing time are a constant in the literature of VI manufacturing. Unfortunately, improvements in one direction often requires deterioration of other quality attribute or increment of the overall processing time. Achieving tight v_f tolerances require long post-filling times, t_{pfill} [132–134]. Although t_{pfill} can be minimized by turning inlets into vents after the filling step [134]. Nevertheless, turning inlets into vent may result in a considerable increment in v_0 [134,222]. High v_f involves lower permeability and, thus, longer filling times, t_{fill} . Even the effect of through thickness impregnation, often forced in VI to reduce required t_{fill} , on final v_0 is unclear [219,234,247]. Furthermore, maximizing v_f during VI processing involves keeping vent pressures,

P^{vent} , at high vacuum levels; however, v_0 would increase, since resin is prone to outgas at pressures close to absolute vacuum due to its minimum air solubility as stated by Henry's law [134,220]. In order to overcome these challenges, in the present chapter, it was addressed the possibility of manufacturing VI specimens with high v_f , tight tolerances and negligible v_0 , while minimizing processing time.

A first set of GTWF-epoxy specimens were manufactured to analyse the effects on fibre-related and void-related attributes of a reduced filling gradient of pressure and an increment of post-filling vent pressure when inlet was turned into vent after preform filling (vent pressure was raised before turning inlet into vent where applicable). Specimens were manufactured from a specific preform assembly configuration suitable for ISFLIP. Manufacturing conditions were arranged according to a 2^2 factorial design.

Then, the experiment was expanded to include the comparisons of the most promising manufacturing conditions previously identified with respect to a traditional VI preform assembly and the common procedure of inlet clamping after preform filling. Again, a 2^2 factorial design was applied and another set of specimens manufactured to assess the real potential of the measures taken in the previous stage.

It must be pointed out that a crucial point to really minimize porosity was the effective degassing procedure developed from the results of the analysis of different degassing strategies performed in Chapter 4.

The compressive pressure history exerted on performs varied according to the filling and post-filling conditions of each run. Different gradients of pressure held during preform filling and re-compaction rates applied during post-filling (compaction was faster at turning inlet into vent than at clamping the inlet) might have affected fibre fraction content obtained via the loss on ignition method, v_f' . Eventually, although some specimens showed slightly lower \bar{v}_f' , no relation appeared to exist between these abnormal results and the mentioned possible causes. The largest difference between specimens in \bar{v}_f' was only 1,5%, too small to be analysed in screening experiments belonging to an early stage of an optimization problem.

Furthermore, v_f' distribution into specimens did not show any trend, as that present in Chapter 4, in which a decreasing gradient of thickness remained trapped into the specimens from the inlet to the venting channels. A large post-filling time was set, $t_{pfill} = 30$ min, fifteen times longer than the maximum filling time of a specimen in which inlet was clamped, $t_{fill} = 119$ s, which is time enough to guarantee thickness homogenization. Nevertheless, PAT II and III mostly

accumulated in the specimen half which was closer to the venting channels, pointing out the possibility of a lack of resin pressure equalization into specimens. It is worth recalling that pressure takes more time to equalize into preforms than thickness during post-filling [132,134]. This situation occurred even in specimens in which inlet was turned into vent and pressure variations should be minimum. Therefore, it was more likely that the real cause was the slowing down of preform impregnation as the flow front moved away from resin inlet.

While in in-plane impregnation, there exists the well-known empirical relation between the modified capillary number, Ca^* , and void formation [200,201]; in through-thickness impregnation, there is a lack of research on the topic of void formation due to flow through dual-scale porous media. The random distribution of porous areas into specimens, beyond the correlation found between porous area fraction, s_0^{II+III} , and processing conditions, makes porosity appearance unpredictable.

Each manufacturing run was recorded with a video camera and due to the translucent nature of the GTWF-epoxy specimens, flow front at the mould face (bottom) was discernible during filling. While flow front at the HPDM face (top) moved as expected, it was noticed the formation of dry spots at the bottom flow front, creating a discontinuous and irregular flow front movement which seemed to be the cause of the random formation of porous areas. Besides, microscopic analysis revealed an accumulation of inter-tow voids in the lower half of samples PAT II and III. The irregular through-thickness flow front movement, which is behind the random distribution of porosity and its accumulation near mould face, was attributed to the intrinsic variability of multi-layer textile preforms [136,137].

As in case of in-plane flow (Chapter 4), most of porosity was present in form of inter-tow voids; although, in the present through-thickness flow experiments, porosity distribution was asymmetric. Pores of up to $A_0^{inter} = 0,75 \text{ mm}^2$ and $\phi_{Feret} = 4,9 \text{ mm}$ were found in PAT III. The large pores located in PAT II and PAT III caused a reduction in mean flexural strength, $\bar{\sigma}_{fM}$, of 8,7%. An interesting point of the asymmetric porosity distribution is that flexural behaviour was only being significantly damaged when specimen mould face was loaded in compression. Besides, it was drawn the conclusion that PAT I was not significantly deteriorating flexural performance, which helped to defined a meaningful response variable for the factorial designs; since, as previously mentioned, no apparent reason was found to explain the appearance of PAT I more than it did not appear when pressure was increased between the filling and post-filling steps.

At analysing the factorial designs in terms of the porous area fraction which caused any deterioration on the flexural behaviour, s_0^{II+III} , a simple increment in vent pressures between

filling and post-filling, $\Delta P_{fill \rightarrow pfill}^{vent} = 5$ kPa, resulted in a notable reduction of the overall specimen void content, providing an implementable solution to the endless trade-off between specimen quality and processing time. While forcing through-thickness impregnation and turning inlet into vent helped to achieve short VI processing times, an effective degassing procedure and the increment of vent pressure between filling and post-filling succeeded at manufacturing nearly free-void specimens. Besides, it cannot be omitted the importance that flow resistance left between preforms and venting channels had to avoid air recirculation when raising the vent pressure.

Different filling gradients of pressure did not show any significant effect on neither fibre and void contents; although, in full gradient runs, $\bar{t}_{fill} = 98$ s was less than half of equivalent reduced gradient runs, $\bar{t}_{fill} = 245$ s. However, it must be pointed out that, in case of not having turned inlet into vent (keeping the flow resistance), post-filling time, t_{pfill} , to reach the ultimate 2% of specimen nominal thickness would have been ≈ 1800 s (full gradient) and ≈ 600 s (reduced gradient). At turning inlet into vent, a considerable time reduction was achieved ($t_{pfill} < 30$ s).

At comparing the new proposed manufacturing procedure with conventional VI practices, inlet clamping and common VI assembly offered worse s_0^{II+III} results. The different flow induced by perforated release films showed a better behavior than continuous through-thickness flow that peel-ply makes possible. In spite of the irregular through thickness flow previously mentioned and caused by preform variability, preform thickness was enough to guarantee convergence of multi-point flows created by the perforated release film. In a set of experiments conducted in parallel to those shown in the present chapter, which involved thinner preforms, a regular pattern of smaller porous areas appeared at the bottom face of the specimens, indicating the unsuccessful convergence of the multiple flows. Therefore, care must be taken when using this kind of perforated release films over thin preforms.

Manufacturing of specimens with $\bar{v}'_f = 54,0\%$ were achieved through a single-cycle debulking. However, further research could explore multiple-cycle debulking to increase v'_f and analyze its effects on porosity. Void size and morphology seemed closely related to fabric architecture and nesting; therefore, at increasing v'_f and, thus, reducing gap between layers, trapped pores should be smaller. Future work should address the effects of larger pressure increments and different gelation temperatures on component quality, always keeping the focus on short processing times.

5.5. Conclusions

In this chapter, different pressure filling and post-filling conditions, and preform assembly configurations have been analysed through a series of specifically manufactured VI specimens, with the purpose of assessing the ability to achieve high fibre content, minimum porosity and short processing times.

Microscopic analysis revealed that through-thickness preform impregnation causes an asymmetric void distribution into the specimens. Inter-tow voids accumulated near specimen mould face, causing a considerable deterioration in mechanical performance (reduction of 8,7% in flexural strength) of those samples containing pore clusters in which mould face was loaded in compression.

Typical trade-offs of component quality associated to VI manufacturing are overcome thanks to a promising non-conventional manufacturing strategy in which, starting from an effective degassing procedure, through-thickness flow is altered by a perforated release film and a flow resistance placed between the preform end and the venting channel, inlet turned into vent after preform filling, and vent pressure raised between filling and post-filling steps (+5 kPa). Void content was virtually eliminated and post-filling time minimized without affecting fibre content ($\bar{v}'_f = 54,0\%$).

Although manufacturing null porosity specimens was not achieved, the proposed methodology has arisen as a promising basis. Further research is required in larger pressure increments that, without involving preform relaxation that may alter fibre content, guarantee bubble collapse of all voids formed during filling and avoid resin outgassing.

Chapter 6

Evaluation of uncertainties of the forming stage of ISFLIP

ISFLIP has been introduced in Chapter 3 as a promising manufacturing technique combining VI and forming; however, due to its early stage of development, it is still shrouded in uncertainty. In this chapter, viability of the presented concept has been proved and formability of ISFLIP specimens according to different geometries was tested.

In ISFLIP, auxiliary materials have an essential role in attainable shapes, since preforms and auxiliary materials are formed together, adding complexity to the overall forming performance. Although individual components of the preform assembly should be chosen to show high formability or drapeability; involved polymeric meshes, fabrics and films present different deformation mechanisms. The primary in-plane deformation mechanism in textile fabrics is intra-ply shear (trellis shear); while in a polymeric film, it is tensile deformation.

Different reinforcements and consumable materials were tested to check formability of the whole ISFLIP assembly and to screen appropriate auxiliary materials. Addressed geometries were a hemisphere shape (uniform double curvature), and a 'C' variable cross-section profile (single curvature shape with high double curvature concentrated in small regions). Formability was compared against intra-ply shear of individual textile reinforcements, usually kept as reference in hand lay-up, to give an insight of drapeability limitations associated to ISFLIP.

While preform distortions caused by wrinkling were visually appreciated; preform distortions caused by sharp bending, not appreciable visually, were assessed through the Inter-Laminar Normal Strength (ILNS) of manufactured specimens and light microscopy.

6.1. Materials and methods

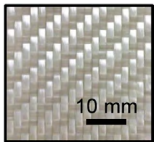
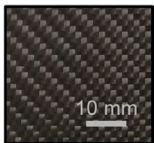
6.1.1. Specimens

In this section it is presented not only constituent materials, but also auxiliary materials, which play a key role in ISFLIP formability due to their interaction with the preform during the forming step. Besides, mould geometries, over which specimens were formed, were also described.

6.1.1.1. Reinforcements and matrix

The reinforcements used in the experimentation were an E-Glass 2/2 Twill-Weave Fabric (GTWF) and a Carbon 2/2 Twill-Weave Fabric (CTWF), both textiles provided by Angeloni (Table 6.1). The matrix was the epoxy system Sicomin SR 8100 (bisphenol A diglycidylether, DGEBA) – SD 8822 (isophorone diamin). This system exhibits low viscosity, 340-390 mPa·s, and shows a working time longer than 200 min at ambient temperature [295].

Table 6.1. Textile properties of reinforcements.

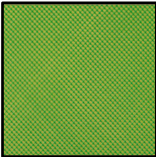
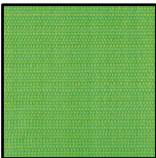
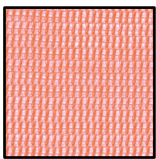

Fabric	Reference	Weave style	Yarn	Areal density [g/m ²]	Thickness [mm]	Ends count [cm ⁻¹]	
						Warp	Weft
GTWF							
	VV 320 T	2/2 twill	E-glass	320	0,28	5	5
CTWF							
	GG 285 T2	2/2 twill	3K HS carbon	285	0,32	7	7

6.1.1.2. Consumables

Selection of auxiliary materials used in the preform assembly and their arrangement are crucial in ISFLIP. Bad drapeability or excessive stiffness of conventional consumables materials may cause a severe restriction to the attainable shapes; hence, auxiliary materials with expectation of high drapeability or flexibility should be considered.

Table 6.2 introduces the disposable materials used in the present experimentation. All listed materials are chemically compatible with epoxy resins and can resist temperatures higher than 80°C, which was the maximum temperature reached during the curing step of the resin system.

Table 6.2. Consumable materials (all materials belong to the catalogue of Airtech Advanced Materials Group).

Material	Description	Thickness [mm]	Maximum width[m]	Service temperature [°C]
Bagging films				
Conventional	Nylon	0,050	7,11	204
High Elongation (HE)	TP elastomer	0,038	3,04	121
High Permeability Distribution Media (HPDM)				
Conventional HPDM (CHPDM)* ¹				
	PP extruded	0,9	1,52	150
Knitted HPDM 1 (KHPDM1)* ¹				
	High density PE knitted	1,2	2,30	125
Knitted HPDM 2 (KHPDM2)* ¹				
	High density PE knitted	1,5	1,52	125
Release films				
Perforated* ²	Polyolefin	0,025	1,52	121
Non-Perforated 1 (NP1)	ETFE	0,015	1,52	220
Non-perforated 2 (NP2)	Polyolefin	0,030	3,04	157
Non-perforated 3 (NP3)	ETFE	0,025	3,04	260
Peel-ply fabrics				
Conventional* ¹				
	Nylon 88g/m ²	0,152	1,52	190

*¹ Picture scales are different.

*² Perforation pattern: $\varnothing 0,4$ mm at 3 mm and staggered 60°.

The non-perforated release film and the knitted mesh KHPDM2 were supplied in a single stuck pack; hence, although both were characterized individually and together, they could only be used stuck in the forming experiments.

6.1.1.3. Size and shape

All specimens consisted on orthotropic preforms of 9 GTWF or 9 CTWF layers, $[(0/90)]_9$. Preforms were stacked over a flat surface and then formed over a hemisphere mould (Figure 6.1) or a modular 'C' variable cross-section profile (Figure 6.2), both constructed in wood.

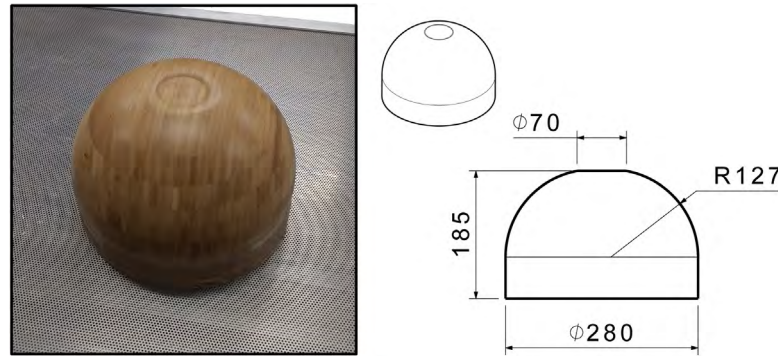


Figure 6.1. Hemisphere mould (dimensions in mm).

The hemisphere mould consisted on a hemisphere shape placed over a circular base of height 60 mm (Figure 6.2.a). The hemisphere shape was lifted to avoid that the minimum achievable concave radius interfered with the doubly curved region. The size of preforms formed over hemisphere moulds was 450x450 mm.

On the other hand, moulds for 'C' variable cross-section profiles consisted on a succession of 'C' cross-section slices placed over an aluminium supporting structure. This modular system let creating cross-section profiles including different sharp joggles (regions of cross-section change) with a single set of components; although only two combinations were studied (Figure 6.2.a and Figure 6.2.b). Preform size in both combinations was 450x320 mm.

It is worth remembering that the thickness of the lower elastic diaphragm should be added to the dimensions depicted in Figure 6.1 and Figure 6.2 to obtain the actual mould dimensions over which preform assemblies were formed. In the presented set of experiments, elastomeric silicone sheets of thickness 1 mm were used.

6.1.2. Manufacturing

Specimens were manufactured according to the process sequence and with the functional prototype presented in Chapter 3, while VI-related steps were based on the manufacturing methodology constructed in Chapters 4 and 5. Processing parameters governing specimen manufacturing are provided in Figure 6.3.

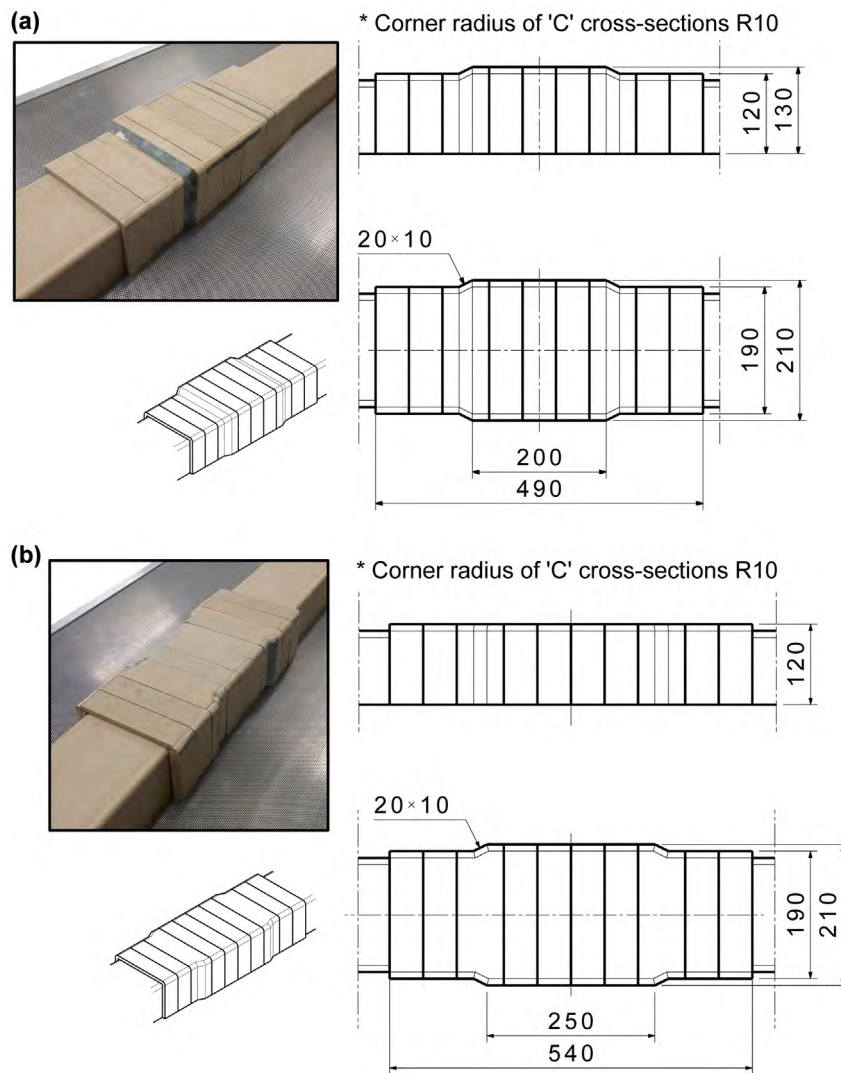


Figure 6.2. Modular 'C' variable cross-section profiles: (a) single joggle and (b) double joggle (dimensions in mm).

Forming rate was not controlled, since with the vacuum pump acting at maximum flow capacity, forming was slow enough. It is worth recalling that, in case of ISFLIP, forming rate is not expected to be a critical issue due to the low viscosity state of the matrix.

In order to analyse the effect of different auxiliary materials on preform formability, two preform assembly configurations were adopted: one in which CHPDM or KHPDM1 were combined with peel-ply as the upper demoulding layer (Figure 6.4.a), and another one in which KHPDM2 was combined with the perforated release film as the upper release layer (Figure 6.4.b). Although Figure 6.4 depicts preform assemblies for hemisphere shapes; assembly configurations in case of 'C' cross-section profiles would only differ in size. Warp and weft directions of reinforcements were aligned with directions x and z .

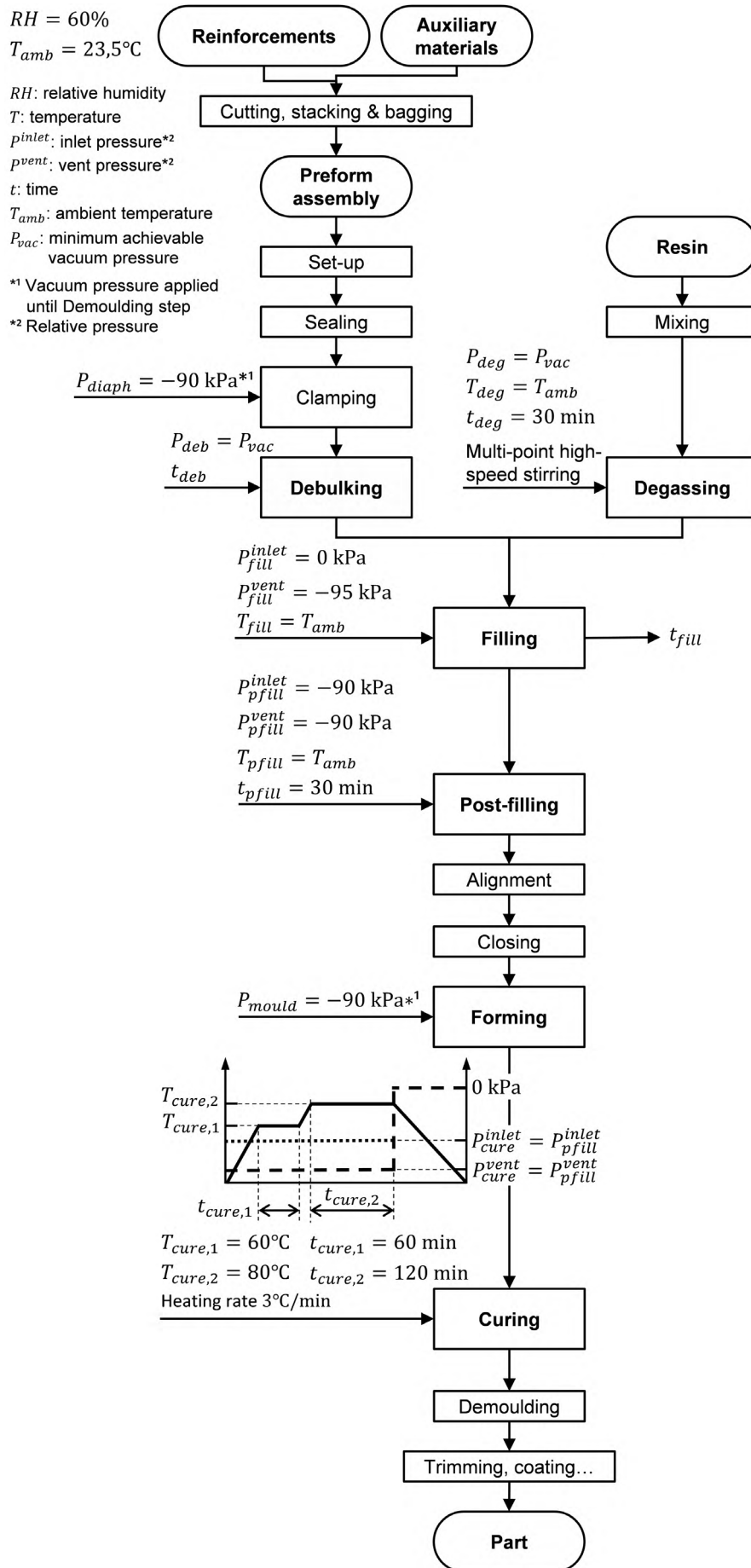


Figure 6.3. Flowchart and governing parameters of ISFLIP process.

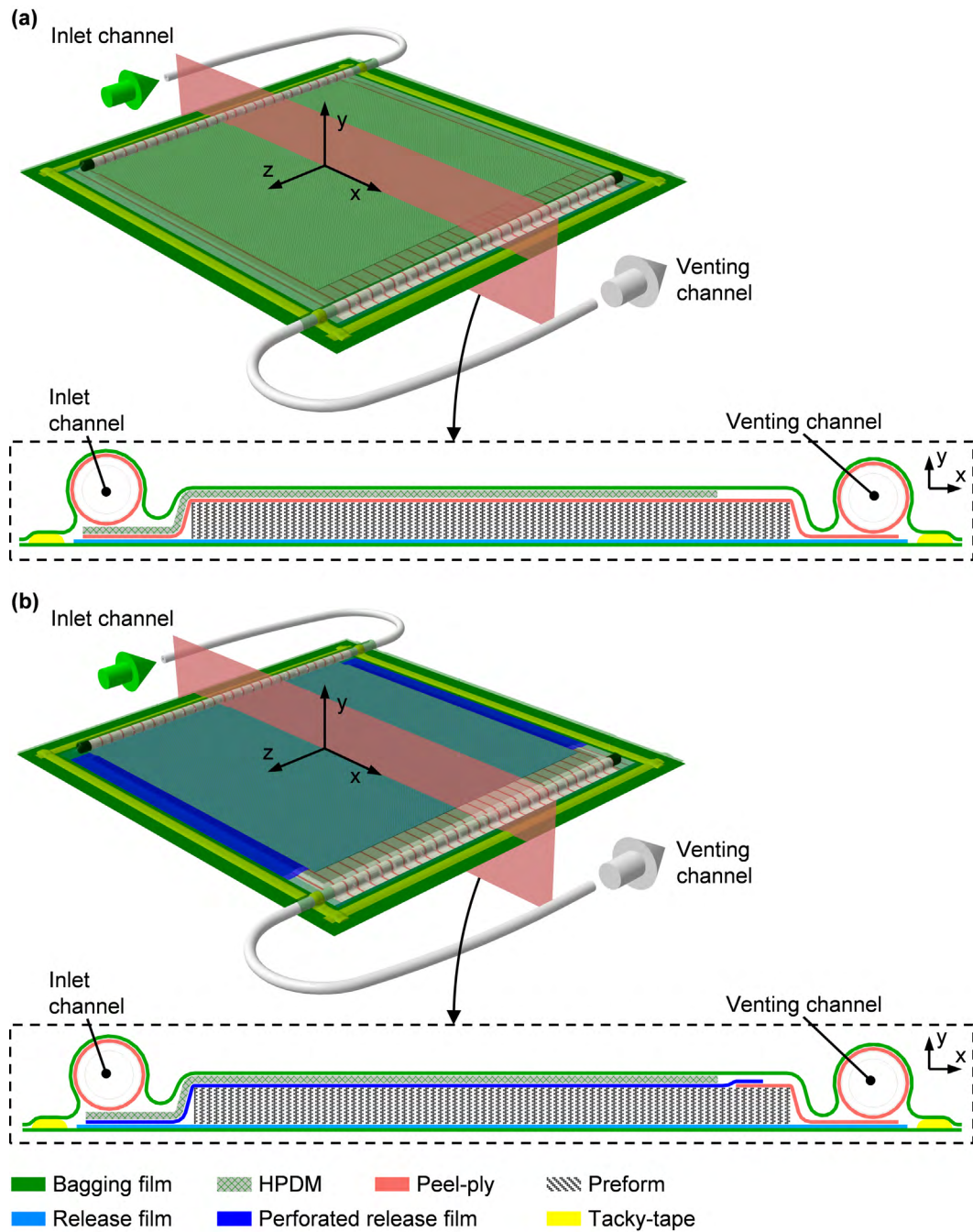


Figure 6.4. ISFLIP preform assemblies for hemisphere shape specimens (schematic dimensions are representative): (a) upper demoulding by peel-ply and (b) upper demoulding by perforated release film.

HE bagging films were used in both configurations. Besides, both inlet and venting channels were placed at considerable distance from preform edges to avoid any interference on preform formability. Both preform assembly configurations were the same configurations studied in Chapter 5; but, instead of a peel-ply fabric as the lower release layer, release film was used.

It is worth pointing out that peel-ply envelopes were placed around spiral tubes used as inlet and venting channels to prevent bagging film damage. In previous VI tests, HE bagging films catastrophically failed due to creep once raising temperature. HE bagging film tended to deform

through any free space, even through the irregular surface of HPDM. In ISFLIP, pressure difference between the interior and the exterior of the preform assembly cavity was considerably lower than in VI,

$$\Delta P = P_{diaph} - P \quad \text{in ISFILP} \quad (34)$$

$$\Delta P = P_{atm} - P \quad \text{in VI} \quad (35)$$

where P_{diaph} is the vacuum pressure between diaphragms, P is the resin pressure into the preform assembly cavity and P_{atm} is the atmospheric pressure. Therefore, stresses acting on bagging films were lower than in conventional VI; but it was preferred to protect spiral tubes due to their large openings through which films could deform.

6.1.3. Materials characterization

A major inconvenient of combining plastic films with textile fabrics and knitted meshes is that dominant in-plane deformation mechanisms are different. Besides, different material layers interact between each other through friction. Consequently, the main in-plane deformation mechanism of reinforcements and consumable materials, and ply-ply shear between reinforcements and auxiliary materials (static friction) were characterized to outline some sort of selection criteria.

6.1.3.1. Bias extension test

Intra-ply shear of reinforcements and peel-ply was measured through the bias extension test. Woven fabrics deforms by trellis shear (yarns rotate at cross-overs). Although a standard test was not available to characterize shear behaviour of technical textile fabrics, it was followed a series of recommendations stated by a group of researchers in a collaborative effort to benchmark characterization tests applied to forming of composite materials [97].

In the bias extension test, a rectangular fabric sample is tested in tension at $\pm 45^\circ$ to the principal fibre directions. The tensile load vs. crosshead displacement curve was converted into the normalized shear force vs. shear angle curve through an iterative procedure described in [97,103]. Schematics of initial and deformed states of samples are shown in Figure 6.5.

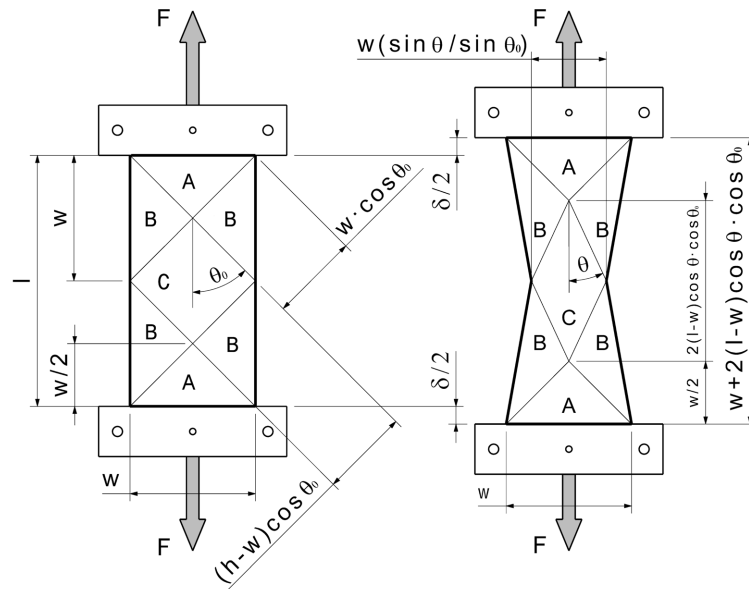


Figure 6.5. Geometric analysis of bias extension test samples for trellis shear characterization: (a) initial state and (b) deformed state (adapted from [100]).

If fabrics are perfectly orthogonal at the onset of the test, and no sliding occurs between warp and weft yarns:

- In zone A, no deformation happens.
- In zone B, specimen stretching leads to a shear deformation half of shear in zone C.
- In zone C, uniform pure shear occurs which is related to the crosshead displacement, δ .

Therefore, assuming that there exist three different areas in terms of shear deformation and these three areas show uniform shear; shear angle in zone C, γ , is given by a simple kinematic analysis of a bias-extension sample (Figure 6.5):

$$\gamma = 2\theta_0 - 2\theta = \frac{\pi}{2} - 2 \cos^{-1} \left(\frac{l_0 + \delta}{\sqrt{2}l_0} \right) \quad (36)$$

where $l_0 = l - w$, w is the initial specimen width, l is the initial specimen length (distance between jaws), and 2θ is the angle formed by warp and weft yarns in zone C.

However, the theoretical shear angle computed by Equation (36) significantly differs from the real one due to translation between warp and weft yarns, and this difference becomes larger as shear angle increases [97,103]. Consequently, all tests were recorded with a video camera, and shear angle was explicitly measured. The open-source image processing package Fiji, based on ImageJ, was used to correct image perspective, and measure the upper and lower angles (2θ) of a rhombus drawn in each bias-extension sample, which delimited zone C (Figure 6.6). Shear angle,

γ , was then computed by subtracting the average of both measured angles from the initial angle ($2\theta_0$).

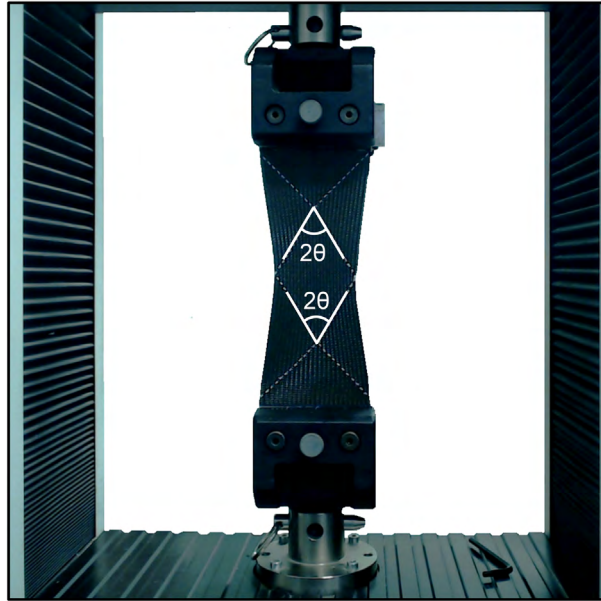


Figure 6.6. Real picture of a deformed sample depicting the two angles experimentally measured.

Finally, the normalized shear force, F_{sh} , was estimated through the previously mentioned iterative process according to the following expression:

$$F_{sh} = \frac{1}{(2l - 3w) \cos \gamma} \left(\left(\frac{l}{w} - 1 \right) \cdot F \cdot \left(\cos \frac{\gamma}{2} - \sin \frac{\gamma}{2} \right) - w \cdot F_{sh} \left(\frac{\gamma}{2} \right) \cdot \cos \frac{\gamma}{2} \right) \quad (37)$$

Sample dimensions in the conducted tests were $l = 200$ mm (distance between jaws) and $w = 100$ mm. Tests were conducted at a crosshead displacement speed of 50 mm/s.

6.1.3.2. Tensile test

Tensile behaviour of thin plastic films and diaphragm sheets was determined according to the procedure stated in the standards UNE-EN ISO 527-1 and UNE-EN ISO 527-3.

Due to the anisotropic nature of most of extruded films and sheets, tensile properties were characterized in longitudinal (extrusion direction) and transversal (perpendicular to extrusion direction) directions. Dimensions of the rectangular samples were 150x25 mm (specimen type 2 specified in UNE-EN ISO 527-3), and the initial distance between jaws was 100 mm. Tests were conducted at a crosshead displacement speed of 50 mm/s.

Since films and sheets are usually supplied in a discrete range of thicknesses, tests were not focused on stress vs. strain behaviour, but in the normalized to the width tensile load, F/w , vs. strain, ϵ . This approach allowed an easier comparison with the results obtained from the bias-extension tests.

The tensile behaviour of all three HPDMs listed in Table 6.2 was also tested in both roll and perpendicular-to-roll directions. Although KHPDM1 and KHPDM2 were knitted meshes of which in-plane deformation included yarn straightening and slippage, and trellis shearing; tensile tests allowed to perform a rough assessment of their in-plane behaviour without exploring in depth each deformation mechanism. Samples dimensions and crosshead displacement speed were equal to those of bias extension samples.

6.1.3.3. Friction test

Most attempts to characterize friction between reinforcements textiles are based on pull-out and pull-through experiments, which are especially useful when materials have to be tested at a higher than ambient temperature [115]. These set-ups are usually used in the characterization of materials in which a high viscosity polymer is present, in form of matrix (prepregs) or yarns (commingled fabrics). Since it was no necessary to perform any test at high temperature, a simpler set-up, based on standard UNE-EN ISO 8295:2005, was chosen (Figure 6.7).

In the adopted set-up, some base materials were adhered to a flat rigid surface; while different materials were attached to a round support, allowing sliding between both materials. Then, an elastic cord was redirected through a pulley to transfer the vertical movement of a universal testing machine to the horizontal movement of the round support, loaded with a specific weight. Through this weight, compaction pressure exerted on materials into the preform assembly was simulated. A weight of 3,5 kg was placed over the round support of diameter 22 mm, being equivalent to -90 kPa, which is the vent pressure held into the preform assembly during the forming stage.

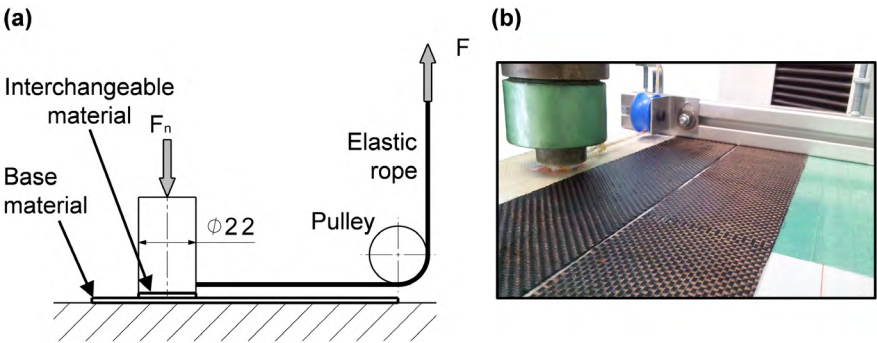


Figure 6.7. Experimental set-up of the friction test: (a) schematic drawing and (b) test execution.

Cord elasticity allowed to progressively load the round support, instead of a sudden loading which would have resulted from a rigid cord. Besides, offset between load force and friction surface was kept as low as possible to minimize misalignments which can lead to an uneven normal pressure distribution.

Only the static coefficient of friction was measured, μ_{st} ; since the elastic cord could altered kinematic coefficient of friction measurements. μ_{st} was computed as the ratio of the universal testing machine load, F , and the normal load exerted by the round support, F_n , at the peak of the load vs. crosshead displacement curve:

$$\mu_{st} = \frac{F}{F_n} \quad (\text{peak of the force vs. crosshead displacement curve}) \quad (38)$$

Dry and wet static coefficients of friction, μ_{st}^{dry} and μ_{st}^{wet} respectively, were calculated for those materials which remain saturated during the forming stage (both reinforcements fabrics and peel-ply). In case of μ_{st}^{wet} , materials were saturated with a synthetic oil 15W40, replicating the effect of resin lubrication.

6.1.4. Specimens characterization

Wrinkles and surface defects can be assessed by visual inspection; even areas of porosity can be bounded visually in E-glass – epoxy specimens; however, internal fibre misalignments cannot be identified visually. Fibre misalignments are usual when stacks of textile reinforcements are formed over tools with tight bending radius, as in case of ‘C’ cross-section profiles.

Therefore, apart from visually assessing ‘C’ cross-section profile specimens in terms of out-of-plane deformation (wrinkling), structural integrity of a sort of samples extracted from bent regions was evaluated through their ILNS behaviour. Moreover, tested samples were also later analysed through light microscopy.

More detailed descriptions of the testing procedures followed, as well as supplementary data to that provided later in the results section, can be consulted in Appendix D for the compression test of ‘L’ shapes samples conducted to measure ILNS, and in Appendix E for light microscopy.

6.1.4.1. Compression test of ‘L’ shape samples

When a force is applied in a curved sample, a through-the-thickness tensile stress is produced. In layered materials such as FRPs, this tensile stress may cause failure at load levels much lower than

predicted by in-plane strength properties due to their anisotropic nature. The through-the-thickness tensile stress at failure is referred as ILNS. The development of ILNS promotes mode-I type of delamination propagation in curved regions. ILNS is quite sensitive to manufacturing quality and defects such as voids and ply folds [306–308].

In the literature, it can be found a number of different experimental set-ups to measure ILNS of simply curved FRP samples [309–311]. The standard ASTM D6415/D6415M proposes a four-point bending configuration to measure ILNS of ‘L’ shape samples. In the present work, it was adopted a compression set-up to measure ILNS of samples trimmed from ‘C’ cross-section profiles manufactured through ISFLIP (Figure 6.8).

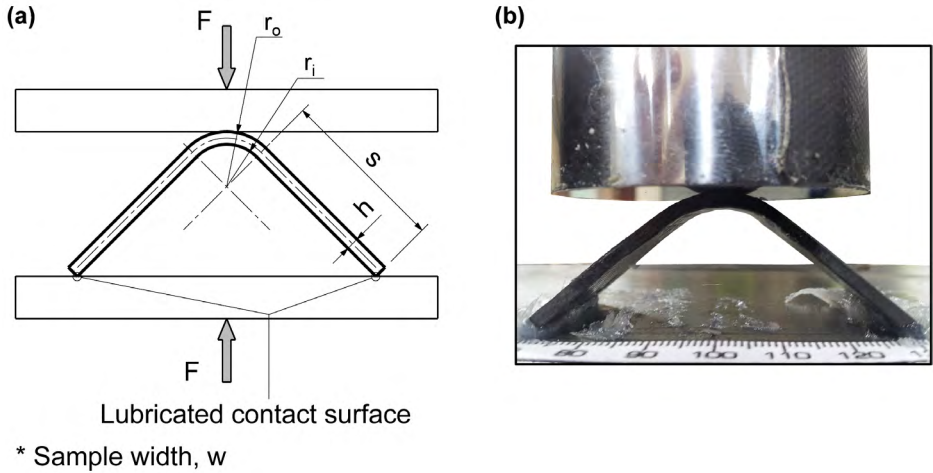


Figure 6.8. Experimental set-up of the compression test of ‘L’ shape samples: (a) schematic drawing and (b) test execution (deformed sample at failure).

The compression fixture consisted on a steel cylinder mounted on a universal testing machine and pushed against a large rigid steel plate. Wax was applied along the contact edges between the sample and the lower plate to facilitate edges sliding during the compression test.

Under loading, it is originated a complex stress state in the curved region: circumferential, radial tensile and shear stresses. Circumferential stresses are produced along fabric direction, being located the maximum circumferential tensile stress at the inner surface and the maximum circumferential compressive stress at the outer surface. The magnitude of both maximum circumferential stresses depends on material properties and sample dimensions in the curved region.

Furthermore, the radial tensile stress, σ_r , ranges from zero at the inner and outer surfaces to a peak around the mean radius. An adequate sample failure produces delamination across the width instead of failure of inner and outer surfaces as in typical three-point flexure testing. The ILNS was given by the maximum radial tensile stress, σ_{rM} , measured during the test.

Although shear stresses are also originated, in the curved region, where failure occurs, inter-laminar normal stresses (σ_r) prevail over inter-laminar shear stresses.

A well-known analytical formulation was developed by Lekhnitskii to describe the complete stress state through the thickness of the specimen and along the curved portion [312]. However, for FRP curved specimens under certain conditions ($E_\theta/E_r \leq 6$ and $r_m/h \geq 2,5$, where E_θ is the modulus of elasticity in the circumferential direction, E_r is the modulus of elasticity in the radial direction, r_m is the mean radius and h is sample thickness in the curved portion) in which large deflections do not happen, it has been shown that the following expression gives consistent results for the maximum radial stress with an error lower than 2% with respect to Lekhnitskii's solution [313]:

$$\sigma_{rM} = \frac{3M}{2wh\sqrt{r_i r_o}} \quad (39)$$

where M is the resultant bending moment at a specific cross-section. σ_{rM} is produced at $r = \sqrt{r_i r_o}$. The imposed condition on material properties, $E_\theta/E_r \leq 6$, is fulfilled by most of laminates based on stacks of woven fabrics.

In Figure 6.9, it is depicted a free-body diagram with forces and moments acting on one of the symmetric halves of a 'L' shape sample.

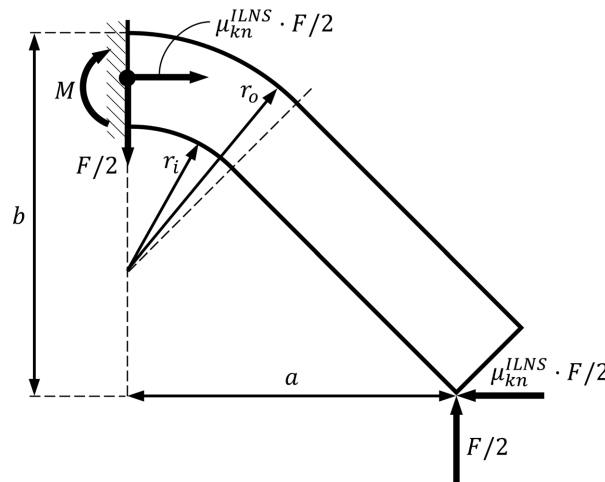


Figure 6.9. Free-body diagram of a compressed 'L' shape sample.

From the balances of forces and moments, M acting on the middle cross-section of the sample was computed such that

$$M = \frac{F}{2}a - \mu_{kn}^{ILNS} \frac{F}{2} \left(b - \frac{r_o - r_i}{2} \right) = \frac{F}{2}a - \mu_{kn}^{ILNS} \frac{F}{2} \left(b_0 - \delta - \frac{r_o - r_i}{2} \right) \quad (40)$$

where the final height of the sample before failure, b , could be calculated from the initial height, b_0 , and the displacement of the crosshead, δ ; the final distance between contact edges, a , was visually assessed through a ruler attached to the supporting plate (Figure 6.8.b); and the estimation of a kinematic coefficient of friction between the contact edges and the supporting plate, μ_{kn}^{ILNS} .

In order to estimate μ_{kn}^{ILNS} , a loading-unloading hysteresis loop cycle was conducted before reaching load levels close to ILNS failure (Figure 6.10). Under the assumptions that μ_{kn}^{ILNS} remained independent on the applied load, F , and energy loss associated to the closed loop corresponded to friction between the sample edges and the supporting plate, μ_{kn}^{ILNS} was computed from an energy balance including the work done by F and the work done by the friction force, $2 \cdot \mu_{kn}^{ILNS} F/2$, such that

$$\mu_{kn}^{ILNS} = \frac{\frac{F_3 + F_2}{2} (\delta_3 - \delta_2) + \frac{F_1 + F_4}{2} (\delta_1 - \delta_4)}{\frac{F_1 + F_4}{4} (a_1 - a_4) - \frac{F_3 + F_2}{4} (a_3 - a_2)} \quad (41)$$

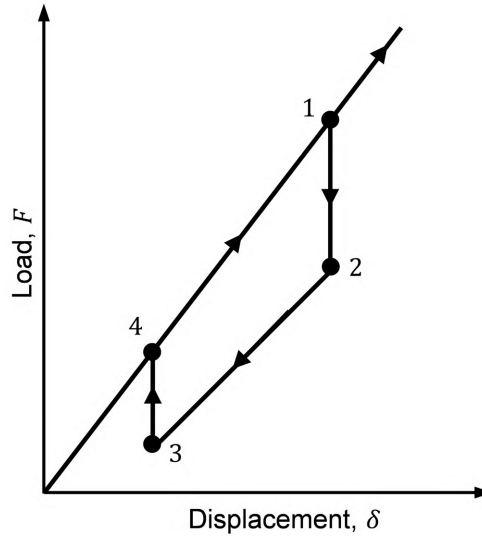


Figure 6.10. Ideal unloading-loading hysteresis loop during compression tests of 'L' shape samples.

From the bending moment acting on the middle cross-section of the samples, the Curved Beam Strength (CBS), another characteristic parameter defined for curved layered specimens, can also be computed such that

$$CBS = M/w \quad (42)$$

Samples were tested at 1 mm/s. Sample dimensions are given in the section in which the results of the compression tests are presented.

6.1.4.2. Light microscopy

Micrographic samples were casted in polyester resin round micrographic specimens, grinded with diamond discs and finally polished with a two-in-one suspension of 6 μm diamond and lubricant. The final polishing step conducted in preparation of micrographic specimens presented in previous chapters was skipped, since the level of detailed required in the present analysis was lower. Multiple micrographs per sample were taken at 50X magnification and stitched to get a picture covering the full sample length. The open-source image processing package Fiji, based on ImageJ, was used to process the micrographs.

6.2. Results

Before going into the analysis of ISFLIP specimens, results of the characterization of reinforcement and auxiliary materials are presented.

6.2.1. Reinforcements and auxiliary materials

6.2.1.1. Intra-ply shear

It is worth emphasizing that the conducted bias-extension tests allowed to perform a quantitative comparison between fabrics; but they did not reflect fabric behaviour into the preform assembly when being formed, since fabrics were also loaded in tension and compacted into the preform assembly, and lubricated by the resin. Additional tension loading increases shear resistance, but larger shear angles can be reached without wrinkling [106–108]; while compaction also increases shear resistance, but attainable shear angles without out-of-plane deformation are smaller [104,105].

The results of the three samples per material that were tested are shown in Figure 6.11. Bias-extension tests were conducted until out-of-plane wrinkling was severe. Beyond the locking angle, out-of-plane deformation of the fabric distorted measured angles from taken pictures; therefore, computed shear angles were not accurately representing the real shear angles into the zone C of the fabrics.

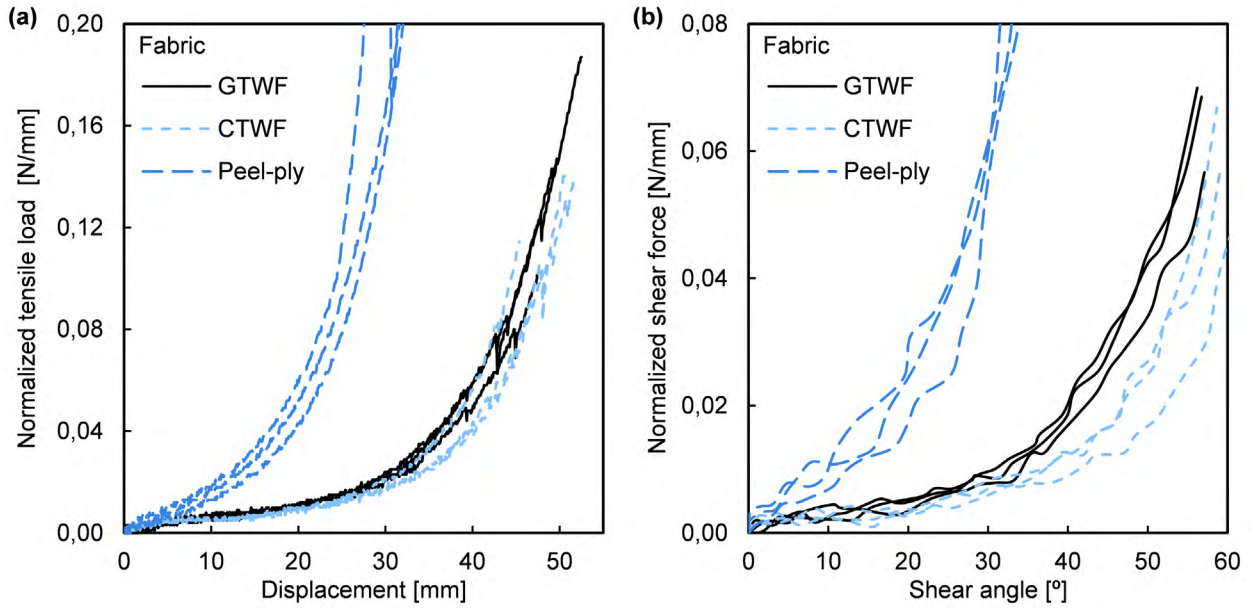


Figure 6.11. Results of the bias-extension tests: (a) normalized to the width tensile load, F/w , vs. crosshead displacement, δ , curve and (b) normalized shear force, F_{sh} , vs. shear angle, γ , curve.

Due to the discrete measurement of shear angles, γ , and the iterative process for computing the normalized shear force, F_{sh} , the resulting F_{sh} vs. γ curves showed considerably higher noise levels than the initial tensile load vs. crosshead displacement curves, as can be observed at comparing Figure 6.11.a and Figure 6.11.b. Nevertheless, this noise did not impede drawing important conclusions from the bias-extension tests.

Shear angles at which out-of-plane deformation, γ_{lock} , occurred were $38,7^\circ$ - $41,2^\circ$ for GTWF, $43,5^\circ$ - $51,1^\circ$ for CTWF and $7,9^\circ$ - $12,1^\circ$ for the conventional peel-ply. Since warp and weft yarns were not perfectly perpendicular at the beginning of the test, absolute angles between yarns at which fabric locking occurred, $2\theta_{lock}$, were $49,7^\circ$ - $53,6^\circ$ for GTWF, $42,4^\circ$ - $45,6^\circ$ for CTWF and $78,6^\circ$ - $82,6^\circ$ for the conventional peel-ply.

While CTWF and GTWF showed a similar trellis shearing behaviour, attainable shear angles in case of the tested peel-ply were smaller than a third of γ_{lock} of both reinforcement fabrics.

6.2.1.2. Tensile response

From the kinematic analysis depicted in Figure 6.5, strain of a hypothetical long diagonal of a square element (representing the unit cell of a woven fabric) suffering trellis shear, ε_D , can be defined in terms of the angle between warp and weft yarns, 2θ , as

$$\varepsilon_D = \frac{2(l-w) \cos \theta \cdot \cos \theta_0 - 2(l-w)(\cos \theta_0)^2}{2(l-w)(\cos \theta_0)^2} = \frac{\cos \theta}{\cos \theta_0} - 1 > 0 \quad (43)$$

Alternatively, the negative strain associated to the short diagonal of the square element, ε_d , can be expressed as

$$\varepsilon_d = \frac{w \cdot \left(\frac{\sin \theta}{\sin \theta_0} \right) - w}{w} = \frac{\sin \theta}{\sin \theta_0} - 1 < 0 \quad (44)$$

According to in-plane shear of tested fabrics, a maximum ε_D of 0,32 mm/mm would have corresponded to CTWF. Auxiliary materials listed in Table 6.2 and tested under tension, apart from perforated release film and CHPDM, showed larger strain, ε , before failure as can be seen in Figure 6.12.

In contrast to predominant plastic deformation of the conventional bagging film tested, elastomeric nature of silicone sheets used as diaphragms and HE bagging film can be observed in Figure 6.12.a and Figure 6.12.b, respectively. It is worth noting that beyond a certain strain which was smaller than $\varepsilon_D = 0,32$ mm/mm, the normalized to the width tensile load, F/δ , was larger in case of the silicone diaphragm of thickness 1 mm than in the conventional bagging film. It must be pointed out that depicted F/δ vs. ε curves of silicone sheets corresponded to the first loading cycle exerted on the material; hence, material softening caused by Mullins effect had not occurred yet [179].

All films showed significant wrinkling in the middle region of the samples along the direction of the applied force during the uniaxial tensile tests. Without going into details of the mechanisms which cause thin films wrinkling from uniaxial tension, wrinkle formation is connected to the bending energy of the film, which decreases as thickness decreases [314,315]. An elongation of $\varepsilon_D = 0,32$ mm/mm in the above-mentioned hypothetical square element suffering trellis shear would correspond to a reduction of the short diagonal such that $\varepsilon_d = -0,49$ mm/mm; hence, due to the low bending resistance of the thin films normally used, wrinkling would probably occur as a response to trellis shear of fabric reinforcements. Film folds might cause surface defects in form of creases due to resin accumulation into the folds and even fabric distortions depending on the magnitude of the fold.

Results of the tensile tests for release films are depicted in Figure 6.12.c. All release films presented a narrow region of elastic deformation. The release film that required the lowest F/δ to deform in the plastic regime was NP1, which was also the thinnest film. The perforated release film showed an especially small strain to failure in the transversal direction (perpendicular-to-roll direction) because of tearing originated at the perforated holes.

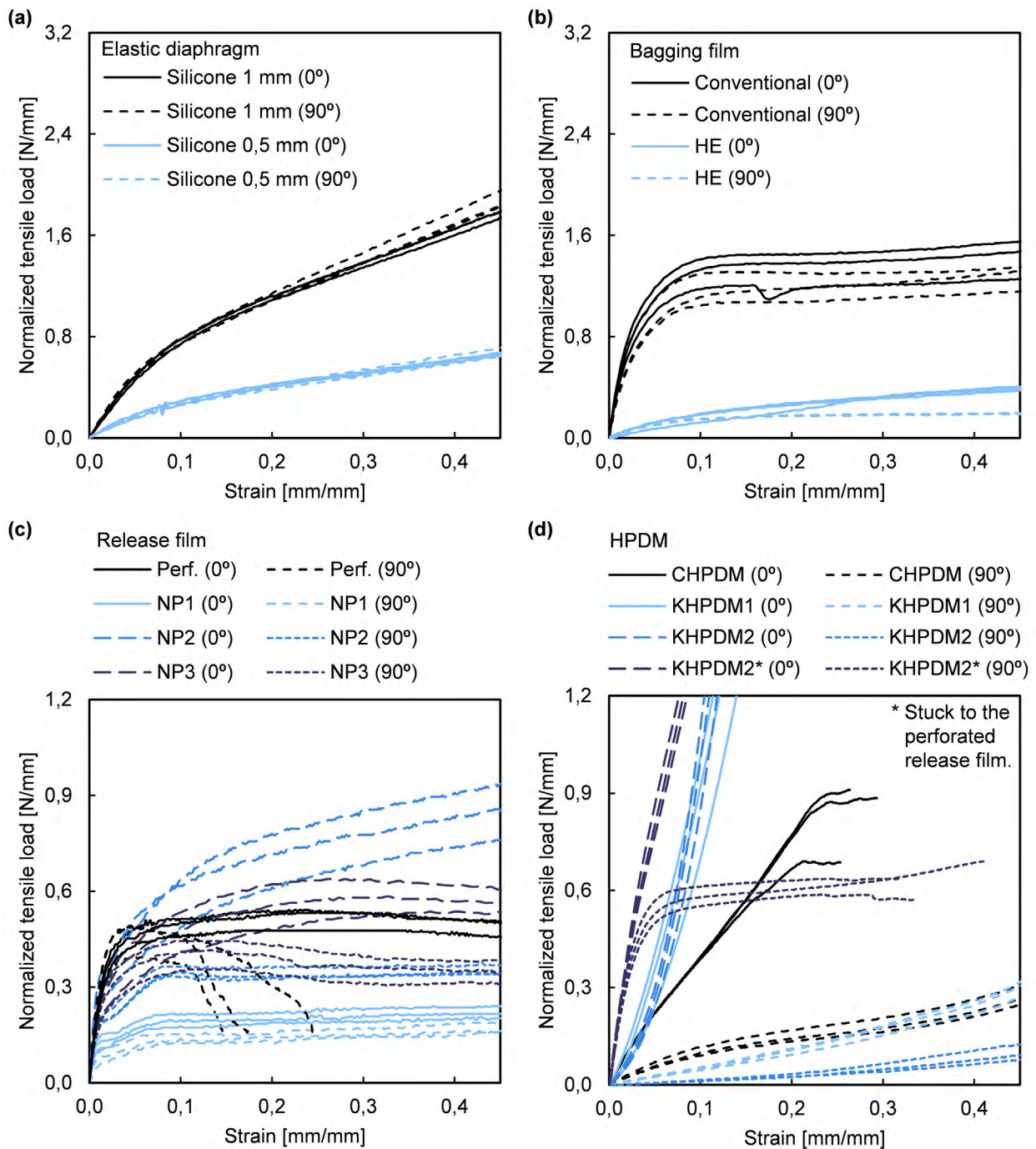


Figure 6.12. Results of the tensile tests of elastic diaphragms, and films and High Permeability Distribution Media (HPDM) listed in Table 6.2 (0° and 90° referring to longitudinal and transversal directions, respectively)

The premature failure of the perforated release film was partially mitigated when being tested in combination with KHPDM2, as shown in Figure 6.12.d; however, attained strain was only slightly larger than the strain taken as reference, $\varepsilon_D = 0,32 \text{ mm/mm}$. Although resistance did not drastically drop, tearing of the perforated release film along considerable regions would have prevented the release film to accomplish its main function, which is to guarantee a safe demoulding of specimens from KHPDM2 and the upper bagging film. In Figure 6.12.d, it can also be seen that

the combined behaviour of KHPDM2 and the perforated release film was actually the sum of their individual responses.

In case of HPDMs (Figure 6.12.d), CHPDM behaviour did not drastically differ from knitted meshes (KHPDM1 and KHPDM2). All meshes showed higher resistance to deformation in the longitudinal direction than in the transversal direction. CHPDM was an extruded mesh showing a diamond pattern, as can be seen in Table 6.2, in which the long and short diagonals were orientated with the loading direction for longitudinal and transversal direction testing, respectively. The diamond pattern deformed by orientating extruded filaments to the tensile loading until final failure.

If tests had been also conducted at $\pm 45^\circ$ directions, CHPDM would have shown even more rigidity with smaller strain to failure; while, knitted meshes would have distorted readapting the woven pattern to the loading direction and showing large deformation with low resistance as in case of the transversal direction. Therefore, in the forming experiments was important to orientate the longitudinal direction of KHPDM1 and KHPDM2 with the warp or weft directions of the reinforcement fabrics.

6.2.1.3. Ply-ply shear

The static coefficients of friction, μ_{st} , computed from the friction tests are depicted in Figure 6.13. At least five runs were conducted for each pair of materials in dry and wet conditions. μ_{st}^{wet} was calculated for those cases in which surface contact for involved materials remains saturated during the forming stage, only contacts between bagging film, and non-perforated release film and silicone diaphragm occur without resin implication.

Lubrication with the synthetic oil helped to reduce slippage resistance, $\mu_{st}^{wet} < \mu_{st}^{dry}$, between reinforcement fabrics and auxiliary materials, as well as variability between different runs; however, lubrication did not significantly affect static coefficients of frictions between reinforcement fabrics. Besides, saturation of fabrics tended to equalize static friction of pairs of materials including one of the reinforcement fabrics. Slippage resistance was minimum for textiles orientated at ± 45 between each other.

As expected, texturized surfaces (perforated release film and conventional peel-ply that were pushed against base materials by an intermediate HPDM layer) involved an increment in both μ_{st}^{dry} and μ_{st}^{wet} with respect to flat surface contact.

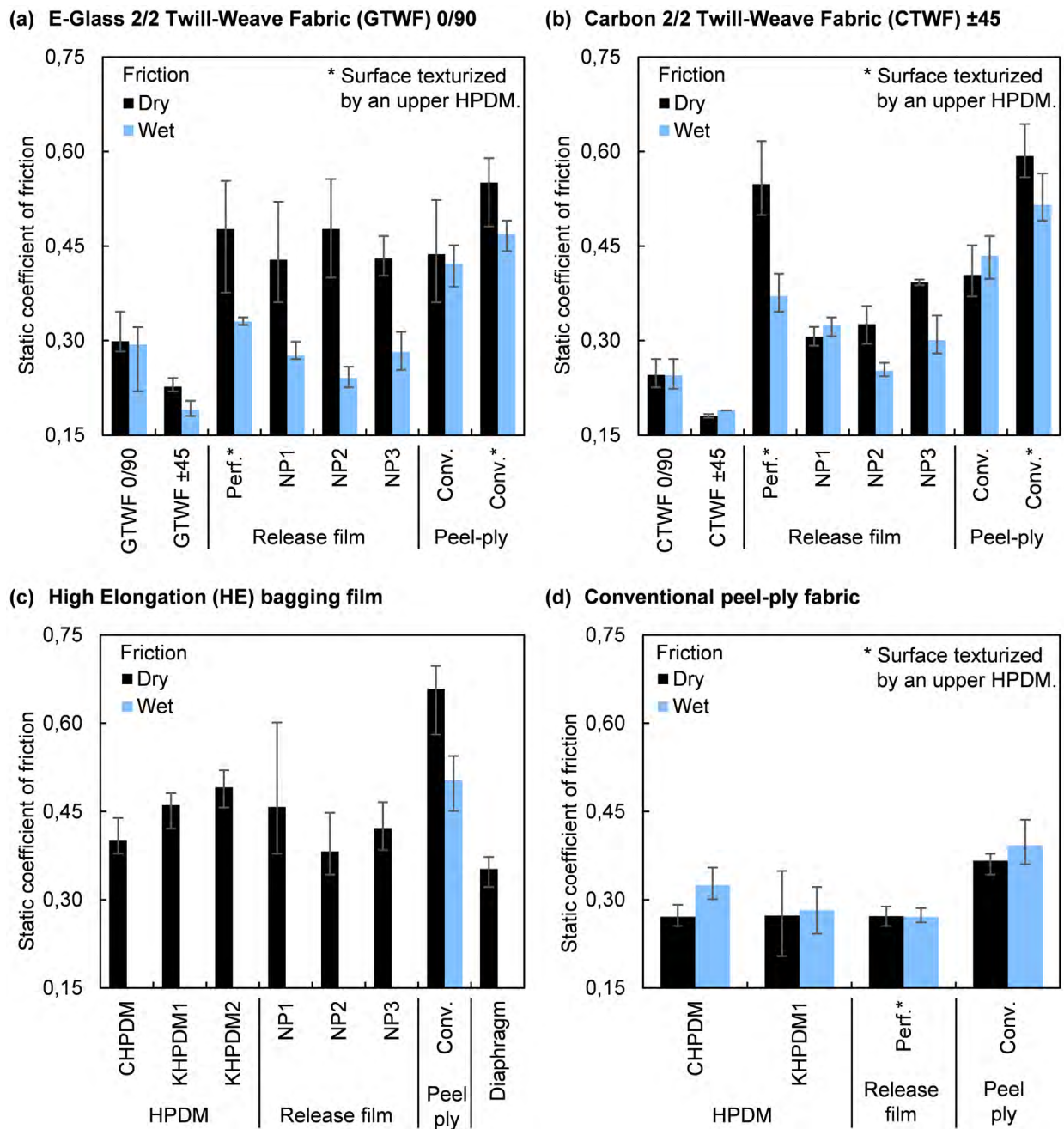


Figure 6.13. Static coefficients of friction of reinforcement and auxiliary materials of the preform assembly. Base materials are (a) GTWF, (b) CTWF, (c) HE bagging film and (d) conventional peel-ply fabric (error bars showing min. and max. values).

Conventional peel-ply showed high coefficients of friction with reinforcement fabrics and itself. μ_{st}^{wet} between reinforcement fabrics and conventional peel-ply was more than 50% higher than μ_{st}^{wet} between reinforcement fabrics and release films. While, μ_{st}^{dry} between silicone diaphragm and HE bagging film was lower than between HE bagging and release films.

Since intra-ply shear deformation in reinforcement textiles is also based on friction between yarns and between fibres, and lubrication did not significantly affect static friction; it would not

be expected a drastic change in trellis shear due to saturation of fabrics with a low viscosity matrix, although kinematic friction, not static, is really occurring.

Friction between HE bagging film and different HPDMs was measured, in spite of not expecting slippage between both materials; since, due to the high flexibility of HE bagging film, it adapts to the intricate extruded or woven pattern of this kind of polymeric meshes.

6.2.2. Formability of hemisphere shape specimens

In order to illustrate ISFLILP processing, some of main steps of the flowchart detailed in Figure 6.3 carried out to manufacture hemisphere shape specimens are depicted in Appendix B.

The main deformation mechanism involved in forming of hemisphere shape specimens is intra-ply shear; since all preforms are orthotropic, having ply-ply shear a minimal effect due to the non-pronounced curvature of the geometry. In case of being quasi-isotropic, the impact of ply-ply shear would have been larger due to different main directions of deformation between layers.

A total of four hemisphere shape specimens were manufactured through ISFLIP to analyse the effect of (I) different HPDMs and (II) peel-ply fabric/release film on formability of the whole assembly. Besides, (III) different orientations with respect to the double diaphragm tooling were also addressed. Specimens are shown in Figure 6.14 (warp and weft yarns orientated in directions x and z).

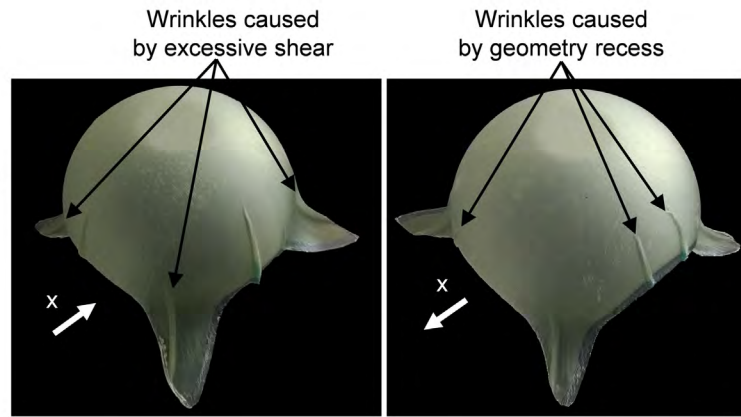
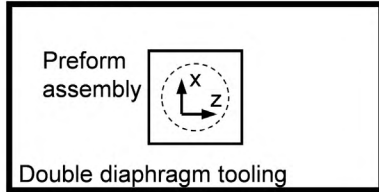
Wrinkles caused by excessive shear and by geometry recess appeared in all the specimens (Figure 6.15). Wrinkles caused by excessive shear occurred because from a certain shear angle, the required energy to continue the in-plane deformation was higher than to start out-of-plane deformation; while, wrinkles caused by geometry recess were induced by membrane compression loads transferred to the preform assembly because of the elastic recovery of the diaphragms, that reduced the stretching level to conform to the shape.

It is worth emphasizing that out-of-plane deformation was not only limited to the preform, but also the rest of materials of the preform assembly and both elastic diaphragms. Consequently, due to large bending rigidity of the whole stack, out-of-plane deformation was concentrated in a few large wrinkles, rather than in many small wrinkles.

In specimens A1, A3 and A4, direction x (flow direction through the HPDM) was aligned with the long side of the double diaphragm tooling. The rotation of 45° of the preform assembly with respect to the double diaphragm tooling (specimen A2) resulted in a reduction of the number and magnitude of the wrinkles caused by geometry recess. Mitigation of this kind of wrinkles could be

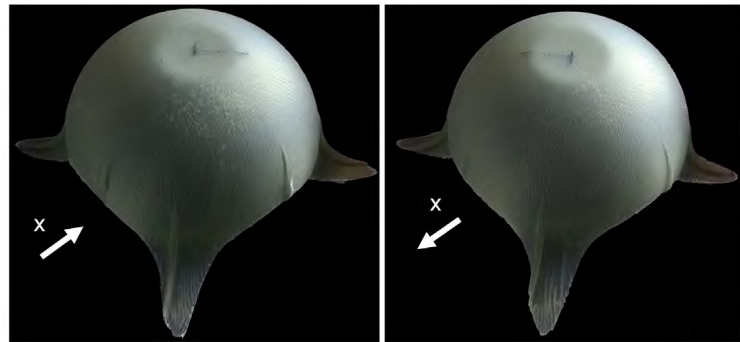
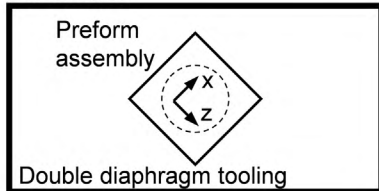
- (a) Specimen A1**
Preform assembly
 HE bagging film
 KHPDM1
 Conv. peel-ply (upper release layer)
 GTWF [(0/90)]₉
 Release film NP1 (lower release layer)

Orientation



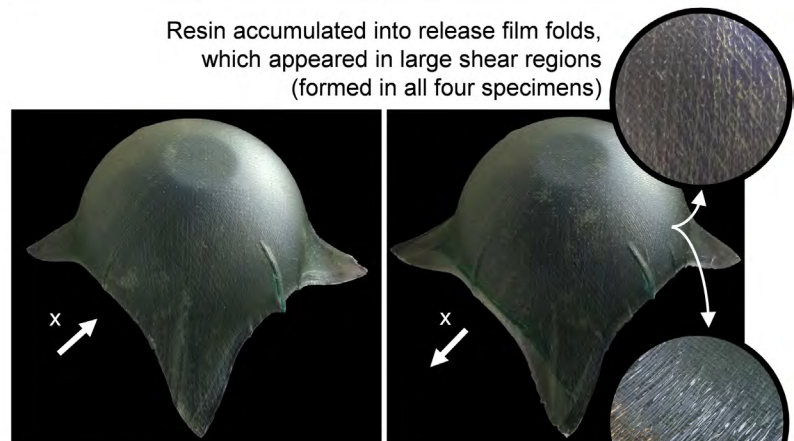
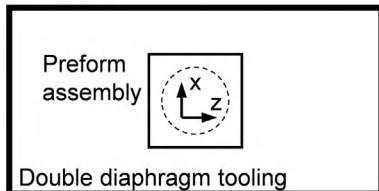
- (b) Specimen A2**
Preform assembly
 HE bagging film
 KHPDM1
 Conv. peel-ply (upper release layer)
 GTWF [(0/90)]₉
 Release film NP1 (lower release layer)

Orientation



- (c) Specimen A3**
Preform assembly
 HE bagging film
 KHPDM2
 Perf. release film (upper release layer)
 GTWF [(0/90)]₉
 Release film NP1 (lower release layer)

Orientation



- (d) Specimen A4**
Preform assembly
 HE bagging film
 CHPDM
 Conv. peel-ply (upper release layer)
 GTWF [(0/90)]₉
 Release film NP1 (lower release layer)

Orientation

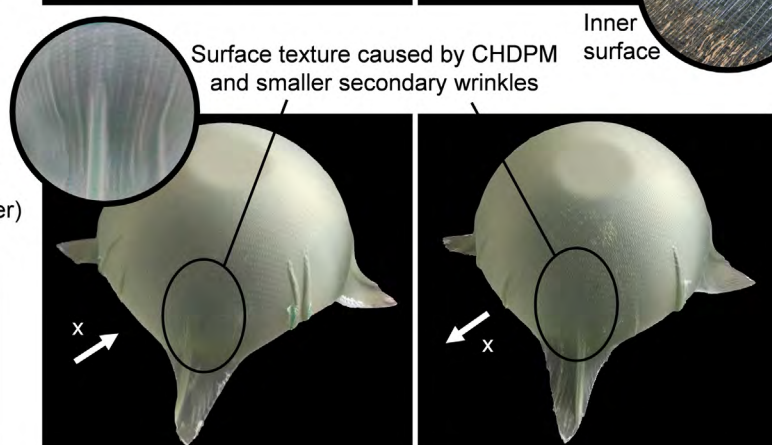
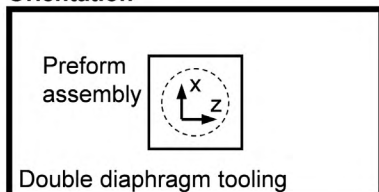


Figure 6.14. Hemisphere shape specimens: preform assembly and orientation details, and isometric views (flow direction through HPDM in direction x).

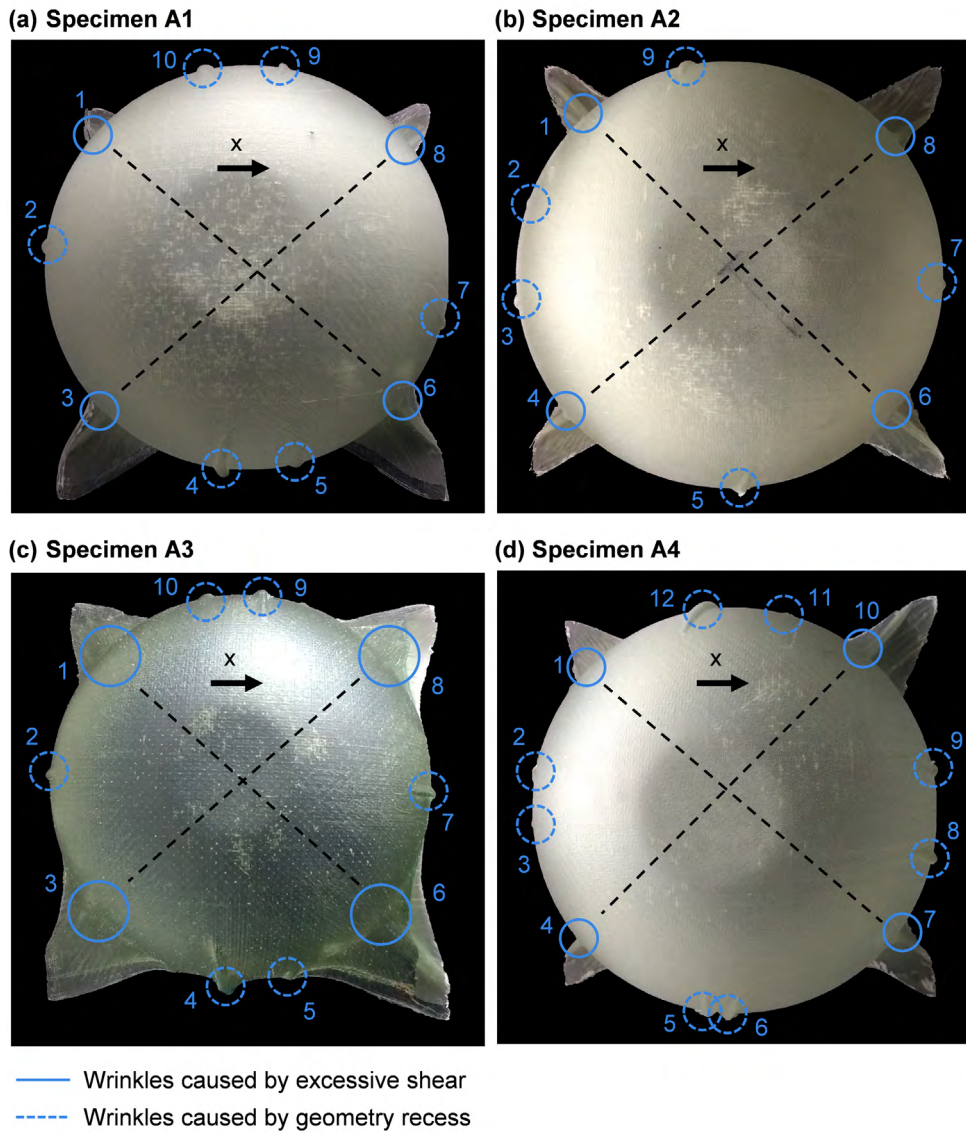


Figure 6.15. Hemisphere shape specimens: top views.

addressed by placing different obstacles into the mould cavity or even modifying the geometry of the cavity to alter the deformation sequence of the whole assembly.

Unexpectedly, combination of KHPDM2 and the perforated release film involved a considerable stiffness increment of the preform assembly, resulting in a poor adaption to the hemisphere mould (Figure 6.14.c). Formed wrinkles were not more severe, which is comprehensible since the preform did not conform to the geometry in the regions that required larger shear.

The lower face of all preforms was covered with the release film NP1. Although it seemed that it did not affect formability of the whole assembly; the release film folded in regions of large shear, causing resin accumulation into these folds and, thus, the appearance of surface imperfections. Low bending stiffness of release film due to its small thickness and compression loads transferred

from the reinforcement textiles to the film caused by intra-ply shear led to the formation of these folds. A detail picture of resin creases formed from film folds is shown in Figure 6.14.c.

The perforated release film used as upper release layer in specimen A3 also folded in regions of large shear; however, surface imperfections created by these folds can pass unnoticed because of the surface texture transferred to the specimen by KHPDM2, which partially masked surface creases (Figure 6.14.c).

It is worth noting that elastomeric bagging films and diaphragms did not apparently form individual wrinkles or folds. In case of diaphragms, because of their large thickness (in comparison to the rest of materials); but, the elastomeric bagging film, with similar thickness of release films, did not seem to form additional folds too.

Although wrinkle formation was not massively worse in case of using a conventional extruded mesh, CHPDM, instead of KHPDM1; in regions of large shear, CHPDM formed secondary wrinkles that were transferred to the upper surface of the specimen in form of surface waviness as can be seen in Figure 6.14.d.

Figure 6.16.a shows the result of a drape simulation based on a purely kinematic approach of a single layer of GTWF over the hemisphere geometry (including diaphragm thickness). The individual layer was initially laid up on directions x and z from the pole O without shearing, and then sheared to accommodate the doubly curved shape. Even considering the largest locking angle, $\gamma_{lock} = 41,2^\circ$, measured through the bias-extension test, an individual layer of GTWF could not have been able to adapt to the hemisphere shape without forming wrinkles.

Nevertheless, distribution of shear angles shown in Figure 6.16.a did not resemble the real behaviour of the preform during ISFLIP forming; since the maximum shear angles measured directly from specimen before arising out-of-plane deformation were considerably smaller, as can be seen in Figure 6.16.b. The maximum shear angle measured in specimen A1 was 22° , significantly smaller than γ_{lock} for GTWF. However, shearing capacity of the conventional peel-ply was increased, since most measurements resulted in angles larger than $\gamma_{lock} = 12,1^\circ$.

Furthermore, it was measured the distance from the pole of each specimen, following the contour of the specimens, to the starting points of the wrinkles, being the maximum distance covered by the hemisphere shape 225 mm. As in case of shear angles and as can be observed in Figure 6.14, there were not substantial changes between specimens, which can lead to the conclusion that diaphragms and preforms dominated the forming behaviour. Auxiliary materials had secondary roles, although their effects cannot be neglected.

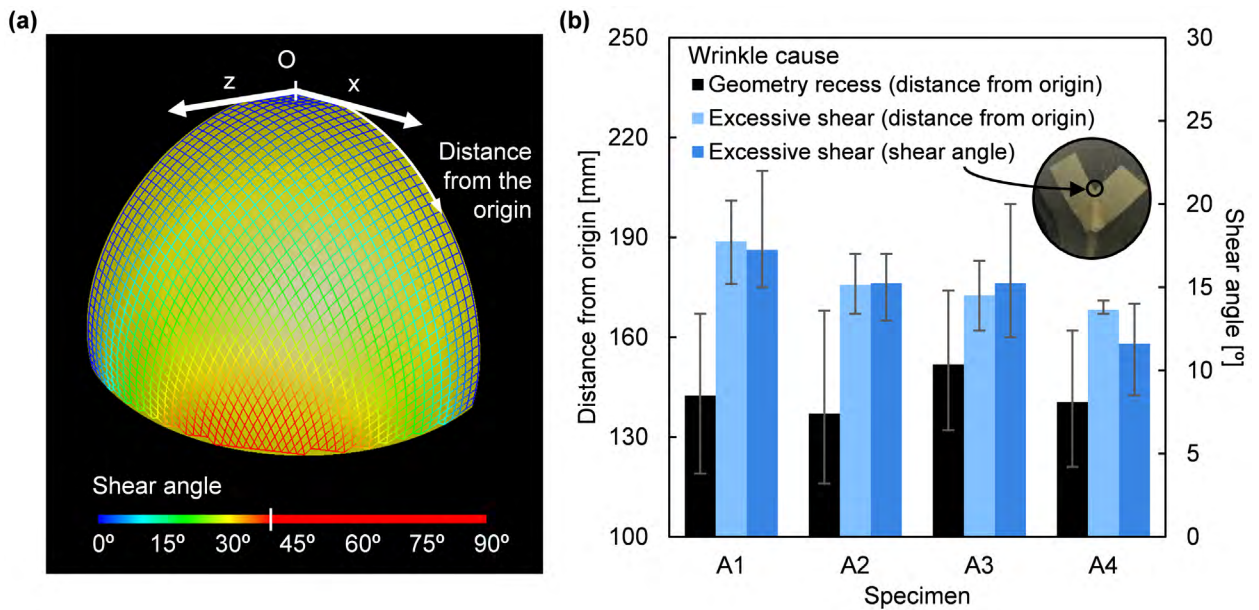


Figure 6.16. (a) Shear angles resulting from kinematic draping over the hemisphere geometry (including diaphragm thickness) with LMAT Interactive Drape software, and (b) measured location (distance from origin) and shear angle at the initial point of wrinkles (error bars showing min. and max. values).

Wrinkles caused by geometry recess formed later in specimen A3 than in the rest of specimens, which can be explained by the poor adaption to the hemisphere shape. In addition, distance measurement in case of wrinkles caused by excessive shear agreed with measured shear angles before wrinkle formation, larger distances corresponded to larger shear angles. Wrinkles formed even later than expected according to kinematic draping, which was possible because of the different forming sequences. In ISFLIP tests, preform were not laid up firstly in warp and weft directions as happened in the drape simulation (directions x and z , respectively).

Finally, it is worth pointing out that porous area fractions of each specimen, although not being measured, seemed to be close to those obtained in Chapter 5, perhaps slightly larger due to the additional flow resistance offered by peel-ply envelopes around the spiral tubes. Specimen A1 showed larger porous area fraction because an improper execution of the procedure of turning the inlet channel into a vent.

6.2.3. 'C' cross-section profiles

In order to illustrate ISFLIP processing, some of main steps of the flowchart detailed in Figure 6.3 carried out to manufacture 'C' cross-section profiles are depicted in Appendix B.

6.2.3.1. Formability

In forming of 'C' cross-section profiles with joggles, both intra-ply shear and ply-ply shear were involved: intra-ply shear in joggle regions and ply-ply shear in bending over tight radii.

A total of four specimens were manufactured through ISFLIP to discern attainable pronounced single and double curvature shapes, and analyse the effect of (I) different HPDMs and (II) peel-ply fabric/release film on formability of the whole assembly. Formed specimens are shown in Figure 6.17 (warp and weft yarns orientated in directions x and z).

Specimen B1 consisted on an orthotropic preform of GTWF (220x320 mm), formed over the aluminium supporting structure; therefore, B1 resulted in a small inner radius of the bending regions of 3 mm. The rest of specimens consisted on orthotropic preforms of CTWF (450x320 mm).

In single curvature regions, no wrinkles were formed, even in case of the small bending radius of specimen B1; hence, slippage between layers was enough to accommodate the required translation between layers. In doubly curved regions, wrinkles of the whole stack, as well as release film folds happened.

In case of specimen B2 (simple joggles), although only subtle wrinkles could be appreciated in the outer surface (Figure 6.17.b), out-of-plane deformation reached the inner surface too. Joggles introduced in the addressed geometries were far more pronounced than typical joggles present in FRP components whose manufacturing process included a forming step.

In case of specimens B3 and B4, wrinkling was more severe. Although apparently similar, wrinkles formed in specimen B3 extended from the outer to the inner surface (Figure 6.17.c); while, in specimen B4, wrinkle morphologies of the outer and inner surfaces differed between each other, pointing out the formation of fabric folds into the preform during the forming stage (Figure 6.17.d). This can be explained by the higher bending rigidity of preform assemblies including KHPDM2 and the perforated release film, as also detected in hemisphere shape specimens.

After analysing formability of presented geometries through kinematic draping (Figure 6.18), it was observed that in case of double joggle specimens, required shearing would have exceeded the locking angle of CTWF. In the drape simulations, after laying up the horizontal section of the fabric, the ply was laid up onto the vertical sections from the large 'C' cross-section side to the small 'C' cross-section side (from right to left in Figure 6.18.a and Figure 6.18.b).

(a) Specimen B1

Preform assembly

HE bagging film

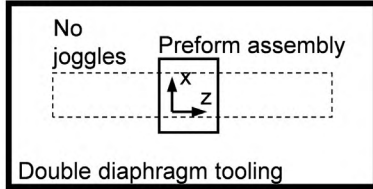
KHPDM2

Perf. release film (upper release layer)

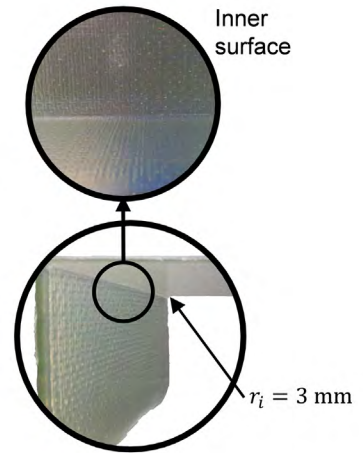
GTWF [(0/90)]₉

Release film NP1 (lower release layer)

Orientation



No defects such as wrinkles or surface protuberances appeared.



(b) Specimen B2

Preform assembly

HE bagging film

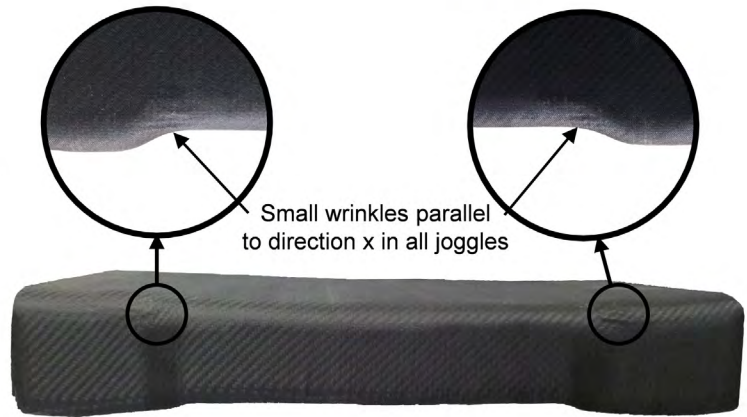
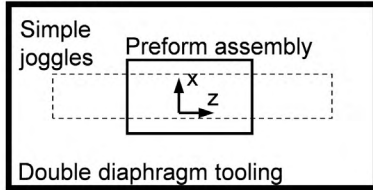
KHPDM1

Conv. peel-ply (upper release layer)

CTWF [(0/90)]₉

Release film NP1 (lower release layer)

Orientation



(c) Specimen B3

Preform assembly

HE bagging film

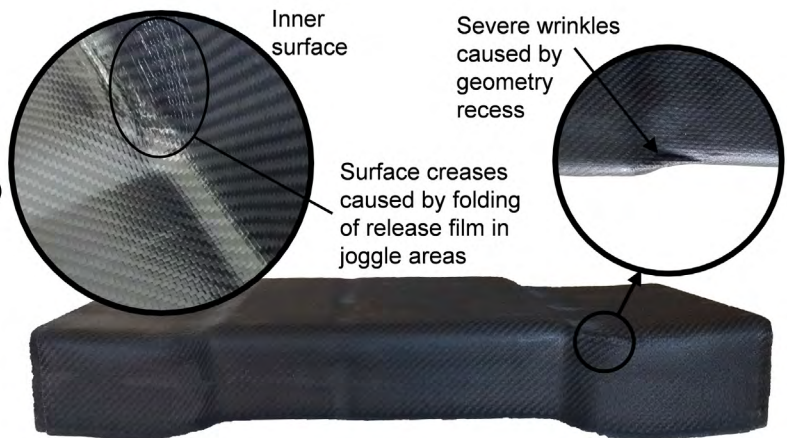
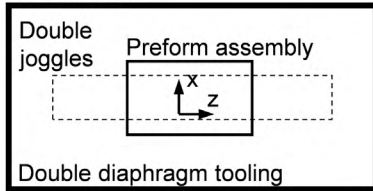
KHPDM1

Conv. peel-ply (upper release layer)

CTWF [(0/90)]₉

Release film NP1 (lower release layer)

Orientation



(d) Specimen B4

Preform assembly

HE bagging film

KHPDM2

Perf. release film (upper release layer)

CTWF [(0/90)]₉

Release film NP1 (lower release layer)

Orientation

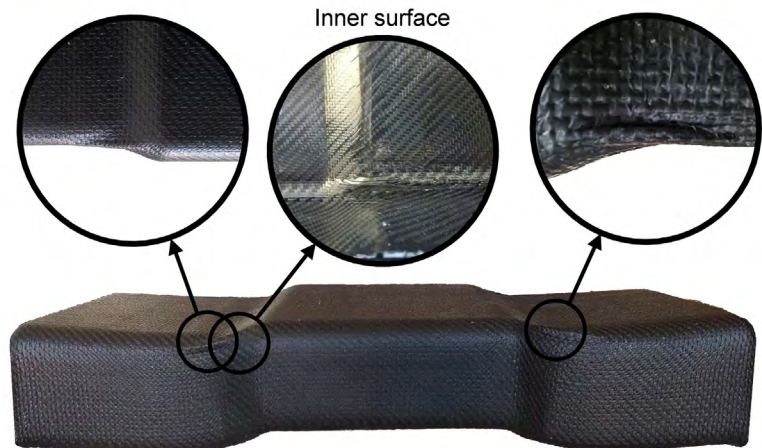
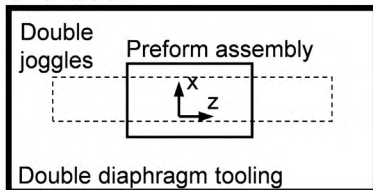


Figure 6.17. 'C' cross-section profile specimens: preform assembly and orientation details, and perspective views (flow direction through HPDM in direction x).

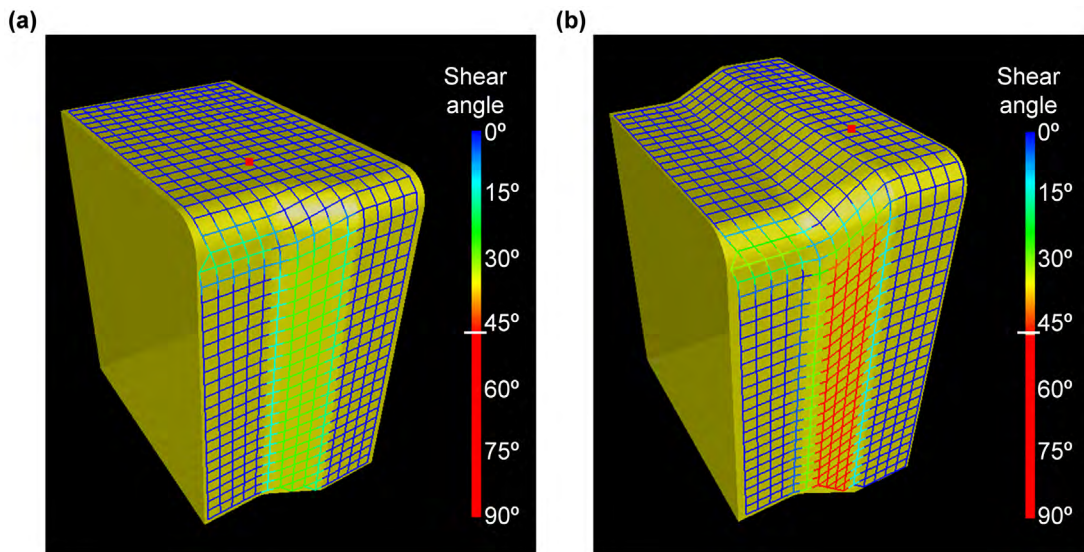


Figure 6.18. Shear angles resulting from kinematic draping over the joggle geometries of the moulds (including diaphragm thickness) of the 'C' cross-section profiles with LMAT Interactive Drape software: (a) simple joggle and (b) double joggle.

In ISFLIP specimens, wrinkles were not formed where maximum shearing was depicted in Figure 6.18, but in the 90° bending region of the joggles because of a different forming sequence. After laying up the horizontal section of the preform assembly, the stack started to be laid up onto the vertical sections of the geometry simultaneously, requiring smaller shear angles, but forcing the out-of-plane deformation of the whole assembly in the corner region of the joggle. Measured shear angles in the vertical sections of the joggles were 13°(+5°/−4°) for specimen B2, 18°(+1°/−2°) for specimen B3, and 19°(+2°/−4°) for specimen B4.

As in case of the hemisphere shape specimens, release films (perforated and non-perforated NP1) folded in areas of large shear (joggles) as shown in Figure 6.17.c. The rest of inner surface of the specimens was mostly free of surface creases caused by release film folds, both flat surfaces and corners; however, in the proximity of the joggle sections, release film folds extended to flat areas and along the corners. A smooth surface finish was achieved in those areas with no resin protuberances caused by film folds.

6.2.3.2. Inter-Laminar Normal Strength (ILNS)

A series of 'L' shape samples were trimmed from specimen B1 and B2 and tested to evaluate their through-thickness mechanical behaviour (Figure 6.19). Each set of samples included one type of textile reinforcement, and showed different dimensions of the curved portion (Figure 6.19.a and Figure 6.19.b). Sample width of each set of samples was determined in order

to include at least twenty yarns. In case of specimen B1, severe thinning occurred due to the sharp bending radius. Mean thickness of the central cross-section of the curved region was only 77% of the mean thickness of the specimen in flat regions. In specimen B2, the mean thickness of the central cross-section was 94% of the mean thickness in flat regions.

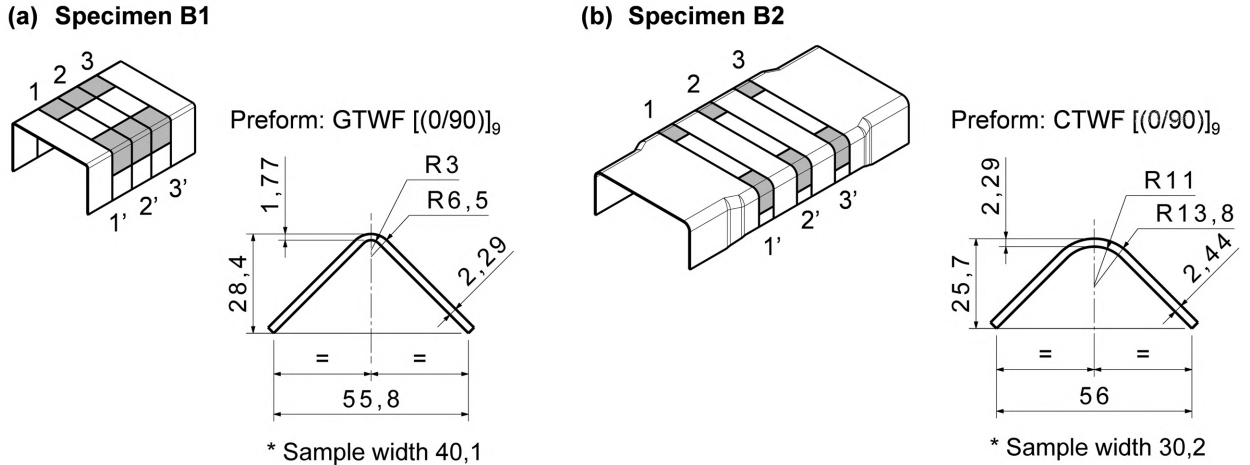


Figure 6.19. Schematic drawing of 'L' shape samples location into each specimen and average dimensions (dimensions in mm).

Figure 6.20.a shows a characteristic load vs crosshead displacement curve of the compression test of 'L' shape samples, showing a quite linear behaviour until fatal failure. Besides, in Figure 6.20.b, it is enlarged the area of the curve comprising the loading-unloading hysteresis loop to estimate the kinematic coefficient of friction between sample edges and the supporting plate. The close loop resembled accurately enough the ideal hysteresis loop depicted in Figure 6.10.

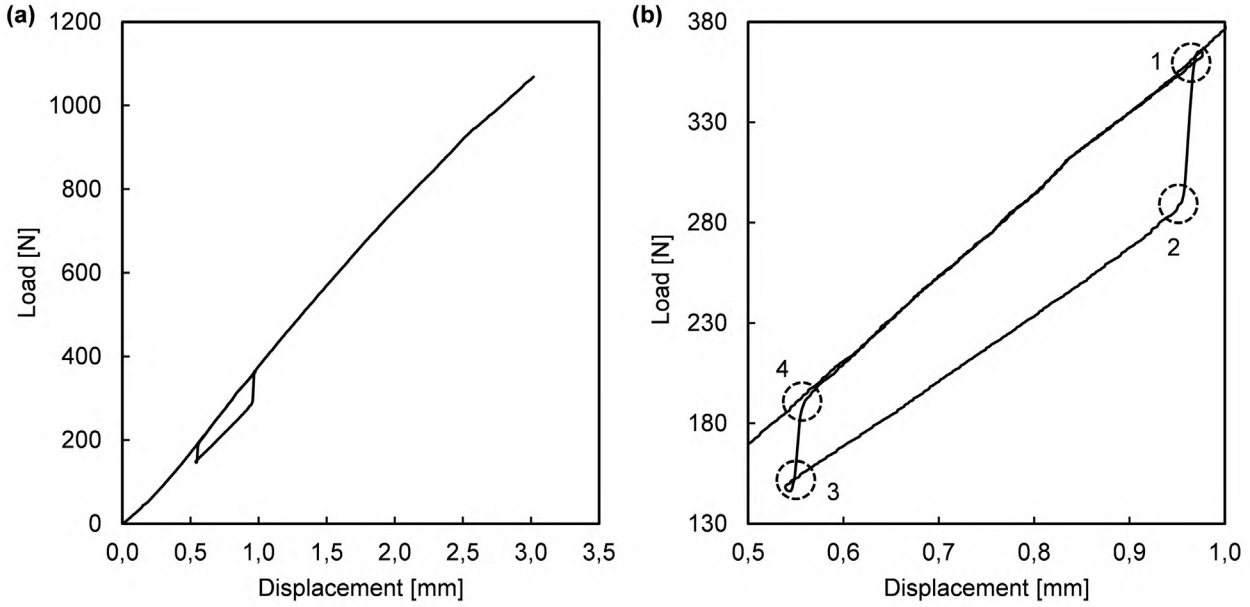


Figure 6.20. Load, F , vs. crosshead displacement, δ , curve of sample B22': (a) complete curve and (b) detail of loading-unloading hysteresis loop for computing the kinematic coefficient of friction.

The results of the compression tests are shown in Figure 6.21. Applied loads, F , at failure and the corresponding CBS are presented in Figure 6.21.a. CBS levels of specimen B2 were considerably larger than of specimen B1 due to geometry reasons: larger thickness and ratio r_m/h (4,4 and 10,6 for specimens B1 and B2, respectively). Good agreement between applied loads and obtained CBS was achieved, in spite of the different hypotheses made.

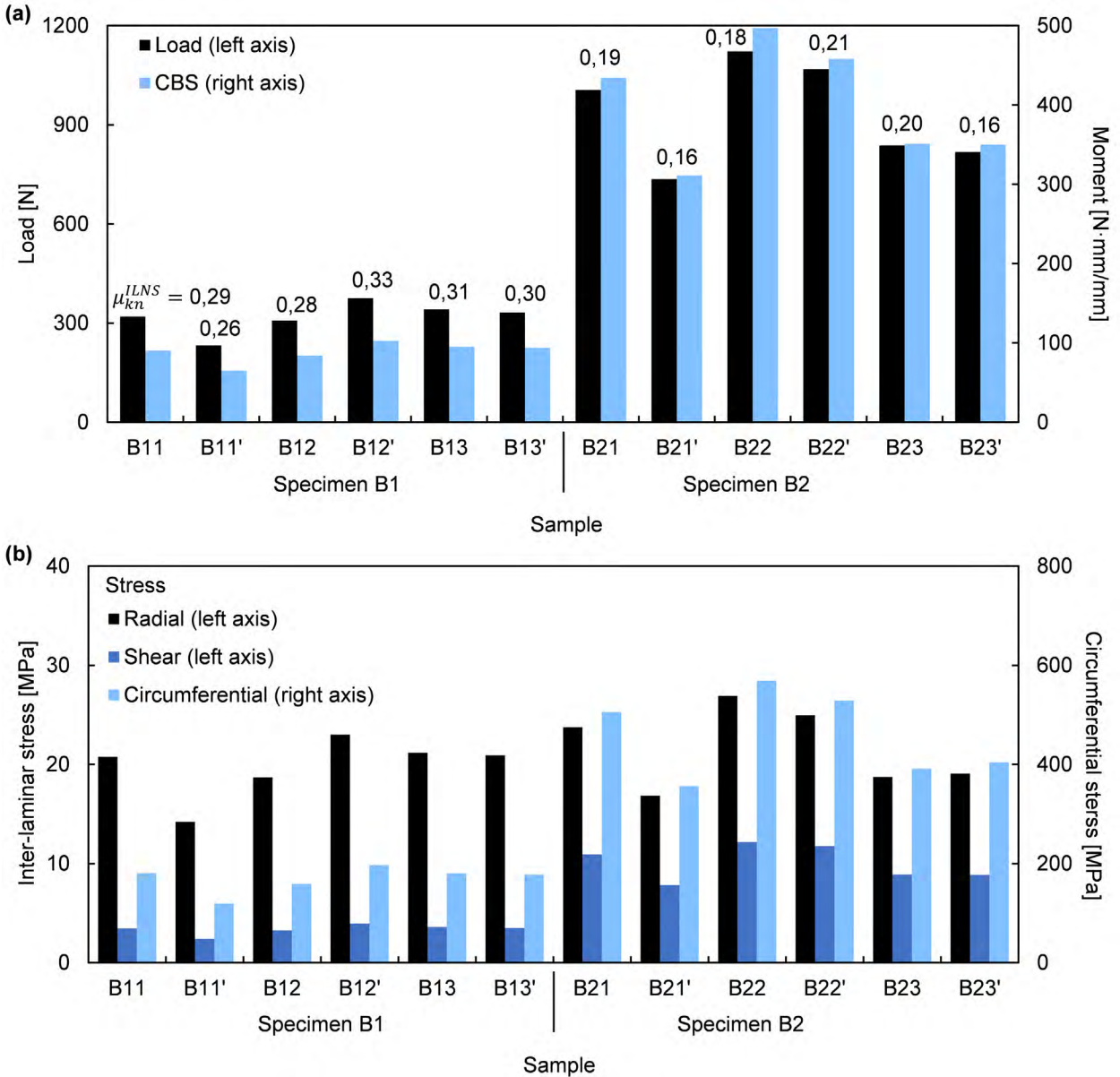


Figure 6.21. Results of the compression tests of 'L' shape samples: (a) crosshead load at failure and Curved Beam Strength (CBS), and (b) resultant stresses at failure.

In Figure 6.21.b, apart from radial stresses at failure, σ_{rM} , circumferential and shear stresses, $\sigma_{\theta M}$ and $\tau_{r\theta}$ respectively, are also represented. Both parameters were estimated without accounting for curvature effects such that

$$\sigma_{\theta M} = \frac{6M}{wh^2} \quad (45)$$

$$\tau_{r\theta M} = \frac{3}{4} \frac{F}{wh} \quad (46)$$

Both estimations gave a conservative value of the real stress state [311], but served as a good indication.

In case of specimen B1, both $\sigma_{\theta M}$ and $\tau_{r\theta}$ showed low levels. It is worth recalling that mean flexural strength computed in Chapter 5 of orthotropic GTWF specimens was 552 MPa. In case of specimen B2, $\sigma_{\theta M}$ reached significant levels of stress; since flexural strength of flat orthotropic CTWF specimens is ~ 750 MPa. Nevertheless, as it will be checked hereafter, samples failed by delamination; thus, it was still considered that ILNS corresponded to estimated σ_{rM} depicted in Figure 6.21.b.

Although it seemed that release film folds were only causing surface defects, those samples with surface imperfections resulted in lower σ_{rM} : B11', B21', B23 and B23'. Mean ILNS of orthotropic GTWF samples (specimen B1) which did not show surface defects was 20,9 MPa (14,2 MPa in case of sample B11', a reduction of 32%), and mean ILNS of orthotropic CTWF samples (specimen B2) which did not show surface defects was 25,2 MPa (18,2 MPa in case of samples showing surface defects, a reduction of 28%).

6.2.3.3. Ply distortions

Some of the samples tested in compression to assess ILNS were also analysed through light microscopy in order to look for possible interior fabric distortions caused by ply-ply shear. A couple of micrographs per specimen are shown in Figure 6.22.

Adequate sample failures were observed in all micrographs, since delamination occurred across sample width instead of failure of inner and outer surfaces due to circumferential stresses. Cracks propagated between layers as expected, passing through fibre yarns occasionally.

Although in the micrographs, multiple delamination cracks could be observed, most of them were concentrated between plies 1 and 2, between plies 2 and 3, and between plies 3 and 4 (being ply 1 the ply of the inner surface). Inter-laminar cracks were closer to the inner surface than it should be according to the predicted location of maximum radial tensile stresses, $\sqrt{r_o r_i}$. These predicted locations of delamination origins should have been located at $0,44h$ and $0,48h$ from the inner surface of the samples for specimens B1 and B2, respectively.

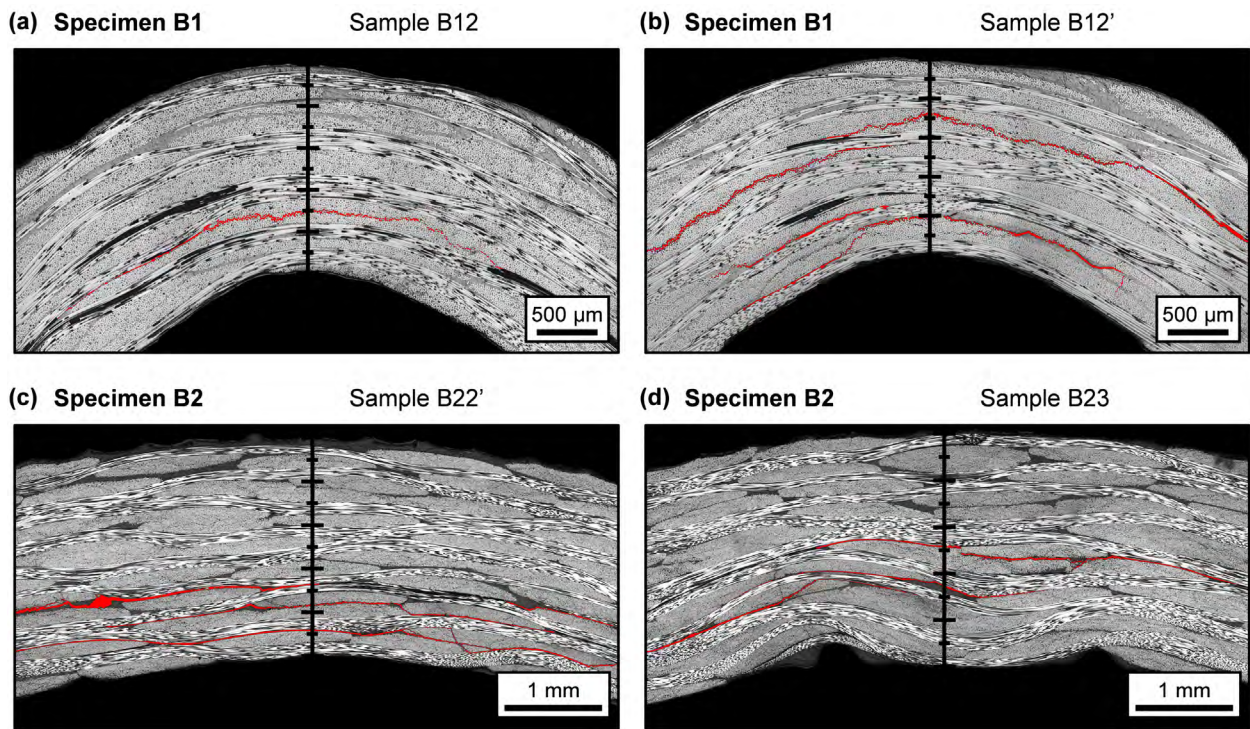


Figure 6.22. Micrographs of 'L' shape samples, highlighting inter-laminar cracks (red).

Since Equation (39) assumes that σ_{rM} takes place at $\sqrt{r_o r_i}$ and the real radial location, r , was closer to the inner surface, it should be expected that Equation (39) was slightly underestimating σ_{rM} .

It must be pointed out that both Lekhnitskii's analytical formulation [312] and Equation (39) assume that anisotropic materials are homogeneous. Therefore, attempts of measuring ILNS in FRP curved specimens are often carried out on UD samples with fibres orientated in the circumferential direction. Samples tested in the present work were far away from being homogeneous in the through-the-thickness direction due to the orthotropic nature of both textile fabrics.

In Figure 6.22.d, it can be observed large resin creases on the inner surface and how fabric waviness was affected, causing a notable distortion of fabrics through the thickness of the sample. Although to a lesser degree, more fabric distortions were also appreciated in other samples containing surface defects.

6.3. Discussion

Forming attempts such as stamping and diaphragm forming are common in the field of FRP manufacturing; hence available literature on this respect is vast. However, normal approaches deal with stacks of textile reinforcements showing similar deformation mechanisms, which does not

mean that interactions between subsequent layers may not be challenging. In quasi-isotropic preforms, for example, due to the phase difference between in-plane principal directions of deformation of subsequent layers, formability is considerably restricted [111,112]. In ISFLIP, the challenge is pushed one step forward since preforms are formed together with a series of auxiliary materials typical of VI. Most of these materials showing different deformation mechanisms.

Consequently, a series of preliminary experiments were conducted to address, in a first instance, the viability of obtaining successful parts made through ISFLIP, and then assess the interactions between different materials present in the preform assembly and limitations imposed over attainable shapes. Auxiliary materials evaluation was mainly focussed on comparing different HPDMs, and confronting the behaviour of release films and peel-ply as demoulding layers. Two different geometry types were tested: a relatively uniform doubled curved shape (hemisphere) and a single curvature shape with highly doubled curved small regions ('C' cross-section profiles with joggles).

Before going further in the discussion of the results presented in the previous section, some comments are made in reference to ISFLIP manufacturing. First of all, it is worth emphasizing that concepts presented in Chapter 3 were perfectly implemented to obtain FRP components through ISFLIP. These components were not free of forming defects, because the proposed analyses aimed to test ISFLIP limits. The VI methodology developed in previous chapters was successfully applied into ISFLIP processing sequence, achieving porosity levels similar to those presented before. Peel-ply wound around spiral tubes to prevent HE bagging film failure by tearing slowed down preform filling. However, the minimum pressure difference between the interior of the preform assembly and into the cavity formed by both diaphragms reduced significantly stress levels exerted on the bagging film; therefore, in future experimentation, peel-ply envelopes might be removed from the preform assembly to avoid increasing the filling time.

On the other hand, ISFLIP, as a double diaphragm forming variant, present some operational limitations which, unlike stamping, cannot be corrected *a posteriori*. In stamping, forming behaviour of reinforcement stacks can be altered by controlling the forces exerted by the blank-holder [176]. Corrective measures in diaphragm forming are difficult to be successfully implemented, highlighting the importance of previous forming simulation.

In ISFLIP experiments, although effects of tested auxiliary materials on final component quality were noticeable, formability was dominated by diaphragms and textile preforms. Diaphragms have to main functions: transmit membrane loads to the preform and serve as an out-of-plane support to avoid wrinkle formation. However, in-plane deformation mechanisms of elastomeric

diaphragms and typical woven reinforcement fabrics are completely different, which can lead to serious forming limitations.

As introduced in the literature review [104,105], due to the combined compaction-shear loading, the capacity of textile fabrics of shearing without inducing out-of-plane deformation was notably reduced with respect to the simple loading case, measured through the bias-extension test. Locking angles, γ_{lock} , were decreased by a factor of two in hemisphere shape specimens.

Nevertheless, conventional peel-ply showed larger shear angles in hemisphere shape specimens than γ_{lock} in bias-extension tests. In double diaphragm forming, apart from the obvious combined compaction-shear loading, membrane tension stresses transmitted by diaphragms play a key role. In spite of being expected that peel-ply acted as a barrier to formability, it was not the case and it would be interesting to explore peel-ply fabrics with more opened and/or twill weaves in future research.

Effects of CHPDM and release films on specimen quality were negative, both inducing surface defects which lead to fabric distortions, as proved in case of release films through compression tests of 'L' shape samples and light microscopy; although they did not seem to significantly affect overall formability. Trellis shear of woven fabrics involves extension in one direction, while shortening in the perpendicular one. This combination of tensile and compressive stresses exerted on thin films, with low bending stiffness, caused release film folding in areas of large preform shear.

In forming processes of prepreg stacks, it is common to cover both part surfaces with release films to avoid material contamination, resulting in similar folds causing surface defects in ISFLIP; although of smaller magnitude, since shearing levels reached are lower. Nevertheless, in case of prepregs, the later autoclave processing removes surface defects leading to smooth surface finishes.

Instead of release films showing narrow elastic deformation regimes, elastomeric films, able to hold large elastic strains, could totally, or at least partially, accommodate shortening caused by trellis shear if they were previously stretched. However, it is worth noting that involved strain levels are high; since for a shear angle of $\gamma = 20^\circ$, strains associated to the diagonals of the unit cell of the woven fabric would be $\varepsilon_D = 0,16$ mm/mm (extension) and $\varepsilon_d = -0,19$ mm/mm (shortening). Stretching of the elastomeric films could be induced during the preparation of the preform assembly or throughout the same forming stage.

Slippage between successive layers is fundamental to minimize forming restrictions added by the distinct in-plane deformation mechanisms shown by different materials. Although tensile loads

exerted by elastic diaphragms on the preform assembly governed the forming process, limiting in-plane loads transferred between the diaphragms and the preform could help the adaption of the whole stack to complex shapes and even reduce wrinkling caused by geometry recess. Out of the preform, due to high static coefficients of friction, μ_{st} , associated to the conventional peel-ply and the impossibility of HE bagging films of sliding over any HPDM due to bagging film collapse during post-filling, slippage between bagging films and diaphragms would be necessary; however lower μ_{st} would be still required, which could be achieved by applying any lubrication agent between both polymeric sheets.

An interesting point on respect to friction between fabric reinforcements is that the lowest μ_{st}^{wet} among all pairs of materials were obtained in case of fabric $\pm 45^\circ$ misalignment. Forming limitations in case of quasi-isotropic preforms is a well-known problem [111,112]. Due to different principal in-plane directions of deformation, large displacements between consecutive plies are necessary, which is a problem when reinforcements move into a high viscous medium. Besides, under these conditions, dependence of friction between reinforcement layers on normal pressure and temperature is significant [114,115]. Conversely, the low friction between misaligned consecutive layers saturated with a low viscosity resin and the capacity to form a preform over a tight radius shown by ISFLIP seemed to be good reasons to be optimistic on formability of quasi-isotropic preforms in ISFLIP.

The functional prototype showed an effective performance during the manufacturing of the different specimens. The key element of the prototype, the double diaphragm tooling, fulfilled perfectly its function, allowing an easy and fast preparation of the preform assembly, and serving as a good flat support of the preform assembly once being clamped; nevertheless, some aspects of the vacuum table and potential moulds raised concerns.

During the forming stage of ISFLIP experiments, it was observed that once the lower diaphragm and the vacuum table were brought into contact, no sliding between them happened. ISFLIP prototype did not facilitate slippage because of the adoption of a perforated aluminium plate with large open area to guarantee vacuum transmission; which might become an important restriction to attainable shapes, particularly in concave shapes. Additionally, sliding between the lower diaphragm and moulds should be also enhanced.

A great advantage of ISFLIP is the possibility of using moulds with no special surface preparation, which facilitated prototyping of moulds used in this work. Actually, the only relevant requirements that moulds have to fulfil are no collapse under compressive pressures exerted due to the pressure difference between the ambient and the air-tightly sealed mould cavity, service

temperature higher than maximum temperature reached along the manufacturing process, and guaranteeing ultimately air evacuation (fundamental in case of concave shapes). Although elastic diaphragms acted as surface softener, irregularities of the modular 'C' cross-section profiles were transferred to specimens; hence, some fine mould details can be transferred between moulds and parts, not only rough details.

It is worthwhile making a last comment on obtained values of ILNS in order to give an appropriate context to the results. As pointed out previously, ILNS dependence on manufacturing is high, since defects such as pores and/or fabric distortions can cause important reduction in ILNS, as shown in Figure 6.21.b. Although ILNS is not a major topic of study, a general trend observed in most studies is the large variability of the results.

In UD curved specimens formed by carbon-epoxy prepregs, ILNS varied between 68,9-82,7 MPa [308] or 59,8-100,3 MPa [316]. However, it has been also reported that in woven carbon-epoxy prepreg specimens, ILNS diminish up to ~28 MPa with low dispersion of the results [317]. Another study found that ILNS for E-glass woven fabrics with polyester resin ranges between 8,4-13,6 MPa [311] and, in case of E-glass/polypropylene commingled fabrics, ILNS varies between 17,4-22,7 MPa [318]. Most of these studies showing coefficients of variation larger than 20%. Therefore, obtained results of the compression tests of 'L' shapes samples were not away from expected performance when woven textiles are involved.

From the work presented, two issues should be explored in further research: characterization of textile reinforcement behaviour under combined compaction-shear loading, and continuing the investigation of effects of auxiliary materials on formability and specimen quality in ISFLIP.

Exerting a compaction pressure onto a textile preform drastically changes its shear behaviour, reducing its in-plane deformation capacity before deforming out of the plane and forming wrinkles. An interesting methodology based on the bias-extension test was followed in [105] to measure the compaction-shear response of textile preforms. Compaction pressure was exerted through an air-tight cavity formed by elastomeric bagging films from which air was evacuated, allowing the control of the compaction pressure through the vacuum level achieved into the cavity. This study should not be only limited to orthotropic preforms, but also extended to quasi-isotropic preforms.

The assessment of auxiliary materials conducted along this chapter through the manufacturing of different ISFLIP specimens is summarized in Table 6.3. Two important conclusions that should be addressed in future work were that peel-plies did not restrict formability as initially expected and conventional release films with small elastic regimes cause surface defects in areas of large shear.

Table 6.3. Qualitative impact on formability and specimen quality, and future prospects of auxiliary materials.

Material	Assessment	Future prospect
Elastomeric bagging film	Low stiffness and large elastic regime of deformation are crucial to avoid restrictions in preform formability.	Explore potential to enhance sliding with elastic diaphragms.
Extruded mesh HPDM	Diamond pattern showed similar behaviour to knitted meshes in diagonal directions, but expected deformation capacity in filament directions would be smaller. Induced the formation of secondary wrinkles in hemisphere shape specimens.	Must be avoided.
Knitted mesh HPDM	High rigidity in longitudinal direction; but with large in-plane deformation capacity in transversal and $\pm 45^\circ$ directions, which are crucial to avoid restrictions in preform formability.	Fundamental in future experimentation.
Release film	Incompatible with textile reinforcements in areas of large shear, leading to surface defects that produce fabric distortions. Drastic increment in bending rigidity of the whole preform assembly when the perforated release film was stuck to the KHPDM2.	Investigation of effects of elastomeric films coated with release agent (perforated if necessary) on surface finish of ISFLIP specimens.
Peel-ply	Striking increment in shear capacity in hemisphere shape specimens with respect to bias-extension tests.	Explore more opened and/or twill fabric architectures.

It would be interesting to explore drapeability of more opened and/or twill-weave peel-ply, and the adoption of elastomeric release films (films coated with a release agent, and perforated to allow resin pass-through in case of being placed between the HPDM and the preform). Testing of the overall behaviour of the complete preform assembly could be also carried out through the testing method described in [105], before conducting more specific ISFLIP manufacturing tests.

6.4. Conclusions

Aiming to prove ISFLIP concept and clarify uncertainties regarding attainable shapes and component quality, a series of orthotropic hemisphere shape specimens and ‘C’ cross-section profiles with pronounced joggles were manufactured. Previous characterization of dominant in-plane deformation mechanisms, and ply-ply shear of reinforcements and auxiliary materials let identifying key aspects affecting preform forming performance in ISFLIP.

Hemisphere shape specimens showed that trellis shear of textile fabrics was significantly restricted due to the combined compaction-shear loading with respect to uncompressed textiles. However, ‘C’ cross-section profiles also showed a noteworthy capacity of forming preforms over tight bending radius without defects. The low coefficient of friction between textiles layers rotated $\pm 45^\circ$ and the proved ability of sliding between consecutive layers required to form ‘C’ cross-section profiles, let be optimistic with the capacity of ISFLIP to form quasi-isotropic preforms without the severe restrictions that other forming techniques present.

Auxiliary materials played a key role in the quality of ISFLIP specimens due to their interaction with reinforcement preforms during the forming step. The use of knitted polymeric meshes as HPDM and elastomeric bagging films was crucial to minimize limitations on attainable shapes. Woven peel-ply unexpectedly arose as a potential consumable material for ISFLIP preform assemblies, increasing shearing capacity with respect to levels reached in bias-extension tests. Besides, release films with small elastic regimes of deformation irremediably led to surface defects in areas of large shear. Defects that in 'C' cross-section profiles resulted in fabric distortion in curved regions.

Although manufactured specimens were not free of forming defects, because the proposed analyses aimed to test ISFLIP limits; it was validated ISFLIP potential of manufacturing FRP specimens with fibre and void content levels similar to those obtained in prior chapters thanks to the adoption of the VI methodology previously developed.

Further investigation and experimentation on characterization of combined compaction-shear behaviour of orthotropic and quasi-isotropic preforms should be addressed in the future, as well as the evaluation of effects of more open and/or twill fabric peel-ply and elastomeric release films on part quality.

This page intentionally left blank

Chapter 7

Discussion and conclusions

This chapter embraces the findings and contributions of the work presented in this thesis as a whole, to highlight the significant conclusions and make recommendations for future investigation, not only for ISFLIP, but also for more general VI.

7.1. Discussion

The main driving force behind this work lied on solving the issues of low FRP performance and long processing times usually associated to VI manufacturing due to its own process limitations, and inefficient and lacking of reproducibility dry preform technologies. ISFLIP arose as a potential response to these problems.

This research project was focused on the development and assessment of ISFLIP as a real alternative to manufacture high performance FRP parts with shorter processing times and higher reproducibility than other conventional VI variants, intending to shorten the distance between RTM and VI techniques in terms of part quality.

ISFLIP is a hybrid process between VI and diaphragm forming in which a flat preform of a stack of reinforcement fabrics is firstly impregnated with a low viscosity matrix and, then, formed over a mould while the matrix is still in the low viscosity state. This process sequence is possible because the preform assembly (preform and auxiliary materials which are air-tightly sealed by bagging films) is clamped between a couple of elastic diaphragms, which keep the preform flat during the infusion stage and allow its subsequent vacuum forming

Although simple in concept, the complexity of implementing ISFLIP quickly came out due to numerous interactions between VI and diaphragm forming elements, requirements and restrictions. Both techniques present a number of overwhelming trade-offs which are difficult to overcome.

Capturing in a dissertation the ideation process of a new manufacturing technique is not trivial. This thesis started just after ISFLIP concept formation and has built a new manufacturing process from its foundations. A meaningful and structured analysis of ISFLIP through the MT (based on function, quality and cost attributes of the applicability of a mechanical component) let identifying some crucial aspects that not only helped to outline a research path, but also find a potential market niche that ISLFIIP can fill.

The MT emerged as an incredibly useful tool to keep ideas ordered, which was terribly useful to draw precise conclusions. Primary aspects were noticeable, such as the necessity of developing a VI process aiming to minimize porosity with high fibre volume fraction and short processing time, or the obvious doubts around quality of components after being formed; but keeping an ordered way of thinking, as the MT encourages, helps to be focussed on non-evident aspects that can be crucial, such as the market niche in terms of size vs. production volume in which ISFLIP looks promising, or pointing out the mistrusts that no contact between the part and the mould could cause in spite of the benefits that this feature also provides. As everybody knows, the devil is in the details.

ISFLIP can handle all kind of 2D textile reinforcements, and TS and TP matrices that can be processed in a low viscosity state. It is suitable to non-reentrant, flat shell shapes and shallow, non-reentrant, dished shell shapes. Due to the initial flat preform configuration, operator participation is minimized and it is facilitated the adoption of automated preforming approaches, gaining reproducibility. Besides, ISFLIP presents the great advantage with respect to other hybrid VI-forming techniques that the double air-tight cavity allows the reliable implementation of non-conventional filling and post-filling strategies to improve part quality while reducing processing time. Finally, ISFLIP would be able to achieve economic short cycle times, unattainable for VI, and manufacture large size parts, which cannot be manufactured through RTM, and, thus, filling a gap that VI and RTM cannot cover.

Although ISFLIP is compatible with any 2D fabric architecture; logic dictates that added value textiles associated to high performance composites should be used to outweigh the cost increment with respect to common VI of auxiliary materials (showing high drapeability or formability) and additional equipment (diaphragm forming equipment).

Establishing the basis of ISFLIP and making it a reality embraced this rigorous analysis, the definition of well-thought-out and elaborate processing sequence and the built of a functional prototype that provided a framework to the process and allowed to carry out the proof-of-concept that, beyond forming uncertainties addressed, implied the work presented in Chapter 6.

The importance of the well-thought-out ISFLIP processing sequence resides, not only in allowing a reliable implementation of the process, but in a reduction of in-mould cycle time since debulking, filling and post-filling are conducted out of the mould. In-mould cycle time is given by forming, curing and demoulding times. Potentially, cycle times of ISFLIP could be even shorter than RTM; however, this competitive advantage could be lost if total filling and post-filling time exceeded in-mould cycle time. Therefore, a VI manufacturing procedure guaranteeing short processing time without affecting part quality was required.

The functional prototype described in Chapter 3 has the double diaphragm tooling system as the most striking point, which allows an easy and fast attachment and detachment of the elastic diaphragms from its rigid frames, important to compensate Mullins effect, and self-stretched the diaphragms when being coupled to the central frame, important to securely place the preform assembly between diaphragms. A negative point of the prototype was the adoption of a flat table configuration for the mould cavity; since once the lower diaphragm and the vacuum table were brought into contact, no sliding between them happened, limiting formability. A more depth cavity with a raised mould would have been a better, although also trickier, solution.

A series of research topics have been defined in Chapter 3 as a result of all previous thinking in ISFLIP. In this thesis, two of them, one focused on VI stage and another in the forming stage, have been addressed: identifying a VI manufacturing methodology which fitted the targets of high performance FRP and short processing times, and assessing uncertainties associated to the forming stage of ISFLIP.

Porosity is a major concern in VI manufacturing due to resin gelation at pressures close to absolute vacuum, at which resin is prone to outgas due to its minimum air solubility as stated by Henry's law. Besides, trade-offs between component quality attributes and processing times are typical in VI due to the operational limitations of the manufacturing process. Unfortunately, improvements in one direction often requires deterioration of other quality attribute or increment of the overall processing time.

Other steps different from filling are usually underestimated in VI, although they are fundamental in final part quality once some understanding of the physics involved in the process is gained. In FRP, the quality of the manufactured material is often assessed through the fibre

volume fraction, v_f , and void volume fraction, v_0 . The former quality attribute directly points out to the material properties, since it refers to the fractions of the constituents; while the later refers to the quantity of defects contained in the composite material. Degassing and debulking steps present the advantage that mostly act independently on v_0 and v_f , respectively. Therefore, achieving VI components with no porosity, inevitably requires an effective degassing procedure.

In Chapter 4, it has been addressed the effectiveness of different degassing procedures on total void content of manufactured parts. The results of the conducted screening experiment supported the idea that conventional vacuum degassing, consisting on exposing a volume of resin to high vacuum levels for a specific amount of time, is not really effective and mechanisms to enhance bubble formation are fundamental. Stirring the resin with a magnetic device while being degassed at ≈ 300 rpm, which enhances bubble formation due to cavitation, arose as an easily implementable and significantly efficient procedure of reducing final specimen void content.

Implications of degassing findings are beyond the objectives of manufacturing no porosity parts; since a lot of literature is published on matrix-dominated mechanical properties of FRP specimens manufacturing via VI in which inefficient degassing or no degassing at all was conducted. In glass-epoxy specimens, porosity can be visually identified due to the translucent nature of the resulting composite material; but in carbon FRP, porosity can remain hidden to researchers awareness. Trapped porosity into specimens avoids taking advantage of the full potential of FRPs.

VI trade-offs between component quality and processing time mainly concentrate in filling and post-filling steps. For this reason, different pressure filling and post-filling conditions, and preform assembly configurations have been analysed in Chapter 5 with the purpose of assessing the ability to achieve high fibre content, tight thickness tolerances, minimum porosity and short processing times, fitting the targets defined for ISFLIP. In this second set of experiments, the promising combination of vacuum degassing and high speed stirring (single stirring point) was updated to include four stirring points at 700 ± 25 rpm (magnetic stirring system); hence, acting in a larger area of the resin pot and enhancing even more bubble formation.

From an effective degassing, void content was virtually eliminated and post-filling time minimized without affecting fibre content ($\bar{v}_f' = 54,0\%$) through altering through-thickness flow by a perforated release film, placing a flow resistance between the preform end and the venting channel, turning inlet into vent after preform filling, and raising vent pressure between filling and post-filling steps (+5 kPa). The novelty of this non-conventional VI manufacturing methodology

does not reside on adopted measures, but in the appropriate combination of them to compensate benefits and drawbacks that the adoption of each measure involves.

Although manufacturing null porosity specimens was not achieved, the proposed methodology is a promising basis which needs to be fine-adjusted in future work. It is worth pointing out that the results obtained and the conclusions drawn from the present study are only qualitatively applicable to other experimental conditions, because outgassing behaviour is closely related to materials involved, not only to manufacturing conditions.

VI is usually perceived as a long lead time manufacturing process, which is true if narrow v_f and thickness tolerances are expected in the manufactured parts in case of conventional inlet clamping after preform filling. Nevertheless, in the same way that the use of HPDM to speed-up preform impregnation (initially introduced in SCRIMP) has extended as the state of the art in VI manufacturing, turning inlet into vent would have to be understood as a similar measure to speed-up post-filling to reduce intra-part v_f variability. Although turning inlet into vents raises concern about final porosity, it has been proven in this thesis that it is possible to integrate it into a manufacturing methodology in which porosity is minimized.

Experimentation conducted in Chapter 4 and Chapter 5 was addressed through rigours DOE based on factorial designs, which are efficient strategies for minimizing cost, time and resources. Two-level factorial designs are often used in screening experiments of process parameters in order to optimize a specific quality attribute, an early stage of the optimization experiment which is usually followed by successive stages that provide more precise results.

Designs were kept as simple as possible while satisfying the required level of scientific soundness for two reasons: drawing intuitive and meaningful conclusions from the statistical analyses, and deepen into manufactured specimens without falling into an overwhelming amount of data. A total of eight VI specimens were manufactured for each proposed screening experiment. Sometimes, increasing the number of experiments can cause the loss of focus on the experiment without adding enough statistical power to facilitate their analysis. Factorial designs are perfect for this purpose, since they are highly flexible to start from simple configurations that can be expanded to more broad designs if necessary, as happened in Chapter 5.

Apart from conducting reliable manufacturing strategies, defining meaningful response variables was fundamental. Although, in the first instance, one can think in v_f and v_0 as the most obvious candidates; the translucent nature of the glass-epoxy specimens allowed to take full advantage of the fraction of the specimens containing porosity (porous area fraction, s_0), which can be thought as an average descriptor of the porous content of the specimen and was easily

measurable through digital image processing. Eventually, the focus of the proposed experiments was achieving no porosity parts; thus reducing s_0 to zero.

The major problem in VI that porosity poses has been also addressed in Chapter 4 and Chapter 5. In case of in-plane impregnated specimens (Chapter 4), severe porosity occurred in large continuous areas; while, in case of through-thickness impregnated specimens (Chapter 5), severe porosity concentrated in separate and random clusters. In general, when porosity occurred, v_0 was higher in porous areas of in-plane impregnated specimens than in porous areas of through-thickness impregnated specimens. Light microscopy revealed that porosity was mostly accumulated in inter-tow regions, with some pores even exceeding specimen thickness. Pore morphology was closely connected to inter-tow gaps into the preforms. Besides, flexural strength decreased up to 8,7-9,1% when porosity was present in the region of samples loaded in compression. While in in-plane impregnated specimens, pores were uniformly distributed along the thickness, in through-thickness impregnated specimens, pores were formed close to the mould face of the specimens (opposite to HPDM face).

Finally, uncertainties associated to the forming stage of ISFLIP have been assessed in Chapter 6. The inclusion of auxiliary materials showing dominant in-plane deformation mechanisms different to trellis shear adds complexity to the already challenging forming of textile preforms. Drapability of textile reinforcements was significantly reduced with respect to simple shear due to the combined compaction-shear loading exerted by the double diaphragm. Maximum shear angles reached in ISFLIP hemisphere shape specimens were only approx. half of locking angles measured through bias-extension tests. This issue is important when addressing attainable part shapes, since maximum curvature will depend on in-plane shear deformation capacity of the textile preform.

Auxiliary materials played a key role in the quality of ISFLIP specimens due to their interaction with reinforcement preforms during the forming step. The use of knitted polymeric meshes as HPDM and elastomeric bagging films was crucial to minimize shape limitations. Woven peel-ply unexpectedly arose as a potential consumable for ISFLIP preform assemblies, increasing shearing capacity with respect to levels reached in bias-extension tests. Besides, release films with small elastic regimes of deformation irremediably led to surface defects (creases) in areas of large shear.

Initially, it was expected that perforated release films had involved higher void content in VI specimens, while peel-ply limited in-plane shear of preform assemblies; but, conversely, flow alteration caused by perforated release films resulted in lower porosity, while peel-ply did not

apparently affect formability of the whole preform assembly. Therefore, initial plans of what preform assemblies had to be comprised by were disrupted.

Beyond forming uncertainties addressed in Chapter 6, it has been validated ISFLIP potential of manufacturing FRP specimens with fibre and void content levels similar to those obtained in prior chapters thanks to the adoption of the VI methodology previously developed. In absence of more experimental evidences, convex shapes with tight bending radius and moderate double curved shapes can be obtained in ISFLIP.

As a summary, the main contributions made through this dissertation, and commented above, are collected in the following list:

- Introduction of a novel LCM manufacturing technique, ISFLIP, which provides an interesting solution to the industry to fill a gap that conventional VI and RTM cannot cover.
- Exemplifying the usefulness of a knowledge management tool such as the MT to deal with a manufacturing process in which trade-offs between function, quality and cost are numerous and critical.
- Unmasking effectiveness of traditional degassing attempts used in the composite field and based on simply holding a volume of resin under high vacuum levels.
- Development of an effective degassing procedure combining vacuum degassing and a multi-point high speed stirring system.
- Encouraging of a new way of addressing VI manufacturing to reduce processing time and increase reproducibility, which are normally opposite to each other.
- Presentation of a VI manufacturing methodology that solves the endless trade-off between fibre and void contents, and processing time.
- Proving the capacity of ISFLIP to manufacture FRP convex components with tight bending radius and moderate double curvature areas.

7.2. Recommendations for future research

From the work presented in this dissertation, future research should be focussed on two directions: VI manufacturing methodology to produce high performance components (maximizing v_f while avoiding porosity formation) being also competitive in manufacturing time, and continuing ISFLIP development.

Resin outgassing and capacity to dissolve voids created due to resin flow through dual-scale heterogeneous porous media depend on gelation conditions (pressure and temperature). Gelation temperature from Chapter 4 to Chapter 5 was decreased from 80°C to 60°C to avoid that resin boiled-off into venting channels as happened at 80°C; however, lower gelation temperature also involves longer gelation time.

In addition, vent pressure increment between filling and post-filling steps has been proved as an effective measure to reduce final porosity. Nevertheless, an excessive increment of vent pressure could cause a reduction in v_f , since pressure into the preform cavity and compaction pressure are coupled through Terzaghi's relation; although, due to the inelastic compressive behaviour of textile preforms, noticeable thickness recovery does not take place if pressure variations from the settling pressure are not large enough.

An effective adoption of the proposed VI manufacturing methodology would require the characterization of the two-dimensional response of pressure increment and gelation temperature response vs. outgassing behaviour, and the one-dimensional response pressure increment vs. preform recovery. VI processes should be designed to guarantee no porosity parts without affecting v_f (and achieving narrow thickness tolerances). Optimum processing conditions will depend not only on involved materials, but also presumably on component size. Therefore, analysing dependence of processing conditions on both part thickness and filling length would be of great interest.

In Chapter 3, two more topics apart from those two addressed along this dissertation were pointed out: mistrusts of cosmetic surface finish and shape tolerances, and simulation of the forming stage. Importance of this two topics have been highlighted in Chapter 6, in which uncertainties associated with the forming stage of ISFLIP were evaluated.

On the one hand, it has been shown that release films with small elastic regime created surface defects in areas of large shear that can even distort fabrics into the component. Adoption of elastomeric release films (films coated with a release agent, and perforated to allow resin pass-through in case of being placed between HPDM and preform) should be considered in order to investigate if elastomeric sheets can accommodate shortening caused by trellis shear. Besides, after observing that peel-ply did not restrict formability as initially expected, the study of drapeability of more opened and/or twill-weave peel-ply should be also addressed

On the other hand, severe wrinkles caused by geometry recess in both hemisphere shape specimens and 'C' cross-section profiles remarked the importance of process simulation. Predicting forming sequence in ISFLIP is not trivial. It is worth remembering that, unlike

stamping, corrective measures in diaphragm forming are difficult to be implemented. In ISFLIP framework, flat preform impregnation facilitates preform modelling and filling simulation; but forming of a stack of dry fabrics embedded in a low viscosity matrix and in contact with materials with different deformation mechanics entails a massive effort in characterising and modelling all materials, and simulating physics involved in the process.

Exerting a compaction pressure onto a textile preform drastically changes its shear behaviour, reducing its in-plane deformation capacity before deforming out of the plane and form wrinkles. Characterization of compaction-shear behaviour is fundamental to experimentally assessed drapeability and obtain input data for the material models to be used in the simulation of the forming stage. Compaction pressure exerted on bias-extension samples could be controlled through the vacuum level into an air-tight cavity created around the sample and the jaws, and formed by elastomeric films. This test method could be used to characterize orthotropic and quasi-isotropic preforms, and even the overall behaviour of the complete preform assembly before conducting specific ISFLIP manufacturing tests.

7.3. Conclusions

Throughout this research project, first steps in ISFLIP development have been made, while deepening in part quality optimization in VI. ISFLIP foundations have been laid, allowing the manufacturing of high performance FRP components.

ISFLIP is an increasingly promising manufacturing process with potential to fill a market gap in part size vs. production volume that VI and RTM cannot cover for a specific geometry type such as shell shapes. Nevertheless, further research on this respect is still necessary to find out shape limitations and, especially, how to minimize them.

A key point of ISFLIP is to implement a VI manufacturing methodology that permits fitting targets of high performance (high fibre content and negligible porosity) and short processing times. Degassing is crucial to obtain VI parts with low porosity, or even trying to achieve non-porous parts. On this purpose, combining vacuum degassing with high speed stirring to enhance bubble formation have been fundamental. Furthermore, it has been also demonstrated that a well-thought-out VI methodology let turning inlets into vents after preform filling to minimize processing time and quickly equalize fibre content without any detrimental effect on void content.

As expected, interactions between different materials included into the preform assembly were critical in the forming stage of ISFLIP. In-plane shear deformation of textile reinforcements,

fundamental to form preforms to double curvature shapes, was significantly restricted due to the combined compaction-shear loading. Besides, auxiliary materials, mostly showing dominant in-plane deformation mechanisms different from fabric reinforcements, play a key role not only on attainable shapes, but also in other quality attributes such as surface finish.

As investigation has progressed, confidence on real ISFLIP potential has been strengthening; however, there is still a long way to go to reach ISFLIP implementation in a real production environment.

Bibliography

1. Juan J, Salán N, Tornero JA. *Sistema y procedimiento de infusión de resina por vacío para la obtención de piezas elaboradas a partir de materiales compuestos*. Spanish Patent 2551180 B2; 2015.
2. Juan J, Salán N, Tornero JA, Gámez J. Road to null porosity in Vacuum Infusion (VI): Part I – Void content minimization via effective degassing. *Submitted for publication in Journal of Composite Materials*. 2017.
3. Juan J, Salán N, Tornero JA, Gámez J. Road to null porosity in Vacuum Infusion (VI): Part II – High performance composites in a competitive time scenario via control of filling and post-filling conditions. *Submitted for publication in Journal of Composite Materials*. 2017.
4. Schlimbach J, Ogale A. Out-of-autoclave curing process in polymer matrix composites. In: Advani SG, Hsiao K-T, editors. *Manufacturing techniques for polymer matrix composites (PMCs)*. Woodhead Publishing; 2012. p. 435–87.
5. Stickler P. Composite Materials for Commercial Transport - Issues and Future Research Direction. In: *Proceedings of the American Society for Composites, 17th Annual Technical Conference*. West Lafayette, United States of America; 2002.
6. Witik RA, Gaille F, Teuscher R, Ringwald H, Michaud V, Works I. Assessing the economic and environmental potential of out of autoclave processing. In: *ICCM 18: 18th International Conference of Composite Materials*. Jeju Island, Korea; 2011.
7. Verrey J, Wakeman MD, Michaud V, Månson J-AE. Manufacturing cost comparison of thermoplastic and thermoset RTM for an automotive floor pan. *Composites Part A: Applied Science and Manufacturing*. 2006;37(1):9–22.
8. van Rijswijk K, Bersee HEN. Reactive processing of textile fiber-reinforced thermoplastic composites - An overview. *Composites Part A: Applied Science and Manufacturing*. 2007;38(3):666–81.
9. Wang CR, Gu YZ, Zhang KM, Li M, Zhang ZG. Rapid curing epoxy resin and its application in carbon fibre composite fabricated using VARTM moulding. *Polymers and Polymer Composites*. 2013;21(5):315–24.
10. Linke M, Greb C, Klingele J, Schnabel A, Gries T. Automating textile preforming technology for mass production of fibre-reinforced polymer (FRP) composites. In: *Woodhead Publishing Series in Textiles*. Woodhead Publishing; 2012. p. 171–95.
11. Mills A. Automation of carbon fibre preform manufacture for affordable aerospace applications. *Composites Part A: Applied Science and Manufacturing*. 2001;32(7):955–62.
12. Beckwith SW. Resin infusion technology: Part 2 – Process definitions and industry variations. *SAMPE Journal*. 2007;43(3):46.
13. Palardy G, Hubert P, Haider M, Lessard L. Optimization of RTM processing parameters for class A surface finish. *Composites Part B: Engineering*. 2008;39(7–8):1280–6.
14. Mouton S, Teissandier D, Sébastien P, Nadeau JP. Manufacturing requirements in design: The RTM process in aeronautics. *Composites Part A: Applied Science and Manufacturing*. 2010;41(1):125–30.
15. Laurenzi S, Grilli A, Pinna M, De Nicola F, Cattaneo G, Marchetti M. Process simulation for a large composite aeronautic beam by resin transfer molding. *Composites Part B: Engineering*. 2014;57(0):47–55.
16. Beckwith SW. Resin infusion technology: Part 1 – Industry highlights. *SAMPE Journal*. 2007;43(1):61.
17. Woods JA, Modin AE, Hawkins RD, Hanks DJ. *Controlled atmospheric pressure resin infusion process*. U. S. Patent 7,334,782 B2; 2008.

18. Niggemann C, Young Seok Song, Gillespie JW, Heider D. Experimental investigation of the Controlled Atmospheric Pressure Resin Infusion (CAPRI) process. *Journal of Composite Materials*. 2008;42(11):1049–61.
19. Bernetich K, Fink BK, Gillespie J, Gillio E. *One-step resin transfer molding of multifunctional composites consisting of multiple resins*. U. S. Patent. 6,048,488; 2000.
20. Gillio EF, McKnight GP, Gillespie JW, Advani SG, Bernetich KR, Fink BK. Processing and properties of co-injected resin transfer molded vinyl ester and phenolic composites. *Polymer Composites*. 1999;20(6):780–8.
21. Bhat P, Merotte J, Simacek P, Advani SG. Process analysis of compression resin transfer molding. *Composites Part A: Applied Science and Manufacturing*. 2009;40(4):431–41.
22. Simacek P, Advani SG. Simulating three-dimensional flow in compression resin transfer molding process. *Revue Européenne des Éléments*. 2005;14(6–7):777–802.
23. Simacek P, Advani SG, Iobst SA. Modeling flow in compression resin transfer molding for manufacturing of complex lightweight high-performance automotive parts. *Journal of Composite Materials*. 2008;42(23):2523–45.
24. Allende M, Mohan R V, Walsh SM. Experimental and numerical analysis of flow behavior in the FASTRAC liquid composite manufacturing process. *Polymer Composites*. 2004;25(4):384–96.
25. Vernin N, Chohra M, Advani S, Alms J. *Vacuum assisted resin transfer molding techniques with flow flooding chamber*. U. S. Patent 2007/0063393 A1; 2007.
26. Alms J, Advani SG. Simulation and experimental validation of flow flooding chamber method of resin delivery in liquid composite molding. *Composites Part A: Applied Science and Manufacturing*. 2007;38(10):2131–41.
27. Foley MF. The flexible resin transfer molding (FRTM) process. *SAMPE Journal*. 1992;28:15–24.
28. Gardiner G. HP-RTM on the rise. *CompositesWorld*. 2015 April.
29. Ghose S, Watson KA, Cano RJ, Britton SM, Jensen BJ, Connell JW, et al. High temperature VARTM of phenylethynyl terminated imides. *High Performance Polymers*. 2009;21(5):653–72.
30. Hutchinson JR, Schubel PJ, Warrior NA. LRTM – A feasible alternative to VI for the manufacture of large scale wind turbine. In: *ICCM17: 17th International Conference of Composite Materials*. Edinburgh, United Kingdom; 2009.
31. Doane WJ, Hall RG. Development of a low-cost, modified resin transfer molding process using elastomeric tooling and automated preform fabrication. *9th DOD/NASA/FAA Conference on Fibrous Composites in Structural Design*. 1992;3:1163–73.
32. Chen V, Hawley A, Klotzsche M, Markus A, Palmer R. Composites technology for transport primary structure. In: *1st NASA Advanced Composite Technology Conference*. 1990.
33. Okoli OI, Lim AP. Resin infusion between double flexible tooling system. U. S. Patent. 7,862,322 B2; 2011.
34. Okoli OI, Puentes CA. In-mold decoration of composites manufactured by resin infusion between double flexible tooling system. U. S. Patent 2011/0014315 A1; 2011.
35. Channer KJ, Cosgriff W, Smith GF, Okoli OI. Development of the double RIFT diaphragm forming process. *Journal of Reinforced Plastics and Composites*. 2002;21(18):1629–35.
36. Thagard JR, Okoli OI, Liang Z, Wang HP, Zhang C. Resin infusion between double flexible tooling: prototype development. *Composites Part A: Applied Science and Manufacturing*. 2003;34(9):803–11.
37. Thagard JR, Okoli OI, Liang Z. Resin Infusion Between Double Flexible Tooling: Evaluation of Process Parameters. *Journal of Reinforced Plastics and Composites*. 2004;23(16):1767–78.

38. Seemann WH. *Plastic transfer molding techniques for the production of fiber reinforced plastic structures*. U. S. Patent 4,902,215; 1990.
39. Eckler JH, Wilkinson TC. Processing and designing parts using structural reaction injection molding. *Journal of Materials Shaping Technology*. 1987;5(1):17–21.
40. Ware M. *Thermal expansion resin transfer moulding*. U. S. Patent 5,061,418 A; 1991.
41. Sloan J. Getting real: Thermoplastic resin transfer molding. *CompositesWorld*. 2016 June.
42. Chang C-Y. Experimental analysis of mold filling in vacuum assisted compression resin transfer molding. *Journal of Reinforced Plastics and Composites*. 2012;31(23):1630–7.
43. Filsinger J, Lorenz T, Stadler F, Utecht S. *Method and device for producing fiber-reinforced composites using an injection method*. U. S. Patent 6,843,953 B2; 2005.
44. Simacek P, Heider D, Gillespie Jr. JW, Advani S. Post-filling flow in vacuum assisted resin transfer molding processes: Theoretical analysis. *Composites Part A: Applied Science and Manufacturing*. 2009;40(6–7):913–24.
45. Simacek P, Eksik Ö, Heider D, Gillespie Jr. JW, Advani S. Experimental validation of post-filling flow in vacuum assisted resin transfer molding processes. *Composites Part A: Applied Science and Manufacturing*. 2012;43(3):370–80.
46. Li W, Krehl J, Gillespie JW, Heider D, Endrulat M, Hochrein K, et al. Process and Performance Evaluation of the Vacuum-Assisted Process. *Journal of Composite Materials*. 2004;38(20):1803–14.
47. Alms JB, Glancey JL, Advani SG. *Apparatus and method for preform relaxation and flow control in liquid composite molding processes*. U. S. Patent 8,210,841 B2; 2012.
48. Alms JB, Advani SG, Glancey JL. Liquid composite molding control methodologies using vacuum induced preform relaxation. *Composites Part A: Applied Science and Manufacturing*. 2011;42(1):57–65.
49. CES Edupack 2014. Granta Design Limited; 2014.
50. Rieber G, Jiang J, Deter C, Chen N, Mitschang P. Influence of textile parameters on the in-plane permeability. *Composites Part A: Applied Science and Manufacturing*. 2013;52(0):89–98.
51. Parnas RS, Flynn KM, Dal-Favero ME. A permeability database for composites manufacturing. *Polymer Composites*. 1997;18(5):623–33.
52. Pearce NRL, Guild FJ, Summerscales J. An investigation into the effects of fabric architecture on the processing and properties of fibre reinforced composites produced by resin transfer moulding. *Composites Part A: Applied Science and Manufacturing*. 1998;29(1–2):19–27.
53. Naik NK, Sirisha M, Inani A. Permeability characterization of polymer matrix composites by RTM/VARTM. *Progress in Aerospace Sciences*. 2014;65(0):22–40.
54. Long AC. *Composites forming technologies*. Woodhead Publishing; 2007.
55. Rozant O, Bourban P, Ma JE. Drapability of dry textile fabrics for stampable thermoplastic preforms. *Composites Part A: Applied Science and Manufacturing*. 2000;31(11):1167–77.
56. Lin H, Sherburn M, Crookston J, Long AC, Clifford MJ, Jonse IA. Finite element modelling of fabric compression. *Modelling and Simulation in Materials Science and Engineering*. 2008;16(3):35010.
57. Yuexin D, Zhaoyuan T, Yan Z, Jing S. Compression responses of preform in vacuum infusion process. *Chinese Journal of Aeronautics*. 2008;21(4):370–7.
58. Tan H, Pillai KM. Multiscale modeling of unsaturated flow in dual-scale fiber preforms of liquid composite molding I: Isothermal flows. *Composites Part A: Applied Science and Manufacturing*. 2012;43(1):1–13.

59. Verrey J, Michaud V, Månson JAE. Dynamic capillary effects in liquid composite moulding with non-crimp fabrics. *Composites Part A: Applied Science and Manufacturing*. 2006;37(1):92–102.
60. Pucci MF, Liotier PJ, Drapier S. Capillary wicking in a fibrous reinforcement - Orthotropic issues to determine the capillary pressure components. *Composites Part A: Applied Science and Manufacturing*. 2015;77:133–41.
61. Sozer EM, Simacek P, Advani SG. RTM in polymer matrix composites. In: Advani SG, Hsiao K-T, editors. *Manufacturing techniques for polymer matrix composites (PMCs)*. Woodhead Publishing; 2012. p. 245–309.
62. Long AC. *Design and manufacture of textile composites*. Taylor & Francis; 2006.
63. Sherburn M. *Geometric and mechanical modelling of textiles*. PhD thesis, University of Nottingham, United Kingdom; 2007.
64. Lomov S V, Huysmans G, Verpoest I. Hierarchy of textile structures and architecture of fabric geometric models. *Textile Research Journal*. 2001;71(6):534–43.
65. Lomov SV, Verpoest I, Peeters T, Roose D, Zako M. Nesting in textile laminates: geometrical modelling of the laminate. *Composites Science and Technology*. 2003;63(7):993–1007.
66. Lomov S V, Verpoest I. Model of shear of woven fabric and parametric description of shear resistance of glass woven reinforcements. *Composites Science and Technology*. 2006;66(7–8):919–33.
67. Lin H, Clifford MJ, Long AC, Sherburn M. Finite element modelling of fabric shear. *Modelling and Simulation in Materials Science and Engineering*. 2009;17(1):15008.
68. Belov EB, Lomov S V, Verpoest I, Peters T, Roose D, Parnas RS, et al. Modelling of permeability of textile reinforcements: lattice Boltzmann method. *Composites Science and Technology*. 2004;64(7–8):1069–80.
69. Verleye B, Croce R, Griebel M, Klitz M, Lomov S V, Morren G, et al. Permeability of textile reinforcements: Simulation, influence of shear and validation. *Composites Science and Technology*. 2008;68(13):2804–10.
70. Gereke T, Döbrich O, Hübner M, Cherif C. Experimental and computational composite textile reinforcement forming: A review. *Composites Part A: Applied Science and Manufacturing*. 2013;46(0):1–10.
71. Beier U, Fischer F, Sandler JKW, Altstädt V, Weimer C, Buchs W. Mechanical performance of carbon fibre-reinforced composites based on stitched preforms. *Composites Part A: Applied Science and Manufacturing*. 2007;38(7):1655–63.
72. Njionhou A, Berthet F, Castanié B. Effects of process parameters on the mechanical properties and morphology of stitched and non-stitched carbon/epoxy liquid resin-infused NCF laminate, out of autoclave and out of oven. *The International Journal of Advanced Manufacturing Technology*. 2012;65(9–12):1289–302.
73. Ivanov DS, White J a. P, Hendry W, Mahadik Y, Minett V, Patel H, et al. Stabilizing textile preforms by means of liquid resin print: a feasibility study. *Advanced Manufacturing: Polymer & Composites Science*. 2015;1(1):26–35.
74. Di Tomasso C, József Gombos Z, Summerscales J. Styrene emissions during gel-coating of composites. *Journal of Cleaner Production*. 2014;83:317–28.
75. Challenor J, Wright D. Aggression in boat builders: A search for altered mood states in boat builders exposed to styrene. *Occupational Medicine*. 2000;50(3):185–92.
76. Rhomberg LR, Goodman JE, Prueitt RL. The Weight of Evidence Does Not Support the Listing of Styrene as “Reasonably Anticipated to be a Human Carcinogen” in NTP’s Twelfth Report on Carcinogens. *Human and Ecological Risk Assessment: An International Journal*. 2013;19(1):4–27.

77. van Rijswijk K, Joncas S, Bersee HEN, Bergsma OK, Beukers A. Sustainable vacuum-infused thermoplastic composites for MW-size wind turbine blades - Preliminary design and manufacturing issues. *Journal of solar Energy Engineering*. 2005;127:570–80.
78. Yan C, Li H, Zhang X, Zhu Y, Fan X, Yu L. Preparation and properties of continuous glass fiber reinforced anionic polyamide-6 thermoplastic composites. *Materials and Design*. 2013;46:688–95.
79. Rijswijk K van, Teuwen JJE, Bersee HEN, Beukers A. Textile fiber-reinforced anionic polyamide-6 composites. Part I: The vacuum infusion process. *Composites Part A: Applied Science and Manufacturing*. 2009;40(1):1–10.
80. Mohd Ishak ZA, Leong YW, Steeg M, Karger-Kocsis J. Mechanical properties of woven glass fabric reinforced in situ polymerized poly(butylene terephthalate) composites. *Composites Science and Technology*. 2007;67(3–4):390–8.
81. Baets J, Dutoit M, Devaux J, Verpoest I. Toughening of glass fiber reinforced composites with a cyclic butylene terephthalate matrix by addition of polycaprolactone. *Composites Part A: Applied Science and Manufacturing*. 2008;39(1):13–8.
82. Wu W, Xie L, Jiang B, Ziegmann G. Simultaneous binding and toughening concept for textile reinforced pCBT composites: Manufacturing and flexural properties. *Composite Structures*. 2013;105:279–87.
83. Gerard P, Glotin M, Hochstetter G. Composite material via in-situ polymerization of thermoplastic (meth) acrylic resins and its use. U. S. Patent 0,256,850 A1; 2014.
84. Zhang K, Gu Y, li M, Zhang Z. Effect of rapid curing process on the properties of carbon fiber/epoxy composite fabricated using vacuum assisted resin infusion molding. *Materials and Design*. 2014;54:624–31.
85. Tsai J-L, Huang B-H, Cheng Y-L. Enhancing fracture toughness of glass/epoxy composites by using rubber particles together with silica nanoparticles. *Journal of Composite Materials*. 2009;43(25):3107–23.
86. Rachmadini Y, Tan VBC, Tay TE. Enhancement of mechanical properties of composites through incorporation of CNT in VARTM - A review. *Journal of Reinforced Plastics and Composites*. 2010;29(18):2782–807.
87. McCrary-Dennis MCL, Okoli OI. A review of multiscale composite manufacturing and challenges. *Journal of Reinforced Plastics and Composites*. 2012;31(24):1687–711.
88. Louis BM, Klunker F, Ermanni PA. Evaluation of nanoalumina and nanosilica particle toughened high glass-transition temperature epoxy for liquid composite molding processes. *Journal of Composite Materials*. 2015;50(11):1533–45.
89. Arnold M, Henne M, Bender K, Drechsler K. The influence of various kinds of PA12 interlayer on the interlaminar toughness of carbon fiber-reinforced epoxy composites. *Polymer Composites*. 2015;36(7):1249–57.
90. White KL, Sue HJ. Delamination toughness of fiber-reinforced composites containing a carbon nanotube/polyamide-12 epoxy thin film interlayer. *Polymer*. 2012;53(1):37–42.
91. Daelemans L, van der Heijden S, De Baere I, Muhammad I, Van Paeppegem W, Rahier H, et al. Bisphenol A based polyester binder as an effective interlaminar toughener. *Composites Part B: Engineering*. 2015;80:145–53.
92. Beier U, Sandler JKW, Altstädt V, Spanner H, Weimer C. Mechanical performance of carbon fibre-reinforced composites based on stitched and bindered preforms. *Composites Part A: Applied Science and Manufacturing*. 2009;40(11):1756–63.

93. van der Heijden S, Daelemans L, De Schoenmaker B, De Baere I, Rahier H, Van Paepegem W, et al. Interlaminar toughening of resin transfer moulded glass fibre epoxy laminates by polycaprolactone electrospun nanofibres. *Composites Science and Technology*. 2014;104:66–73.
94. Borg C. An introduction to spread tow reinforcements: Part 1 – Manufacture and properties. *Reinforced Plastics*. 2015;59(4):194–8.
95. Ohlsson F. An introduction to spread tow reinforcements. Part 2: Design and applications. *Reinforced Plastics*. 2015;59(5):228–32.
96. Lim T-C, Ramakrishna S. Modelling of composite sheet forming: a review. *Composites Part A: Applied Science and Manufacturing*. 2002;33(4):515–37.
97. Cao J, Akkerman R, Boisse P, Chen J, Cheng HS, de Graaf EF, et al. Characterization of mechanical behavior of woven fabrics: Experimental methods and benchmark results. *Composites Part A: Applied Science and Manufacturing*. 2008;39(6):1037–53.
98. Harrison P, Clifford MJ, Long AC. Shear characterisation of viscous woven textile composites: a comparison between picture frame and bias extension experiments. *Composites Science and Technology*. 2004;64(10–11):1453–65.
99. Lussier D. *Shear characterization of textile composite formability*. Master thesis, University of Massachusetts, United States; 2002.
100. Lebrun G, Bureau MN, Denault J. Evaluation of bias-extension and picture-frame test methods for the measurement of intraply shear properties of PP/glass commingled fabrics. *Composite Structures*. 2003;61(4):341–52.
101. Harrison P, Abdiwi F, Guo Z, Potluri P, Yu WR. Characterising the shear–tension coupling and wrinkling behaviour of woven engineering fabrics. *Composites Part A: Applied Science and Manufacturing*. 2012;43(6):903–14.
102. Harrison P. Normalisation of biaxial bias extension test results considering shear tension coupling. *Composites Part A: Applied Science and Manufacturing*. 2012;43(9):1546–54.
103. Launay J, Hivet G, Duong A V, Boisse P. Experimental analysis of the influence of tensions on in plane shear behaviour of woven composite reinforcements. *Composites Science and Technology*. 2008;68(2):506–15.
104. Lin H, Long AC, Sherburn M, Clifford MJ. Modelling of mechanical behaviour for woven fabrics under combined loading. *International Journal of Material Forming*. 2008;1(1):899–902.
105. Alshahrani H, Hojjati M. Influence of double-diaphragm vacuum compaction on deformation during forming of composite prepregs. *Journal of Science: Advanced Materials and Devices*. 2016;1–5.
106. Lin H, Wang J, Long AC, Clifford MJ, Harrison P. Predictive modelling for optimization of textile composite forming. *Composites Science and Technology*. 2007;67(15–16):3242–52.
107. Boisse P, Hamila N, Vidal-Sallé E, Dumont F. Simulation of wrinkling during textile composite reinforcement forming. Influence of tensile, in-plane shear and bending stiffnesses. *Composites Science and Technology*. 2011;71(5):683–92.
108. Allaoui S, Boisse P, Chatel S, Hamila N, Hivet G, Soulat D, et al. Experimental and numerical analyses of textile reinforcement forming of a tetrahedral shape. *Composites Part A: Applied Science and Manufacturing*. 2011;42(6):612–22.

109. Skordos AA, Monroy Aceves C, Sutcliffe MPF. A simplified rate dependent model of forming and wrinkling of pre-impregnated woven composites. *Composites Part A: Applied Science and Manufacturing*. 2007;38(5):1318–30.
110. Sadighi M, Rabizadeh E, Kermansaravi F. Effects of laminate sequencing on thermoforming of thermoplastic matrix composites. *Journal of Materials Processing Technology*. 2008 May;201(1–3):725–30.
111. ten Thije R. *Finite element simulations of laminate composite forming processes*. PhD thesis, Universiteit Twente, Netherlands; 2007.
112. ten Thije RHW, Akkerman R. A multi-layer triangular membrane finite element for the forming simulation of laminated composites. *Composites Part A: Applied Science and Manufacturing*. 2009 Jul;40(6–7):739–53.
113. Cornelissen B, Sachs U, Rietman B, Akkerman R. Dry friction characterisation of carbon fibre tow and satin weave fabric for composite applications. *Composites Part A: Applied Science and Manufacturing*. 2014;56:127–35.
114. Ten Thije RHW, Akkerman R, Ubbink M, Van Der Meer L. A lubrication approach to friction in thermoplastic composites forming processes. *Composites Part A: Applied Science and Manufacturing*. 2011;42(8):950–60.
115. Sachs U, Akkerman R, Fetfatsidis K, Vidal-Sallé E, Schumacher J, Ziegmann G, et al. Characterization of the dynamic friction of woven fabrics: Experimental methods and benchmark results. *Composites Part A: Applied Science and Manufacturing*. 2014;67:289–98.
116. Cornelissen B, Rietman B, Akkerman R. Frictional behaviour of high performance fibrous tows: Friction experiments. *Composites Part A: Applied Science and Manufacturing*. 2013;44:95–104.
117. Nosrat Nezami F, Gereke T, Cherif C. Analyses of interaction mechanisms during forming of multilayer carbon woven fabrics for composite applications. *Composites Part A: Applied Science and Manufacturing*. 2016;84:406–16.
118. Allaoui S, Hivet G, Wendling A, Ouagne P, Soulat D. Influence of the dry woven fabrics meso-structure on fabric/fabric contact behavior. *Journal of Composite Materials*. 2012;46(6):627–39.
119. Robitaille F, Gauvin R. Compaction of textile reinforcements for composites manufacturing. I: Review of experimental results. *Polymer Composites*. 1998;19(2):198–216.
120. Somashekar AA, Bickerton S, Bhattacharyya D. An experimental investigation of non-elastic deformation of fibrous reinforcements in composites manufacturing. *Composites Part A: Applied Science and Manufacturing*. 2006;37(6):858–67.
121. Robitaille F, Gauvin R. Compaction of textile reinforcements for composites manufacturing. III: Reorganization of the fiber network. *Polymer Composites*. 1999;20(1):48–61.
122. Cheng JJ, Kelly PA, Bickerton S. A rate-independent thermomechanical constitutive model for fiber reinforcements. *Journal of Composite Materials*. 2012;46(2):247–56.
123. Yenilmez B, Senan M, Sozer EM. Variation of part thickness and compaction pressure in vacuum infusion process. *Composites Science and Technology*. 2009;69(11–12):1710–9.
124. Walbran WA, Verleye B, Bickerton S, Kelly PA. Prediction and experimental verification of normal stress distributions on mould tools during liquid composite moulding. *Composites Part A: Applied Science and Manufacturing*. 2012;43(1):138–49.
125. Bickerton S, Buntain MJ, Somashekar AA. The viscoelastic compression behavior of liquid composite molding preforms. *Composites Part A: Applied Science and Manufacturing*. 2003;34(5):431–44.

126. Kelly PA, Umer R, Bickerton S. Viscoelastic response of dry and wet fibrous materials during infusion processes. *Composites Part A: Applied Science and Manufacturing*. 2006;37(6):868–73.
127. Kelly PA. A viscoelastic model for the compaction of fibrous materials. *Journal of The Textile Institute*. 2011;102(8):689–99.
128. Robitaille F, Gauvin R. Compaction of textile reinforcements for composites manufacturing. II: Compaction and relaxation of dry and H₂O-saturated woven reinforcements. *Polymer Composites*. 1998;19(5):543–57.
129. Yenilmez B, Sozer EM. Compaction of e-glass fabric preforms in the Vacuum Infusion Process, A: Characterization experiments. *Composites Part A: Applied Science and Manufacturing*. 2009;40(4):499–510.
130. Yenilmez B, Sozer EM. Compaction of e-glass fabric preforms in the vacuum infusion process: (a) use of characterization database in a model and (b) experiments. *Journal of Composite Materials*. 2013;47(16):1959–75.
131. Govignon Q, Bickerton S, Kelly PA. Simulation of the reinforcement compaction and resin flow during the complete resin infusion process. *Composites Part A: Applied Science and Manufacturing*. 2010;41(1):45–57.
132. Govignon Q, Bickerton S, Morris J, Kelly PA. Full field monitoring of the resin flow and laminate properties during the resin infusion process. *Composites Part A: Applied Science and Manufacturing*. 2008;39(9):1412–26.
133. Timms J, Bickerton S, Kelly PA. Laminate thickness and resin pressure evolution during axisymmetric liquid composite moulding with flexible tooling. *Composites Part A: Applied Science and Manufacturing*. 2012;43(4):621–30.
134. Govignon Q, Bickerton S, Kelly PA. Experimental investigation into the post-filling stage of the resin infusion process. *Journal of Composite Materials*. 2013;47(12):1479–92.
135. Potter K, Khan B, Wisnom M, Bell T, Stevens J. Variability, fibre waviness and misalignment in the determination of the properties of composite materials and structures. *Composites Part A: Applied Science and Manufacturing*. 2008;39(9):1343–54.
136. Potter K. Understanding the origins of defects and variability in composites manufacture. In: *ICCM17: 17th International Conference of Composite Materials*. Edinburgh, United Kingdom; 2009.
137. Mesogitis TS, Skordos AA, Long AC. Uncertainty in the manufacturing of fibrous thermosetting composites: A review. *Composites Part A: Applied Science and Manufacturing*. 2014;57(0):67–75.
138. Chen B, Chou T-W. Compaction of woven-fabric preforms: nesting and multi-layer deformation. *Composites Science and Technology*. 2000;60(12–13):2223–31.
139. Chen B, Lang EJ, Chou T-W. Experimental and theoretical studies of fabric compaction behavior in resin transfer molding. *Materials Science and Engineering: A*. 2001;317(1–2):188–96.
140. Pillai KM. Governing equations for unsaturated flow through woven fiber mats. Part 1. Isothermal flows. *Composites Part A: Applied Science and Manufacturing*. 2002;33(7):1007–19.
141. Simacek P, Advani SG. A numerical model to predict fiber tow saturation during liquid composite molding. *Composites Science and Technology*. 2003;63(12):1725–36.
142. Bréard J, Henzel Y, Trochu F, Gauvin R. Analysis of dynamic flows through porous media. Part I: Comparison between saturated and unsaturated flows in fibrous reinforcements. *Polymer Composites*. 2003;24(3):391–408.
143. Pillai KM. Modeling the unsaturated flow in liquid composite molding processes: A review and some thoughts. *Journal of Composite Materials*. 2004;38(23):2097–118.

144. Michaud V. A Review of Non-saturated Resin Flow in Liquid Composite Moulding processes. *Transport in Porous Media*. 2016;115(3):581–601.
145. Luo Y, Verpoest I, Hoes K, Vanheule M, Sol H, Cardon A. Permeability measurement of textile reinforcements with several test fluids. *Composites Part A: Applied Science and Manufacturing*. 2001;32(10):1497–504.
146. Wang SK, Li M, Gu YZ, Li YX, Zhang ZG. Comparisons of wettability and capillary effect evaluated by different characterizing methods. In: *ICCM 18: 18th International Conference of Composite Materials*. Jeju Island, Korea; 2011.
147. Laine B, Arbter R, Binetruy C, Bizet L, Beraud JM, Demaria C, et al. Experimental determination of textile permeability: a benchmark exercise. In: *FPCM 10: 10th International Conference on Flow Processes in Composite Materials*. Ascona, Switzerland; 2010.
148. Swery EE, Allen T, Comas-Cardona S, Govignon Q, Hickey C, Timms J, et al. Efficient experimental characterisation of the permeability of fibrous textiles. *Journal of Composite Materials*. 2016;50(28):4023–38.
149. Roy T, Dulmes C. Experimental Investigations of the unsaturated flow in Liquid Composite Molding. In: *Proceedings of the 5th Canadian International Composites Conference*. Vancouver, Canada; 2005. p. 1–12.
150. Roy T, Pillai KM. Characterization of dual-scale fiber mats for unsaturated flow in liquid composite molding. *Polymer Composites*. 2005;26(6):756–69.
151. Zhou F, Kuentzer N, Simacek P, Advani SG, Walsh S. Analytic characterization of the permeability of dual-scale fibrous porous media. *Composites Science and Technology*. 2006;66(15):2795–803.
152. Kuentzer N, Simacek P, Advani SG, Walsh S. Permeability characterization of dual scale fibrous porous media. *Composites Part A: Applied Science and Manufacturing*. 2006;37(11):2057–68.
153. Vernet N, Ruiz E, Advani S, Alms JB, Aubert M, Barburiski M, et al. Experimental determination of the permeability of engineering textiles: Benchmark II. *Composites Part A: Applied Science and Manufacturing*. 2014;61(0):172–84.
154. Correia NC, Management I, Frias RR. A study on the determination of stochastic reinforcement permeability in constant injection pressure conditions. In: *ICCM17: 17th International Conference of Composite Materials*. Edinburgh, United Kingdom; 2009.
155. Endruweit A, Ermanni P. The in-plane permeability of sheared textiles. Experimental observations and a predictive conversion model. *Composites Part A: Applied Science and Manufacturing*. 2004;35(4):439–51.
156. Loix F, Badel P, Orgéas L, Geindreau C, Boisse P. Woven fabric permeability: From textile deformation to fluid flow mesoscale simulations. *Composites Science and Technology*. 2008;68(7–8):1624–30.
157. Liotier P-J, Govignon Q, Swery E, Drapier S, Bickerton S. Characterisation of woven flax fibres reinforcements: Effect of the shear on the in-plane permeability. *Journal of Composite Materials*. 2015;49(27):3415–30.
158. Meier R, Walbran A, Hahn C, Zaremba S. Methods to determine the permeability of dry textile reinforcements. *Journal of Plastics Technology*. 2014;10(4).
159. Okonkwo K, Simacek P, Advani SG, Parnas RS. Characterization of 3D fiber preform permeability tensor in radial flow using an inverse algorithm based on sensors and simulation. *Composites Part A: Applied Science and Manufacturing*. 2011;42(10):1283–92.
160. Gokce A, Chohra M, Advani SG, Walsh SM. Permeability estimation algorithm to simultaneously characterize the distribution media and the fabric preform in vacuum assisted resin transfer molding process. *Composites Science and Technology*. 2005;65(14):2129–39.

161. Lugo J, Simacek P, Advani SG. Analytic method to estimate multiple equivalent permeability components from a single rectilinear experiment in liquid composite molding processes. *Composites Part A: Applied Science and Manufacturing*. 2014;67:157–70.
162. Kaufmann M, Zenkert D, Åkermo M. Cost/weight optimization of composite prepreg structures for best draping strategy. *Composites Part A: Applied Science and Manufacturing*. 2010;41(4):464–72.
163. Schubel PJ. Cost modelling in polymer composite applications: Case study – Analysis of existing and automated manufacturing processes for a large wind turbine blade. *Composites Part B: Engineering*. 2012;43(3):953–60.
164. Potter K, Ward C, Hazra K. Improving the manufacture of complex geometries. In: *The 10th Composites UK Annual Conference*. Birmingham, United Kingdom; 2010.
165. Potluri P, Atkinson J. Automated manufacture of composites: handling, measurement of properties and lay-up simulations. *Composites Part A: Applied Science and Manufacturing*. 2003;34(6):493–501.
166. Lin H, Clifford MJ, Taylor PM, Long AC. 3D mathematical modelling for robotic pick up of textile composites. *Composites Part B: Engineering*. 2009;40(8):705–13.
167. Do D, John S, Herszberg I. 3D deformation models for the automated manufacture of composite components. *Composites Part A: Applied Science and Manufacturing*. 2006;37(9):1377–89.
168. Lukaszewicz DH-JA, Ward C, Potter KD. The engineering aspects of automated prepreg layup: History, present and future. *Composites Part B: Engineering*. 2012;43(3):997–1009.
169. Belhaj M, Deleglise M, Comas-Cardona S, Demouveau H, Binetruy C, Duval C, et al. Dry fiber automated placement of carbon fibrous preforms. *Composites Part B: Engineering*. 2013;50(0):107–11.
170. Magnussen CJ. *A fabric deformation methodology for the automation of fiber reinforced polymer composite manufacturing*. Master thesis, Iowa State University, United States; 2011.
171. Schlangen LA. *A methodology for the automation of dry fabric layup for fiber reinforced polymer composites*. Master thesis, Iowa State University, United States; 2012.
172. Zhu S. *An automated fabric layup machine for the manufacture of the fiber reinforced polymer composite*. Master thesis, Iowa State University, United States; 2013.
173. Haanappel SP, ten Thije RHW, Sachs U, Rietman B, Akkerman R. Formability analyses of uni-directional and textile reinforced thermoplastics. *Composites Part A: Applied Science and Manufacturing*. 2014;56:80–92.
174. Soulat D, Cheruet A, Boisse P. Simulation of continuous fibre reinforced thermoplastic forming using a shell finite element with transverse stress. *Computers & Structures*. 2006;84(13–14):888–903.
175. Jamin T, Dube M, Laberge Lebel L. Effect of stamp-forming parameters and bend radius on the mechanical performance of curved beam carbon fiber/polyphenylene sulfide specimens. *Journal of Composite Materials*. 2016;50(9):1213–25.
176. Chen S, Harper LT, Endruweit a., Warrior N a. Formability optimisation of fabric preforms by controlling material draw-in through in-plane constraints. *Composites Part A: Applied Science and Manufacturing*. 2015;76:10–9.
177. Potter K, Ward C. Draping processes for composites manufacture. In: *Advances in composites manufacturing and process design*. Woodhead Publishing; 2015. p. 93–109.
178. Bersee HE., Beukers A. Diaphragm forming of continuous fibre reinforced thermoplastics: influence of temperature, pressure and forming velocity on the forming of Upilex-R® diaphragms. *Composites Part A: Applied Science and Manufacturing*. 2002;33(7):949–58.

179. Diani J, Fayolle B, Gilormini P. A review on the Mullins effect. *European Polymer Journal*. 2009; 45(3):601–12.
180. Hallander P, Akermo M, Mattei C, Petersson M, Nyman T. An experimental study of mechanisms behind wrinkle development during forming of composite laminates. *Composites Part A: Applied Science and Manufacturing*. 2013;50:54–64.
181. Sjölander J, Hallander P, Åkermo M. Forming induced wrinkling of composite laminates: a numerical study on wrinkling mechanisms. *Composites Part A: Applied Science and Manufacturing*. 2015;81:41–51.
182. Alshahrani H, Hojjati M. Analysis of formability of thick composite component under double-diaphragm forming process. In: *2nd International Conference on Production Automation and Mechanical Engineering*. 2016. p. 185–9.
183. Krebs J, Friedrich K, Bhattacharyya D. A direct comparison of matched-die versus diaphragm forming. *Composites Part A: Applied Science and Manufacturing*. 1998;29:183–8.
184. Delaloye S, Niedermeier M. Optimization of the diaphragm forming process for continuous fibre-reinforced advanced thermoplastic composites. *Composites Manufacturing*. 1995;6(3):135–44.
185. Pantelakis S., Baxevani E. Optimization of the diaphragm forming process with regard to product quality and cost. *Composites Part A: Applied Science and Manufacturing*. 2002;33(4):459–70.
186. Pantelakis SG, Katsiropoulos CV, Labeas GN, Sibois H. A concept to optimize quality and cost in thermoplastic composite components applied to the production of helicopter canopies. *Composites Part A: Applied Science and Manufacturing*. 2009;40(5):595–606.
187. Terzaghi K. *Theoretical soil mechanics*. John Wiley & Sons; 1943.
188. Summerscales J, Searle TJ. Low-pressure (vacuum infusion) techniques for moulding large composite structures. *Proceedings of the Institution of Mechanical Engineers, Part L: Journal of Materials Design and Applications*. 2005;219(1):45–58.
189. Beckwith SW. Resin infusion technology: Part 3 – A detailed overview of RTM and VIP technologies. *SAMPE Journal*. 2007;43(4):66–70.
190. Hsiao K-T, Heider D. Vacuum assisted resin transfer molding (VARTM) in polymer matrix composites. In: Advani SG, Hsiao K-T, editors. *Manufacturing techniques for polymer matrix composites (PMCs)*. Woodhead Publishing; 2012. p. 310–47.
191. Jeong H. Effects of voids on the mechanical strength and ultrasonic attenuation of laminated composites. *Journal of Composite Materials*. 1997;31(3):276–92.
192. Chambers AR, Earl JS, Squires CA, Suhot MA. The effect of voids on the flexural fatigue performance of unidirectional carbon fibre composites developed for wind turbine applications. *International Journal of Fatigue*. 2006;28(10):1389–98.
193. Guo Z-S, Liu L, Zhang B-M, Du S. Critical void content for thermoset composite laminates. *Journal of Composite Materials*. 2009;43(17):1775–90.
194. Stamopoulos A, Tserpes K, Prucha P, Vavrik D. Evaluation of porosity effects on the mechanical properties of carbon fiber-reinforced plastic unidirectional laminates by X-ray computed tomography and mechanical testing. *Journal of Composite Materials*. 2015;50(15):2087–98.
195. Neitzel M, Blinzler M, Edelmann K, Hoecker F. Surface quality characterization of textile-reinforced thermoplastics. *Polymer Composites*. 2000;21(4):630–5.

196. Kanerva M, Saarela O. The peel ply surface treatment for adhesive bonding of composites: A review. *International Journal of Adhesion and Adhesives*. 2013;43(0):60–9.
197. Park CH, Lee W II. Modeling void formation and unsaturated flow in liquid composite molding processes: a survey and review. *Journal of Reinforced Plastics and Composites*. 2011;30(11):957–77.
198. Leclerc JS, Ruiz E. Porosity reduction using optimized flow velocity in Resin Transfer Molding. *Composites Part A: Applied Science and Manufacturing*. 2008;39(12):1859–68.
199. Park CH, Lebel A, Saouab A, Bréard J, Lee W II. Modeling and simulation of voids and saturation in liquid composite molding processes. *Composites Part A: Applied Science and Manufacturing*. 2011;42(6):658–68.
200. Rohatgi V, Patel N, Lee LJ. Experimental investigation of flow-induced microvoids during impregnation of unidirectional stitched fiberglass mat. *Polymer Composites*. 1996;17(2):161–70.
201. Hamidi YK, Aktas L, Altan MC. Three-dimensional features of void morphology in resin transfer molded composites. *Composites Science and Technology*. 2005;65(7–8):1306–20.
202. Ledru Y, Bernhart G, Piquet R, Schmidt F, Michel L. Coupled visco-mechanical and diffusion void growth modelling during composite curing. *Composites Science and Technology*. 2010;70(15):2139–45.
203. Wood JR, Bader MG. Void control for polymer-matrix composites (1): Theoretical and experimental methods for determining the growth and collapse of gas bubbles. *Composites Manufacturing*. 1994;5(3):139–47.
204. Wood JR, Bader MG. Void control for polymer-matrix composites (2): Experimental evaluation of a diffusion model for the growth and collapse of gas bubbles. *Composites Manufacturing*. 1994;5(3):149–58.
205. Labordus M. Voids and bubbles during vacuum infusion. In: *ICCM13: 13th International Conference of Composite Materials*. Beijing, China; 2001.
206. Schubel PJ, Parsons AJ, Lester EH, Warrior N a., Rudd CD. Characterisation of thermoset laminates for cosmetic automotive applications: Part II – Cure and residual volatile assessment. *Composites Part A: Applied Science and Manufacturing*. 2006;37(10):1747–56.
207. Lundstrom TS, Gebart BR, Lundemo CY. Void formation in RTM. *Journal of Reinforced Plastics and Composites*. 1993;12(12):1339–49.
208. Schubel PJ, Warrior N a., Kendall KN, Rudd CD. Characterisation of thermoset laminates for cosmetic automotive applications: Part I – Surface characterisation. *Composites Part A: Applied Science and Manufacturing*. 2006;37(10):1734–46.
209. Herring ML, Mardel JI, Fox BL. The effect of material selection and manufacturing process on the surface finish of carbon fibre composites. *Journal of Materials Processing Technology*. 2010;210(6–7):926–40.
210. Kim PJ, Lee DG. Surface quality and shrinkage of the composite bus housing panel manufactured by RTM. *Composite Structures*. 2002;57(1–4):211–20.
211. Schubel PJ, Johnson MS, Warrior N a., Rudd CD. Characterisation of thermoset laminates for cosmetic automotive applications: Part III – Shrinkage control via nanoscale reinforcement. *Composites Part A: Applied Science and Manufacturing*. 2006;37(10):1757–72.
212. Exner W, Kohn A, Szewieczek A, Opitz M, Mahrholz T, Sinapius M, et al. Determination of volumetric shrinkage of thermally cured thermosets using video-imaging. *Polymer Testing*. 2016;49:100–6.
213. Haider M, Hubert P, Lessard L. Cure shrinkage characterization and modeling of a polyester resin containing low profile additives. *Composites Part A: Applied Science and Manufacturing*. 2007;38(3):994–1009.
214. Lee DH, Lee W II, Kang MK. Analysis and minimization of void formation during resin transfer molding process. *Composites Science and Technology*. 2006;66(16):3281–9.

215. Olivero KA, Barraza HJ, O'Rear EA, Altan MC. Effect of injection rate and post-fill cure pressure on properties of resin transfer molded disks. *Journal of Composite Materials*. 2002;36(16):2011–28.
216. Barraza HJ, Hamidib YK, Aktasb L, O'Rear EA., Altan MC. Porosity reduction in the high-speed processing of glass-fiber composites by Resin Transfer Molding (RTM). *Journal of Composite Materials*. 2004;38(3):195–226.
217. Lundström TS, Gebart BR. Influence from process parameters on void formation in resin transfer molding. *Polymer Composites*. 1994;15(1):25–33.
218. Afendi M, Banks WM, Kirkwood D. Bubble free resin for infusion process. *Composites Part A: Applied Science and Manufacturing*. 2005;36(6):739–46.
219. Kuentzer N, Simacek P, Advani SG, Walsh S. Correlation of void distribution to VARTM manufacturing techniques. *Composites Part A: Applied Science and Manufacturing*. 2007;38(3):802–13.
220. Kedari VR, Farah BI, Hsiao K-T. Effects of vacuum pressure, inlet pressure, and mold temperature on the void content, volume fraction of polyester/e-glass fiber composites manufactured with VARTM process. *Journal of Composite Materials*. 2011;45(26):2727–42.
221. Gestring I, Mewes D. Degassing of molten polymers. *Chemical Engineering Science*. 2002;57(16):3415–26.
222. Govignon Q, Kazmi SMR, Hickey CMD, Bickerton S. Control of laminate quality for parts manufactured using the resin infusion process. In: *ICCM18: 18th International Conference of Composite Materials*. Jeju Island, Korea; 2011.
223. Acheson JA, Simacek P, Advani SG. The implications of fiber compaction and saturation on fully coupled VARTM simulation. *Composites Part A: Applied Science and Manufacturing*. 2004;35(2):159–69.
224. Simáček P, Advani SG. Desirable features in mold filling simulations for liquid composite molding processes. *Polymer Composites*. 2004;25(4):355–67.
225. Klunker F, Aranda S, Surjoseputro W, Wu W, Ziegmann G. Modelling the resin infusion process. Part II: Accounting for deformation of textiles by analogy to thermomechanical models. *Zeitschrift Kunststofftechnik/Journal of Plastics Technology*. 2012;(2):179–205.
226. Correia NC, Robitaille F, Long AC, Rudd CD, Šimáček P, Advani SG. Analysis of the vacuum infusion moulding process: I. Analytical formulation. *Composites Part A: Applied Science and Manufacturing*. 2005;36(12):1645–56.
227. Park CH, Saouab A. Analytical modeling of composite molding by resin infusion with flexible tooling: VARI and RFI processes. *Journal of Composite Materials*. 2009;43(18):1877–900.
228. Goncharova G, Cosson B, Deléglise Lagardère M. Analytical modeling of composite manufacturing by vacuum assisted infusion with minimal experimental characterization of random fabrics. *Journal of Materials Processing Technology*. 2015;219:173–80.
229. Koorevaar A. How flow analysis technology improves the vacuum infusion process. In: *ACMC/SAMPE Conference on Marine Composites*. 2003. p. 11–2.
230. Brouwer WD, van Herpt ECF., Labordus M. Vacuum injection moulding for large structural applications. *Composites Part A: Applied Science and Manufacturing*. 2003;34(6):551–8.
231. Montes N, Sanchez F, Falco A. Optimal flow behaviour formulation for LCM processes based on homotopy maps and flow pattern configuration spaces. In: *ICCM17: 17th International Conference of Composite Materials*. Edinburgh, United Kingdom; 2009.

232. Simacek P, Advani SG. Resin flow simulations in Liquid Composite Molding processes: recent advances and future directions. In: *ICCM17: 17th International Conference of Composite Materials*. Edinburgh, United Kingdom; 2009.
233. Yang B, Tang Q, Wang S, Jin T, Bi F. Three-dimensional numerical simulation of the filling stage in resin infusion process. *Journal of Composite Materials*. 2016;50(29):4171–86.
234. Aktas L, Bauman DP, Bowen ST, Saha MC, Altan MC. Effect of distribution media length and multiwalled carbon nanotubes on the formation of voids in VARTM composites. *Journal of Engineering Materials and Technology*. 2011;133(4):1–9.
235. Hsiao K-T, Mathur R, Advani SG, Gillespie J. W. J, Fink BK. A closed form solution for flow during the vacuum assisted resin transfer molding process. *Journal of Manufacturing Science and Engineering*. 2000;122(3):463–75.
236. Mathur R, Heider D, Hoffmann C, Gillespie JW, Advani SG, Fink BK. Flow front measurements and model validation in the vacuum assisted resin transfer molding process. *Polymer composites*. 2001;22(4):477–90.
237. Young SS, Jae RY. Modeling of resin infusion in vacuum assisted resin transfer molding. *Polymer Composites*. 2008;29(4):390–5.
238. Lawrence JM, Fried P, Advani SG. Automated manufacturing environment to address bulk permeability variations and race tracking in resin transfer molding by redirecting flow with auxiliary gates. *Composites Part A: Applied Science and Manufacturing*. 2005;36(8):1128–41.
239. Modi D, Correia N, Johnson M, Long A, Rudd C, Robitaille F. Active control of the vacuum infusion process. *Composites Part A: Applied Science and Manufacturing*. 2007;38(5):1271–87.
240. Swan S, Yuksel T, Kim D, Gurocak H. Automation of the vacuum assisted resin transfer molding process for recreational composite yachts. *Polymer Composites*. 2015 October.
241. Matsuzaki R, Kobayashi S, Todoroki A, Mizutani Y. Flow control by progressive forecasting using numerical simulation during vacuum-assisted resin transfer molding. *Composites Part A: Applied Science and Manufacturing*. 2013;45:79–87.
242. Gourichon B, Binetruy C, Krawczak P. Experimental investigation of high fiber tow count fabric unsaturation during RTM. *Composites Science and Technology*. 2006;66(7–8):976–82.
243. Patel N, Lee LJ. Modeling of void formation and removal in liquid composite molding. Part II: Model development and implementation. *Polymer Composites*. 1996;17(1):104–14.
244. Lundström TS. Bubble transport through constricted capillary tubes with application to resin transfer molding. *Polymer Composites*. 1996;17(6):770–9.
245. Vila J, Gonzalez C, LLorca J. Fabric compaction and infiltration during vacuum-assisted resin infusion with and without distribution medium. *Journal of Composite Materials*. 2016;51(5):687–703.
246. Chen D, Arakawa K, Xu C. Reduction of void content of vacuum-assisted resin transfer molded composites by infusion pressure control. *Polymer Composites*. 2015;36(9):1629–37.
247. Simacek P, Advani SG. Modeling resin flow and fiber tow saturation induced by distribution media collapse in VARTM. *Composites Science and Technology*. 2007;67(13):2757–69.
248. Caglar B, Yenilmez B, Sozer EM. Modeling of post-filling stage in vacuum infusion using compaction characterization. *Journal of Composite Materials*. 2014;49(16):1947–60.
249. Garschke C, Weimer C, Parlevliet PP, Fox BL. Out-of-autoclave cure cycle study of a resin film infusion process using in situ process monitoring. *Composites Part A: Applied Science and Manufacturing*. 2012;43(6):935–44.

250. Agius SL, Magniez KJC, Fox BL. Cure behaviour and void development within rapidly cured out-of-autoclave composites. *Composites Part B: Engineering*. 2013;47:230–7.
251. Hernández S, Sket F, Molina-Aldareguía JM, González C, Llorca J. Effect of curing cycle on void distribution and interlaminar shear strength in polymer-matrix composites. *Composites Science and Technology*. 2011;71(10):1331–41.
252. Hernández S, Sket F, González C, Llorca J. Optimization of curing cycle in carbon fiber-reinforced laminates: Void distribution and mechanical properties. *Composites Science and Technology*. 2013;85:73–82.
253. Tempelman E, Shercliff H, van Eyben BN. *Manufacturing and Design: understanding the principles of how things are made*. First edit. Elsevier Ltd; 2014.
254. Harrison P, Yu W-R, Long AC. Rate dependent modelling of the forming behaviour of viscous textile composites. *Composites Part A: Applied Science and Manufacturing*. 2011;42(11):1719–26.
255. Ashby MF. Processes and process selection. In: Ashby MF, editor. *Materials selection in mechanical design*. Fourth Edi. Oxford: Butterworth-Heinemann; 2011. p. 367–414.
256. Feraboli P, Masini A, Taraborrelli L, Pivetti A. Integrated development of CFRP structures for a topless high performance vehicle. *Composite Structures*. 2007;78(4):495–506.
257. Wood K. Composite leaf springs: Saving weight in production suspension systems. *Composites Technology*. 2014 February.
258. Andersson HM, Lundström TS, Langhans N. Computational fluid dynamics applied to the vacuum infusion process. *Polymer Composites*. 2005;26(2):231–9.
259. Carbon composite pedestrian bridge installed in Madrid. *Reinforced Plastics*. 2011;55(3):43–4.
260. Spirit ships first A350 spar component. *Reinforced Plastics*. 2011;55(1):4.
261. Kopp G, Beeh E, Schöll R, Kobilke A, Straßburger P, Krieschera M. New lightweight structures for advanced automotive vehicles – Safe and modular. *Procedia - Social and Behavioral Sciences*. 2012;48:350–62.
262. Geenen B. *Gaudi chair*. Available from: <http://bramgeenen.com/> [Accessed 2016 Nov 30].
263. Winther. *Bike trailer Dolphin NE*. Available from: <http://www.wintherbikes.com/product-items/dolphin-ne-trailer/> [Accessed 30th November 2016].
264. Sloan J. More and more composites blowing in the wind. *CompositesWorld*. 2016 August.
265. Candor. *Product line for radiotherapy*. Available from: <http://www.candor-dk.com/product-line/> [Accessed 30th November 2016].
266. Stellar. *Kayak Apex 75 ICF Sprint K1*. Available from: <http://www.stellarkayaks.com/apex-75.html> [Accessed 30th November 2016].
267. 2014 JEC Europe Review. *Composites Technology*. 2014 June.
268. Heider D, Simacek P, Dominauskas A, Deffor H, Advani S, Gillespie JW. Infusion design methodology for thick-section, low-permeability preforms using inter-laminar flow media. *Composites Part A: Applied Science and Manufacturing*. 2007;38(2):525–34.
269. Poodts E, Minak G, Mazzocchetti L, Giorgini L. Fabrication, process simulation and testing of a thick CFRP component using the RTM process. *Composites Part B: Engineering*. 2014;56:673–80.
270. Ruiz E, Trochu F. Numerical analysis of cure temperature and internal stresses in thin and thick RTM parts. *Composites Part A: Applied Science and Manufacturing*. 2005;36(6):806–26.
271. Esposito L, Sorrentino L, Penta F, Bellini C. Effect of curing overheating on interlaminar shear strength and its modelling in thick FRP laminates. *International Journal of Advanced Manufacturing Technology*. 2016;1–8.

272. Sorrentino L, Esposito L, Bellini C. A new methodology to evaluate the influence of curing overheating on the mechanical properties of thick FRP laminates. *Composites Part B: Engineering*. 2016;109(16):187–96.
273. Wisnow MR, Potter KD. Understanding composite distortion during processing. In: Long AC, editor. *Composite forming technologies*. Woodhead; 2007. p. 177–96.
274. Rogers W, Hoppins C, Gombos Z, Summerscales J. In-mould gel-coating of polymer composites: a review. *Journal of Cleaner Production*. 2014;70:282–91.
275. Bergström R, Piironen O, Ylhäinen A. Improving surface quality in vacuum infused parts. *Reinforced Plastics*. 2008;52(3):26–30.
276. Herring ML, Fox BL. The effect of a rapid curing process on the surface finish of a carbon fibre epoxy composite. *Composites Part B: Engineering*. 2011;42(5):1035–43.
277. Wang CS, Iobst SA. Reducing fiber readout of structural composite panels. *Journal of Reinforced Plastics and Composites*. 2008;28(19):2377–86.
278. Bénard Q, Fois M, Grisel M. Influence of fibre reinforcement and peel ply surface treatment towards adhesion of composite surfaces. *International Journal of Adhesion and Adhesives*. 2005;25(5):404–9.
279. Gombos ZJ, Summerscales J. In-mould gel-coating for polymer composites. *Composites Part A: Applied Science and Manufacturing*. 2016;91:203–10.
280. Toro N, Okoli OI, Wang HP. In-mold coating of composites manufactured by resin infusion between double flexible tooling process. *Journal of Reinforced Plastics and Composites*. 2005 May 1;24(7):725–33.
281. Puentes CA, Okoli OI, Park YB. Determination of effects of production parameters on the viability of polycarbonate films for achieving in-mold decoration in resin infused composite components. *Composites Part A: Applied Science and Manufacturing*. 2009;40(4):368–75.
282. Chiu P, Okoli OI. In-mold coating of composites manufactured by the resin infusion between double flexible tooling process by means of co-infusion. *Journal of Reinforced Plastics and Composites*. 2006;25(5):543–51.
283. Crump LS. *In-mold coating by a multiple step infusion process*. U. S. Patent 7,588,800 B2; 2009.
284. Solomon FA, Okoli OI. Experimental evaluation of co-infusion as a viable method for in-mold coating of composite components. *Journal of Reinforced Plastics and Composites*. 2009;28(16):1975–86.
285. Endruweit A, Long AC. Influence of stochastic variations in the fibre spacing on the permeability of bi-directional textile fabrics. *Composites Part A: Applied Science and Manufacturing*. 2006 May;37(5):679–94.
286. Endruweit A, Long AC, Robitaille F, Rudd CD. Influence of stochastic fibre angle variations on the permeability of bi-directional textile fabrics. *Composites Part A: Applied Science and Manufacturing*. 2006 Jan;37(1):122–32.
287. Skordos a. a., Sutcliffe MPF. Stochastic simulation of woven composites forming. *Composites Science and Technology*. 2008 Jan;68(1):283–96.
288. Brillant M, Hubert P. Modelling and characterization of thickness variations in L-shape out-of-autoclave laminates. In: *ICCM 18: 18th International Conference of Composite Materials*. Jeju Island, Korea; 2011.
289. Esawi AMK, Ashby MF. Cost estimates to guide pre-selection of processes. *Materials & Design*. 2003 Dec;24(8):605–16.
290. Bader MG. Selection of composite materials and manufacturing routes for cost-effective performance. *Composites Part A: Applied Science and Manufacturing*. 2002 Jul 1;33(7):913–34.

291. Weiland F, Weimer C, Dumont F, Katsiropoulos C V, Pantelakis SG, Sitaras I, et al. Process and cost modelling applied to manufacture of complex aerospace composite part. *Plastics, Rubber and Composites*. 2013;42(10):427–36.
292. Åkermo M, Åström BT. Modelling component cost in compression moulding of thermoplastic composite and sandwich components. *Composites Part A: Applied Science and Manufacturing*. 2000;31(4):319–33.
293. Baskaran M, Sarrionandia M, Aurrekoetxea J, Acosta J, Argarate U, Chico D. Manufacturing cost comparison of RTM, HP-RTM and CRTM for an automotive roof. In: *ECCM16: 16th European Conference on Composite Materials*. Sevilla, Spain; 2014. p. 22–6.
294. Hagnell MK, Åkermo M. A composite cost model for the aeronautical industry: Methodology and case study. *Composites Part B: Engineering*. 2015;79:254–61.
295. Mas Martínez M. *Estudio del proceso de curado de una resina epoxi de baja viscosidad mediante FT-IR y análisis de viscosidad*. Master thesis, Universitat Politècnica de Catalunya, Spain; 2013.
296. Jakobsen J. *Liquid composite moulding simulation*. Master thesis, Universitat Politècnica de Catalunya, Spain; 2014.
297. Montgomery DC. Two-level fractional factorial designs. In: *Design and analysis of experiments*. Fifth edit. John Wiley & Sons; 2000. p. 303–62.
298. Quinn GP, Keough MJ. Analysis of covariance. In: *Experimental design and data analysis for biologists*. Cambridge University Press; 2002. p. 339–58.
299. Kastner J, Plank B, Salaberger D, Sekelja J. Defect and Porosity Determination of Fibre Reinforced Polymers by X-ray Computed Tomography. In: *2nd International Symposium on NDT in Aerospace*. Hamburg, Germany; 2010.
300. Bodaghi M, Cristóvão C, Gomes R, Correia NC. Experimental characterization of voids in high fibre volume fraction composites processed by high injection pressure RTM. *Composites Part A: Applied Science and Manufacturing*. 2016;82:88–99.
301. Hurtado FJ, Kaiser AS, Viedma A, Diaz S. Numerical study of the vacuum infusion process for laminated composites with different fiber orientations. *Journal of Reinforced Plastics and Composites*. 2015;34(3): 196–212.
302. Loos AC, Tuncol G, Long K, Cano RJ, Jensen BJ, Weiser ES. Flow visualization and modeling of the resin infusion process during manufacture of fiber metal laminates By VARTM. In: *ICCM17: 17th International Conference of Composite Materials*. Edinburgh, United Kingdom; 2009.
303. Halimi F, Golzar M, Asadi P, Beheshty M. Core modifications of sandwich panels fabricated by vacuum-assisted resin transfer molding. *Journal of Composite Materials*. 2012;47(15):1853–63.
304. Montgomery DC. The 2k factorial design. In: *Design and analysis of experiments*. Fifth edit. John Wiley & Sons; 2000. p. 218–86.
305. Benjamini Y, Braun H. John Tukey's contributions to multiple comparisons. *ETS Research Report Series*. 2002 Dec 1;(2):i-27.
306. Wisnom MR, Jones MI, Hill GFJ. Interlaminar tensile strength of carbon fibre-epoxy specimen size, layup and manufacturing effects. *Advanced Composites Letters*. 2001;10(4):171–7.
307. Zhou G, Callahan J, Nash P, Ripley P, Rishton J. Investigation of interlaminar behaviour in angled laminate beams with crease. In: *ECCM15: 15th European Conference on Composite Materials*. Venice, Italy; 2012.

308. Makeev A, Seon G, Nikishkov Y, Lee E. Methods for assessment of interlaminar tensile strength of composite materials. *Journal of Composite Materials*. 2015;49(7):783–94.
309. Shivakumar K, Allen H, Avva V. Interlaminar tension strength of graphite/epoxy composite laminates. *AIAA journal*. 1994;32(7).
310. Hiel CC, Sumich M, Chappell DP. A curved beam test specimen for determining the interlaminar tensile strength of a laminated composite. *Journal of Composite Materials*. 1991;25:854–68.
311. Cui W, Liu T, Len J, Ruo R. Interlaminar tensile strength (ILTS) measurement of woven glass/polyester laminates using four-point curved beam specimen. *Composites Part A: Applied Science and Manufacturing*. 1996 Jan;27(11):1097–105.
312. Lekhnitskiĭ SG. *Anisotropic Plates*. Translated from the Second Russian Edition by S.W. Tsai and T. Cheron. New York: Gordon and Breach; 1968.
313. Kedward K, Wilson R, McLean S. Flexure of simply curved composite shapes. *Composites*. 1989;20(6): 527–36.
314. Cerda E, Mahadevan L. Geometry and physics of wrinkling. *Physical review letters*. 2003;90(7):74302.
315. Nayyar V, Ravi-Chandar K, Huang R. Stretch-induced stress patterns and wrinkles in hyperelastic thin sheets. *International Journal of Solids and Structures*. 2011;48(25–26):3471–83.
316. Roos R, Kress G, Barbezat M, Ermanni P. Enhanced model for interlaminar normal stress in singly curved laminates. *Composite Structures*. 2007 Oct;80(3):327–33.
317. Arca M a, Coker D. Experimental investigation of CNT effect on curved beam strength and interlaminar fracture toughness of CFRP laminates. *Journal of Physics: Conference Series*. 2014;524:12038.
318. Hufenbach W, Hornig a., Zhou B, Langkamp a., Gude M. Determination of strain rate dependent through-thickness tensile properties of textile reinforced thermoplastic composites using L-shaped beam specimens. *Composites Science and Technology*. 2011 May;71(8):1110–6.

Appendices

In the second volume of this thesis it is collected a series of appendices that provide supplementary information to this main document of the dissertation. These appendices are listed here below.

A. Cause and effect diagrams

B. Workbenches and equipment

C. Process monitoring

D. Specimen characterization

E. Light microscopy

F. Experimental design and data analysis